**UNIVERSITEIT ANTWERPEN**

**Faculteit Wetenschappen**

**Departement Fysica**

# Vortex Matter in Mesoscopic Superconductor / Ferromagnet Heterosystems

*A theoretical study of the critical parameters, the vortex configurations and flux pinning in superconductors textured by magnetic structures*

---

# Vortexmaterie in Mesoscopische Supergeleider / Ferromagneet Heterosystemen

*Een theoretische studie van de kritische parameters, de vortexconfiguraties en flux pinning in magnetisch gestructureerde supergeleiders*

Proefschrift voorgelegd tot het behalen van de graad van
doctor in de wetenschappen
aan de Universiteit Antwerpen te verdedigen door

**Milorad Milošević**

Promotor: Prof. dr. F. M. Peeters

Antwerpen, 2004

# Dankwoord

*De voorbije jaren, tijdens de voorbereiding van mijn doctoraatsthesis, heb ik de steun gekregen van een aantal mensen die ik hier speciaal wil vermelden.*

*In de eerste plaats wil ik mijn promotor François Peeters bedanken. Ik dank u, omdat u mij de kans gegeven heeft om naar België te komen, voor het geloof en vertrouwen in mijn kunnen. Ook bedankt voor de goede begeleiding, leerrijke discussies en de continuë motivatie. Uw enthousiasme werkte aanstekelijk, en ik had me geen betere promotor kunnen wensen.*

*Prof. Tadiću, neizmerno hvala na pruženoj šansi za ovo izuzetno naučno i životno iskustvo. Nadam se da sam bar delimično opravdao Vaše poverenje.*

*In the beginning of my PhD study, I had the privilege to collaborate with Sergey Yampolskii, whose example taught me a lot about hard work and patience in science. Hereby I also want to send my immense gratitude to Denis Vodolazov whose suggestions and explanations, besides the friendship, were crucial for my thesis.*

*Most of my research was motivated by experiments done in KULeuven. This seems as an appropriate moment to thank Margriet Van Bael, Martin Lange, and Dušan Golubović for their extraordinary work, continuous interest in my contributions in this field, and always fruitful discussions.*

*And, of course, many thanks to my colleagues: first among equal, Minghui, office-mates Michiel, Yun-Mi, Bartek and Alexei, Yosyp, Golib, Giovanni, my co-patriots Igor, Pedja and Vladan, Peter, Kwinten, Tom, Azamat, Leonardo, Wandemberg, Clara, György, Balazs, Bart, Karen, Ben, Algis, Egidijus, Irina, Jacques, Jirong, Joseph, het beste secretariaat in de wereld Lieff and Patsy, ...*

*Mijn vrienden uit Antwerpen wil ik ook bedanken omdat zij van mijn leven buiten de studies een prachtige tijd gemaakt hebben. Dino, Maria, Saša, Annemie, Darko, Leslie, Darko G., alle buren, mijn basket-vrienden van Red Vic, bedankt voor alles.*

*Ipak, moja najveća podrška leži u ljudima koje u srcu nosim. U celokupnoj rodbini, u prijateljima, Nemanji, Duci, Pejki, Ani, Dragani, Nenadu, Željku, koji u Srbiji strpljivo čekaju na svaki moj mail, a uvek mi se podjednako obraduju, starim liscima iz Omladinske - Neksiju, Vladi i Miletu, i damama Cici i Gogi, i naravno Oliveri koja trpi sve moje hirove.*

*I na kraju, nemam dovoljno reči da iskažem zahvalnost i ljubav svojim roditeljima, za beskrajno strpljenje, ogromnu veru i podsticaj, i toliko mnogo toga žrtvovanog za mene i moje napredovanje.*

*Miško*
*July, 2004.*

# *Contents*

# 1

# *Introduction*

Superconductivity and ferromagnetism are two of the most important collective states in solid state physics and their interaction has been studied for several decades. They seem to be extremely similar in their appearance, in the nature of their occurrence, and from many other points of view. However, since the strong internal fields in ferromagnets have a destructive action on the superconducting Cooper pairs, the ferromagnetism and superconductivity have also been considered as two antagonistic phenomena for a long time. Creating artificial hybrid nanostructures composed of both superconductors (SC) and ferromagnets (FM) gives rise to a lot of new physical phenomena like the appearance of the $\pi$-phase in FM/SC multilayers [1], or strong vortex pinning in SC films by arrays of magnetic dots [2]. Systems composed of alternating magnetic and superconductive layers are of interest not only because they are model systems for the interplay of competing superconducting and magnetic order parameters, but also because of numerous possible applications. The ongoing rapid miniaturization of electronic circuits requires access to increasingly smaller electrical components and superconducting microelectronics is one of the favorites that are likely to emerge after the silicon era. Unfortunately, the superconducting state is very fragile and is destroyed when the magnetic field $H$, the current density $j$ or the temperature $T$ exceed their corresponding critical values. Intense efforts have been made to optimize these parameters and

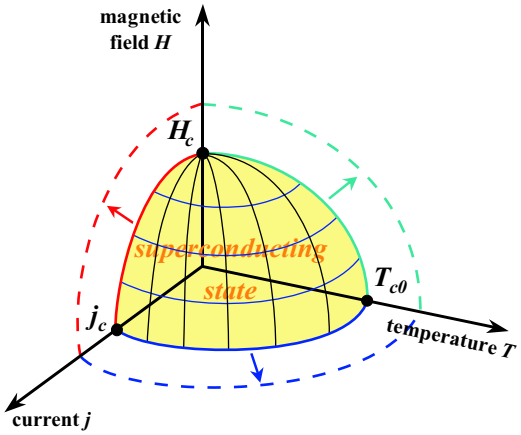


FIG. 1.1: Schematic diagram of the expansion of the critical parameters of the superconductor [after Ref. [3]].

to enlarge the boundaries of the superconducting state in the $(T, j, H)$-space (see Fig. 1.1).

The electrical and magnetic properties of superconducting materials are completely changed when the sample boundaries, playing the role of a confining potential, or the sample composition are manipulated at a scale of the order of one of the characteristic length scales. Therefore, new physical properties can be expected in mesoscopic superconducting samples with sizes comparable to the coherence length $\xi$ or the magnetic penetration depth $\lambda$ [4, 5]. In this thesis we investigate theoretically how the critical parameters of mesoscopic superconductors can be improved and how the superconducting state looks alike. The aim of this thesis is to describe the effects of depositing ferromagnetic structures on superconductors. In particular, such nanostructured ferromagnets strongly alter the vortex structure in its neighborhood. Furthermore, magnetic dots act as efficient pinning centra for external flux lines, leading to an increase of $j_c$ and $H_c$ (see Fig. 1.1). The influence of anisotropy, geometry, position and dimensions of the ferromagnet (single or regular lattice), as well as an additional homogeneous magnetic field, on the critical parameters of the superconductor, is investigated.
The thesis consists of five chapters:

**Chapter 1** gives a short introduction to some theoretical and experimental aspects of superconductivity and magnetism. We present the derivation of the Ginzburg-Landau equations which are the central equations in the theoretical framework of this thesis. The characteristic length scales and the difference between type-I and type-II superconductors are discussed. For mesoscopic

superconductors we define giant vortex and multivortex states, and the vorticity $L$ which characterizes the different vortex configurations. We also discuss briefly vortex pinning in type-II superconductors. The second part of this chapter is devoted to the basic concepts of magnetism and provides a description of magnetostatic calculations. Finally, the applications of hybrid ferromagnet/superconductor nanosystems and their experimental realizations are discussed.

**Chapter 2** presents theoretical results on the magnetic pinning of vortices in superconducting films by single magnets. Within the London approximation, we investigate the vortex pinning properties of ferromagnets of different magnetization orientation (in- or out-of-plane) and geometry (disks, rings, squares, triangles, asymmetrical magnets with cavities, etc.). We also discuss the possible vortex configurations, with special emphasis on the appearance of antivortices in the system.

**Chapter 3** describes the superconducting state of a thin mesoscopic superconducting disk with a magnetic dot or current loop on top. In the light of recent experiments [6, 7], we investigate using the Ginzburg-Landau theory the different possible vortex states which can nucleate in the disk, depending on its radius $R$ and the properties of the magnetic structure. In the second part of this chapter, we show the $H - R$ and $H - T$ phase diagrams, with several important features.

**Chapter 4** reports on the vortex structure of a superconducting film with a single magnetic dot on top. Due to the phase conservation, we found, within the Ginzburg-Landau theory, a shell-structured vortex-antivortex configuration with total vorticity zero. In these new vortex states, giant vortex is surrounded by ring(s) of antivortices. We study the properties of this "vortex molecule" depending on the size and shape of the magnet (circular or square disks).

**Chapter 5** finally deals with superconducting films with regular arrays of magnetic dots on top. First, we investigate the SC/FM structures where the stray field of the magnetic dots is sufficiently large to generate vortices in the superconductor even in zero applied field. In the second part, we add the homogeneous external magnetic field, and study the pinning phenomena, commensurability effects and the so-called field-polarity dependent pinning. At last, we give the theoretical interpretation of the recently experimentally observed [8] *magnetic-field-induced superconductivity* phenomenon.

## 1.1 INTRODUCTION TO SUPERCONDUCTIVITY

### 1.1.1 Historical overview

Superconductivity was discovered in 1911 by Heike Kamerlingh Onnes, the Dutch physicist known for his research into phenomona at extremely low temperature. In 1908, Onnes had become the first person to liquify helium, which resulted in the Nobel prize in 1913. He was investigating the electrical properties of various substances at liquid helium temperature (4.2 degrees Kelvin) when he noticed that the resistivity of mercury dropped abruptly at 4.2K to a value below the resolution of his instruments [see Fig. 1.2]. The same properties were observed in some other metals, such as lead and tin. This new phenomenon, on account of its extraordinary electrical properties, was called *superconductivity*.

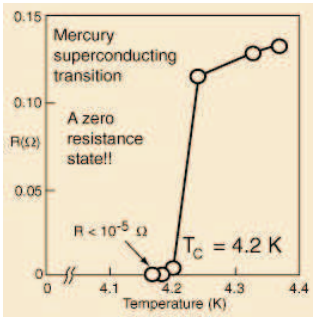


FIG. 1.2: The resistance of a specimen of mercury versus absolute temperature which marked the discovery of superconductivity [from Ref. [9]].

By 1933 W. Meissner and R. Ochsenfeld discovered that superconductors are more than a perfect conductor of electricity, they also have an interesting magnetic property of excluding a magnetic field when cooled through the critical temperature [see Fig. 1.3] [10]. A superconductor will not allow a magnetic field to penetrate its interior. It causes currents to flow that generate a magnetic field inside the superconductor that just balances the field that would have otherwise penetrated the material. This effect, called the *Meissner effect* will occur only if the magnetic field is relatively small. If the magnetic field becomes too great, it penetrates the interior of the metal and the metal loses its superconductivity.

Whenever a new scientific discovery is made, researchers must strive to explain it theoretically. However, it took more than two decades after the experimental discovery of superconductivity, before the first phenomenological theory describing the superconducting mechanism was developed by brothers London (in 1935, see paragraph 1.1.1.2) [11]. Although macroscopic, this theory proved to be useful for describing the superconducting behavior and vortex states in extreme type-II superconductors. However, the London theory treats vortices as point-like objects and does not take into account the finite size and

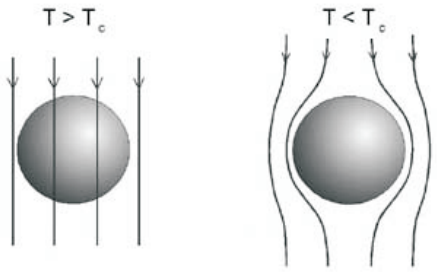


Fig. 1.3: Meissner effect in a superconducting sphere cooled under the critical temperature in a constant applied magnetic field. Below the transition temperature, the magnetic field lines are ejected from the sphere.

the inner structure of the vortex. In 1950, the phenomenological Ginzburg-Landau theory of superconductivity was proposed by Landau and Ginzburg (see paragraph 1.1.1.3) [12]. This theory, which combined Landau's theory of second-order phase transitions with a Schrödinger-like wave equation, had great success in explaining the macroscopic properties of superconducters. In particular, Abrikosov showed that Ginzburg-Landau theory predicts the division of superconductors into two categories now referred to as type-I and type-II, and described the mixed state of type-II superconductors [13]. The microscopic theory of superconductivity was finally proposed in 1957 by Bardeen, Cooper, and Schrieffer (see paragraph 1.1.1.4) [14]. The BCS theory explained the superconducting current as a superfluid of "Cooper pairs", pairs of electrons interacting through the exchange of phonons. In 1959, Gor'kov showed that the BCS theory reduced to the Ginzburg-Landau theory close to the critical temperature. For their work, Bardeen, Cooper, and Schrieffer received the Nobel Prize in 1972. This theory, which is based on the fact that pairs of electrons are formed proved, however, to be inadequate for explaining superconductivity in the technically most important materials. These type-II superconductors allow superconductivity and magnetism to exist at the same time and remain superconductive in high magnetic fields. Alexei Abrikosov succeeded in explaining this phenomenon theoretically. His starting point was a theory that had been formulated for type-I superconductors by Vitaly Ginzburg and others, but which proved to be so comprehensive that it was also valid for the new type. Although these theories were formulated in the 1950s, they have gained renewed importance in the rapid development of materials with completely new properties. That is why Abrikosov and Ginzburg were awarded the Nobel Prize for their contributions to the theory of superconductivity in 2003, together with Anthony Leggett who formulated the decisive theory explaining how the atoms interact and are ordered in superfluids, in the 1970s [15].

| Laureat | Discovery or invention awarded by Nobel prize | Year of discovery | Year of award |
|---|---|---|---|
| H. Kamerlingh Onnes | First to liquefy helium (led to discovery of superconductivity) | 1911 | 1913 |
| John Bardeen<br>Leon N. Cooper<br>J. Robert Schrieffer | Development of BCS theory | 1957 | 1972 |
| Leo Esaki | Tunnelling phenomena in semiconductors (Esaki diode) | 1958 | 1973 |
| Ivar Giaever | Experiments on tunnelling in superconductors | 1960 | |
| Brian D. Josephson | Theoretical formulation of the Josephson effect | 1962 | |
| J. Georg Bednorz<br>Alexander Müller | Discovery of High-$T_c$ superconductors | 1986 | 1987 |
| Vitaly Ginzburg | The Ginzburg-Landau theory and following contributions | 1950 | 2003 |
| Alexei Abrikosov | Theoretical explanation of Type-II superconductivity | 1957 | |
| Anthony Leggett | Theory of superfluidity | 1975 | |

Table 1.1: Nobel prize laureates in the field of superconductivity.

The breakthrough in the understanding of the quantum mechanical basis of superconductivity led to further progress in superconducting circuits and components: Brian D. Josephson analyzed the transfer of superconducting carriers between two superconducting metals, separated by a very thin layer of normal-conducting material. He found that the quantum phase, which determines the transport properties, is an oscillating function of the voltage applied over this kind of junction. The Josephson effect has important applications in precision measurements, since it establishes a relation between voltage and frequency scales. Josephson received one-half of the Physics Nobel Prize for 1973. Ivar Giaever, who invented and studied the detailed properties of the "tunnel junction", an electronic component based on superconductivity, shared the second half with Leo Esaki for work on tunnelling phenomena in semiconductors.

Just when it became a general belief that superconductivity as phenomenon was explained, new surprises appeared on the horizon. In 1986, K. Alex Müller and J. Georg Bednorz of IBM Zurich published results showing indications of superconductivity in lanthanum-based cuprate perovskite material at about 35K (12K better than the highest known critical temperature at the time, for $Nb_3Ge$), the first high-$T_c$ superconductor (HTS) [17]. It was shortly found that replacing lanthanum with yttrium, i.e. making YBCO, raised the critical temperature to 92K, which was important because liquid nitrogen could then be used as a refrigerant (at atmospheric pressure, the boiling point of nitrogen is 77K). Bednorz and Müller received the 1987 Nobel Prize in Physics for their groundbreaking work. At the time Bednorz and Müller began their work, the idea of a high-temperature ceramic superconductor was considered to be so crazy that they did their research quietly - not even telling their colleagues what they were doing. They tried more than two hundred combinations of ceramic oxides before achieving success. By 1993, cuprates with a $T_c$ of 133K at atmospheric pressure were found ($HgBa_2Ca_2Cu_3O_8$) [18]. After this discovery

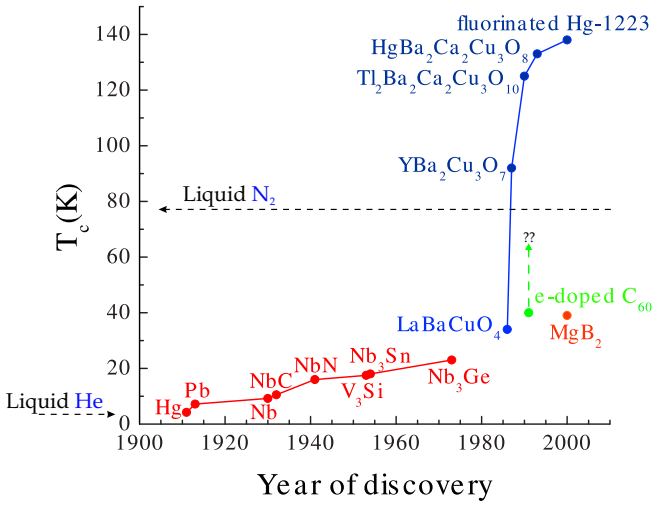


Fig. 1.4: The critical temperature $T_c$ of different superconductors versus their year of discovery: red dots denote the low $T_c$ superconductors, blue the cuprates, green the fullerenes and orange $MgB_2$ [after Ref. [20]].

further efforts to find cuprates with higher $T_c$ failed until 2000, when a slight increase in the transition temperature was detected for fluorinated Hg-1223 samples ($T_c = 138$K) [19].

The BCS theory was unable to describe many properties of the high-$T_c$ materials. The electron-phonon mechanism became questionable. New mechanisms, such as the so-called d-wave pairing, has been proposed. But, at present, the question of why the high-$T_c$ superconductors have such high-$T_c$ values is still unanswered.

Crystalline $C_{60}$ is normally an insulator, but in 1991 it was shown that electron-doped $C_{60}$ fullerenes are superconducting with a critical temperature up to 40K [21]. The possibility of raising the critical temperature by field-effect hole-doping or increasing the intermolecular distance was recently of strong interest, although retracted work of Schön *et al.* has not been reproduced until now. Dagotto *et al.* suggested that the $T_c$ could be increased further, effectively ending the dominance of cuprates in the high-$T_c$ arena [22]. Also smaller $C_{36}$ fullerenes are expected to have higher critical temperatures [23].

Recently, magnetization and resistivity measurements established a transition temperature of 39K in $MgB_2$ [24], which is the highest yet known for a non-copper-oxide and non-fullerene superconductor. Furthermore, this material is expected to be very useful for applications, due to its enhanced mechanical properties, as compared to high-$T_c$ superconductors.

The causes for and consequences of these observations pose great challenges to physicists, chemists, and materials scientists. Even though "the liquid nitrogen barrier" has been broken, many of the great promises of superconductivity technology have yet to be realized. The difficulties with the materials can be attributed to many of the material and engineering problems of HTS's, e.g. making long HTS wire than can carry large current without energy loss and can retain excellent superconducting properties over long periods of time without chemical and physical degradation.

However, commercial applications of HTS technology in fields such as electric power, transportation, electronics and medicine are now appearing. Current applications of HTS include thin films, magnetic resonance imaging (MRI), wireless communication filters, and ultra-fast computer chips. By the year 2010, it is estimated that the global superconductivity market will be in excess of 50 million.

*1.1.1.1 Applications of superconductors* Soon after Kamerlingh Onnes discovered superconductivity, scientists began dreaming up practical applications for this strange new phenomenon. Powerful new superconducting magnets could be made much smaller than a resistive magnet, because the windings could carry large currents with no energy loss. Generators wound with superconductors could generate the same amount of electricity with smaller equipment and less energy. Once the electricity was generated it could be distributed through superconducting wires. Energy could be stored in superconducting coils for long periods of time without significant loss.

The recent discovery of high temperature superconductors brings us a giant step closer to the dream of early scientists. Applications currently being explored are mostly extensions of current technology used with the low temperature superconductors. Current applications of high temperature superconductors include; magnetic shielding devices, medical imaging systems, superconducting quantum interference devices (SQUIDS), infrared sensors, analog signal processing devices, and microwave devices. As our understanding of the properties of superconducting material increases, applications such as; power transmission, superconducting magnets in generators, energy storage devices, particle accelerators, levitated vehicle transportation, rotating machinery, and magnetic separators will become more practical.

The ability of superconductors to conduct electricity with zero resistance can be exploited in the use of electrical transmission lines. Currently, a substantial fraction of electricity is lost as heat through resistance associated with traditional conductors such as copper or aluminum. A large scale shift to superconductivity technology depends on whether wires can be prepared from the brittle ceramics that retain their superconductivity at 77 K while supporting large current densities.

The field of electronics holds great promise for practical applications of superconductors. The miniaturization and increased speed of computer chips are

limited by the generation of heat and the charging time of capacitors due to the resistance of the interconnecting metal films. The use of new superconductive films may result in more densely packed chips which could transmit information more rapidly by several orders of magnitude. Superconducting electronics have achieved impressive accomplishments in the field of digital electronics. Logic delays of 13 picoseconds and switching times of 9 picoseconds have been experimentally demonstrated. Through the use of basic Josephson junctions scientists are able to make very sensitive microwave detectors, magnetometers, SQUIDs and very stable voltage sources.

The use of superconductors for transportation has already been established using liquid helium as a refrigerant. Prototype levitated trains have been constructed in Japan by using superconducting magnets.

Superconducting magnets are already crucial components of several technologies. Magnetic resonance imaging (MRI) is playing an ever increasing role in diagnostic medicine. The intense magnetic fields that are needed for these instruments are a perfect application of superconductors. Similarly, particle accelerators used in high-energy physics studies are very dependent on high-field superconducting magnets.

New applications of superconductors will increase with critical temperature. Liquid nitrogen based superconductors has provided industry more flexibility to utilize superconductivity as compared to liquid helium superconductors. The possible discovery of room temperature superconductors has the potential to bring superconducting devices into our every-day lives.

High-temperature superconductors are recent innovations from scientific research laboratories. New commercial innovations begin with the existing technological knowledge generated by the research scientist. The work of commercialization centers on the development of new products and the engineering needed to implement the new technology. Superconductivity has had a long history as a specialized field of physics. Through the collaborative efforts of government funded research, independent research groups and commercial industries, applications of new high-temperature superconductors will be in the not so distant future. Time lags however, between new discoveries and practical applications are often great. The discovery of the laser in the early 60's has only recently been appreciated today through applications such as laser surgery, laser optical communication, and compact disc players. After the discovery of the transistor in 1947, it took almost 40 years to introduce the one megabyte memory chip which is vital to today's powerful computers. Modern discoveries in superconductivity go far beyond piece-meal improvements in electric devices. They have opened the door on a totally new technology and stretch the imagination to the discovery of new applications. Future generations will witness significant changes in electricity generation, transmission and storage; impacts in microelectronics, communication, and computers; and advances in solid state science. If history serves as a guide, the wonderland of superconductor applications is destined to be achievable in the foreseeable future with

determination, persistence and patience all guided by vision and imaginative experimentation.

*1.1.1.2 London theory* More than 20 years after the discovery of superconductivity, the theoreticians developed the first phenomenological theory to describe this phenomenon. It was proposed by brothers London in 1935 [11]. The first assumption of this theory is that Newton's $2^{nd}$ law can be written in the following form:

$$m^* \frac{d\vec{v}_s}{dt} = -e^* \vec{E}, \tag{1.1}$$

where $m^*$ is the mass of the supercurrent charge carriers, $e^*$ is the charge of the carriers, $\vec{v}_s$ is the supercurrent velocity, and $\vec{E}$ is the applied electric field. If one takes the supercurrent density to be of the form $\vec{j}_s = -e\vec{v}_s n_s$, where $n_s$ is the superconducting carrier density, then the above equation becomes

$$\frac{\partial \vec{j}_s}{\partial t} = \frac{n_s e^2}{m^*} \vec{E} \ . \tag{1.2}$$

With the inclusion of Faraday's law, one obtains the following relation:

$$\frac{\partial}{\partial t} \left[ \vec{\nabla} \times \vec{j}_s + \frac{n_s e^2}{m^* c} \vec{H} \right] = 0. \tag{1.3}$$

Such a result is true of any perfect conductor. However, notice that any temporally constant value of $\vec{j}_s$ and magnetic field $\vec{H}$ will satisfy the above relation. Hence, a magnetic field that penetrated the sample in the normal state would be locked into the interior of the crystal as it passed into the superconducting phase. This, of course, does not happen, so the London brothers final assumption was to restrict the family of solutions of the above equation to those that satisfy:

$$\vec{\nabla} \times \vec{j}_s = -\frac{n_s e^2}{m^* c} \vec{H}. \tag{1.4}$$

This equation states that dissipationless supercurrents flow at the surface of the crystal to completely shield the sample interior from the external magnetic field. Moreover, the above relation also predicts that any magnetic flux initially passing through the crystal will be completely expelled upon entering into the superconducting state.

The combination of the equation (1.4) with the Maxwell equation for the magnetic field $\vec{\nabla} \times \vec{H} = 4\pi \vec{j}_s / c$ leads to

$$\vec{\nabla}^2 \vec{H} = \frac{1}{\lambda_L^2} \vec{H}, \tag{1.5}$$

with

$$\lambda_L = \sqrt{\frac{m^* c^2}{4\pi n_s e^2}}. \tag{1.6}$$

The solution to this $2^{nd}$ order partial differential equation for a slab is simply a decaying exponential of the form $H = H' \exp(-x/\lambda_L)$. Thus one defines the first characteristic length scale of a superconductor, $\lambda_L$, the London penetration depth, which is the direct analog of the skin depth in a metal. It is simply the characteristic length that an external magnetic field can penetrate into the bulk of a superconducting crystal before decaying away. For atomic superconductors like Pb, Hg, and Sn, the penetration depth is on the order of nanometers.

Without giving a microscopic explanation of the superconducting mechanism, the London theory proved to be successful in describing the superconducting behavior and vortex states in extreme type-II superconductors, where vortices can be considered as point-like objects. However, for non-extreme type-II superconductors, the London theory does not give sufficiently accurate information about the vortex structure, and it is this information that is one of the important aspects of this thesis.

*1.1.1.3 Ginzburg-Landau theory* The GL theory (Ginzburg and Landau, 1950 [12]) extends Landau's theory of second-order phase transitions [25] to a spatially varying complex order parameter $\psi(\vec{r})$ ($|\psi(\vec{r})|^2 = n_s/2$ is a complex order parameter which is nonzero at $T < T_c$ and vanishes at $T \geq T_c$ through a second order phase transition). The resulting gradient term is made gauge-invariant by combining it with the vector potential $\vec{A}(\vec{r})$ where $\vec{\nabla} \times \vec{A}(\vec{r}) = \vec{H}(\vec{r})$ is the local magnetic field.

The two Ginzburg-Landau equations are obtained by minimization of the GL free energy functional $\mathcal{F}\{\psi, \vec{A}\}$ with respect to $\psi$ and $\vec{A}$, i.e. from $\delta\mathcal{F}/\delta\psi = 0$ and $\delta\mathcal{F}/\delta\vec{A} = 0$:

$$\begin{aligned} \mathcal{F}\{\psi, \vec{A}\} &= \frac{H_c^2}{4\pi} \int \Big[ -|\psi|^2 + \frac{1}{2}|\psi|^4 + \frac{1}{2}|(-i\nabla - \mathbf{A})\psi|^2 \\ &\quad + \kappa^2 (\vec{H} - \vec{H}_0)^2 \Big] \, dV. \end{aligned} \tag{1.7}$$

where $\vec{H}_0$ denotes the applied magnetic field. Eq. (1.7) is given in dimensionless form, where all distances are measured in units of the coherence length $\xi$, the vector potential $\vec{A}$ in $c\hbar/2e\xi$, the magnetic field $\vec{H}$ in $H_{c2} = c\hbar/2e\xi^2 = \kappa\sqrt{2}H_c$, and the order parameter $\psi$ in $\psi_0 = \sqrt{-\alpha/\beta}$, such that $|\psi| = 1$ in the Meissner state and $|\psi| = 0$ in the normal conducting state, with $\alpha$, $\beta$ being the GL coefficients. The derivation of the GL equations and its validity is described in full detail in section 1.3.

If desired, the electric field $\vec{E} = -\partial\vec{A}/\partial t$ and the time dependence may be introduced by the assumption $\partial\psi/\partial t = -\gamma\delta\mathcal{F}/\delta\psi$ with $\gamma = \text{const}$ [26]. An extension to anisotropic non-cubic superconductors is possible by multiplication of the gradient term in Eq. (1.7) by an "effective mass tensor" [27]. For the $H_{c2}$-anisotropy in cubic superconductors (like Nb) see Ref. [28].

The phenomenological GL theory is one of the most elegant and powerful concepts in physics, which was applied not only to superconductivity (see textbooks [29, 31–33]) but also to other phase transitions, to nonlinear dynamics, to dissipative systems with self-organizing pattern formation, and even to cosmology (melting of a lattice of "cosmic strings", Ref. [34]; vortex lattice in electro-weak theory, Ref. [35]). With this theory it became possible to describe spatial distribution of superconducting electrons in type-I and type-II superconductors, taking into account the finite size of the vortices. This was impossible within the framework of the London theory.

*1.1.1.4 BCS theory* In 1957, the microscopic mechanism of superconductivity was described by Bardeen, Cooper and Schrieffer [14]. The formalism of this theory is much more complex than the one of the Ginzburg-Landau theory which will be used in the major part of this thesis. The vortex structure and the critical parameters can be precisely calculated using the Ginzburg-Landau theory and the microscopic level is not necessary at all for the purpose of this thesis. Therefore, the discussion of the BCS theory will be limited to the basics.

BCS theory starts from the assumption that there is some attraction between electrons, which can overcome the Coulomb repulsion. In many superconductors, the attractive interaction between electrons (necessary for pairing) is brought about indirectly by the interaction between the electrons and the vibrating crystal lattice (the phonons). Roughly speaking, the picture is the following: An electron moving through a conductor will cause a slight increase in concentration of positive charges in the lattice around it; this increase in turn can attract another electron. In effect, the two electrons are then held together with a certain binding energy. If this binding energy is higher than the energy provided by kicks from oscillating atoms in the conductor (which is true at low temperatures), then the electron pair will stick together and resist all kicks, thus not experiencing resistance. However, the results of BCS theory do not depend on the origin of the attractive interaction. Note that the original results of BCS (discussed below) were describing an "s-wave" superconducting state, which is the rule among low-temperature superconductors but is not realized in many "unconventional superconductors", such as the "d-wave" high-temperature superconductors. Extensions of BCS theory exist to describe these other cases, although they are insufficient to completely describe the observed features of high-temperature superconductivity.

Therefore, BCS theory gives an approximation for the quantum-mechanical state of the system of (attractively interacting) electrons inside the metal. This state is now known as the "BCS state". Whereas in the normal metal electrons move independently, in the BCS state they are bound into "Cooper pairs" by the attractive interaction [36].

BCS theory includes several important theoretical predictions that are independent of the details of the interaction (note that the quantitative predictions

mentioned below hold only for sufficiently weak attraction between the electrons, which is however fulfilled for many low temperature superconductors - the so-called "weak-coupling case"). These have been confirmed in numerous experiments:

- Since the electrons are bound into Cooper pairs, a finite amount of energy is needed to break these apart into two independent electrons. This means there is an energy gap for single-particle excitation, unlike in the normal metal (where the state of an electron can be changed by adding an arbitrarily small amount of energy). This energy gap is highest at low temperatures but vanishes at the transition temperature when superconductivity ceases to exist. BCS theory correctly predicts the variation of this gap with temperature. It also gives an expression that shows how the gap grows with the strength of the attractive interaction and the (normal phase) density of states at the Fermi energy. Furthermore, it describes how the density of states is changed on entering the superconducting state, where there are no electronic states any more at the Fermi energy. The energy gap is most directly observed in tunneling experiments and in reflection of microwaves from the superconductor.

- The ratio between the value of the energy gap at zero temperature and the value of the superconducting transition temperature (expressed in energy units) takes the universal value of 3.5, independent of material.

- Due to the energy gap, the specific heat of the superconductor is suppressed strongly (exponentially) at low temperatures, there being no thermal excitations left. However, before reaching the transition temperature, the specific heat of the superconductor becomes even higher than that of the normal conductor (measured immediately above the transition) and the ratio of these two values is universally given by 2.5.

- BCS theory correctly predicts the Meissner effect, i.e. the expulsion of a magnetic field from the superconductor and the variation of the penetration depth (the extent of the screening currents flowing below the metal's surface) with temperature.

- It also describes the variation of the critical magnetic field (above which the superconductor can no longer expel the field but becomes normalconducting) with temperature. BCS theory relates the value of the critical field at zero temperature to the value of the transition temperature and the density of states at the Fermi energy.

In 1959 Gor'kov showed that the Ginzburg-Landau theory was just a limiting form of the BCS theory, valid near $T_c$ and suitable to deal with spatially varying situations [16]. He showed that the order parameter $\Psi$ can be seen as the wavefunction of the center-of-mass motion of the Cooper-pairs.

Obviously, the BCS theory provides a microscopic foundation of the phenomenological London and Ginzburg-Landau theories, which both can be derived as a limiting case of the BCS theory. However, the GL theory has proven to be very useful to explore numerous superconducting phenomena. Therefore this theory will be described in more detail in the next paragraphs.

### 1.1.2 Derivation of the Ginzburg-Landau theory and the general boundary condition

In 1950, Ginzburg and Landau developed a phenomenological theory in which they introduced the spatially varying wavefunction $\Psi(\vec{r})$ as complex order parameter which vanishes when superconductor is heated above the critical temperature $T_c$ (the second order transition). The Ginzburg-Landau theory is actually based on Landau's general theory of second order phase transitions. According to this theory, the free energy may be expanded in powers of the order parameter, close to the superconducting/normal transition at the critical temperature $T_c$, where the order parameter is small. From this assumption directly follows that the GL theory is in principle valid only near $T_c$. In reality, this theory has proven to be very useful even deep in the superconducting state.

In what follows, we will describe the main principles of the GL theory and derive the well known Ginzburg-Landau equations. We use the standard notation (see, for example, textbooks [29, 31, 32]), where $\vec{H}(\vec{r})$ denotes the local value of the magnetic field, related to the vector potential as $\mathrm{rot}\vec{A}(\vec{r})$. The magnetic induction $\vec{B}$ can be found as the averaged value of $\vec{H}$ over microscopic lengths and will be written as $\langle\vec{H}\rangle$. The applied field (in general, inhomogeneous) will be denoted by $\vec{H}_0(\vec{r})$.

**The GL-functional for the free energy** Near $T_c$ the Gibbs free energy of a superconductor can be expressed as [32]

$$\mathcal{G}_{sH_0} - \mathcal{G}_{nH_0} = \int \left\{ \alpha |\Psi|^2 + \frac{1}{2}\beta |\Psi|^4 + \frac{1}{2m^*} \left| \left( -i\hbar\vec{\nabla} - \frac{e^*}{c}\vec{A} \right) \Psi \right|^2 - \frac{(\vec{H} - \vec{H}_0)^2}{4\pi} \right\} dV_s \ , \tag{1.8}$$

where $H$ is the local microscopic field at a given point of the superconductor and $G_{sH_0} - G_{nH_0}$ is the difference between the free energy of the sample in a superconducting state and the normal state in applied magnetic field $H_0$. The integration is performed over the volume of the superconductor $V_s$.

Every part of the integrand in Eq. (1.8) describes some physical property. In principle, it is possible to introduce some extra terms in the energy functional in order to describe the superconducting state deeper in the superconducting phase (see, for example, Ref. [37]), but the achieved corrections are very small

and rarely considered. The first part of Eq. (1.8) is the expansion of the energy difference between the superconducting and normal state for a homogeneous superconductor in the absence of an applied magnetic field in powers of $|\Psi|^2$ (it can be shown from the microscopic theory that only even powers of $|\Psi|$ appear in this expansion) near the zero-field critical temperature $T_{c0}$,

$$\alpha\,|\Psi|^2 + \frac{\beta}{2}\,|\Psi|^4 \ , \tag{1.9}$$

where $\alpha$ and $\beta$ are some phenomenological expansion coefficients which are characteristics of the material. The coefficient $\alpha$ is negative and changes sign as temperature is increased over $T_{c0}$ ($\alpha \propto (T - T_{c0})$), while $\beta$ is a positive constant, independent of temperature. By minimizing expression (1.9) one can extract the Cooper-pair density corresponding to the energy minimum at temperatures below $T_{c0}$ as $|\Psi_0|^2 = -\alpha/\beta$.

The next term in the integrand of Eq. (1.8) is clearly the kinetic energy of the Cooper-pairs:

$$\frac{1}{2m^*}\left|\left(-i\hbar\vec{\nabla} - \frac{e^*}{c}\vec{A}\right)\Psi\right|^2 \ , \tag{1.10}$$

where the mass of a Cooper-pair $m^*$ is two times the mass of an electron $m$, and the charge of the Cooper-pair $e^*$ is two times the charge of the electron $e$. It describes the energy cost when the superconducting density is non-homogeneous.

The last term Eq. (1.8)

$$-\frac{(\vec{H} - \vec{H}_0)^2}{4\pi} \ , \tag{1.11}$$

describes the magnetic energy of the magnetic field of the supercurrents, which measures the response of the superconductor to an external field and is nothing else than the difference between the local and applied magnetic field. Note that for a superconductor in an external field, the equilibrium state is not defined by the Helmholtz free energy but the Gibbs free energy which we are actually calculating in Eq. (1.8). The difference lies in the energy of the magnetic field of the supercurrents in an applied magnetic field, which is introduced in the definition of the Gibbs free energy and can be expressed as $1/4\pi \int (\vec{H} - H_0)\vec{\cdot}\,\vec{H}_0\ dV_s$.

Note that $\mathcal{G}_{sH_0} - \mathcal{G}_{nH_0}$ is a function of $\Psi(\vec{r})$ and $\vec{A}(\vec{r})$. Minimizing the energy functional (1.8) with respect to the order parameter and the vector potential leads to the Ginzburg-Landau equations which will be derived below.

**First Ginzburg-Landau equation** In order to obtain the minimum of the total Gibbs free energy, we vary expression (1.8) with respect to $\Psi^*$ [32]:

$$\int \left\{\alpha\Psi\delta\Psi^* + \beta\Psi\,|\Psi|^2\,\delta\Psi^* + \frac{1}{2m^*}\vec{\varphi}\cdot\left(i\hbar\vec{\nabla} - \frac{e^*}{c}\vec{A}\right)\delta\Psi^*\right\} dV_s = 0 \ , \tag{1.12}$$

where

$$\vec{\varphi} = \left(-i\hbar\vec{\nabla} - \frac{e^*}{c}\vec{A}\right)\Psi \ , \tag{1.13}$$

and $V_s$ is the sample volume (outside the sample $\Psi = 0$). The last term of Eq. (1.12) can be rewritten as

$$\frac{i\hbar}{2m^*}\left[-\int \delta\Psi^*\vec{\nabla}\cdot\vec{\varphi}dV_s + \int \vec{\nabla}\cdot(\delta\Psi^*\vec{\varphi})\,dV'\right] - \frac{e^*}{2m^*c}\int \vec{\varphi}\cdot\vec{A}\delta\Psi^* dV_s \ , \quad (1.14)$$

by making use of $\vec{\nabla}\cdot(\delta\Psi^*\vec{\varphi}) = \vec{\varphi}\cdot\vec{\nabla}\delta\Psi^* + \delta\Psi^*\vec{\nabla}\cdot\vec{\varphi}$.

Substituting Eq. (1.14) in Eq. (1.12) and using Gauss theorem $\int \vec{\nabla}\cdot\vec{T}dV_s = \oint \vec{n}\cdot\vec{T}dS_s$ we obtain

$$\int\left\{\alpha\Psi\delta\Psi^* + \beta\Psi\left|\Psi\right|^2\delta\Psi^* - \frac{i\hbar}{2m^*}\delta\Psi^*\vec{\nabla}\cdot\vec{\varphi} - \frac{e^*}{2m^*c}\vec{\varphi}\cdot\vec{A}\delta\Psi^*\right\}dV' + \\ + \frac{i\hbar}{2m^*}\oint_{S_s}\vec{n}\cdot\delta\Psi^*\vec{\varphi}dS_s = 0 \ , \quad (1.15)$$

where $S_s$ is the sample surface. Finally, after resubstituting function $\vec{\varphi}$ and some simple transformations, the trivial solution of Eq. (1.15) follows from the set of equations

$$\int\left\{\alpha\Psi\delta\Psi^* + \beta\Psi\left|\Psi\right|^2\delta\Psi^* - \frac{1}{2m^*}\left(-i\hbar\vec{\nabla} - \frac{e^*}{c}\vec{A}\right)^2\Psi\delta\Psi^*\right\}dV_s = 0 \ , \quad (1.16)$$

and

$$\frac{i\hbar}{2m^*}\oint_{S_s}\vec{n}\cdot\delta\Psi^*(-i\hbar\vec{\nabla} - \frac{e^*}{c}\vec{A})\Psi dS_s = 0 \ . \quad (1.17)$$

As expressions (1.16) and (1.17) must be valid for an arbitrary function $\delta\Psi^*$, we obtain the first equation of the Ginzburg-Landau theory and its boundary condition:

$$\alpha\Psi + \beta\left|\Psi\right|^2\Psi + \frac{1}{2m^*}\left(-i\hbar\vec{\nabla} - \frac{e^*}{c}\vec{A}\right)^2\Psi = 0 \ , \quad (1.18)$$

$$\vec{n}\cdot(-i\hbar\vec{\nabla} - \frac{e^*}{c}\vec{A})\Psi\Big|_{boundary} = 0 \ , \quad (1.19)$$

where $\vec{n}$ is the unit vector normal to the surface of the superconductor. This condition expresses that no supercurrent can pass perpendicular to the sample boundary (Neumann boundary condition) and is applied to the finite superconducting samples. Note that periodic boundary conditions for $\Psi$ and $\vec{A}$ would also satisfy Eq. (1.17), for a surface encircling the unit cell in the calculation since the periodicity provides equal values of the integrand on opposite sides of the cell and the surface vector $\vec{n}$ pointing *out* of the integration region ensures that the integral cancels out. Later in this thesis, the exact form of the periodic boundary conditions for description of an infinite superconducting film will be explained.

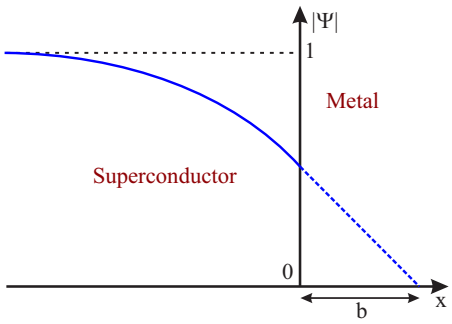


Fig. 1.5: The superconducting / normal metal interface: the illustration of the spatial dependence of the superconducting order parameter $|\Psi|$ where $b$ denotes the extrapolation length [29].

However, for a superconductor-normal metal interface the Eq. (1.17) (and consequently the boundary condition) must be modified due to exchange of electrons between two materials. De Gennes [29] has generalized the expression (1.19) to

$$\vec{n} \cdot (-i\hbar\vec{\nabla} - \frac{2e^*}{c}\vec{A})\Psi\Big|_{boundary} = \frac{i}{b}\Psi\Big|_{boundary}, \tag{1.20}$$

which assures that no supercurrent passes perpendicular to the sample boundary. The quantity $b$ (real number) is called the extrapolation length, since it measures the distance outside the boundary (in the normal metal) where the order parameter becomes zero, if the slope at the interface is maintained (see Fig. 1.5). The exact value of the extrapolation length is determined by the medium adjacent to the superconductor, which can be sorted in three main groups:

- vacuum or an insulator: $b \to \infty$,
- normal metals: $b > 0$, and for ferromagnets: $b \to 0$,
- a superconducting layer with a higher $T_c$: $b < 0$.

The latter are promising from the point of view of *enhancing the critical parameters* since for negative $b$ the order parameter near the surface increases, leading to higher critical fields and critical temperatures. However, such investigation is out of the scope of this thesis (for more details, see Refs. [38, 39]).

**Second Ginzburg-Landau equation** The next step in the derivation of the GL theory is the minimization of the Gibbs free energy (1.8) with respect to $\vec{A}$:

$$\frac{1}{2m^*}\int\left[\left(-\frac{e^*}{c}\delta\vec{A}\Psi^*\right)\cdot\left(-i\hbar\vec{\nabla}\Psi-\frac{e^*}{c}\vec{A}\Psi\right)+\left(i\hbar\vec{\nabla}\Psi^*-\frac{e^*}{c}\vec{A}\Psi^*\right)\cdot\left(-\frac{e^*}{c}\delta\vec{A}\Psi\right)\right]dV+\frac{1}{4\pi}\int\left(\mathrm{rot}\,\vec{A}-\vec{H}_0\right)\cdot\mathrm{rot}\,\delta\vec{A}dV=0\ , \tag{1.21}$$

with $\vec{H}=\mathrm{rot}\,\vec{A}$, and integration over the entire space. The first integral can be rewritten as

$$\int\left[\frac{i\hbar e}{m^*c}\left(\Psi^*\vec{\nabla}\Psi-\Psi\vec{\nabla}\Psi^*\right)+\frac{4e^2}{m^*c^2}\left|\Psi\right|^2\vec{A}\right]\cdot\delta\vec{A}\,dV=0\ . \tag{1.22}$$

Using the formula $\mathrm{div}\left[\vec{a}\times\vec{b}\right]=\vec{b}\cdot\mathrm{rot}\,\vec{a}-\vec{a}\cdot\mathrm{rot}\,\vec{b}$ ($\vec{b}=\mathrm{rot}\,\vec{A}-\vec{H}_0$ and $\vec{a}=\delta\vec{A}$), the second integral in Eq. (1.21) becomes

$$\frac{1}{4\pi}\int\left\{\delta\vec{A}\cdot\mathrm{rot}\,\mathrm{rot}\,\vec{A}+\mathrm{div}\left[\delta\vec{A}\times\left(\mathrm{rot}\,\vec{A}-\vec{H}_0\right)\right]\right\}dV=0\ . \tag{1.23}$$

After making use of Gauss's theorem the last part of Eq. (1.23) can be expressed as

$$\int\mathrm{div}\left[\delta\vec{A}\times\left(\mathrm{rot}\,\vec{A}-\vec{H}_0\right)\right]dV=\oint_S d\vec{S}\cdot\left[\delta\vec{A}\times\left(\mathrm{rot}\,\vec{A}-\vec{H}_0\right)\right]. \tag{1.24}$$

This integral equals zero because $S$ is the boundary of the entire space at infinity where $\mathrm{rot}\,\vec{A}=\vec{H}=\vec{H}_0$ for finite-size superconductors. Even in the case of infinite superconducting structures in periodic magnetic field, one may choose the periodic boundary conditions, making sure that the surface integral given above cancels out at the unit-cell boundary (see section 1.1.2.3). Finally, Eq. (1.21) reads

$$\int\left[\frac{i\hbar e}{m^*c}\left(\Psi^*\vec{\nabla}\Psi-\Psi\vec{\nabla}\Psi^*\right)+\frac{4e^2}{m^*c^2}\left|\Psi\right|^2\vec{A}+\frac{1}{4\pi}\mathrm{rot}\,\mathrm{rot}\,\vec{A}\right]\cdot\delta\vec{A}\,dV=0\ . \tag{1.25}$$

Condition of validity for arbitrary $\delta\vec{A}$ can be fulfilled only if the expression in the square brackets is zero. Knowing that the current density $\vec{j}_s$ in the superconductor is given by the Maxwell equation

$$\vec{j}_s=\frac{c}{4\pi}\mathrm{rot}\,\mathrm{rot}\,\vec{A}\ , \tag{1.26}$$

we obtain the final expression of the second Ginzburg-Landau equation:

$$\vec{j}_s=-\frac{i\hbar e}{m^*}\left(\Psi^*\vec{\nabla}\Psi-\Psi\vec{\nabla}\Psi^*\right)-\frac{4e^2}{m^*c}\left|\Psi\right|^2\vec{A}\ . \tag{1.27}$$

*1.1.2.1 Characteristic length scales* The Ginzburg-Landau theory introduces two important characteristic length scales: the coherence length $\xi(T)$ and the penetration depth $\lambda(T)$. The coherence length $\xi(T)$ indicates the typical length scale over which the size of the order parameter can vary (Fig. 1.6). The typical length scale over which the magnetic field $\vec{H}$ varies is the penetration depth $\lambda(T)$. $\lambda$ and $\xi$ can be derived from the first and second Ginzburg-Landau equation, respectively:

$$\alpha\Psi + \beta\left|\Psi\right|^2\Psi + \frac{1}{2m^*}\left(-i\hbar\vec{\nabla} - \frac{2e}{c}\vec{A}\right)^2\Psi = 0\ , \tag{1.28}$$

$$\vec{j}_s = -\frac{i\hbar e}{m^*}\left(\Psi^*\vec{\nabla}\Psi - \Psi\vec{\nabla}\Psi^*\right) - \frac{4e^2}{m^*c}\left|\Psi\right|^2\vec{A}\ . \tag{1.29}$$

In this discussion, we consider a superconductor in a weak magnetic field with the sample dimensions much greater than the magnetic penetration depth. In a first order approximation, the value of Cooper-pair density can be replaced by its equilibrium zero-field value

$$\left|\Psi\right| = \Psi_0 = \sqrt{-\frac{\alpha}{\beta}}\ . \tag{1.30}$$

The Eq. (1.29), after taking curl of both sides of the equation, now becomes

$$\mathrm{rot}\vec{j}_s = -\frac{4e^2}{m^*c}\left|\Psi\right|^2\mathrm{rot}\vec{A} \tag{1.31}$$

Using Eq. (1.4) and Maxwell equation, and taking into account that $\alpha < 0$, this can be rewritten as

$$\vec{H} + \frac{m^*c^2\beta}{16\pi e^2\left|\alpha\right|}\,\mathrm{rot}\,\mathrm{rot}\,\vec{H} = 0\ , \tag{1.32}$$

which, upon comparing to the expression in Eq. (1.5), gives

$$\lambda(T) = \sqrt{\frac{m^*c^2}{16\pi e^2\left|\Psi_0\right|^2}} = \sqrt{\frac{m^*c^2}{8\pi e^2 n_s}} = \sqrt{\frac{m^*c^2\beta}{16\pi\left|\alpha\right|e^2}}\ , \tag{1.33}$$

where the density of superconducting electrons $n_s = 2\left|\Psi_0\right|^2 = 2\left|\alpha\right|/\beta$ and the mass of a Cooper-pair is two times the electron mass $m$: $m^* = 2m$.

Let us now consider a second example where $\Psi$ varies only in the $z$-direction, but the applied magnetic field is zero. In this case the first GL equation (1.28) becomes

$$-\frac{\hbar^2}{2m^*}\frac{d^2}{dz^2}\Psi + \alpha\Psi + \beta\Psi^3 = 0\ . \tag{1.34}$$

Assuming $\Psi$ is real, we can introduce a dimensionless order parameter

$$\Psi = f\Psi_0\ , \tag{1.35}$$

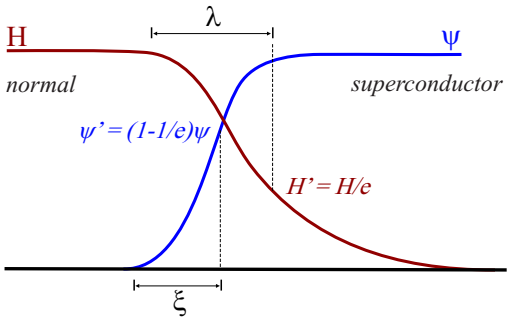


FIG. 1.6: The spatial distribution of the order parameter $\Psi$ and the magnetic field $h$ at the superconducting/normal surface boundary [after Ref. [31]].

where $\psi_0$, corresponding to the state with lowest free energy when $\alpha < 0$, is given by Eq. (1.30). Thus, Eq. (1.34) becomes

$$-\frac{\hbar^2}{2m^*\,|\alpha|}\frac{d^2f}{dz^2} - f + f^3 = 0. \tag{1.36}$$

A natural length scale for spatial variations of the order parameter is therefore

$$\xi(T) = \sqrt{\frac{\hbar^2}{2m^*\,|\alpha|}}\,, \tag{1.37}$$

which is known as the GL coherence length. Note that both the GL coherence length and the GL penetration depth are temperature dependent quantities, since $\alpha$ depends on the temperature as $\alpha \propto (T - T_{c0})$. It is therefore clear that both $\lambda$ and $\xi$ are proportional to $(1 - T/T_{c0})^{-1/2}$. One should notice that these characteristic lengths diverge at the critical temperature $T_{c0}$. The exact temperature dependence of $\xi$ and $\lambda$ depends on the purity of the material, defined by the elastic mean free path $l_{el}$ [29, 31]:

$$\xi(T) = 0.74\xi_o\,(1 - T/T_{c0})^{-1/2} \text{ when } l_{el} \gg \xi_o \text{ (pure)}, \tag{1.38}$$

$$\xi(T) = 0.855\sqrt{\xi_o l_{el}}\,(1 - T/T_{c0})^{-1/2} \text{ when } l_{el} \ll \xi_o \text{ (dirty)}, \tag{1.39}$$

and

$$\lambda(T) = \frac{\lambda_L(0)}{\sqrt{2}}\,(1 - T/T_{c0})^{-1/2} \text{ when } l_{el} \gg \xi_o \text{ (pure)}, \tag{1.40}$$

$$\lambda(T) = \frac{\lambda_L(0)}{\sqrt{2}}\sqrt{\frac{\xi_o}{1.33 l_{el}}}\,(1 - T/T_{c0})^{-1/2} \text{ when } l_{el} \ll \xi_o \text{ (dirty)}, \tag{1.41}$$

where $\xi_o$ and $\lambda_L(0)$ denote the BCS coherence length and the London penetration depth at absolute zero temperature, respectively. These expressions are valid only in the neighborhood of $T_c$. The important result is that according to Eqs. (1.39) and (1.41), in the dirty limit, as $l_{el}$ decreases (i.e. the superconductor becomes more impure), $\lambda(T)$ increases, while $\xi(T)$ decreases. Thus at all temperatures $\lambda(T) >> \xi(T)$ in an impure material. The high-temperature superconductors have short coherence lengths of the order of $\xi = 1.2$ to 1.5nm. Since the electron mean free path $l_{el}$ is typically $\sim$ 15nm in these materials, then they are well within the clean limit.

*1.1.2.2 Ginzburg-Landau equations and their validity* While a normal metallic system should be considered quantum-mechanically by solving the Schrödinger equation:

$$\frac{1}{2m}\left(-\imath\hbar\vec{\nabla} - \frac{e}{c}\vec{A}\right)^2 \Psi + U\,\Psi = E\,\Psi\,, \tag{1.42}$$

a superconducting system is described by the two coupled Ginzburg-Landau (GL) equations, derived in previous paragraphs:

$$\frac{1}{2m^*}(-i\hbar\vec{\nabla} - \frac{e^*}{c}\vec{A})^2\psi + \beta|\psi|^2\psi = -\alpha\psi \tag{1.43}$$

$$\vec{j_s} = \frac{c}{4\pi}\,\vec{\nabla}\times\vec{h} = -\frac{i\hbar e^*}{2m^*}\left(\psi^*\vec{\nabla}\psi - \psi\vec{\nabla}\psi^*\right) - \frac{{e^*}^2}{m^*c}\,|\psi|^2\,\vec{A}\,, \tag{1.44}$$

with $\vec{A}$ the vector potential which corresponds to the microscopic field $\vec{h} = \mathrm{rot}\vec{A}$, $U$ the potential energy, $E$ the total energy, $\alpha$ a temperature dependent parameter changing sign from $\alpha > 0$ to $\alpha < 0$ as $T$ is decreased through $T_c$, $\beta$ a positive temperature independent constant, $m^*$ the effective mass which can be chosen arbitrarily and is generally taken as twice the free electron mass $m$.

Note that the first GL equation (Eq. (1.43)), with the nonlinear term $\beta|\psi|^2\psi$ neglected, is the analogue of the Schrödinger equation (Eq. (1.42)) with $U = 0$, when making the following substitutions: $\psi(\Psi)$, $e^*(e)$, $-\alpha(E)$ and $m^*(m)$. The superconducting order parameter $\psi$ corresponds to the wave function $\Psi$; the effective charge $e^*$ in the GL equations is $2e$, i.e. the charge of a Cooper pair; the temperature dependent GL parameter $\alpha$ (related to the coherence length $\xi(T)$, see previous paragraph) plays the role of $E$ in the Schrödinger equation.

The boundary conditions for interfaces between normal metal-vacuum and superconductor-vacuum are, however, different:

$$\Psi\Psi^*|_{boundary} = 0$$

$$(-\imath\hbar\vec{\nabla} - \frac{e^*}{c}\vec{A})\psi\Big|_{\perp,boundary} = 0 \tag{1.45}$$

i.e. for normal metallic systems the density is zero (Neumann BC), while for superconducting systems, the gradient of $\psi$ (for the case $\vec{A} = 0$) has no

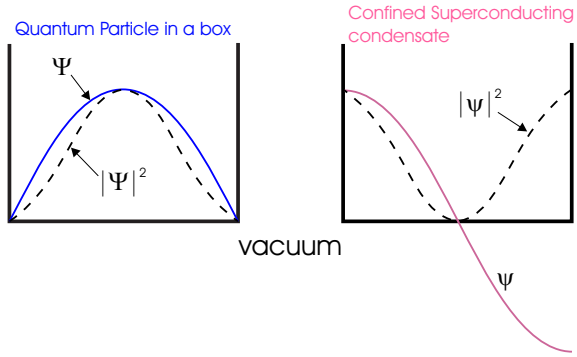


FIG. 1.7: Schematic illustration of different boundary conditions at metal-vacuum and superconductor-vacuum interfaces [after Ref. [3]].

component perpendicular to the boundary (Dirichlet BC, see Fig. 1.7). As a consequence, the supercurrent cannot flow through the boundary.

In this thesis, the Ginzburg-Landau equations will be used in a dimensionless form. The distances will be measured in units of the coherence length $\xi = \hbar/\sqrt{-2m^*\alpha}$, the order parameter in $\psi_0 = \sqrt{-\alpha/\beta}$ and the vector potential in $c\hbar/2e\xi$. $\kappa = \lambda/\xi$ is the Ginzburg-Landau parameter, and $\lambda = c\sqrt{m^*/\pi}/4e\psi_0$ is the penetration length. The magnetic field is measured in the second critical magnetic field $H_{c2} = c\hbar/2e\xi^2 = \kappa\sqrt{2}H_c$, where $H_c = \sqrt{4\pi\alpha^2/\beta}$ is the critical field.

Using these dimensionless variables and the London gauge, $\mathrm{div}\vec{A} = 0$, Eqs. (1.43)-(1.45) can be rewritten in the following form:

$$\left(-i\vec{\nabla} - \vec{A}\right)^2 \psi = \psi\left(1 - |\psi|^2\right) \ , \tag{1.46}$$

$$-\kappa^2 \Delta\vec{A} = \frac{1}{2i}\left(\psi^*\vec{\nabla}\psi - \psi\vec{\nabla}\psi^*\right) - |\psi|^2\,\vec{A} \ , \tag{1.47}$$

with the boundary condition:

$$\vec{n}\cdot\left(-i\vec{\nabla} - \vec{A}\right)\psi\Big|_{boundary} = 0 \ . \tag{1.48}$$

Here, we include the temperature dependence through characteristic lengths $\xi$ and $\lambda$, following from the GL theory (see paragraph 1.1.2.1)

$$\xi(T) = \frac{\xi(0)}{\sqrt{|1 - T/T_{c0}|}} \ , \tag{1.49}$$

$$\lambda(T) = \frac{\lambda(0)}{\sqrt{|1 - T/T_{c0}|}} \ , \tag{1.50}$$

$$H_{c2}(T) = H_{c2}(0)\left|1 - \frac{T}{T_{c0}}\right| \ , \tag{1.51}$$

where $H_{c2}(0) = c\hbar/2e\xi(0)^2$ and $T_{c0}$ is the critical temperature at zero magnetic field.

Considering the validity of the Ginzburg-Landau equations, several points need to be discussed [33]:

- Firstly, Landau general theory of second order transitions assumes that the free energy can be expanded in powers of $\psi$ [25]. Second, the coefficient $\alpha$ is assumed positive in high temperature phase, changes sign at the transition and becomes negative under the critical temperature ($\alpha \propto (T - T_{c0})$), while $\beta$ is a positive constant, independent on temperature. None of these assumptions are generally applicable, but Gor'kov showed theoretically that the Landau expansion is valid in the case of superconductors [16].

- $\Psi$ must be a slowly varying function over distances of the order of $\xi_0$. A necessary condition for the validity of the theory is, therefore, $\xi(T) \gg \xi_0$. From the temperature dependence of the coherence length (see previous paragraph) follows the condition

$$\frac{T_{c0} - T}{T_{c0}} \ll 1, \tag{1.52}$$

  meaning that this condition is fulfilled only for temperatures close to $T_{c0}$, the critical temperature in zero field.

- The local relation between the current and the vector potential, yielded by the Ginzburg-Landau equations, will be valid only if $\vec{H}$ and $\vec{A}$ are slowly varying functions over distances of the order of $\xi_0$. In order for this to be true, it is necessary that $\lambda(T) \gg \xi_0$, leading to the relation

$$\frac{T_{c0} - T}{T_{c0}} \ll \left[\frac{\lambda_L(0)}{\xi_0}\right]^2 , \tag{1.53}$$

  which sets us back to the condition of temperatures close to $T_{c0}$.

Despite the above criteria, and ensured applicability only close to the superconducting/normal transition, it turns out that the validity range of the Ginzburg-Landau theory is much larger. In particular, in mesoscopic superconductors the Ginzburg-Landau theory has been successfully used deep into the superconducting phase (see for example Ref. [40]). De Gennes [29] demonstrated that the GL model is valid for any temperatures in strong magnetic fields. Comparison of the critical current measurements in thin *Al* stripes with the theoretical predictions of BCS and GL formalisms by Romijn *et al.* [30] showed that two theories agree with each other up to very low temperatures (below $0.1T_c$). Substantiated by the experimental findings, it appears that due to the small mean-path-length in the samples, the GL theory is more relevant in

this case. Actually, most of the mesoscopic superconductors are in the so-called "dirty" limit, and that is the main reason of the phenomenologically proven applicability of the GL formalism far away from the S/N boundary.

*1.1.2.3 Details of the numerical approach* In order to solve the GL-equations, one is in general left with a three dimensional problem. In the following section, we present the details of the numerical procedure we used to obtain results presented in this thesis.

**Restriction to thin superconductors.** In this thesis we focused on thin superconductors, mainly with thickness smaller than the characteristic lengths of the SC. Tinkham was first to consider thin superconducting films in an applied homogeneous field, either parallel or perpendicular to the film surface [41]. It is well known that in thick superconductors the magnetic field penetrates only into a small depth $\lambda$ and that screening currents flow in the surface layer, decaying exponentially in the bulk beyond this length. Thus, in perpendicular geometry (of interest in this thesis), the whole current is confined to a narrow surface layer of width $\lambda$. However, one question arises: what happens when the superconductor is thinner than the London penetration depth? Tinkham argued, as is now generally accepted, that the currents and the vector potential in thin superconductors may be considered constant over the thickness. Consequently, they have *no* $z$-component, and the boundary condition (1.48) is automatically fulfilled at top and bottom surfaces of the SC film. Recently, Prozorov *et al.* [42] confirmed Tinkham's original assumption, considering in detail the current density (in)homogeneity throughout the thickness of superconducting films. The results for the current distribution over SC thickness, following from Ref. [42] are shown in Fig. 1.8.

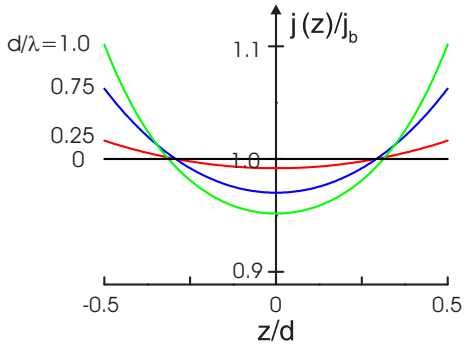


FIG. 1.8: Current density distribution vs. normalized depth $z/d$ for the indicated $d/\lambda$ ratios. The current distribution becomes more homogeneous as the ratio $d/\lambda$ decreases. $j_b$ corresponds to "uniform" bulk current density in the $d/\lambda = 0$ limit.

Therefore, for superconductor (SC) with thickness $d < \lambda, \xi$ the distribution of current and the corresponding vector potential can be assumed to be uniform in the $z$ direction. From the first GL equation (1.46) then follows the same behavior for the order parameter, and, as far as the order parameter is concerned the 3D problem is reduced to a 2-dimensional superconductor. We use this property of thin superconductors and average the Ginzburg-Landau equations (1.46) and (1.47) over SC-thickness. They now read

$$\left(-i\vec{\nabla} - \vec{A}\right)^2 \Psi = \Psi\left(1 - |\Psi|^2\right) \ , \tag{1.54}$$

and

$$-\Delta_{3D}\vec{A} = \frac{d}{\kappa^2}\delta(z)\vec{j}_{2D} \ , \tag{1.55}$$

with

$$-\vec{j}_{2D} = \frac{1}{2i}\left(\Psi^*\vec{\nabla}_{2D}\Psi - \Psi\vec{\nabla}_{2D}\Psi^*\right) - |\Psi|^2\,\vec{A} \ . \tag{1.56}$$

The indices 2D and 3D refer to two- and three-dimensional operators, and $\vec{j}_{2D}$ is the superconducting current density in the film. One should notice that the thin-film approximation enters the second GL equation through the Dirac delta function on the right side, which facilitates solving this equation using the standard Fourier transformation. Please note that the 3D nature of the magnetic field distribution following from Eq. (1.55) is completely retained.

In the case of finite size superconductors, the SC-vacuum boundary condition remains

$$\vec{n}\cdot\left(-i\vec{\nabla}_{2D} - \vec{A}\right)\Psi\Big|_{boundary} = 0, \tag{1.57}$$

which expresses that no supercurrent can pass perpendicular to the disk surface. The boundary condition for the vector potential is such that the total magnetic field far away from the superconductor equals the total applied magnetic field (the contribution of the field of the supercurrents diminishes as one goes further away from SC).

In the case of infinite superconducting films, periodic boundary conditions around the simulation region should be used. However, standard periodicity may be used only if the applied vector potential is periodic itself. In general case, periodic boundary conditions for $\vec{A}$ and $\Psi$ have the form [43]

$$\vec{A}(\vec{\rho} + \vec{b}_i) = \vec{A}(\vec{\rho}) + \vec{\nabla}\eta_i(\vec{\rho}), \tag{1.58}$$

$$\Psi(\vec{\rho} + \vec{b}_i) = \Psi exp(2\pi i\eta_i(\vec{\rho})/\Phi_0), \tag{1.59}$$

where $\vec{b}_i$, $i = x, y$ are the lattice vectors, and $\eta_i$ is the gauge potential which cannot be chosen freely but must preserve the single valuedness of $\vec{A}$ and $\Psi$. These boundary conditions mean that $\vec{A}$, $\Psi$ are invariant under lattice translations combined with specific gauge transformations. Other quantities, such as the magnetic field, the current and the order parameter density are periodic.

One should notice that these boundary conditions reduce to their standard form for $\eta_i = 0$. The adequate choice of the gauge potential $\eta_i$ will be discussed for particular applied magnetic fields (from magnetic structure with and without homogeneous magnetic field, applied current, etc.) throughout the thesis. For example, in the case of a superconductor in a homogeneous magnetic field $H_0$, the applied vector potential has the form $\vec{A}_{0\phi} = 0.5\ H_0\rho$ (in polar coordinates). Therefore, simple periodic boundary condition $\vec{A}(\vec{\rho}+\vec{b}_i) = \vec{A}(\vec{\rho})$ would not interpret correctly the applied vector potential (one would obtain "zig-zag" behavior over distance, instead of a monotonously increasing one). It can be shown that the gauge $\eta_x = H_0 L_x y$, and $\eta_y = 0$, where $L_x$ is the size of the square unit cell ($L_x = Ly$) provides periodicity of both the vector potential and order parameter.

**Free energy.** In order to calculate the Gibbs free energy of this system, we start from the dimensionless expression

$$\begin{aligned}\mathcal{F} &= \frac{\mathcal{G}_{sH} - \mathcal{G}_{nH}}{H_c^2 V/8\pi} \\ &= \int \left\{ -2\left|\Psi\right|^2 + \left|\Psi\right|^4 + 2\left|\left(-i\vec{\nabla} - \vec{A}\right)\Psi\right|^2 + 2\kappa^2\left(\vec{H} - \vec{H}_0\right)^2 \right\} dV. \end{aligned} \tag{1.60}$$

where $\mathcal{G}_{nH}$ is the free energy of the normal phase when an external field $\vec{H}_0$ (in general inhomogeneous) is applied.

Using mathematical transformations and the Gauss theorem $\int \vec{\nabla}\cdot\vec{D}\ dV = \oint \vec{n}\cdot\vec{D}\ dS$, the third term in the integrand in Eq. (1.60) can be written as

$$\begin{aligned}\int \left|\left(-i\vec{\nabla} - \vec{A}\right)\Psi\right|^2 dV = \oint \vec{n}\cdot\left[\Psi^*\left(-i\vec{\nabla} - \vec{A}\right)\Psi\right] dS \\ + \int \Psi^*\left(-i\vec{\nabla} - \vec{A}\right)^2 \Psi\ dV. \end{aligned} \tag{1.61}$$

The first term on the right side equals zero due to the boundary conditions described in the previous paragraph. Note that this holds both for the SC-vacuum boundary (Eq. (1.57)) and the periodic structure (Eq. (4.4)). The second term we rewrite with the help of the first GL equation (1.54) and finally we have

$$\int \left|\left(-i\vec{\nabla} - \vec{A}\right)\Psi\right|^2 dV = \int \left(\left|\Psi\right|^2 - \left|\Psi\right|^4\right) dV\ . \tag{1.62}$$

After substituting back in Eq. (1.61), we obtain

$$\mathcal{F} = \int \left[\left(\vec{H} - \vec{H}_0\right)^2 \kappa^2 - \frac{1}{2}\left|\Psi\right|^4\right] dV\ , \tag{1.63}$$

where $\vec{H} = \mathrm{rot}\,\vec{A}$. Using the vector relations $\vec{\nabla}\cdot\left(\vec{a}\times\vec{b}\right) = \vec{b}\cdot\left(\vec{\nabla}\times\vec{a}\right) - \vec{a}\cdot\left(\vec{\nabla}\times\vec{b}\right)$ and $\vec{a}\times\left(\vec{\nabla}\times\vec{a}\right) = 0$, and the London gauge $\vec{\nabla}\cdot\vec{A} = 0$, the free energy

becomes

$$\mathcal{F} = \int \left\{ \left( \vec{A} - \vec{A}_0 \right) \cdot \left[ \nabla^2 \left( \vec{A} - \vec{A}_0 \right) \right] \kappa^2 - \frac{1}{2} \left| \Psi \right|^4 \right\} dV \ , \tag{1.64}$$

where $\vec{A}_0$ denotes the vector potential of the applied magnetic field in the absence of a superconductor. We now apply the relation $\overrightarrow{j} = -\kappa^2 \nabla^2 \overrightarrow{A}$, and arrive to the final expression for the Gibbs free energy (in units of $H_c^2 V / 8\pi$)

$$\mathcal{F} = \frac{1}{V} \int \left[ 2 \left( \vec{A} - \vec{A}_0 \right) \cdot \vec{j} - \left| \Psi \right|^4 \right] d\vec{r}. \tag{1.65}$$

Here, the dimensionless supercurrent is given by

$$\vec{j} = \frac{1}{2i} \left( \Psi^* \vec{\nabla} \Psi - \Psi \vec{\nabla} \Psi^* \right) - \left| \Psi \right|^2 \vec{A} \ . \tag{1.66}$$

**Numerical procedure.** For the fixed applied magnetic field, we solve the two coupled Ginzburg-Landau equations *self-consistently*. Both equations are solved using the link variable approach [44] for a finite-difference representation of the order parameter and the vector potential on a uniform cartesian space grid $(x, y)$ with a typical grid spacing of less than $0.1\xi$. In order to provide time relaxation and ensure convergence of our calculations, we add the time derivatives of the order parameter and the vector potential to the left side of Eqs. (1.54) and (1.55), respectively, which are then iterated over time.

For a given applied magnetic field, we start from the applied vector potential as initial condition in our calculation, as if no superconductor is present. The first step is to solve the first GL equation (1.54). According to Kato *et al.* [44], the time dependent Ginzburg-Landau equation (1.54) can be written as

$$\frac{\partial \Psi}{\partial t} = -\frac{1}{12} \left[ \left( \frac{\vec{\nabla}}{i} - \vec{A} \right)^2 \Psi + (1 - T) \left( \left| \Psi \right|^2 - 1 \right) \Psi \right] + \widetilde{f}(\vec{r}, t) \ , \tag{1.67}$$

where $T$ is the temperature and $\widetilde{f}(\vec{r}, t)$ is a dimensionless random force. It is essential to put the gauge field $A$ on the links of the computational lattice, which is achieved by introducing the link variables between $\vec{r}_1$ and $\vec{r}_2$ as

$$U_\mu^{\vec{r}_1, \vec{r}_2} \equiv \exp \left[ -i \int_{\vec{r}_1}^{\vec{r}_2} \vec{A}_\mu \left( \vec{r} \right) \cdot d\vec{\mu} \right], \tag{1.68}$$

with $\mu = x, y$.

In our calculation, the whole system is mapped on a square grid. The second derivative from Eq. (1.67) is discretized as (the indices denote the lattice points

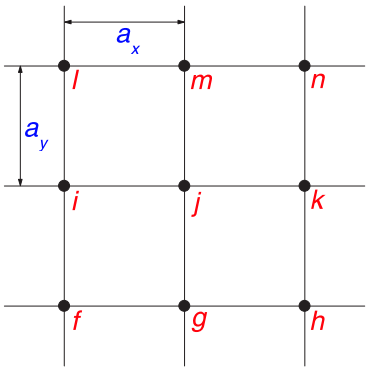


FIG. 1.9: Schematic diagram of the uniform Cartesian grid-point lattice used in the simulations [from Ref. [44]].

as illustrated in Fig. 1.9)

$$\begin{aligned}
&\left(\frac{\nabla_\mu}{i} - A_\mu\right)^2 \Psi_j = \\
&= -\nabla_\mu^2 \Psi_j + i\nabla_\mu(A_\mu \Psi_j) + A_\mu^2 \Psi_j + iA_\mu \nabla_\mu \Psi_j \\
&= \frac{1}{U_\mu^j}\left(-2iA_\mu U_\mu^j \nabla_\mu \Psi_j - iU_\mu^j \Psi_j(\nabla_\mu A_\mu - iA_\mu^2) + U_\mu^j \nabla_\mu^2 \Psi_j\right). \quad (1.69)
\end{aligned}$$

After substituting $\nabla_\mu U_\mu^j = -iA_\mu U_\mu^j$ and $\nabla_\mu^2 U_\mu^j = -iU_\mu^j(\nabla_\mu A_\mu - iA_\mu^2)$, and some trivial transformations, we obtain

$$\left(\frac{\nabla_\mu}{i} - A_\mu\right)^2 \Psi_j = \frac{1}{U_\mu^j}\nabla_\mu(\nabla_\mu(U_\mu^j \Psi_j)). \quad (1.70)$$

Finally, for $\mu = x$ (analogously for $\mu = y$) we have

$$\begin{aligned}
\left(\frac{\nabla_x}{i} - A_x\right)^2 \Psi_j &= \frac{1}{U_x^j}\frac{1}{a_x}\left(\frac{U_x^k \Psi_k - U_x^j \Psi_j}{a_x} - \frac{U_x^j \Psi_j - U_x^i \Psi_i}{a_x}\right) \\
&= \frac{U_x^{kj}\Psi_k - 2\Psi_j + U_x^{ij}\Psi_i}{a_x^2}. \quad (1.71)
\end{aligned}$$

The discretized time dependent Ginzburg-Landau equation can be now written as

$$\begin{aligned}
\frac{\partial \Psi}{\partial t} = \frac{1}{12}\Bigg[&\frac{U_x^{kj}\Psi_k}{a_x^2} + \frac{U_x^{ij}\Psi_i}{a_x^2} + \frac{U_y^{mj}\Psi_m}{a_x^2} + \frac{U_y^{gj}\Psi_g}{a_x^2} - \frac{4\Psi_j}{a_x^2} \\
&+ (1-T)\left(|\Psi_j|^2 - 1\right)\Psi_j\Bigg] + \widetilde{f}_j(t). \quad (1.72)
\end{aligned}$$

Although in general this approach works for $a_x \neq a_y$, in our simulations we used an uniform grid ($a_x = a_y$).

We make use of Eq. (1.72) in solving Eq. (1.54) for the initial vector potential. First, we solve the linearized GL equation, by setting the non-linear part to zero value. This solution is then substituted in the non-linear equation, a new solution is found, and substituted back in the equation. In this recurrent procedure based on a Gauss-Seidel technique, convergence is finally reached and the first GL equation is solved [45]. From this equation we know the value of the order parameter $\Psi$ in every grid point. These values we now use in equation (1.56) to calculate the current densities $j_x$ and $j_y$ in every grid point. Equation (1.56) can be written as

$$j_{x,y} = \frac{1}{2}\left[\Psi^* \left(\frac{1}{i}\frac{\partial}{\partial x,y} - A_{x,y}\right)\Psi + \Psi\left(\frac{1}{i}\frac{\partial}{\partial x,y} - A_{x,y}\right)^* \Psi^*\right] , \qquad (1.73)$$

where again link variable approach comes into play through similar transformations as in Eqs. (1.69)-(1.72)

$$\left(\frac{1}{i}\nabla_x - A_x\right)\Psi_j \rightarrow -i\frac{1}{U_x^j}\nabla_x(U_x^j\Psi_j) = -i\frac{U_x^{kj}\Psi_k - \Psi_j}{a_x} , \qquad (1.74)$$

and

$$\left(\frac{1}{i}\nabla_y - A_y\right)\Psi_j \rightarrow -i\frac{1}{U_y^j}\nabla_y(U_y^j\Psi_j) = -i\frac{U_y^{mj}\Psi_m - \Psi_j}{a_x} . \qquad (1.75)$$

From the supercurrents a new value for the vector potential can be calculated using the second GL equation (1.55). Finally, this vector potential is substituted back in the first GL equation (1.72) and the whole procedure described above is repeated until a convergent solution of both GL equations is found (typically $\sim 10^5$ iteration steps).

In this way, we solve self-consistently two coupled GL equations for *fixed* magnetic field. Once a solution is obtained at a given magnetic field, the field is increased (or decreased) and this solution is used as the initial value in the new calculation. In doing so, the program stays within the same local minimum of the free energy and follows this minimum as a function of the magnetic field. At a certain field, the minimum ceases to exist and the program runs towards a new minimum which is a different solution of the Ginzburg-Landau equations. Then, the magnetic field is changed further and one can investigate the magnetic field range over which the new minimum is stable by sweeping the field up and down. However, our experience tells us that in doing so one can often be "stuck" in a metastable regime. One of the possible escapes is to perform the same calculation for each magnetic field value, but without using the previously found state as input for the iteration scheme. For example, one can start from different initial conditions for the order parameter (for example, $\Psi = 1$ or $\Psi \sim 0$ in every point, or simply randomized order parameter), trying to get as many different solutions as possible. In such a way, it is possible to

investigate a full spectrum of superconducting states, and by comparing their energies (Eq. (1.65)) determine the actual ground state for each value of the applied magnetic field. This is of special interest in experimental applications and crucial for this thesis.

### 1.1.3 Behavior of superconductors in an applied field

Conventional superconductivity - also known as s-wave singlet superconductivity - occurs when electrons with opposite spins bind together to form Cooper pairs with zero momentum and spin. Typically, magnetic field destroys superconductivity because the energy it generates perturbs the close interaction between these electron pairs.

*Orbital effect* The most common way that a magnetic field destroys superconductivity is by disturbing the orbital effect, where the electrons in a pair orbit each other, acquiring more and more energy from the magnetic field. Once this energy becomes greater than that which unites the two electrons, the electron pairs break apart and superconductivity is suppressed (since the electrons have opposite momenta, the Lorentz force acts in opposite directions, pulling the pair apart).

*Paramagnetic effect* The other way magnetic fields can destroy s-wave superconductivity, known as the paramagnetic or spin effect, occurs when a strong magnetic field attempts to align the spins of both the electrons along the field direction. When the magnetic field is turned on, one electron gains energy while the other loses it. If that difference becomes bigger than the amount of energy holding the electrons together, the pairs are broken and superconductivity is gone. But when electrons exhibit the extremely rare phenomenon known as p-wave spin, where both are spinning in the same direction, the magnetic field cannot destroy superconductivity by the spin-effect. This is because while the field may change the electrons' total energy, it doesn't change the difference in energy between them.

Materials that are not only able to withstand magnetic fields, but in which superconductivity can even be induced by applying a magnetic field, are very rare, and up to now only (EuSn)$Mo_6S_8$, organic $\lambda$-$(BETS)_2FeCl_4$ materials, and $HoMo_6S_8$ show this unusual behavior. The first material where field-induced superconductivity (FIS) was observed is (EuSn)$Mo_6S_8$ [47] (see Fig. 1.10). This compound is a superconductor with $T_c = 3.8K$. As the magnetic field increases, the superconductivity is destroyed for small fields and restored again at about $10T$ and temperature below $0.5K$. This phenomenon is well understood in terms of the Jaccarino-Peter compensation effect [48]; the internal magnetic field created by the Eu moments through the exchange interaction is compensated by the external magnetic field. The second material that shows

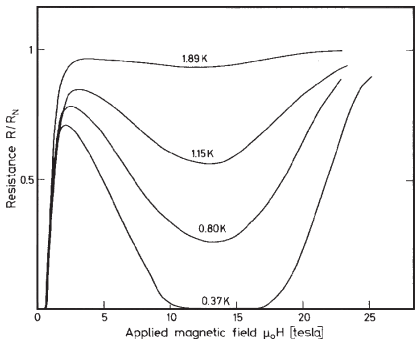


Fig. 1.10: Normalized resistance of $Eu_{0.75}Sn_{0.25}Mo_6S_{7.2}Se_{0.8}$ as function of an applied field ($H \leq 25T$) at various temperatures [from Ref. [47]].

FIS, but at lower magnetic fields ($\sim 0.1T$) is $HoMo_6S_8$ [49]. However, here FIS mechanism is hidden behind a purely electromagnetic field compensation effect between the applied and the internal magnetic fields. In 2001, FIS in organic $\lambda$-$(BETS)_2FeCl_4$ was discovered in ultra high fields between 18 and $41T$ [50]. In this compound an exchange interaction between the $Fe^{3+}$ moments and the conduction electrons is expected, and the Jaccarino-Peter compensation effect may be a possible FIS mechanism. The surprisingly strong anisotropic superconducting transition for $\lambda$-$(BETS)_2FeCl_4$ suggests that the low dimensionality of the electronic system is closely related to the mechanism of superconductivity in this material.

Although in this thesis we consider only s-wave superconductivity, in the following chapters we will show that FIS can also be realized in hybrid superconductor/ferromagnet structures. However, before that, we will introduce two main groups of the conventional superconductors, which differ in their behavior when exposed to the magnetic field.

*1.1.3.1 Type-I and type-II superconductors* The value of the Ginzburg-Landau parameter $\kappa = \lambda(T)/\xi(T)$ determines the behavior of a bulk superconductor in an applied magnetic field ($H_0$). Depending on $\kappa$ being smaller or larger than $1/\sqrt{2} \simeq 0.71$, a distinction can be made between type-I and type-II superconductors:

$$\kappa < 1/\sqrt{2} \rightarrow \text{ type-I superconductors,}$$
$$\kappa > 1/\sqrt{2} \rightarrow \text{ type-II superconductors.}$$

All superconducting chemical elements except niobium are type-I superconductors. Besides niobium, all superconducting alloys, chemical compounds and the high-$T_c$ superconductors belong to the second group. One should note that this rigid distinction holds only for bulk superconductors. In mesoscopic samples, the behavior of the superconductor depends not only on $\kappa$ but on the geometrical parameters as well, as will be discussed later in this thesis (section

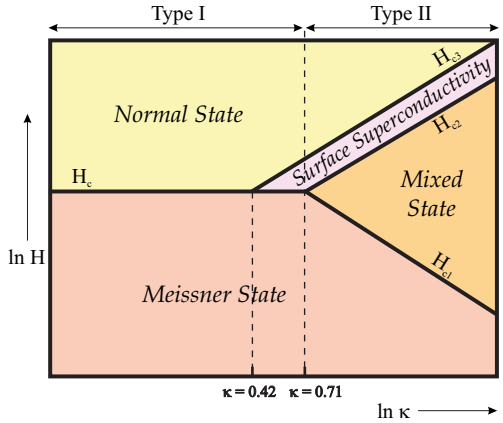


FIG. 1.11: The dependence of the characteristics of bulk superconductors on the value of the Ginzburg-Landau parameter $\kappa$. $H_c$ and $H_{ci}|_{i=1-3}$ are explained in the text and denote the critical fields determining regions with different behavior of the superconductor [after Ref. [46]].

1.1.5). The dependence of the superconducting characteristics on the value of $\kappa$ is illustrated in Fig. 1.11.

Bulk samples with $\kappa < 0.42$ are pure type-I superconductors. For fields below the thermodynamical critical field $\vec{H}_c$ the superconductor is in the Meissner state and all flux is expelled from the sample. At the critical field the magnetic field penetrates the sample, superconductivity is destroyed and the sample becomes normal. For $0.42 < \kappa < 1/\sqrt{2} \simeq 0.71$ we still consider the superconductor to be of type-I kind, although the Meissner state does not change immediately into the normal state with increasing field. At the field $\vec{H}_c$ flux can penetrate the inner part of the sample, while near the surface of the sample, a layer remains superconducting (so-called surface superconductivity). For fields higher than the surface critical field $\vec{H}_{c3}$ the whole sample is in the normal state.

On the other hand, type II superconductors ($\kappa > 0.71$) have remarkably different behavior, as described below.

- The Meissner effect in type-II superconductors is complete only in very weak fields, $H_0 < H_{c1}$. The lower critical field $H_{c1}$ is much less than the thermodynamic critical field $H_c$.

- At $H_0 > H_{c1}$ magnetic field lines penetrate the superconductor. Nevertheless, even in the equilibrium state the penetration is not complete. The flux $\phi$ is smaller than in the normal state, meaning that persistent currents still exist. Actually, the magnetic flux appears to be quantized in units of the flux quantum $\phi_0 = hc/2e$, and penetrates the superconductor in the form of *vortices*. In 1957, Abrikosov found that these vortices

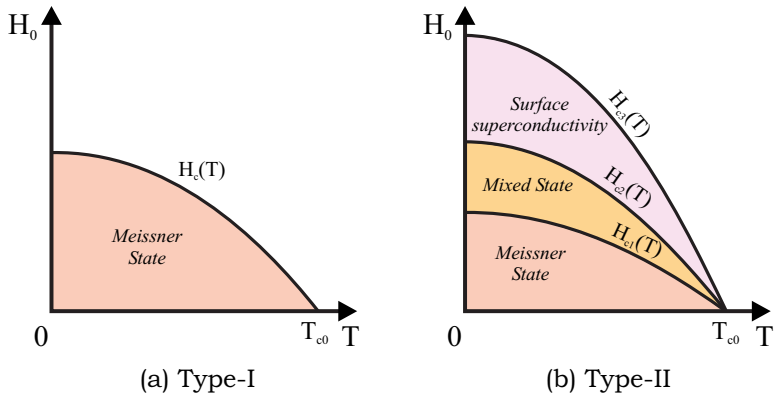


Fig. 1.12: $H-T$ phase diagram for a type-I (a) and a type-II (b) bulk superconductor.

construct a triangular lattice inside the superconductor. Such a situation holds at $H_{c1} < H_0 < H_{c2}$ where $H_{c2}$ is the so-called upper critical field, much greater than $H_c$. Such a magnetic field range with partial field penetration in the superconductor has been discovered by Shubnikov (1937) and is called the *Shubnikov phase*. Another names for this region are the *Abrikosov vortex state*, and the *mixed state*.

- At $H_0 > H_{c2}$ a macroscopic sample does not repel the flux, and $B \equiv H$. At the same time, at $H_{c2} < H_0 < H_{c3}$ a thin surface superconducting layer still exists (for bulk superconductors $H_{c3} = 1.69H_{c2}$). After $H_{c3}$ field is exceeded, superconductivity is destroyed and the entire sample is in the normal state.

The critical fields $H_c$, $H_{c1}$, $H_{c2}$ and $H_{c3}$ depend on temperature. The $H-T$ phase diagram for type-I and type-II bulk superconductors are shown in Fig. 1.12. Both types have also a different behavior of the magnetization as a function of the external magnetic field. This can be seen from Fig. 1.13. The magnetization of a superconductor is defined as $\vec{M} = (\vec{B} - \vec{H}_0)/4\pi$ where $\vec{B}$ is the magnetic induction and can be obtained by averaging the local magnetic field over the sample volume ($\vec{B} = \langle\vec{H}\rangle$).

At $H_0 < H_c$ a type-I bulk superconductor is in the Meissner state and all flux is expelled from the sample: $\langle\vec{H}\rangle = 0$ and $-4\pi\vec{M} = \vec{H}_0$. At larger fields, the applied field penetrates into the superconductor which becomes normal: $\langle\vec{H}\rangle = \vec{H}_0$ and $\vec{M} = 0$. Type-II superconductors are in the Meissner state at $H_0 < H_{c1}$ and $-4\pi\vec{M} = \vec{H}_0$. In the mixed state ($H_{c1} < H_0 < H_{c2}$) the absolute value of the magnetization $|\vec{M}|$ decreases with increasing field until it vanishes at the second critical field. It is interesting that the areas below the curves in Fig. 1.13 are the same for type-I and type-II superconductors.

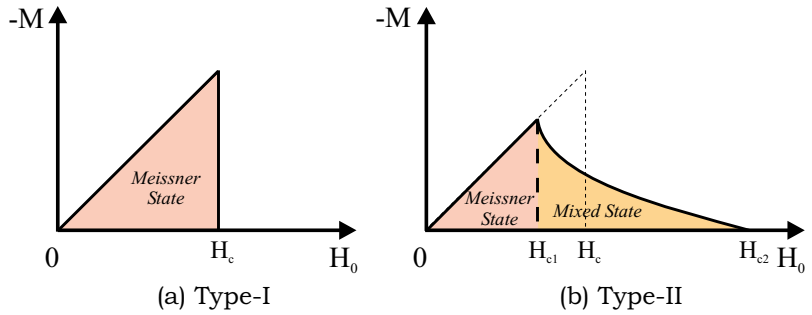


FIG. 1.13: The magnetization as a function of the applied magnetic field for type-I and type-II bulk superconductors.

### 1.1.4 Vortex structure and pinning

*1.1.4.1 Fluxoid quantization* The fluxoid quantization condition says that the total magnetic flux through a superconductor is quantized and can only be an integer multiple of the flux quantum $\Phi_0$, given by:

$$\Phi_0 = \frac{ch}{2e} = 2.067 \times 10^{-7} \text{ Gs cm}^2, \tag{1.76}$$

with $h = 2\pi\hbar$.

This condition is easily obtained from the Ginzburg-Landau formalism. If one introduces the magnitude $|\psi|$ and the phase $\phi$ of the order parameter, the second Ginzburg-Landau equation (Eq. (1.27)) can be written as

$$\vec{j}_s = \frac{2e\hbar}{m}|\psi|^2\vec{\nabla}\phi - \frac{4e^2}{mc}|\psi|^2\vec{A}. \tag{1.77}$$

Let us now calculate the contour integral of the vector potential around a closed path $C$, i.e.

$$\int_C \vec{A}\cdot d\vec{l} = \int_S rot\vec{A}\cdot d\vec{S} = \int_S \vec{h}\cdot d\vec{S} = \Phi. \tag{1.78}$$

This integral obviously gives the magnetic flux through the contour $C$. Using Eq. (1.77), we obtain

$$\Phi = \int_C \vec{A}\cdot d\vec{l} = -\frac{mc}{4e^2}\int_C \frac{\vec{j}_s}{|\psi|^2}\cdot d\vec{l} + \frac{c\hbar}{2e}\int_C \vec{\nabla}\phi\cdot d\vec{l}. \tag{1.79}$$

The last integral does not necessarily vanish, because the only general requirement is that the modulus of the order parameter $\psi$ is a single valued function, i.e. the phase of $\psi$ varies by $2\pi n$, where $n$ is an integer, when we make a

complete turn around $C$. Consequently, Eq. (1.79) predicts the fluxoid quantization

$$\Phi = n\frac{ch}{2e} - \frac{mc}{4e^2}\int_C \frac{\vec{j}_s}{|\psi|^2}\cdot\vec{dl}. \tag{1.80}$$

If the path of integration is chosen to be a contour where $\vec{j}_s = 0$, or $j_s$ is orthogonal to $\vec{dl}$, the relation becomes $\Phi = n\Phi_0$, showing that the flux trapped in a superconductor is quantized.

*1.1.4.2 The vortex lattice in a type-II superconducting film* The penetration of vortices into type-II superconductors was predicted first by A. A. Abrikosov when he discovered a two-dimensional periodic solution of the Ginzburg-Landau (GL) equations [13]. Abrikosov correctly interpreted this solution as a periodic arrangement of flux lines, the flux-line lattice. Each flux line (or fluxon, vortex line) carries one quantum of magnetic flux $\Phi_0 = h/2e = 2.07 \times 10^{-15}$ Tm$^2$, which is caused by the supercurrents circulating in this vortex. The magnetic field peaks at the vortex positions. The vortex core is a tube in which superconductivity is weakened; the position of the vortex is defined by the line at which the superconducting order parameter vanishes. For well separated or isolated vortices, the radius of the tube of magnetic flux equals the magnetic penetration depth $\lambda$, and the core radius is somewhat larger than the superconducting coherence length $\xi$, see Fig. 1.14(a). With increasing applied magnetic field, the spacing $a_0$ between the vortices decreases, consequently the average flux density $\bar{B}$ increases, and one has $\bar{B} = 2\Phi_0/\sqrt{3}a_0^2$ for the triangular flux-line lattice, see Fig. 1.14(b). The flux tubes then overlap such that the periodic induction $B(x, y)$ is nearly constant, with only a small relative variation about

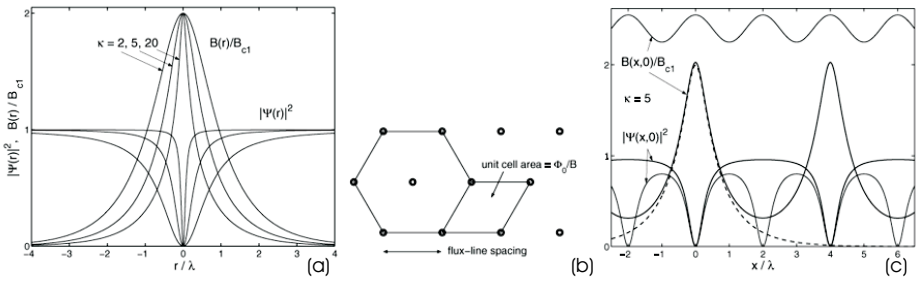


FIG. 1.14: (a) Magnetic field $B(r)$ and order parameter $|\psi|^2$ of an isolated flux line, calculated from Ginzburg-Landau theory for $\kappa = 2,\ 5$, and 20; (b) The triangular flux-line lattice; (c) Two profiles of $B(x, y)$ and $|\psi|^2$ along the $x$-axis (a nearest-neighbor direction) for vortex lattices with spacings $a_0 = 4\lambda$ (solid lines) and $a_0 = 2\lambda$ (thin lines). The dashed line shows the magnetic field of an isolated flux-line from (a) [from Ref. [51]].

its average $\bar{B}$. With further increase of $\bar{B}$ also the vortex cores begin to overlap such that the amplitude of the order parameter decreases until it vanishes when $\bar{B}$ reaches the upper critical field $B_{c2} = \mu_0 H_{c2} = \Phi_0/(2\pi\xi^2)$, where superconductivity disappears. Fig. 1.14(c) shows profiles of the magnetic field $H(x, y)$ and of the order parameter $|\psi(x, y)|^2$ for two values of $\bar{H}$ corresponding to flux-line spacings $a_0 = 4\lambda$ and $a_0 = 2\lambda$.

At low inductions $\bar{B} \ll B_{c2}$ and large $\kappa \gg 1$, the properties of the vortex lattice may be calculated from London theory, to which the GL theory reduces when the magnitude $|\psi|$ of the GL function $\psi$ is nearly constant. In the London limit, $B(x, y)$ is the linear superposition of the fields of isolated vortices; the London expressions for $B(x, y)$ and for the energy apply thus also to nonperiodic arrangements of vortices. We give below several important expressions that will be used in the rest of the thesis.

The interaction energy between two vortices in a superconducting film with thickness $d$ can be calculated in the London approximation from the increased energy associated with the overlapping magnetic fields of vortices [52] as:

$$U_{ij}(r_{ij}) = -\frac{\Phi_0^2}{8\pi^2\lambda}\left(dK_0\left(r_{ij}\right) + 2\int_0^\infty dq \frac{J_0(qr_{ij})}{k^2 Q}\right), \tag{1.81}$$

where $k = \sqrt{1+q^2}$, $Q = k(k + q\coth(kd/2))$, $r_{ij}$ is the distance between the two vortex cores, $K_0(x)$ is the MacDonald function, and $J_n(x)$ denotes the Bessel function. Thus, vortices with the same field polarity have a repulsive mutual interaction, which diverges at short distances. This repulsion leads to the formation of the Abrikosov lattice, when pinning is negligible.

The components of the vortex magnetic field in London approximation are [52]

$$h_{vz}^{(i)}(\rho, z) = \frac{\Phi_0}{2\pi\lambda^2}\left[K_0\left(\frac{R}{\lambda}\right) - \int_0^\infty \frac{dq\, q^2}{kQ} J_0\left(\frac{qR}{\lambda}\right)\frac{\cosh\left(kz/\lambda\right)}{\sinh\left(kd/2\lambda\right)}\right], \tag{1.82}$$

$$h_{v\rho}^{(i)}(\rho, z) = \frac{\Phi_0}{2\pi\lambda^2}\int_0^\infty \frac{dq\, q}{Q} J_1\left(\frac{qR}{\lambda}\right)\frac{\sinh\left(kz/\lambda\right)}{\sinh\left(kd/2\lambda\right)}, \tag{1.83}$$

$$h_{vz}^{(o)}(\rho, z) = \frac{\Phi_0}{2\pi\lambda^2}\int_0^\infty \frac{dq\, q}{Q} J_0\left(\frac{qR}{\lambda}\right)\exp\left(-q\frac{2\left|z\right| - d}{2\lambda}\right), \tag{1.84}$$

$$h_{v\rho}^{(o)}(\rho, z) = \frac{\Phi_0}{2\pi\lambda^2}\,\mathrm{sgn}(z)\int_0^\infty \frac{dq\, q}{Q} J_1\left(\frac{qR}{\lambda}\right)\exp\left(-q\frac{2\left|z\right| - d}{2\lambda}\right), \tag{1.85}$$

$$h_{v\varphi}^{(i)} = h_{v\varphi}^{(o)} = 0, \tag{1.86}$$

where indexes $i$ and $o$ denote the regions inside and outside the superconductor, and $R$ is the distance between the vortex and the point of interest.

When the thickness of a superconducting film $d$ is smaller than the London penetration depth ($d < \lambda$), some consequences for the vortex structure arise. In a perpendicular magnetic field, the distance over which the field can be screened is given by a thickness-dependent effective penetration depth $\lambda_{eff}$:

$$\lambda_{eff} = \frac{\lambda^2(T)}{d}. \tag{1.87}$$

Pearl was able to show [53] that this strongly affects the radial dependence of the circulating sheet current density and the magnetic field of a vortex; instead of the usual $\exp(-r/\lambda)$ dependence for large distances in bulk superconductors, the field decays only with $1/r^3$ in thin films. As a result, the interaction energy between vortices is changed to $U_{ij} \sim 1/r_{ij}$, similar to the Coulomb interaction between electric charges [54]. This means that vortices in thin films are interacting over a much longer range than in bulk superconductors.

*1.1.4.3 Flux pinning* The distribution and microscopic properties of pinning centers can qualitatively influence the thermodynamic and vortex transport properties of the superconducting sample. For example, one of the most important characteristics of a type-II superconductor, the value of the critical current, is determined by the balance of the Lorentz force and the pinning force acting on the flux lines. The Lorentz force is proportional to the transport current, and tends to drive the flux lines into motion, leading to the dissipation of energy and destroying the zero resistance state. Pinning forces created by isolated defects in the material oppose the motion of the flux lines and increase the critical current. Many kinds of artificial pinning centers have been proposed and developed to increase the critical current, ranging from the dispersal of small non-superconducting second phases to creation of defects by proton, neutron, or heavy ion irradiation [55, 56]. In all of these methods, the pinning centers are randomly distributed over the superconducting material, causing them to operate well below their maximum efficiency. A novel approach to the problem came with advances in lithography, which allowed for regular structuring and modulation of the sample properties over a large surface area [57]. Long-range correlation in the position of the pinning centers resulted in the interplay between the length scales characterizing the pinned lattice and the vortex lattice. These commensuration effects lead to a rich structure in the field dependence of the critical current, and a wide variety of new dynamical states. The presence of magnetic material in the vicinity of the superconductor may also affect vortices, and serve as a very effective pinning center, as will be discussed later in this thesis.

**Pinning mechanisms.** Although numerous realizations of vortex pinning have been proposed and analyzed, all pinning mechanisms can be divided in two main groups: core pinning and electromagnetic pinning [58].

*Electromagnetic pinning* is due to the perturbation of the supercurrents around vortices and of their local magnetic fields. The usual rotational symmetry of the screening currents is broken by the defects. The kinetic energy of the supercurrents can be lowered when vortices are situated on the pinning sites, resulting in an attraction between vortices and pinning centers. The important length scale here is the penetration depth $\lambda$ [59].

At point defects *core pinning* is the origin of the attractive interaction between vortices and defects. A local variation of $T_c$ or $\kappa$ at the defect results in a minimization of the free energy when the vortex core is located at the position of the defect. Other examples for core pinning sites are dislocations and grain boundaries. More effective core pinning is achieved when the size of the pinning site is of order of $\xi$ or $\lambda$.

*1.1.4.4 Vortex imaging* Quite considerable amount of time on the scale of human life has elapsed between the discovery of superconductivity (1911) and the fulfillment of the first direct spatially resolved experiment on superconductors (1947). This classic experiment was proposed to elucidate the distribution of normal and superconducting regions in the intermediate state. It was carried out by Meshkovskii and Shalnikov [60] by means of thin bismuth wire. The resistivity of the wire strongly depends on the magnetic field at low temperature. Using such a field detector, it was possible to examine a magnetic flux pattern and then to obtain the distribution of superconducting regions of the tin semi-sphere in the presence of a magnetic field.

**Scanning tunnelling microscopy (STM).** Gert Binnig and Heinrich Rohrer were awarded the Nobel Prize in Physics in 1986 for the development of the scanning tunneling microscope and were jointly honored with Ernst Ruska for his work on the development of electron microscopy. Scanning tunnelling microscopy is a technique which allows imaging solid surfaces with unprecedented resolution. The operation of a scanning tunnelling microscope (STM) is based on the so-called tunnelling current, which starts to flow when a sharp tip approaches a conducting surface at a distance of approximately one nanometer. The tip is mounted on a piezoelectric tube, which allows tiny movements by applying a voltage at its electrodes. Thereby, the electronics of the STM system control the tip position in such a way that the tunnelling current and, hence, the tip-surface distance is kept constant, while at the same time scanning a small area of the sample surface. This movement is recorded and can be displayed as an image of the surface topography. Under ideal circumstances, the individual atoms of a surface can be resolved and displayed. It should be noted, however, that STM images not only display the geometric structure of the surface, but also depend on the electronic density of states of the sample,

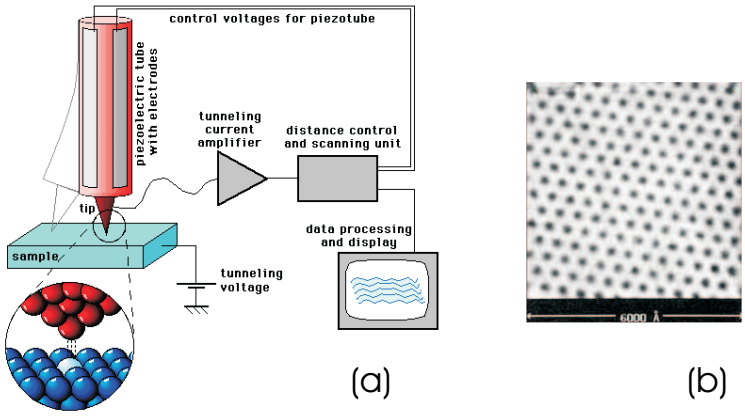


Fig. 1.15: (a) Schematic drawing of the experimental setup; (b) STM image of Abrikosov vortex lattice in $NbSe_2$ [from Ref. [61]].

as well as on special tip-sample interaction mechanisms which are not fully understood yet.

In order to investigate vortex pinning it is interesting to image the position of the vortex in the superconductor together with the structure of the superconductor. An STM can do this; it can determine both the topography of the surface on the atomic scale and the position of the normal core of the vortices, since its signal is proportional to the normal electron states density.

Although the STM itself does not need vacuum to operate (it works in air as well as under liquids), ultrahigh vacuum is required to avoid contamination of the samples from the surrounding medium.

**Lorentz microscopy.** The dynamic behavior of the vortex pattern resulting from a change of the temperature or magnetic field can be visualized by Lorentz microscopy. This technique is based on a transmission electron microscope. The cooled superconducting thin film is placed under the detecting plate in the presence of magnetic field (see Fig. 1.16). The surface of the sample is tilted by 45° both to the incident electron beam and to the magnetic field. The moving electrons are deflected by the magnetic field of the vortices due to the Lorentz force. With the defocused electron beam, the vortex becomes visible as a globule, one side bright and the other side dark with the separation line parallel to the projection of the vortex on the image plane. The vortex image size is dependent on the defocusing distance. It defines the resolution and the limit value of the magnetic field.

In Ref. [62] measurements of the Nb thin film with artificially introduced defects (holes) have been presented. The authors have shown high resolution

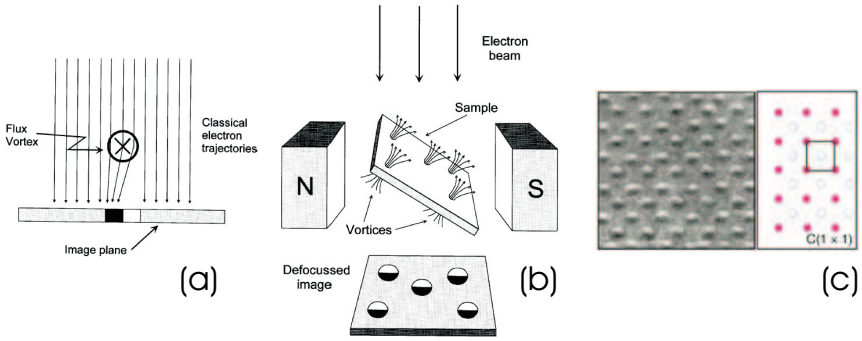


FIG. 1.16: (a) Classical response of a beam of electrons incident on a horizontal flux line; (b) Schematic diagram of the Lorentz microscopy setup; (c) Lorentz microscopy image of a vortex lattice in film with artificial periodic pinning [from Ref. [62]].

Lorentz micrographs of the vortex configurations with a different symmetry, related to the commensurability effects between the pinning arrays and the vortex lattice.

**Scanning Hall probe microscopy (SHPM).** Scanning Hall probe microscopy (SHPM) measures the lateral dependence of the magnetic stray field emanating from sample surfaces. Compared with other techniques, SHPM has the advantage of being non-invasive, very quick (about 1 image/second) and to deliver absolute values for the magnetic field. The biggest disadvantage is the relatively poorer resolution.

Vortex imaging is nothing else than mapping the magnetic field as a function of position on the materials surface. One way of creating such a map is with scanning Hall probe microscopy. A Hall probe measures the magnitude of the perpendicular component of the magnetic field at a point just above the surface of the material, then proceeds scanning across the material taking measurements until the map is created. It uses a conducting cross made with a two-dimensional electron gas (2-DEG) to measure magnetic field. As charge carriers move through the magnetic field, they shift to one side of the two-dimensional wire, creating a bias potential across the other two leads, which is directly proportional to the average magnetic field across the active region.

Over the last decade, the laboratory of S. J. Bending at Bath, United Kingdom, developed a low-noise Scanning Hall Probe Microscope with unprecedented magnetic field sensitivity of $2.9 10^{-8}$ T/Hz$^{1/2}$ at 77K, high spatial resolution of $0.2 - 0.8$ $\mu$m, scan range $25\mu$m $\times$ $25\mu$m at 77 K, operating in real-time ($\sim$ 1 frame/s) for studying flux profiles [64]. Recently, they observed

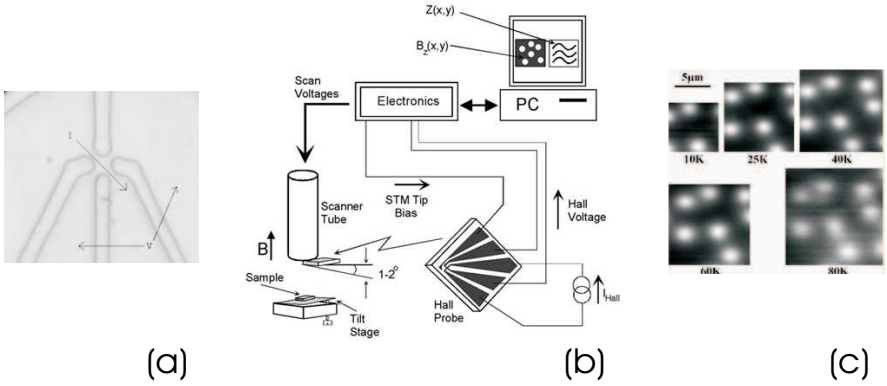


Fig. 1.17: (a) Hall probe: current flows across the active area, and voltage is measured perpendicular to the current; (b) Schematic diagram of the scanning Hall probe microscope; (c) Scanning Hall probe images of vortices [from Ref. [63]].

various vortex patterns in superconductor/ferromagnet heterostructures, which are one of the main objectives of this thesis.

**Magneto-optical imaging technique (MO).** The magneto-optical (MO) ima-ging was introduced by P. B. Alers (1957) and W. deSerbo (1960) and has been successfully applied to investigations of flux penetration and trapping in conventional superconductors and HTSC. The physical idea behind the magneto-optical imaging is the Faraday effect, i.e., rotation of the light polarization induced by magnetic field. On 13 September, 1845, Michael Faraday wrote in his diary "*...magnetic force and light were proved to have relation to each other. This fact will most likely prove exceedingly fertile and of great value in the investigation of both conditions of natural force*".

A number of different materials have been applied as indicators in MO imaging: cerous nitrate-glycerol, various europium compounds (EuS, EuSe) and bismuth-substituted iron garnets. Today, the most popular indicator is the ferri-magnetic Bi:YIG film with in-plane spontaneous magnetization. Application of a perpendicular magnetic field creates an out-of-plane component of the magnetization responsible for the Faraday rotation. At small magnetic fields the polarization rotation angle $\Theta$ depends on the field linearly, $\Theta = d\ VH$, where $d$ is the distance travelled by the light in the medium, and $V$ is a material parameter called the Verdet constant. Typically, $V$ is of the order of 0.1 $^\circ/(mT\ \mu m)$. At sufficiently high fields the indicator saturates as its magnetization vector becomes maximally aligned with the field.

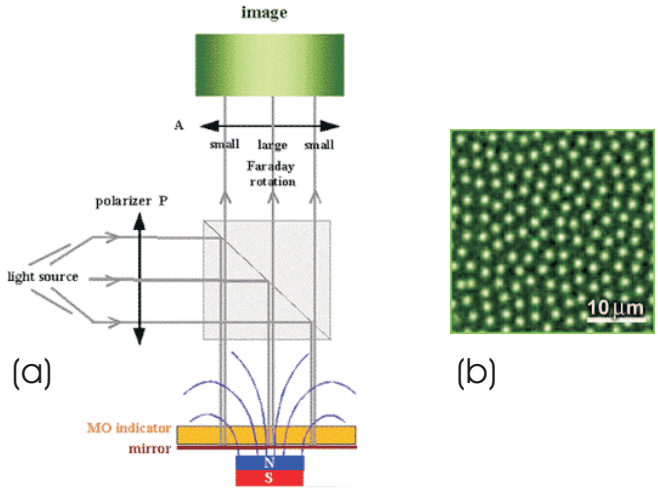


FIG. 1.18: (a) Schematic drawing of the magneto-optical setup; (b) MO image of vortex lattice in $NbSe_2$ [from Ref. [65]].

In the experimental setup, the MO indicator is placed in the light beam path between a polarizer and an analyzer crossed by 90 degrees. If a magnetic field is present perpendicularly to the film, the magnetization of the Bi:YIG will be tilted out of the plane. The perpendicular component of the magnetization will cause a Faraday rotation of the light. The rotation angle will be small where the magnetic field is small, and large in regions of high fields. After leaving the analyzer the light will therefore have an intensity distribution that reflects the magnitude of the field in the plane of the indicator film.

### 1.1.5 Mesoscopic superconductivity

Recent progress in microfabrication and measurement techniques made it possible to study the properties of superconducting samples with sizes comparable to the penetration depth $\lambda$ and the coherence length $\xi$. In such samples, called *mesoscopic* the properties of a superconductor are considerably influenced by confinement effects. Therefore, the nucleation of the superconducting state depends strongly on the boundary conditions imposed by the sample shape, i.e., on the topology of the system, which makes the behavior of the mesoscopic samples significantly different from the bulk ones. For example (see paragraphs 1.1.3-1.1.4), in thin superconducting films the distinction between type-I and type-II superconductivity does not depend only on the Ginzburg-Landau parameter $\kappa$, but also on the sample thickness. Since the effective London penetration depth $\Lambda = \lambda^2/d$ increases considerably in films with thickness $d < \lambda$ (see paragraph 1.1.4.2), the vortex state can appear in thin film samples

with $\kappa < 1/\sqrt{2}$. In this case one introduces the effective Ginzburg-Landau parameter $\kappa^* = \Lambda/\xi$ which defines the type of superconductivity: type-I when $\kappa^* < 1/\sqrt{2}$ and type-II when $\kappa^* > 1/\sqrt{2}$. In 2D-confined mesoscopic samples the distinction between type-I and type-II superconductors is determined not only by $\kappa$ and the thickness $d$, but also by the lateral dimensions of the sample (see e.g. Refs. [45, 66]). In such samples there is a competition between the triangular Abrikosov distribution of vortices, as being the lowest energy configuration in bulk material and thin films, and the sample boundary which tries to impose its geometry on the vortex distribution [45, 67]. Recently Cabral *et al.* [68] showed that a large circular disk will favor vortices situated on a ring near the boundary and only far away from the boundary its influence diminishes and the triangular lattice may reappear. The rich variety of vortex matter in mesoscopic samples was observed depending on the geometry, the size, the applied field and the temperature. For example, giant-, multi-vortex states or a combination of them (with same or opposite polarity) can nucleate in mesoscopic superconductors.

In the **multivortex** state, the flux penetrates the mesoscopic sample at several positions where individual vortices are created. In this respect, the multivortex state in confined samples is the analogon of the Abrikosov vortex state in bulk superconductors. These vortices are defined by their separate zeros of the Cooper-pair density, followed by a superconducting phase change of $2\pi$ around each of them. When the sample is sufficiently small, these vortices can overlap so strongly that it is more favorable to form one big **giant vortex**, corresponding with only one minimum in the Cooper-pair density and a multiple $2\pi$-phase change. Figs. 1.19(a,b) show the Cooper-pair density for a multivortex state and a giant vortex state in a superconducting square with sides $a/\xi = 7.0$. High Cooper-pair density is given by red regions, low by blue regions (therefore the blue spots correspond to vortices). In this case, the sample was exposed to a homogenous magnetic field. Throughout this thesis, we

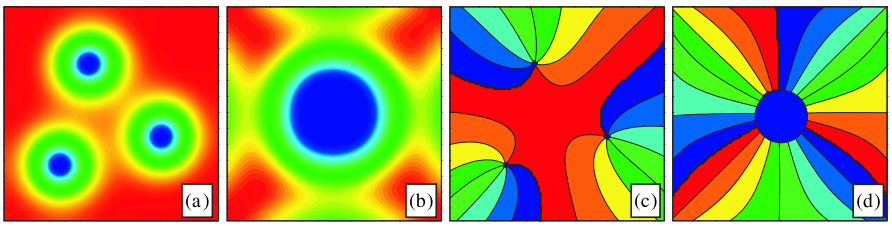


Fig. 1.19: The Cooper-pair density contourplots for the multi- and the giant vortex state (a-b) with vorticity $L = 3$ (High/low density - red/blue color), and the corresponding superconducting phase of the order parameter (c-d) ($2\pi/0$ - red/blue) in a superconducting square with sides $a/\xi = 7.0$ in a homogeneous magnetic field $H/H_{c2} = 0.47$.

will investigate vortex structure of mesoscopic superconductors in *inhomogeneous* magnetic field, where different multivortex states are possible, some of them involving vortices of different polarity.

Therefore, for a given mesoscopic sample, different superconducting states (giant vortex states, multivortex states, their combination, etc.) can nucleate for a particular applied magnetic field. These states have a different free energy and a different vortex configuration, and it is important to try to characterize them by a single quantity. For this purpose **vorticity** $L$ was introduced (see Ref. [69]). For multivortex states evolved in a homogeneous magnetic field, the vorticity is nothing else than the number of vortices. To determine the vorticity of the giant vortex state one has to look at the phase of the order parameter. Along a closed path around the vortex, the phase of the order parameter changes always with $L$ times $2\pi$. Fig. 1.19(c) shows the contour plot of the phase of the order parameter for the multivortex state of Fig. 1.19(a). Blue indicate phases near zero and red phases near $2\pi$. By going around near the boundary of the disk, the phase changes 3 times with $2\pi$. This means that the total vorticity of the disk is $L = 3$. By going around one single vortex the phase changes with $2\pi$ and $L = 1$. In Fig. 1.19(d) the phase of the order parameter is shown for the giant vortex configuration of Fig. 1.19(b). By going around the giant vortex, the phase of the order parameter changes 3 times with $2\pi$, which means that the giant vortex state alone has vorticity $L = 3$.

However, in the case of an inhomogenous applied magnetic field (for example, SC in the field of a ferromagnet), the determination of vorticity is not straightforward. Namely, although the rule of the $2\pi$-change of phase around the vortex still applies, the vorticity of a multivortex does not always correspond to the number of zeros in the order parameter distribution. Due to the inhomogeneity of the field, vortices with opposite polarity may appear (so-called antivortices, with phase-change of $2\pi$ in the opposite direction, and therefore individual vorticity -1) leading to the *decrease* of the *total* vorticity (for example, the vorticity of a multivortex structure consisting of 3 vortices and 3 antivortices equals zero). Such vortex-antivortex configurations are recently of great interest in the scientific community, and will be discussed throughout this thesis.

## 1.2 INTRODUCTION TO MAGNETISM

The basic concepts of magnetism have been well understood for many years. Magnets are used throughout industry, in everything from childrens toys to motors to hard disk drives. As technology continues to advance, we will need to understand magnetism on a much smaller-length scale. At lengths under a micron, macroscopic magnetic models are no longer adequate to describe the behavior of the magnetic material. The study of micromagnetics strives to understand magnetism on the smallest-length scale possible.

### 1.2.1 Magnetic properties and hysteresis

There are three types of magnetic materials. Diamagnetic materials, such as bismuth and antimony, are weakly repelled by both poles of a magnet, so they become magnetized opposite in direction to the external magnetic field. Paramagnetic materials, such as aluminum and platinum, react only slightly to a magnetizing force, and tend to magnetize in the direction of the external field. Ferromagnetic materials have a non-vanishing magnetization even in the absence of an external field. Ferromagnetism is generally what is meant when people talk about magnetism. Ferromagnetic elements include iron, nickel, and cobalt at room temperature, gadolinium below 16 degrees Fahrenheit, dysprosium at cryogenic temperatures, and a wide range of alloys [70]. Ferromagnetic materials become magnetized when there are more electrons with their spins

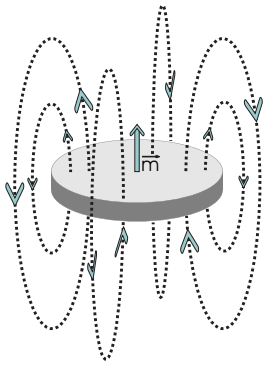


Fig. 1.20: The magnetic field lines illustrating the distribution of the magnetic field around a magnetic disk.

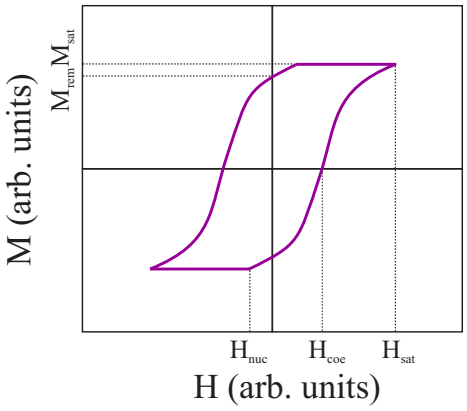


Fig. 1.21: Schematic presentation of a hysteresis loop of ferromagnetic material. $H_{nuc}$, $H_{coe}$ and $H_{sat}$ are the nucleation, coercive and saturation field, respectively, $M_{sat}$ is the saturation magnetization and $M_{rem}$ is the remanent magnetization.

(and magnetic moments) in one direction than the other. Magnetic moments want to line up with the external magnetic field, because this is their lowest energy state. However, as you look at the field lines of a magnetic dipole (Fig. 1.20), it is easy to see that at the dipole, the field lines point in one direction, but at some distance away, the field lines point in the opposite direction. This change in direction of the field lines is linked to an effect called the demagnetizing field, which ultimately causes the material to be divided up into small sections called domains. Within these domains, the moments tend to line up almost perfectly, but it takes a large force to align the net moment of each domain with each other. When they are aligned to the point where adding more energy would not align them any more, the material is at its maximum magnetization, or saturation magnetization. The magnetization process is not reversible, though, as shown by a hysteresis loop (Fig. 1.21) [71]. For instance, when an external magnetic field is applied, and then reduced back to zero, there is a residual magnetization left on the material. In other words, the moments tend to remain aligned to a certain extent. This is known as remanence. The coercive force is the opposing magnetic intensity required to remove the residual magnetism. Saturation magnetization, remanence, and coercivity are three properties of magnetic materials that are important when working on the microscopic level as well as the macroscopic level.

### 1.2.2 Magnetostatics

In this paragraph, we give the basic theoretical background for the magnetostatic calculations of the stray field of ferromagnetic structures (see, e.g. Ref. [72]), which we extensively use throughout the thesis. Starting point are the two Maxwell-equations:

$$\vec{\nabla} \cdot \vec{B} = 0, \qquad \vec{\nabla} \times \vec{H} = \vec{j}. \tag{1.88}$$

For our magnetostatic problem we have $\vec{M}(\vec{r}) \neq 0$ and $\vec{j} \equiv 0$, so that Eq. (1.88) can be rewritten as

$$0 = \vec{\nabla} \cdot \vec{B} = \mu_0 \vec{\nabla} \cdot (\vec{H} + \vec{M}), \tag{1.89}$$

and consequently

$$-\vec{\nabla} \cdot \vec{H} = \vec{\nabla} \cdot \vec{M}. \tag{1.90}$$

Since $\vec{\nabla} \times \vec{H} = 0$, we can define a scalar magnetic potential $\varphi_m$ with

$$\vec{H} = -\vec{\nabla}\varphi_m \tag{1.91}$$

and therefore we have

$$\Delta\varphi_m = \vec{\nabla} \cdot \vec{M}. \tag{1.92}$$

Eq. (1.92) corresponds to the Poisson equation, which is well-known from electrostatics. Analogous to electrostatics, we find the solution of Eq. (1.92)

by solving the integral

$$\varphi_m(\vec{r}) = -\frac{1}{4\pi}\int d^3r' \frac{\vec{\nabla}\cdot\vec{M}(\vec{r})}{|\vec{r}-\vec{r}'|} \tag{1.93}$$

Applying the formula of Gauss, we end up with

$$\varphi_m(\vec{r}) = -\frac{1}{4\pi}\vec{\nabla}_r \cdot \int d^3r' \frac{\vec{M}(\vec{r})}{|\vec{r}-\vec{r}'|}. \tag{1.94}$$

This equation gives the magnetostatic potential $\varphi_m(\vec{r})$ of an arbitrarily-shaped ferromagnet with the magnetization distribution $\vec{M}(\vec{r})$. Once $\varphi_m(\vec{r})$ is calculated, the stray field follows from Eq. (1.91).

### 1.2.3 Magnetization measurement techniques

*1.2.3.1 Magneto-Optical Kerr Effect measurements* The magneto-optical Kerr effect (MOKE) is observed as a net rotation and elliptical polarization of incident vertically linearly polarized light as it is reflected off a magnetized sample. This change in the polarization state of an incident electromagnetic wave arises due to the interaction of the electric and magnetic fields of the waves with the spin of the electrons in the material. The magnitude of this change in polarization is proportional to the magnetization of the sample. Linearly polarized light can be depicted as a combination of equal amounts of right and left circularly polarized light. Right and left circularly polarized light effectively have different indices of refraction in magnetized media as they are absorbed and reemitted differentially depending on the direction and strength of the sample's magnetization [73]. The reflected light is then the sum of unequal proportions of right and left circularly polarized light; that is, the reflected light is now elliptically polarized with its axis of polarization rotated by an amount $\Theta_k$, called the Kerr angle. The Kerr angle is approximately given by the expression:

$$\Theta_k = Im\left(\frac{N_+ - N_-}{N_+N_- - 1}\right) \tag{1.95}$$

where $N_+$ and $N_-$ are the complex propagation velocities of right and left circularly polarized light, respectively. Thus, by passing this reflected light through a crossed polarizer, one can pick off the component orthogonal to the direction of the incident light. By measuring its magnitude as a function of an external magnetic field applied to the sample, a hysteresis loop for the sample can be constructed.

*1.2.3.2 SQUID magnetometry* The superconducting quantum interference device (SQUID) consists of two superconductors separated by thin insulating layers to form two parallel Josephson junctions. The device may be configured as

a magnetometer to detect incredibly small magnetic fields - small enough to measure the magnetic fields in living organisms. Squids have been used to measure the magnetic fields in mouse brains to test whether there might be enough magnetism to attribute their navigational ability to an internal compass.

- Threshold for SQUID: $10^{-14}$T
- Magnetic field of heart: $10^{-10}$T
- Magnetic field of brain: $10^{-13}$T

The great sensitivity of the SQUID devices is associated with measuring changes in magnetic field associated with one flux quantum. If a constant biasing current is maintained in the SQUID device, the measured voltage oscillates with the changes in phase at the two junctions, which depends upon the change in the magnetic flux. Counting the oscillations allows you to evaluate the flux change which has occurred. The net result is that a SQUID functions as a flux-to-voltage converter with unrivaled energy sensitivity.

In most practical systems in use today, the SQUID is located inside a small cylindrical, superconducting magnetic shield in the middle of a liquid helium

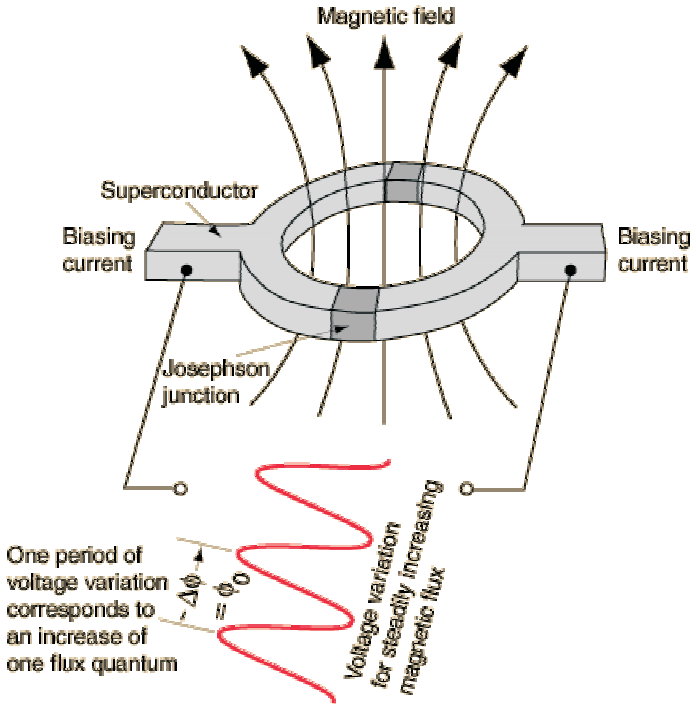


FIG. 1.22: Schematic illustration of a SQUID magnetometer.

dewar. Superconducting pickup coils, typically configured as gradiometers that detect the difference in one component of the field between two points, are located at the bottom of the dewar, and the subject is placed beneath the magnetometer. The rest of the hardware is designed to minimize helium boil off, eliminate rf interference, and to not contribute Johnson noise or distort any external AC fields [74].

## 1.3 SUPERCONDUCTOR / FERROMAGNET SYSTEMS: APPLICATIONS AND EXPERIMENTS

### 1.3.1 Superconducting levitation

The magnet suspension over the superconductor resembles interaction of two permanent magnets placed above each other with same poles oriented to each other. It is, however,a highly unstable position. With a permanent magnet and a superconductor a very effective and stable configuration is achieved by the following trick: Before the "superconductor" is cooled down to the superconducting state, the permanent magnet is placed into a close distance (few millimeters) from it. As the "superconductor" is still in normal state, magnetic field of the permanent magnet penetrates the entire "superconductor". After cooling the superconductor below its critical temperature, the sufficiently high magnetic field cannot be expelled from the superconductor volume as this would be energetically not favorable. Instead, vortices are formed in the superconductor. The normal cores of vortices are screened by superconducting screening currents and each vortex carries one quantum of magnetic flux. The external magnetic field is thus "frozen" in the superconductor. As vortices are at the superconductor surface bound to external magnetic field, each change of the external field is translated to the superconductor interior. But it is not easy to move vortices. The superconductor opposes to any change of the original configuration of the external magnetic field, both in magnitude and direction. An effective magnetic trap is thus formed that keeps the permanent magnet in its original position. The additional screening currents induced by the external field change force the magnet to return into its original place. This constitutes a very stable and efficient magnetic trap working with the magnet placed either above the superconductor (levitated) or below it (suspended). When the permanent magnet suspended over or below the superconductor is brought into rotation, it stays in revolution for a very long time, especially in vacuum where any friction is absent. This is the principle of superconducting loss less bearing, superconducting motor or superconducting gear. The latter, in a huge dimensions can serve as an energy storage device, an old dream of scientists. Smaller gears can be used for stabilization of a space craft as their large kinetic energy brakes a change of the gear orientation. This application is

particularly appropriate in the space for the low temperature there, which enables a natural and effective cooling of the high-Tc superconductor. Probably the most attractive application of the superconducting levitation at present is the magnetically levitated train, MagLev. Thanks to low friction this train is able to reach extreme speeds. The present record, reached by the train of 5 wagons on April 14, 1999 near Tokyo, Japan, is 554 km/h.

### 1.3.2 Enhancement of critical current by magnetic nano-structuring

Another aspect that makes superconductor/ferromagnet hybrid systems interesting to study is vortex pinning. Superconductors with high critical current densities $j_c$ are crucial for applications such as superconducting magnets for the generation of high magnetic fields and superconducting wires for current transport. Vortex pinning and $j_c$ are directly related with each other, since the motion of flux lines creates an electric field, causing dissipation and resulting in the appearance of a resistive state. An enhancement of $j_c$ can be achieved by pinning of vortices by defects, as explained in section 1.1.4.3. Recently, Bulaevskii *et al.* predicted that stripe domains in a magnetic film with perpendicular anisotropy can enhance the flux pinning by two orders of magnitude compared to pinning by columnar defects [75], due to the interaction between the magnetic flux $\phi$ of the vortices and the magnetic moment $m$ of the ferromagnet. In 1998, Morgan and Ketterson investigated the role of a regular array of out-of-plane magnetic dipoles embedded in a superconducting film and found enhanced pinning effects when the flux lattice and the dipole lattice were commensurate. In particular, they measured the superconducting critical current of niobium films with an embedded array of ferromagnetic nickel particles.

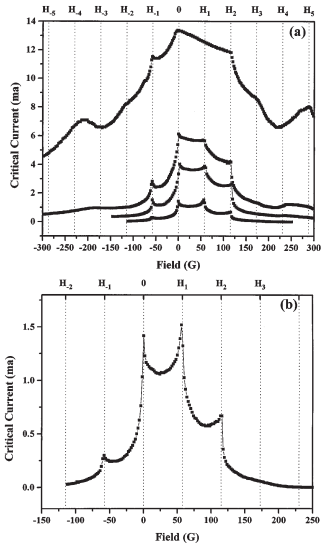


FIG. 1.23: (a) Critical current as a function of field for the high density triangular array at $T = 8.00,\ 8.40,\ 8.46$, and 8.52K (top to bottom) ($T_c = 8.56$K). (b) Enlargement of the $T = 8.52$K sweep [from Ref. [76]].

Critical current measurements as a function of applied homogenous magnetic field are shown in Fig. 1.23 for triangular magnetic dot array at several temperatures. The vertical lines indicate integer multiples of the first commensurate field $H_1$ (14.4Gs, one vortex per pinning site). As expected, one should notice strong increase in the critical current at the so-called matching fields, where all vortices in the sample are strongly pinned. The pinning mechanisms involved here, the nature of the magnet-vortex interaction and the matching vortex structures will be one of the most important objectives of this thesis.

### 1.3.3 Magnetic-field-compensators and magnetic phase-shifters

When the applied magnetic field exceeds a certain critical value, superconductivity is suppressed due to orbital and spin pair breaking effects. This very general property of superconductors sets strong limits for their practical applications, since, in addition to applied magnetic fields, the current sent through a superconductor also generates magnetic fields, which can lead to a loss of zero resistance. As explained in section 1.1.3, some rare materials are not only able to withstand magnetic fields, but in them superconductivity can be induced by applying a magnetic field, contrary to conventional superconductors which are the subject of this thesis.

Last year, M. Lange *et al.* found that field-induced superconductivity can also be realized in hybrid superconductor/ferromagnet nanostructured bilayers [8]. The basic idea is quite straightforward (see Fig. 1.24): a lattice of magnetic dots with out-of-plane magnetization is placed on top of a superconducting film.

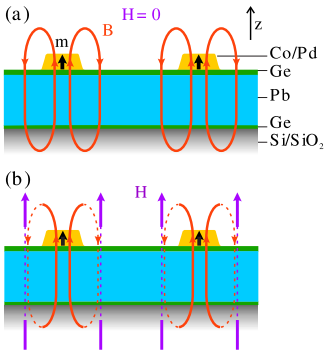


Fig. 1.24: Schematic drawing of the investigated hybrid superconductor/ferromagnet sample. (a) The magnetic stray field $B$ of the dots is comparable with the field of a magnetic dipole. (b) A magnetic field $H$ applied in the z direction can be compensated by the dipole stray field between the dots, resulting in the conditions necessary for the observation of magnetic field-induced superconductivity [from Ref. [8]].

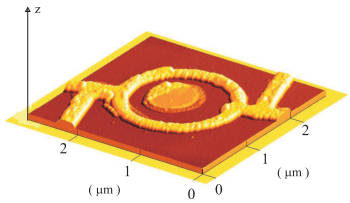


FIG. 1.25: An Atomic Force Microscopy image of the device [from Ref. [78]].

The magnetic stray field of each dot $B_z$ has a positive z component of the magnetic induction under the dots and a negative one in the area between the dots. Added to a homogeneous magnetic field these dipole fields enhance the z component of the effective magnetic field $\mu_0 H_{eff} = \mu_0 H + B_z$ in the small area just under the dots and, at the expense of that, reduce $H_{eff}$ everywhere else in the film. This new field compensation effect is not restricted to specific superconductors, so that this feature could be achieved in any superconducting film with a lattice of magnetic dots. Therefore, a nanoengineered lattice of magnetic dipoles can be used to selectively enhance the critical fields of superconducting films. Besides improving the critical fields, the dipole array field compensator can also be used to design logical devices in which superconductivity is controlled by switching between the two polarities of the magnetized dot array.

Various macroscopic solid state structures can exhibit quantum behavior, potentially interesting for quantum computing [77]. Very recently, Golubović *et al.* designed and investigated the contactless magnetic phase shifter for flux-based superconducting qubits [78]. The phase shift is achieved by placing a magnetic dot with perpendicular magnetization in the center of a loop made of a conventional s-wave superconductor (see Fig. 1.25). The flux generated by the dot creates an additional current in the superconducting loop giving rise to a phase shift. The phase shift in this device is a result of a quite basic and general property of superconductors and can be implemented without any limitations. By conveniently varying the parameters of the dot it is possible to introduce any phase shift in the loop. The magnetic phase shifter can, therefore, be used as an external current source with a high stability.

### 1.3.4 Rectification effects in SC/FM heterostructures

Recently, Villegas et al. fabricated a device that controls the motion of flux quanta in a niobium superconducting film grown on an array of nanoscale triangular Ni magnetic dots [79]. They observed the controllable rectification of the vortex motion, due to the asymmetry of the fabricated magnetic pinning centers. In order to interpret the experimental results, we can separate all

vortices into two groups: (i) pinned vortices, which move from one triangular-shaped pinning trap to another and, thus, are directly affected by the pinning potential (marked red in Fig. 1.26); and (ii) interstitial vortices, which move in between triangles and do not directly interact with the pinning traps (marked blue in Fig. 1.26). However, the interstitial vortices can indirectly feel the spatial asymmetry through their interactions with the pinned vortices. It can be shown that pinned (red) vortices create an effective asymmetric potential, with the opposite asymmetry or opposite polarity for the other (blue) vortices. When all the vortices are subjected to an ac drive force, this "inverted polarity" potential rectifies the motion of the interstitial vortices in one direction. The original pinning potential rectifies the motion of the pinned vortices along the opposite direction, because they feel a potential with opposite polarity. Therefore, as illustrated in Fig. 1.26, the vortex flow in the sample changes direction as the saturation number of the pinning site is exceeded ($n = 3$) and the interstitial vortices appear.

This device allows a versatile control of the motion of vortices in superconducting films. Simple modifications and extensions of it would allow the

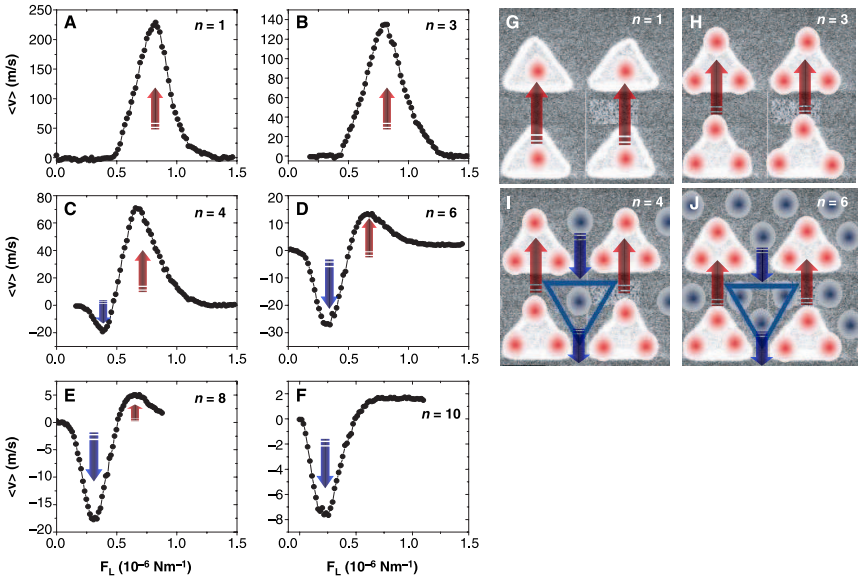


Fig. 1.26: (A to F) Net velocity of vortices versus the ac Lorentz force amplitude ($\omega = 10$ kHz), for several matching magnetic fields at $T = 0.98T_c$; $n$ indicates the number of vortices per unit cell of the array. Red and black arrows show the direction of the net flow of these vortices. (G to J) Sketch of the positions of the vortices for several matching fields. Vortices pinned on the triangles are shown in red and interstitial vortices in blue [from Ref. [79]].

pile-up (magnetic lensing), shaping, or "sculpting" of micromagnetic profiles inside superconductors. Vortex lenses made of oppositely oriented triangles would provide a strong local increase of the vortex density at its focus regions. Thus, extensions of these types of systems could allow the motion control of flux quanta and provide a step toward devices based on the flow of magnetic flux quanta.

# 2

# *Magnetic pinning of vortices in superconducting films: The magnet - vortex interaction in London approximation*

## 2.1 INTRODUCTION

The value of the critical current is one of the decisive factors for the usefulness of a superconductor (SC). Large values of the critical currents in superconductors are usually obtained through pinning of vortices to different inhomogeneities in a superconductor. In this respect, external and internal surfaces can be treated as inhomogeneities [80]. Pinning centra are introduced e.g. by locally destroying the crystal structure through e.g. bombardment with high energy particles. Recently, nanostructuring of a superconducting film with a regular area of holes [57] has lead to a large increase of the critical current, in particular at the so-called matching magnetic fields. An alternative approach is to deposit an area of ferromagnetic dots near a superconducting film which acts as very effective trapping centra for the vortices. Recently, it was predicted [75], although not verified, that an increase of the pinning effects by two orders of magnitude can be realized. After substantial progress in the preparation of regular magnetic arrays on superconductors [2] and considering the importance of such structures for magnetic device and storage technologies, these hybrid systems became very interesting both from a theoretical and an experimental point of view. Macroscopic pinning phenomena have already been explored experimentally, [2, 81, 82] but a theoretical analysis of the magnetic and superconducting response in such systems is still lacking. In the majority of recently

proposed models [83–87] the inhomogeneous magnetic field of a ferromagnet induces screening currents in a SC, which, in turn, generate a magnetic field influencing the applied field. Consequently, this problem must be solved self-consistently. Furthermore, the finite thickness of both the superconductor and the ferromagnetic material was not taken into account in previous theoretical treatments.

Other theoretical studies involving finite size ferromagnets were mainly restricted to the problem of a magnetic dot with out-of-plane magnetization embedded in a superconducting film [88, 89]. Marmorkos *et al.* [88] solved the non-linear Ginzburg-Landau (GL) equation numerically, with appropriate boundary conditions for an infinitely long ferromagnetic cylinder penetrating the superconducting film, and found a correspondence between the value of the magnetization and the vorticity of the most energetically favorable giant-vortex state. At that time, the interaction between a small ferromagnetic particle, which may be considered as a point magnetic dipole (MD), and a type II superconductor was of interest [90, 91], and the magnetostatic energy and levitation force acting on a dipole were calculated, but still within a thin film approximation. In experiments [92], the magnetic field of the MD was supposed to be weak, and not able to drastically change the structure of the superconducting state in the sample. Obviously, the MD could create additional vortices near the surface, and this process can be described theoretically as proposed in Ref. [91], by a simple comparison of the free energies of the system with and without vortex. However, the spontaneous creation of a vortex-antivortex pair as a possible lower energy state was never considered.

Motivated by recent experiments [76, 93], we focus in this chapter on a system consisting of a type II thin superconducting film (SC) and a ferromagnet (FM) placed above (below) it which acts as a pinning center. We study in detail, using the London approximation, how the system is perturbed in the neighborhood of the magnet. The superconducting film lies in the $z = 0$ xy-plane while the FM is positioned at $(x, y, z) = (0, 0, a)$, and is magnetized in the positive z- or x-axis direction. To avoid the proximity effect and exchange of electrons between FM and SC we suppose a thin layer of insulating oxide between them as is usually the case in the experiment.

This chapter is organized as follows. In the next section we present the theoretical formalism. In Sec. 2.3, we discuss the pinning potential of the magnetic dipole with in- or out-of-plane magnetization. We also calculate the total interaction energy in the system in the presence of vortex-antivortex pairs, and determine their most favorable position. The question of stability of such vortex configurations is also addressed. In Sec. 2.4, we consider the case of a finite-size FMs, magnetized out-of-plane, as a more realistic experimental situation. First, we discuss the differences in vortex pinning by magnetic disk and magnetic annulus (ring). Also, the vortex-magnet interaction energy and supercurrent induced in the superconductor are calculated analytically and the profiles are shown. We use these results further to investigate the manipulation

of vortices in the case of a more complicated geometry of the magnet, i.e. magnetic disk with an off-center hole(s). The pinning properties of the magnet with square or triangular shape are then analyzed and the most favorable trajectory of the vortex with respect to the magnet edge is discussed. Finally, in Sec. 2.5, in-plane magnetized ferromagnets are considered as pinning centers. To begin with, we discuss the pinning potential of the magnetic stripe, a plane of in-plane magnetized dipoles, perpendicular to the SC plane. Then we investigate the field-polarity dependent pinning in the case of an in-plane magnetized bar on top of a superconductor and compare our results with the experimental ones, with special emphasis on the influence of the geometry of the magnet on the pinning of external flux lines. At last, the effect of the presence of symmetric defects in the magnet geometry is discussed, and the summary is given.

## 2.2 THEORETICAL FORMALISM

We consider a ferromagnet of arbitrary shape with homogeneous out-of-plane magnetization $\vec{M}$, placed outside a type II SC film interacting with a single vortex in the SC. Within the London approximation, the Gibbs free energy of this system is given by [94]

$$F = \frac{1}{8\pi}\int dV\left[\vec{h}^2 + \lambda^2(rot\vec{h})^2\right] - \int dV\left[\vec{h}_v\cdot\vec{M}\right], \tag{2.1}$$

where $\lambda$ is the penetration depth, $\vec{h}$ is the total field present in the system, and $\vec{h}_v$ and $\vec{M}$ denote the magnetic field of the vortex and magnetization of the FM, respectively. The second integral in Eq. (2.1) represents the potential energy of the FM in the magnetic field of the vortex. In this chapter, we focus on the ferromagnet-vortex interaction energy, and the terms in Eq. (2.1) regarding the self energy of the vortex and the magnet are omitted. In the case of a point magnetic dipole, the second integral in Eq. (2.1) corresponds to the exclusion of the volume of the FM when integration is performed [91]. Therefore, we may rewrite Eq. (2.1) as

$$F = \frac{1}{8\pi}\int dV^{(i)}\left[\vec{h}^2 + \lambda^2(rot\vec{h})^2\right] + \frac{1}{8\pi}\int dV^{(o)}\vec{h}^2 - \frac{1}{8\pi}\int dV^{(fm)}\vec{h}^2.$$

Using the identity

$$\vec{h}^2 = \vec{A}\cdot rot\vec{h} + div\left(\vec{A}\times\vec{h}\right),$$

we obtain

$$F = \frac{1}{8\pi}\int dV\left[rot\vec{h}\cdot\left(\vec{A}+\lambda^2 rot\vec{h}\right)\right] - \frac{1}{8\pi}\int d\vec{S}\cdot\left(\vec{h}\times\vec{A}\right) - \frac{1}{8\pi}\int dV^{(fm)}\vec{h}^2.$$

Here we integrate over the volume inside $V^{(i)}$ and outside $V^{(o)}$ the superconductor, while $V^{(fm)}$ denotes the volume of the ferromagnet. $V$, by default,

corresponds to "the whole space" and equals $V^{(i)} + V^{(o)}$. We choose the surface $S$ far away from the superconductor where we can apply the boundary condition $\vec{h} \to 0$. Due to the London equation, the field of the ferromagnet inside the SC satisfies

$$\vec{h}_m + \lambda^2 rot\left(rot\vec{h}_m\right) = 0. \tag{2.2}$$

The magnetic field and corresponding vector potential can be written as $\vec{h} = \vec{h}_m + \vec{h}_v$, $\vec{A} = \vec{A}_m + \vec{A}_v$ where indexes $v$ and $m$ refer to the vortex and ferromagnet, respectively. Now, from Eq. (2.1) we obtain the vortex-FM interaction energy as

$$\begin{aligned} F_{mv} &= \frac{1}{8\pi}\int dV\left[rot\vec{h}_m \cdot \left(\vec{A}_v + \lambda^2 rot\vec{h}_v\right)\right] \\ &= \frac{1}{2c}\int dV^{(i)}\left[\vec{j}_m \cdot \vec{\Phi}_v\right] + \frac{1}{2}\int dV^{(o)}\vec{A}\cdot rot\vec{M} - \int dV^{(fm)}\vec{h}\cdot\vec{M} \end{aligned}$$

which after simple integral transformations becomes

$$F_{mv} = \frac{1}{2c}\int dV^{(i)}\left[\vec{j}_m \cdot \vec{\Phi}_v\right] - \frac{1}{2}\int dV^{(fm)}\vec{h}_v\cdot\vec{M}, \tag{2.3}$$

where $\vec{\Phi}_v = (\Phi_\rho, \Phi_\varphi, \Phi_z) = (0, \Phi_0/(2\pi\rho), 0)$ denotes the vortex magnetic flux vector ($\Phi_0$ is the flux quantum), and $\vec{M}$ is the magnetization of the magnet. As one can see, the interaction energy in this system consists of two parts, namely, (i) the interaction between the Meissner currents generated in the SC ($\vec{j}_m$) by the FM and the vortex, and (ii) the interaction between the vortex magnetic field and the MD. In the Appendix, we show analytically that in the case of a point magnetic dipole (MD) these two contributions to energy are equal. Due to the superposition principle, the finite FMs with homogeneous magnetization can be represented as an infinite number of dipoles. Consequently, the vortex-magnet interaction energy equals

$$U_{mv} = -\int dV^{(fm)}\vec{h}_v\cdot\vec{M}. \tag{2.4}$$

In order to obtain the current induced in the superconductor by the ferromagnet, one should solve first the equation for the vector potential [95]

$$rot\left(rot\vec{A}_m\right) + \frac{1}{\lambda^2}\Theta\left(d/2 - |z|\right)\vec{A}_m = 4\pi rot\vec{M}. \tag{2.5}$$

This equation is rather complicated to be handled for a finite size FM, but, expressions for the induced SC current in an infinite superconducting film with thickness $d$ ($-\frac{d}{2} < z < \frac{d}{2}$) in the magnetic dipole case (with magnetic moment $m$) can be analytically derived. The results for both vector potential and magnetic field, for different orientations of the magnetic moment of the dipole, are given in the Appendix.

To find the supercurrent induced by a finite size FM above the superconductor, we make once more use of the superposition principle and integrate the components of the current, induced by magnetic dipoles, over the volume of the ferromagnet. Thus, the value of the total current follows from ($\alpha = x, y$)

$$j_\alpha(x,y,z) = \int j_\alpha^{md}(x,y,z)\; dV^{(fm)}. \tag{2.6}$$

## 2.3 THE POINT MAGNETIC DIPOLE AS A PINNING CENTER

### 2.3.1 Out-of-plane magnetized dipole

The superconducting current induced in an infinite superconducting film with thickness $d$ ($-\frac{d}{2} < z < \frac{d}{2}$) by a magnetic dipole with *out-of-plane magnetization*, i.e. $\vec{m} = m\vec{e}_z$ located at $z = a$ is obtained as a solution of Eq. (2.5) ($\vec{M} = \vec{m}\delta(x)\delta(y)\delta(z-a)$) which is given by

$$j_\varphi(\rho,z) = -\frac{cm\Phi_0}{2\pi\lambda^3}\int_0^\infty dq \exp\left\{-q\left(|a| - \frac{d}{2}\right)\right\} q^2 J_1(q\rho) C\,(q,z)\,, \tag{2.7}$$

with

$$C\,(q,z) = \frac{k\;\cosh\left[k\left(\frac{d}{2}+z\right)\right] + q\;\sinh\left[k\left(\frac{d}{2}+z\right)\right]}{(k^2+q^2)\;\sinh(kd) + 2kq\;\cosh(kd)}, \tag{2.8}$$

where $k = \sqrt{1+q^2}$, $\rho = \sqrt{x^2+y^2}$, sinh and cosh denote the hyperbolic trigonometric functions and $J_v(x)$ is the Bessel function. For a MD placed under the SC, one should replace $z$ by $-z$ in Eq. (2.8). The magnetic moment of the dipole is measured in units of $m_0 = \Phi_0\lambda$, and all distances are scaled in

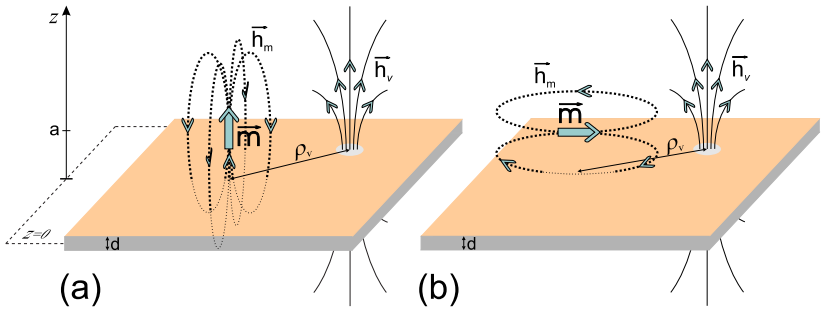


Fig. 2.1: An oblique view of the systems under investigation with (a) out- and (b) in-plane directed magnetic dipole above a superconducting film interacting with a vortex.

units of $\lambda$. These units will be used in the rest of the chapter. Clearly, Eq. (2.5) can also be used for a film of finite dimensions $L$ in the limits $\rho, a << L$. The above integral (2.7) can be solved analytically for certain asymptotic limits

$$j_\varphi(\rho,z)=\begin{cases} -\frac{3cm\Phi_0\rho l}{2\pi\lambda^3\left(\rho^2+l^2\right)^{5/2}}\frac{\cosh(d/2+z)}{\sinh(d)},\ \rho >> \max(l,1/d) \text{ or } l >> \max(\rho,1/d), \\ -\frac{cm\Phi_0}{4\pi\lambda^3}\left[\frac{\rho}{\left(\rho^2+l^2\right)^{3/2}}+\frac{d\left(\sqrt{\rho^2+l^2}-l\right)}{2\rho\sqrt{\rho^2+l^2}}\right],\ \rho,l<\frac{1}{d},\ d<<1, \end{cases} \tag{2.9}$$

where $l=|a|-\frac{d}{2}$ is the distance between the MD and the top surface of the SC film.

Inserting the well known expression for the magnetic field of a vortex (see Eq. (A3) in the Appendix), into Eq. (2.3) we find

$$F_{mv}=\frac{m\Phi_0^2}{2\pi\lambda}U_\perp\left(\rho_v\right), \tag{2.10}$$

where $\rho=\rho_v$ denotes the position of the vortex, and

$$U_\perp\left(\rho_v\right)=-\int_0^\infty dq\frac{q}{k(k+q\coth(kd/2))}J_0\left(q\rho_v\right)\exp(-ql). \tag{2.11}$$

In some limiting cases it is possible to solve this integral analytically:

(1) for $d<<1$ and $\rho_v<1/d$ we found: $U_\perp\left(\rho_v\right)\approx -d/\left(2\left(\rho_v^2+l^2\right)^{1/2}\right)$;
(2) for $d<1$ and:
  (a) $\rho_v>l$: $U_\perp\left(\rho_v\right)\approx -d/\left(2\left(\rho_v^2+l^2\right)^{1/2}\right)+\pi d^2\left[H_0(\rho_v d/2)-Y_0(\rho_v d/2)\right]/8$,
  (b) $\rho_v>>1/d$: $U_\perp\left(\rho_v\right)\approx -2/\left(d\rho_v^3\right)$;
(3) for $d>1$ and $\rho_v>>\max(l,1/d)$ or $l>>\max(\rho_v,1/d)$:
  $U_\perp\left(\rho_v\right)\approx -l/\left(\rho_v^2+l^2\right)^{3/2}$;
(4) for $d>>1$, $l<<1$ and $\rho_v>>l$:
  $U_\perp\left(\rho_v\right)\approx -l/\left(\rho_v^2+l^2\right)^{3/2}+\left[I_0\left(\rho_v/2\right)K_0\left(\rho_v/2\right)-I_1\left(\rho_v/2\right)K_1\left(\rho_v/2\right)\right]/2$.

Here, $H_v(x)$ and $Y_v(x)$ ($I_v(x)$, $K_v(x)$) denote the Struve and Bessel function (modified Bessel functions), respectively. One should notice that our asymptotic results for a thin SC film differ from those given in Eq. (7) of Ref. [87] by a factor of two, and are in agreement with the calculations of Ref. [91] (Eq. (3.16) of Ref. [91]).

In Fig. 2.2(a,b) the interaction energy as function of the position of the vortex is shown, for different (a) vertical positions of the magnetic dipole, and (b) thickness of the SC. Please note that the asymptotic expressions for an extremely thin SC, namely $d<<1$, give a very good description of the interaction potential (see inset of Fig. 2.2(b)). As expected, the interaction energy in this system is axially symmetric and this is illustrated in Fig. 2.2(c). In Fig. 2.2(a), we notice that the energy curves for different vertical positions of the dipole cross each other for large MD-vortex distances, for the case of a thick

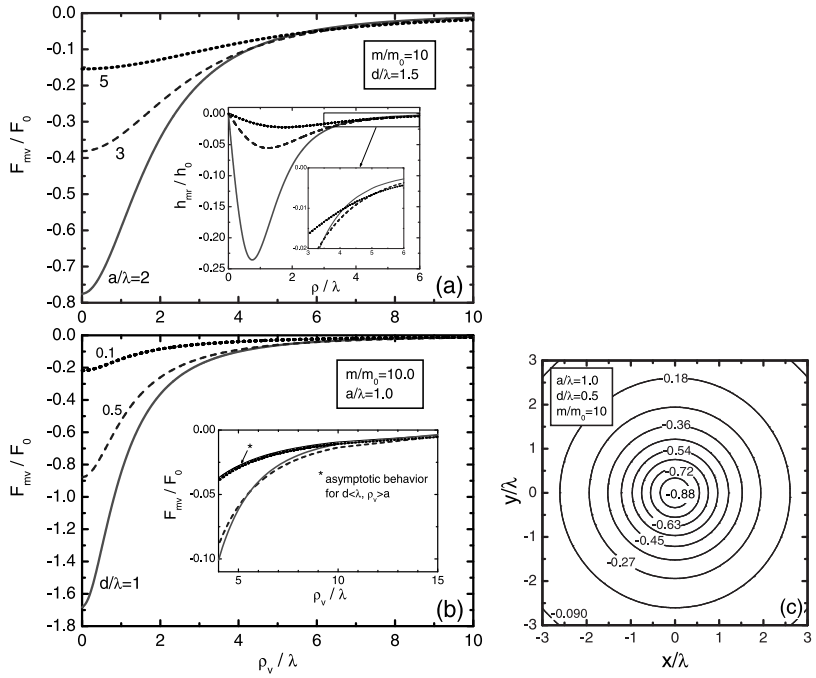


Fig. 2.2: The interaction energy of the vortex with an out-of-plane magnetic dipole (MD) in units of $F_0 = \Phi_0^2/(\pi\lambda)$ as a function of the position of the vortex ($\rho_v$): a) for different position of the MD; b) for different thickness of the superconductor; and c) the contour plot of the interaction potential. Inset in (a) illustrates the component of the total MD magnetic field in the presence of the SC, tangential to the SC surface ($h_0 = m_0/\lambda^3$). Inset in (b) depicts the asymptotic behavior for specific values of the parameters.

SC, namely $d > 1$. Consequently, comparing two vertical positions of the dipole, for a MD which is higher above the SC film, interaction with the vortex is stronger at large distances, i.e. $\rho_v >> 1/d$ (see our approximate results above, i.e. case (3)). This can be understood as follows. For a thick superconductor, the magnetic field does not penetrate through the SC, and the component of the field tangential to the surface becomes important. When the MD approaches the SC surface, the value of this field component at large distances from the dipole increases, as shown in the inset of Fig. 2.2(a). Therefore, the interaction between the dipole and the vortex is stronger for smaller $l$ when the MD-vortex distance $\rho_v$ is small, and opposite, for large $\rho_v$, the interaction energy grows if $l$ is larger.

Naturally, the minimum of the interaction energy depicts the energetically favorable position of the vortex. Therefore, from Fig. 2.2 one notices that for parallel alignment of the MD magnetization and the vortex the interaction will

be purely attractive, and the vortex is pinned under the MD, independently of the parameters of the system (thickness of the SC, vertical position of the MD and its magnetization strength, etc.). These parameters only determine the strength of this attractive interaction. For the anti-parallel orientation of the magnetic moment, the vortex is repelled.

### 2.3.2 In-plane magnetized dipole

Following the same procedure, for a MD with *in-plane magnetization* ($\vec{m} = m\vec{e}_\rho$, for $\varphi = 0$, and $\vec{m} = 0$ for $\varphi \neq 0$) we have

$$F_{mv} = \frac{m\Phi_0^2}{2\pi\lambda} U_\parallel(\rho_v, \varphi), \tag{2.12}$$

where $\varphi$ is the angle in the SC plane between the direction of the magnetic moment of the dipole and the point of interest, and

$$U_\parallel(\rho_v, \varphi) = \int_0^\infty dq \frac{q\cos\varphi}{k(k + q\coth(kd/2))} J_1(q\rho_v)\exp(-ql), \tag{2.13}$$

for which we obtain the following analytic asymptotic results:
(1) for $d < 1$ :
$U_\parallel(\rho_v, \varphi) \approx -d\cos\varphi_v/2\left\{l/\left(\rho_v\sqrt{\rho_v^2 + l^2}\right) + \pi d/4\left[H_{-1}(\rho_v d/2) + Y_1(\rho_v d/2)\right]\right\}$;
(2) for $d << 1$ : $U_\parallel(\rho_v, \varphi) \approx \rho_v d\cos\varphi_v/\left(2\sqrt{\rho_v^2 + l^2}\left(l + \sqrt{\rho_v^2 + l^2}\right)\right)$;
(3) for $d > 1$ and $\rho_v >> \max(l, 1/d)$ or $l >> \max(\rho_v, 1/d)$ :
$U_\parallel(\rho_v, \varphi) \approx \rho_v\cos\varphi/\left(\rho_v^2 + l^2\right)^{3/2}$;
(4) for $d >> 1$, $l << 1$ and $\rho_v >> l$:
$U_\parallel(\rho_v, \varphi) \approx \cos\varphi\left[\rho_v/\left(\rho_v^2 + l^2\right)^{3/2} + (1 + \rho_v)\exp(-\rho_v)/\rho_v^2\right]$.

In Fig. 2.3(a,b), the energy is plotted as function of the position of the vortex when it is moved along the direction of the MD magnetization ($\varphi = \pi$), and Fig. 2.3(c) shows the complete contour plot. The vortex is attracted to one side (where the magnetic field of the MD penetrates the SC in the same direction as the vortex, see Fig. 2.1(b)) and repelled on the opposite side of the MD. Moreover, it is pinned in a spot whose position does not depend on the magnetization of the MD but it is influenced by the vertical position of the dipole and the thickness of the SC. When the dipole approaches the SC or the thickness of the superconductor is increased, the interaction becomes stronger and the vortex will move closer to the MD.

From our asymptotic expressions for the interaction energy the most favorable position of the vortex can be easily obtained by minimizing the energy. In the thin film approximation ($d << 1$), we obtain $\rho_v^* = \sqrt{2 + 2\sqrt{5}}l/2 \approx 1.272\ l$, while for $d > 1$, but $l >> 1/d$ we have $\rho_v^* = l/\sqrt{2} \approx 0.7071\ l$. In Fig. 2.4(a) we

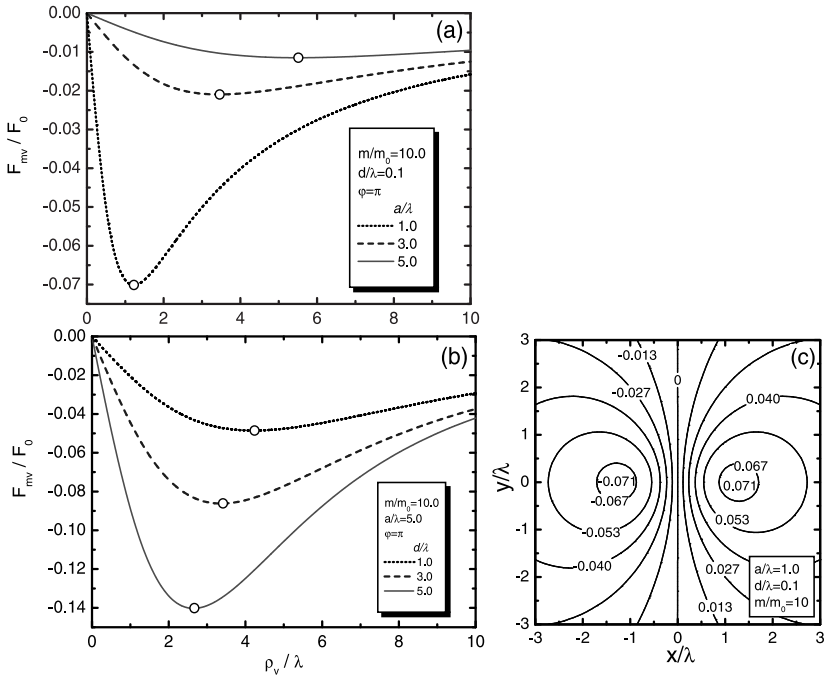


Fig. 2.3: The interaction energy of the vortex with an in-plane magnetic dipole (MD) in units of $F_0 = \Phi_0^2/(\pi\lambda)$ as a function of the position of the vortex ($\rho_v$): a) for different vertical position of the MD; b) for different thickness of the superconductor; and c) the contour plot of the interaction potential. Open circles denote the energetically favorable position of the vortex.

show the $d-$dependence of the equilibrium position as function of the thickness of the SC. The $\rho_v^*(l)$ function is in general non-linear, as shown in Fig. 2.4(b). A peculiar fact is that for $d > 2$, the energetically preferable position of the vortex depends only on $l$. This follows from the fact that the magnetic field of the dipole penetrates only in the surface layer of the superconductor down to the penetration depth $\lambda$ so that further increase of the SC thickness does not affect the total interaction. From Fig. 2.4(b) one should notice that our asymptotic results describe nicely the behavior of the system for $d << 1$ or $l >> d$, when $d > 1$.

For the case of in-plane MD, it should be emphasized that the vortex is attracted to the side of the MD where the magnetic field is parallel to the field of the vortex, which is similar to the case of the out-of-plane magnetized dipole. This conclusion also follows from the observation of the interaction between the induced currents and the vortex. For in-plane magnetized MD above the superconductor, the components of the superconducting current in

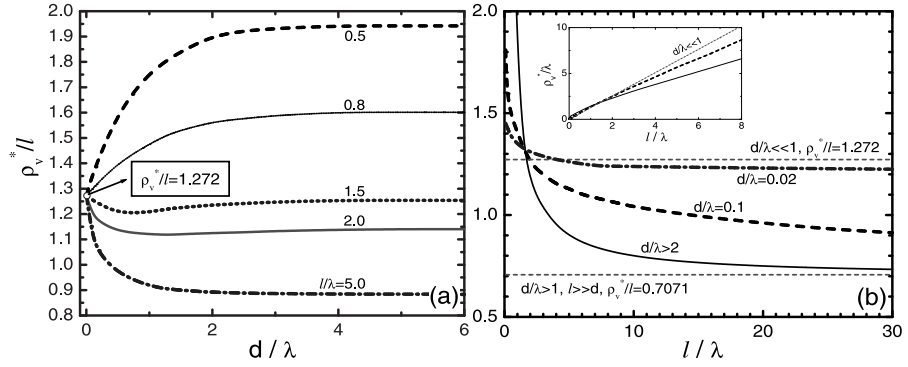


FIG. 2.4: The position of the vortex ($\rho_v^*$) as function of the thickness of the superconductor ($d$) and distance between the in-plane magnetized dipole and the SC surface ($l = a - d/2$). $\rho_v^*$ is scaled by $l$ or by $\lambda$ (inset of (b)).

the absence of vortices are given by

$$j_\rho(\rho,\varphi,z) = -\frac{cm\Phi_0 \sin\varphi}{2\pi\lambda^3\rho}\int_0^\infty dq\exp(-ql)qJ_1(q\rho)C(q,z), \tag{2.14}$$

$$j_\varphi(\rho,\varphi,z) = \frac{cm\Phi_0 \cos\varphi}{2\pi\lambda^3}\int_0^\infty dq\exp(-ql)q^2\left(\frac{J_1(q\rho)}{q\rho} - J_0(q\rho)\right)C(q,z), \tag{2.15}$$

$$j_z(\rho,\varphi,z) = 0. \tag{2.16}$$

We obtained the following asymptotic behavior of these components:

a) $\rho >> \max(l, 1/d)$ or $l >> \max(\rho, 1/d)$

$$j_\rho(\rho,\varphi,z) = -\frac{cm\Phi_0 \sin\varphi}{2\pi\lambda^3\left(\rho^2+l^2\right)^{3/2}}\frac{\cosh(d/2+z)}{\sinh(d)}, \tag{2.17}$$

$$j_\varphi(\rho,\varphi,z) = \frac{cm\Phi_0 \cos\varphi}{2\pi\lambda^3\left(\rho^2+l^2\right)^{3/2}}\frac{2\rho^2-l^2}{\rho^2+l^2}\frac{\cosh(d/2+z)}{\sinh(d)}, \tag{2.18}$$

b) $\rho, l < \frac{1}{d},\ d << 1$

$$j_\rho(\rho,\varphi,z) = -\frac{cm\Phi_0 \sin\varphi}{4\pi\lambda^3}\frac{\sqrt{\rho^2+l^2}-l}{\rho^2\sqrt{\rho^2+l^2}}, \tag{2.19}$$

$$j_\varphi(\rho,\varphi,z) = \frac{cm\Phi_0 \cos\varphi}{4\pi\lambda^3}\left[\frac{\sqrt{\rho^2+l^2}-l}{\rho^2\sqrt{\rho^2+l^2}} - \frac{l}{\left(\rho^2+l^2\right)^{3/2}}\right]. \tag{2.20}$$

For the case of the MD under the SC, these currents change sign. The detailed expressions for the magnetic fields and the vector potential as solution of

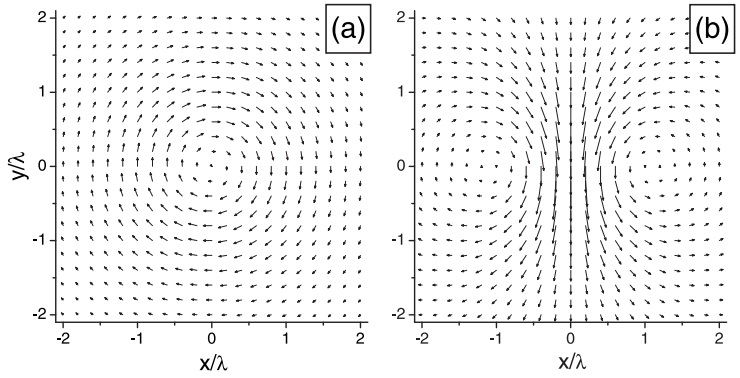


Fig. 2.5: The screening current density in the SC film with $d = 0.5\lambda$ for: a) out-of-plane and b) in-plane magnetized magnetic dipole with $m = m_0$ positioned at $a = 1.0\lambda$ above the superconducting film.

Eq. (2.5) are given in the Appendix. The vector plots of the screening currents for both directions of the MD magnetization are presented in Fig. 2.5.

Previous theoretical studies [96] on the interaction of a magnetic moment and a vortex used a Gibbs free energy argument to show that this force was attractive. In our case, the pinning force between a vortex and the MD consists of two parts: (i) the interaction between the vortex fringing field and the magnetic moment, and (ii) the interaction between the vortex and the screening currents created in response to the magnetic dipole field. One should notice (Fig. 2.5(a)) that although the magnetic field of a MD with out-of plane magnetization changes sign in the SC plane, the superconducting screening current is always in the same direction, and therefore, the interaction between the MD and a vortex with parallel orientation of the field is attractive (consequently, the vortex will sit under the MD), and analogously, for anti-parallel orientation of the magnetic fields they repel each other.

For the case of a MD with in-plane magnetization, the Meissner current vector plot in Fig. 2.5(b) shows that the direction of the current is such that the vortex is attracted to the region where the magnetic field of a MD is parallel to it and repelled on the other side of a MD due to the opposite direction of the current.

### 2.3.3 Pinning of multiple vortices and/or anti-vortices

*2.3.3.1 In-plane magnetization* Obviously, in the case of in-plane magnetization, the vortex will be repelled on the side of the MD to which the magnetic moment points to and pinned on the opposite side (and vice versa for the antivortex). The case when the dipole itself creates vortices was experimentally investigated by Van Bael *et al.* [93], where it was found that the stray field of the in-plane magnetic dipole induces a vortex-antivortex pair (VA) at the poles, at positions predicted by our analysis (vortex towards negative pole, antivortex towards positive pole). Therefore, this asymmetric pinning potential provides stability for *vortex-antivortex* configurations. One would expect that the position of the pinning sites depends on the magnetic moment of the MD and the number of flux quanta carried by each vortex. To determine the preferable position of the vortex-antivortex pair in the presence of an in-plane MD we put the vortex at $(\rho_v, \varphi_v)$ and the antivortex at $(\rho_{av}, \varphi_{av})$ with respect to the MD and calculate their interaction with the dipole. The vortex-antivortex interaction energy is given by [52]

$$F_{v-av}(R, L_v, L_{av}) = -\frac{L_v L_{av} \Phi_0^2}{8\pi^2 \lambda} \left( dK_0(R) + 2 \int_0^\infty dq \frac{J_0(qR)}{k^2 Q} \right), \qquad (2.21)$$

where $R = \sqrt{\rho_v^2 + \rho_{av}^2 - 2\rho_v \rho_{av} \cos(\varphi_v - \varphi_{av})}$ is the distance between the vortex and antivortex, $K_0(x)$ is the MacDonald function, and $L_v$, $L_{av}$ are the vorticity of the vortex and anti-vortex, respectively.

First, let us suppose that the vortex-antivortex pair appears due to the stray field of the dipole. In that case, this pair nucleates where the superconducting current is maximal, namely, under the dipole (Fig. 2.5(b)), with vortex and antivortex situated on opposite sides of the dipole. Therefore, due to the symmetry of the applied potential (Fig. 2.3(c)), we may assume that $\rho_v = \rho_{av}$, and $\varphi_v = \pi - \varphi_{av}$. To investigate the stability of such a pair of vortices, we calculate the total interaction energy in this system with respect to the position of the vortices. The results are shown as contourplots in Fig. 2.6 for different values of the magnetic moment of the dipole. The lowest value of the interaction energy gives the energetically favorable position of the vortex-antivortex pair [apart from the global minimum at $x = 0$ (zero distance between vortices), where the energy equals $-\infty$]. Obviously, the lateral motion of vortices is forbidden by the high energy barriers, while along the direction of the dipole, also an energy barrier exists, but lower than the lateral ones, showing us the preferable direction of possible vortex-antivortex annihilation.

Knowing this, we put the vortex and antivortex along the direction of the MD, in such a way that $\rho_v = \rho_{av}$, and $\varphi_v = \pi$, $\varphi_{av} = 0$, and investigate the pinning potential as function of the distance of the vortex and antivortex from the MD. We substitute $R = 2\rho_v$ in Eq. (2.21) and add this energy to the values of the MD-vortex and MD-antivortex attraction energy obtained

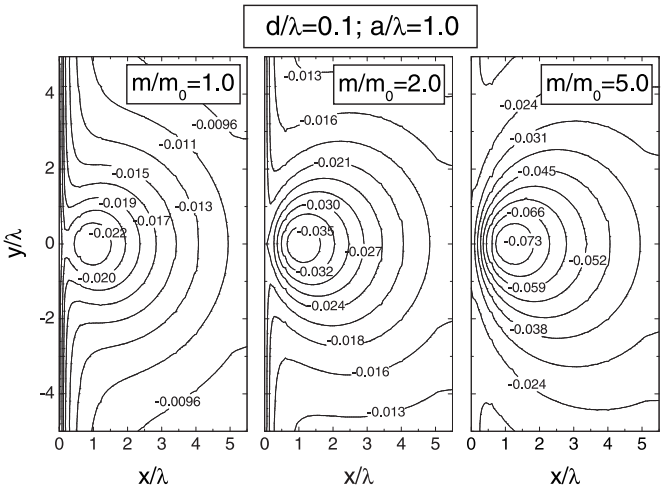


Fig. 2.6: The total interaction energy (in units of $F_0 = \Phi_0^2/(\pi\lambda)$) between the in-plane magnetic dipole (MD) and the vortex and the antivortex placed at opposite sides of the dipole for different values of the magnetic moment $m$.

from Eq. (2.12). The result is shown in Fig. 2.7 for (a) different values of the vorticity ($L_v$, $L_{av}$), and (b) different magnetization and $L_v = L_{av} = 1$. After minimization of the total energy over $\rho_v$, we obtain the position of the vortex-antivortex pair. In the thin superconductor case ($d < 1$) this leads to the non-linear equation

$$\frac{2\pi m\rho_v}{\sqrt{l^2+\rho_v^2}\left(l+\sqrt{l^2+\rho_v^2}\right)}\left[1-\rho_v^2\left(\frac{1}{l^2+\rho_v^2}+\frac{1}{\sqrt{l^2+\rho_v^2}\left(l+\sqrt{l^2+\rho_v^2}\right)}\right)\right] = \frac{L_vL_{av}}{L_v+L_{av}}. \tag{2.22}$$

Although all forces acting in the system are attractive, it is clearly visible that annihilation of vortices can be prevented by their strong confinement at the poles of the MD (the position of vortex-antivortex pairs is illustrated by the open circles in Fig. 2.7). The interaction energy shows an absolute minimum for $\rho_v = 0$, implying the annihilation, but in order to do that vortices have to cross a potential barrier. Therefore, the vortex-antivortex configuration can be stable in this system. To determine if this vortex state is metastable or the ground state one should compare its total energy to the one without vortices. In that case, the existence of the pairs as the ground state will not depend only on the magnetization of the dipole but also on the parameters of the superconductor (i.e. $\lambda, \xi$) which influence the equilibrium phase diagram via the self-energy of the vortices.

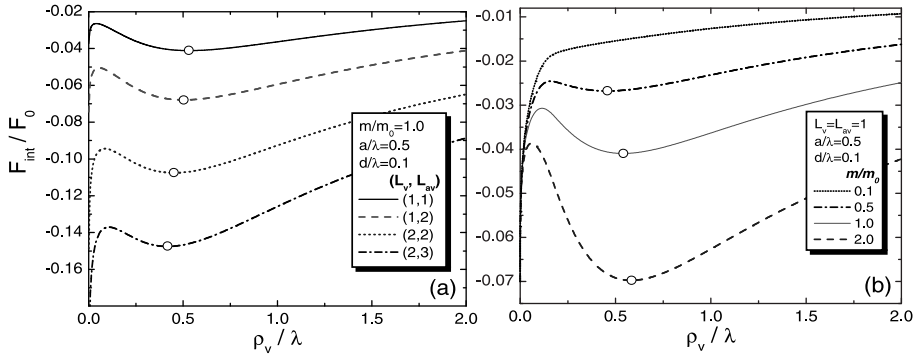


FIG. 2.7: The interaction energy of a vortex-antivortex pair and an in-plane MD, as function of the position of the vortex ($\vec{\rho}_{av} = -\vec{\rho}_v$), along the direction of the magnetization of the dipole for: a) different values of the vorticity of the vortex and the antivortex, and b) for single-quantized vortices but different value of the magnetization of the dipole. The open circles denote the local minimum of the interaction energy.

From Fig. 2.7(b) it is clear that in the case of $L_v = L_{av} = 1$ there exists a critical MD magnetization for which the annihilation barrier disappears. More generally, the critical value of the magnetic moment of the MD, in the thin SC film limit, follows from Eq. (2.22) (by the condition that the equation has no solution) and is given by

$$m^* = 1.08529 \, \frac{L_v L_{av} l}{L_v + L_{av}}. \tag{2.23}$$

From this equation the critical values of the vorticity, when attraction becomes stronger than the pinning, can also be estimated. For $L_v = L_{av}$ we have $m^* = 1.08529 L_v l/2$ and using the fact that $\Phi^+/\Phi_0 = 2m/l$ for an in-plane MD we obtain the critical condition $\Phi^+/\Phi_0 = 1.08529 L_v$, where $\Phi^+$ denotes the flux through the region of the positive stray field of the dipole at the SC surface. This implies that there is a connection between the appearance of stable vortex-antivortex pairs and the amount of penetrating flux of the magnetic dipole. Notice that the critical $\Phi^+$ is not exactly quantized in units of $\Phi_0$ which is a mesoscopic effect [97]. The quantization condition $\Phi = \oint_C \vec{A} \cdot \vec{dl} = L\Phi_0$ cannot be used because it is not possible to construct a contour $C$ around the positive stray field region where the current is zero (see Fig. 2.5(b)). The inhomogeneous magnetic field of the dipole stimulates the creation of a vortex and an antivortex at opposite poles. These vortices cannot be treated independently and it turns out that larger flux is needed in order not only to create this pair but also to keep them apart.

As shown above, for the case of the experimentally important thin SC film approximation, the position of the vortex-antivortex pair with respect to the

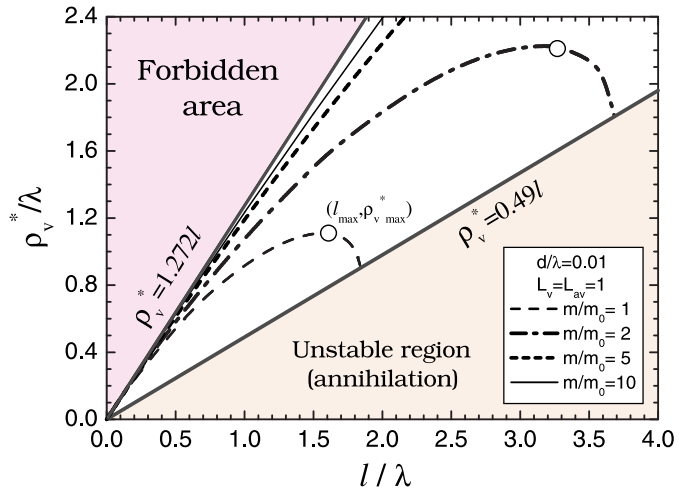


Fig. 2.8: The position of the vortex-antivortex pair ($\rho_v^*$) as function of the distance between the in-plane magnetized dipole and the SC surface ($l = a - d/2$), for different values of the magnetization of the dipole.

dipole can be obtained from Eq. (2.22). This position depends both on the vertical position of the dipole and its magnetization strength. For fixed magnetic moment of the dipole, the vortex-antivortex pair can only be stabilized for $l$ below some critical value which is obtained from Eq. (2.23). If we put $m = m^*$ in Eq. (2.22), we obtain the simple dependence $\rho_v^* = 0.4904 l^*$. The dependence of $\rho_v^*$ on $l$ is shown in Fig. 2.8, for different values of the magnetization, where also the stability region of the vortex-antivortex pair is indicated. One can see three regions in this diagram: i) the region where the vortex-antivortex pair is unstable, which is bounded by $\rho_v^* = 0.4904 l$, for any value of the magnetization of the MD, ii) the region of stability, and iii) the forbidden area, for $\rho_v^* > 1.272 l$. The latter condition follows from Section 1.3.2 (see Fig. 2.4(b)). Notice that with increasing distance between the dipole and the SC film, the pinning sites move further from the center of the dipole, up to a certain point when the interaction between vortices overwhelms the pinning force. After that, the distance between vortex and antivortex decreases and they finally annihilate. The maximum distance $\rho_v^*$ follows from Eq. (2.22) by taking the derivative with respect to $l$ and leads to $\rho_{v\ max}^* = 0.7071 l_{max}$ (open dots in Fig. 2.8), which again corresponds to the single vortex situation for $l >> d$ (see Fig. 2.4).

*2.3.3.2 Out-of-plane magnetization* Due to the strong field inhomogeneity and the reversal of the direction of the magnetic field in the vicinity of the MD with out-of plane magnetization, and the fact that the net magnetic flux due to the MD in the SC plane equals zero, one expects that vortex-antivortex

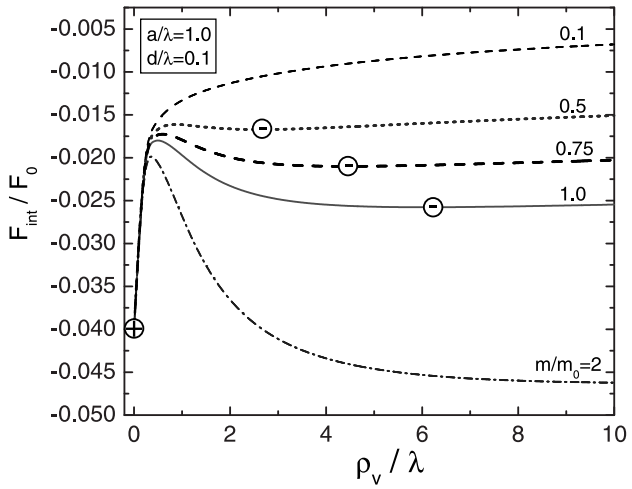


FIG. 2.9: The total interaction energy between an out-of-plane magnetic dipole (MD), the vortex (+) under it and the antivortex (-) at a distance $\rho_v$. This illustrates vortex-antivortex pair stabilization by the short range interaction with the MD.

configurations might be stable in such applied field. As shown in Fig. 2.2, an individual vortex is strongly attracted by the MD and the antivortices are repelled. Therefore we artificially put one vortex with vorticity $L_v$ under the MD and assume the existence of a ring of $n_{av}$ single antivortices around it, with radius $\rho_v$. Adding the interaction between each two vortices to our previous expression for the interaction energy, we obtain the total interaction energy

$$\begin{aligned} F_{int} &= \frac{m\Phi_0^2}{2\pi\lambda}\left(L_v U_\perp(0) - n_{av}U_\perp(\rho_v)\right) + n_{av}F_{v-av}(\rho_v, L_v, 1) - \\ &\quad - \frac{n_{av}}{2}\sum_{j=1}^{n_{av}-1} F_{v-av}(\rho_v\sqrt{2-2\cos\frac{2\pi j}{n_{av}}}, 1, 1), \end{aligned} \tag{2.24}$$

where the first two terms describe the dipole-vortex and dipole-antivortex interactions, the third term is the vortex-antivortex attraction term, and the last term is the repulsion energy between antivortices. The function $F_{v-av}$ is given by Eq. (2.21). Although the vortex is attracted by the antivortices, annihilation is prevented by the repulsion between the antivortex and the MD (for example, see Fig. 2.9, for $L_v = n_v = 1$ ). Naturally, this energy barrier becomes smaller with decreasing magnetic moment of the dipole. Nevertheless, if a barrier exists, the interaction energy shows one local minimum, meaning that antivortices would not be repelled to infinity but to a certain point. The position of this local minimum we obtained in the same manner as previously,

which within the thin film approximation, leads to the equation

$$\frac{4\pi m\rho_v^2}{\left(l^2+\rho_v^2\right)^{3/2}} = 2L_v - n_{av} + 1. \tag{2.25}$$

From this expression, the threshold value of the magnetic moment (when the potential barrier appears) is obtained as

$$m^* = \left(\frac{3}{4}\right)^{3/2} \frac{(2L_v - n_{av} + 1)\, l}{\pi}. \tag{2.26}$$

For lower values of the magnetic moment, the energetic barrier between vortices disappears and annihilation can not be prevented. Analogously, for fixed magnetic moment, increasing vorticity $L_v$ of the vortex will make the attraction stronger and for a certain value of $L_v$, antivortices will be able to overcome the barrier. This critical value of vorticity can also be estimated from Eq. (2.26). One should notice that we leave the possibility of $L_v \neq n_{av}$, which corresponds to the experimental situation when first positive external flux lines are pinned by the magnetic center, and then the polarity of the applied field is changed. Using $\Phi^+/\Phi_0 = 4\sqrt{3}\pi/9\ m/l$ for out-of-plane magnetic dipole polarization, we find for $m = m^*$ that the critical condition becomes $\Phi^+/\Phi_0 = (2L_v - n_{av} + 1)/2$, where $\Phi^+$ denotes the flux through the region of positive stray field of the dipole. One should notice that the first stable vortex-antivortex pair ($L_v = n_{av} = 1$) appears for $\Phi^+ = \Phi_0$, and further increase of vorticity is a quantized process, with $\Delta\Phi^+ = \Phi_0/2$ necessary for stability for each one-unit-increase of $L_v$ and $n_{av}$. Also in this case we cannot define a path around the positive stray field region where the superconducting current is zero (see Fig. 2.5(a)) and consequently the flux quantization condition does not apply here.

In this treatment, we assumed the presence of a giant vortex under the dipole as an energetically preferable state. It is well known that in infinite superconductors, thus in the absence of boundaries imposing the symmetry of the superconducting state, the giant vortex splits into multivortices. Since in our case an inhomogeneous applied magnetic field dictates the behavior of superconducting electrons, it is not clear which state carries less energy. Which central vortex configuration is realized depends on the parameters of the superconductor, i.e. $\xi$, $\lambda$ and $d$, which come into play through the self energy of the involved vortices. Therefore, for a particular superconducting film, we extend our approach to the case of multivortices surrounded by an multi-antivortex ring. Namely, we investigate the stability of $N$ vortex-antivortex pairs symmetrically arranged around the dipole, where vortices sit on a ring with radius $\rho_v$, and antivortices occupy the corresponding positions on the ring with radius $\rho_{av}$. We apply the same approach as before, calculating the interaction energy in a similar manner as in Eq. (2.24), where the interaction between each two vortices is included. After minimization of the interaction energy with respect

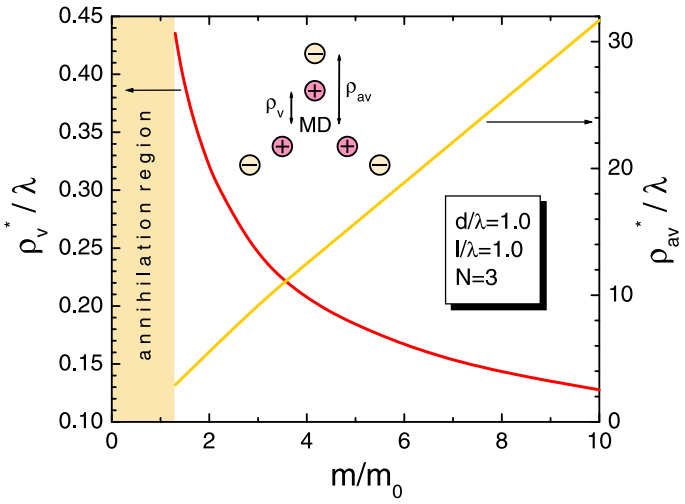


FIG. 2.10: The energetically favorable position of the vortex (+) and the antivortex (-) in the case of $N = 3$ pairs placed symmetrically around the out-of-plane magnetic dipole (MD). The inset illustrates the configuration.

to the parameters $\rho_v$ and $\rho_{av}$, we obtain numerically the energetically favorable positions of the vortices. The results are shown in Fig. 2.10, for the case of $N = 3$ (see inset). Increasing magnetization of the dipole increases the distance between vortices and antivortices in a way that vortices come closer to the dipole and antivortices are repelled further away. It should be noted that a certain critical value of the magnetization is needed to prevent annihilation. In Fig. 2.11 we give this threshold value as function of $l$ for different values of $N$. One should note that this value of magnetic moment implies again the quantization of the penetrating flux (as in the case of a giant vortex surrounded by antivortices), but with $\Delta\Phi^+ = 1.0489\Phi_0$ necessary for stability of the first pair, and slightly decreasing for additional pairs. For $N > 4$, $\Delta\Phi^+$ becomes smaller than the flux quantum. The interpretation of this behavior can be that multivortices eventually join into a giant vortex, or that a different geometry of the superconducting state appears. For example, for larger number of pairs, due to the large linear density of vortices along the ring, they could rearrange, forming more than a single ring.

Fig. 2.11 gives only the critical condition for stability of vortex-antivortex pairs. However, which configuration has the lowest energy and is thus the energetically preferable state cannot be inferred from this figure. In order to compare the energies of states with different number of pairs, i.e. $N$, we include the self-energy of individual vortices in the calculation

$$F_v = \frac{\Phi_0^2}{16\pi^2\lambda}\left[d\ \ln\frac{\lambda}{\xi} + 2\tanh\left(\frac{d}{2}\right)\ ln\left(1+\coth\left(\frac{d}{2}\right)\right)\right]. \qquad (2.27)$$

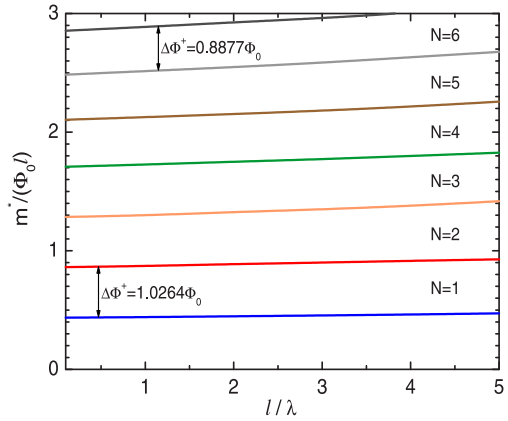


Fig. 2.11: The stability phase diagram for $N$ vortex-antivortex pairs around the out-of-plane magnetized dipole, as function of the distance between the dipole and the SC surface ($l$) and the magnetic moment $m$. Solid lines denote the critical value of the moment needed for the stability of such vortex-antivortex configurations.

The numerical results, as referred to the Meissner state, are shown in Fig. 2.12, for a thin SC film with $\lambda/\xi = 10$. With increasing magnetic moment of the dipole the energetically favorable state goes through successive states in which $N$ increases. If we calculate again the flux $\Delta\Phi^+$ which now corresponds to the appearance of the next $N$ state as the ground state, we find that $\Delta\Phi^+ = 1.97\Phi_0$, for the appearance of the first pair, and for $N \geq 2$, the additional flux slightly decreases with increasing $N$, starting from $\Delta\Phi^+ = 1.089\Phi_0$, for $N = 2$. Larger

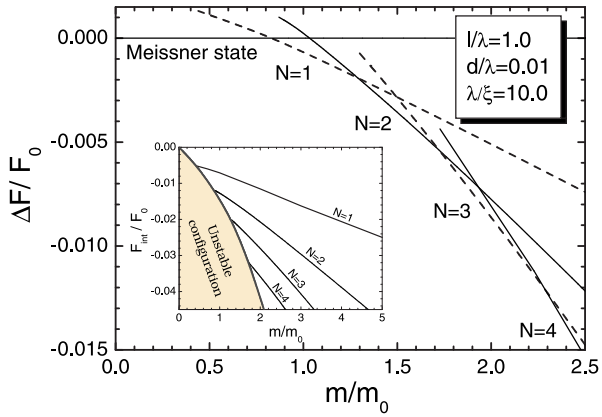


Fig. 2.12: The free energy difference between the states with $N$ vortex-antivortex pairs around the dipole and the Meissner state, for a thin SC film with $\lambda/\xi = 10$ and the out-of-plane dipole positioned at $l/\lambda = 1.0$. Inset shows the total interaction energy in the corresponding $N$-states.

flux needed for the first vortex-antivortex state can be explained by the fact that this cylindrically asymmetrical state appears in a symmetrical magnetic potential. For $N \geq 2$, the results correspond to our previous analysis. It should be stressed that these results depend on the parameters of the superconductor, namely $\lambda$ and $\xi$, which come into play through the self-energy of the vortices. This is in contrast to the interaction energy (see the inset of Fig. 2.12) which, in the London approximation, is independent of $\xi$.

## 2.4 THE INTERACTION BETWEEN A SUPERCONDUCTING VORTEX AND AN OUT-OF-PLANE MAGNETIZED FERROMAGNETIC DISK: INFLUENCE OF THE MAGNET GEOMETRY

### 2.4.1 Magnetic disk (ring) - vortex interaction

In this section, we investigate the interaction between a vortex in an infinite type II superconducting film with thickness $d$ ($-\frac{d}{2} < z < \frac{d}{2}$) and the magnetic disk with radius $R$ and thickness $D$ with *out-of-plane magnetization*, i.e. $\overrightarrow{M} = \Theta(R-\rho)\Theta(z_1-z)\Theta(z-z_0)m\overrightarrow{e_z}/(R^2\pi D)$ (in units of $M_0 = \Phi/\lambda^2$) located at distance $l$ above (under) the SC ($z_0 = l$, $z_1 = l + D$).

Inserting the well known expression for the magnetic field of a vortex outside the SC (see Eqs. (A.7, A.8) in Appendix) into Eq. (2.4) we find the expression for the magnetic disk-vortex interaction

$$U_{mv} = \frac{MR\Phi_0^2}{\lambda}\, U_\perp(\rho_v), \tag{2.28a}$$

where $\rho = \rho_v$ denotes the position of the vortex, and

$$U_\perp(\rho_v) = \int_0^\infty dq \frac{1}{qQ} J_1(qR)\, J_0(q\rho_v)\, E(q,l,D), \tag{2.28b}$$

where $Q = k(k + q\coth(kd/2))$, and $E(q,l,D) = e^{-ql}\left(e^{-qD} - 1\right)$.

For the case of a thin ferromagnetic disk above the thin superconducting film ($d, D < 1$), the following asymptotics can be obtained:

(1) for $\rho_v < R$, we found

$$U_\perp(\rho_v) \approx -\frac{dDR}{2}\left(\frac{1}{l + \sqrt{l^2+R^2}} - \frac{\rho_v^2}{4}\frac{1}{(l^2+R^2)^{3/2}}\right); \tag{2.29a}$$

(2) for $\rho_v > R$ and $\rho_v \sim l$,

$$U_\perp(\rho_v) \approx -\frac{dDR}{4}\left(\frac{1}{\sqrt{l^2+\rho_v^2}} - \frac{R^2}{8}\frac{2l^2-\rho_v^2}{(l^2+\rho_v^2)^{5/2}}\right); \tag{2.29b}$$

(3) for $\rho_v > R, l$,

$$U_\perp(\rho_v) \approx -\frac{dDR}{4}\left(\frac{1}{\sqrt{l^2+\rho_v^2}} - \frac{d\pi}{4}\left[H_0\left(\frac{\rho_v d}{2}\right) - Y_0\left(\frac{\rho_v d}{2}\right)\right]\right). \quad (2.29c)$$

Here, $H_v(x)$ and $Y_v(x)$ denote the Struve and Bessel function, respectively.

In the case of a FM on top of the SC ($l = 0$), the above asymptotics (2.29(a)-(c)) can be expressed in a more precise way:

(1) for $\rho_v < R$,

$$U_\perp(\rho_v) \approx -\frac{dD}{\pi} E\left(\frac{\rho_v^2}{R^2}\right); \quad (2.30a)$$

(2) for $\rho_v > R$,

$$\begin{aligned} U_\perp(\rho_v) \approx & -\frac{dDR}{\pi}\left\{\frac{1}{\rho_v}\left[\frac{\rho_v^2}{R^2}E\left(\frac{R^2}{\rho_v^2}\right) + \left(1-\frac{\rho_v^2}{R^2}\right)K\left(\frac{R^2}{\rho_v^2}\right)\right]\right. \\ & \left. + \frac{d\pi^2}{16}\left[H_0\left(\frac{\rho_v d}{2}\right) - Y_0\left(\frac{\rho_v d}{2}\right)\right]\right\}. \end{aligned} \quad (2.30b)$$

$K(x)$ and $E(x)$ are the complete elliptic integrals of the first and second kind, respectively. Further expansion of the asymptotic behavior of the energy at large distances (Eqs. (2.29c) and (2.30b)) gives $U_\perp(\rho_v) \approx -DR/d\rho_v^3$. One should note that although Eq.(2.30a) describes perfectly asymptotic behavior of Eq. (2.28b), its physical interpretation is questionable, since for $l = 0$ superconductivity under the magnetic disk would be strongly suppressed due to the proximity effect.

When we take the derivative of the interaction energy, Eq. (2.28), over $\rho_v$ we obtain the force acting on a vortex in the presence of a magnetic disk:

$$F_{mv} = \frac{MR\Phi_0^2}{\lambda^2} F_\perp(\rho_v), \quad (2.31a)$$

with

$$F_\perp(\rho_v) = \int_0^\infty dq \frac{1}{Q} J_1(qR) J_1(q\rho_v) E(q,l,D). \quad (2.31b)$$

For the case of a thin FM on top of a thin SC ($d, D < 1$, $l = 0$), we derived the following asymptotics

(1) for $\rho_v < R$,

$$F_\perp(\rho_v) \approx \frac{dD}{\pi\rho_v}\left[E\left(\frac{\rho_v^2}{R^2}\right) - K\left(\frac{\rho_v^2}{R^2}\right)\right]; \quad (2.32a)$$

(2) for $\rho_v > R$,

$$F_\perp(\rho_v) \approx \frac{dD}{\pi R}\left[E\left(\frac{R^2}{\rho_v^2}\right) - K\left(\frac{R^2}{\rho_v^2}\right)\right] - \frac{d^3 DR}{16}\frac{\pi}{2}\left[Y_1\left(\frac{\rho_v d}{2}\right) + H_{-1}\left(\frac{\rho_v d}{2}\right)\right]. \quad (2.32b)$$

The latter expression reduces in the extreme $\rho_v >> R$ limit to $F_\perp(\rho_v) \approx -3DR/d\rho_v^4$, which is consistent with the asymptotic behavior of the interaction energy.

The results for the full numerical calculation of Eq. (2.28) are shown in Fig. 2.13(a) for a magnetic disk with radius $R = 3.0$, and three values of the thickness $D = 0.1, 0.5, 1.0$, fixed total magnetic moment $m = 1.0$ ($M = m/V^{(fm)}$), and at distance $l = 0.1$ above the SC with thickness $d = 0.1$. The energy is expressed in units of $U_0 = \Phi_0^2/\pi\lambda$) and the force in $F_0 = \Phi_0^2/\pi\lambda^2$. The magnetic-vortex interaction increases if the magnet is made thinner, since the magnetization in that case increases due to the fact that the magnetic moment of the magnetic disk is kept constant in this calculation. Also the magnetic field of the disk becomes more peaked near the magnet edge. In Fig. 2.13(b), the dependence of the interaction energy on the thickness of the SC is shown. The increased thickness of the SC makes the interaction stronger, due to the stronger response of the SC to the presence of the magnet. Notice that increasing the thickness beyond $d >> \lambda$ does not influence the energy (dashed curve in Fig. 2.13(b), $Q \approx k(k+q)$ in Eq. (2.28)). The vortex is attracted by the magnetic disk when the magnetization and the vortex are oriented parallel, independently of the value of the parameters. The interaction energy has its minimum just under the center of the disk, which is the energetically most favorable position of the vortex. The force acting on the vortex is purely attractive and it has its maximum at the edge of the magnetic disk (see Fig. 2.13(c)). For large distances between the magnetic disk and the vortex the interaction approaches the value obtained in the previous section for the case of a magnetic dipole. Note that in the limit $R \to 0$ and $D \to 0$, Eq. (2.28) corresponds to the out-of-plane dipole case of Eq. (2.10). In Refs. [86, 98] the interaction energy between a magnetic nanostructure and a vortex in a thin superconductor ($d << 1$) was calculated. In their case, the thickness of the magnet was not taken into account (assumed to be infinitely thin), the superconducting film was taken very thin ($d << \lambda$) and the FM was placed on top of the SC (in the same $z = 0$ plane) which corresponds to $l = 0$ in our case. In these limits, our equations reduce to the same expressions for the interaction energy like those given in Refs. [86, 98]. But note that the analytical expressions are still not completely reached in the distance range shown in Fig. 2.13 and therefore a numerical calculation of the full integral is necessary in order to obtain the magnet-vortex interaction energy. Therefore, from this point of view, our expression offers much more information (non-zero thickness of both

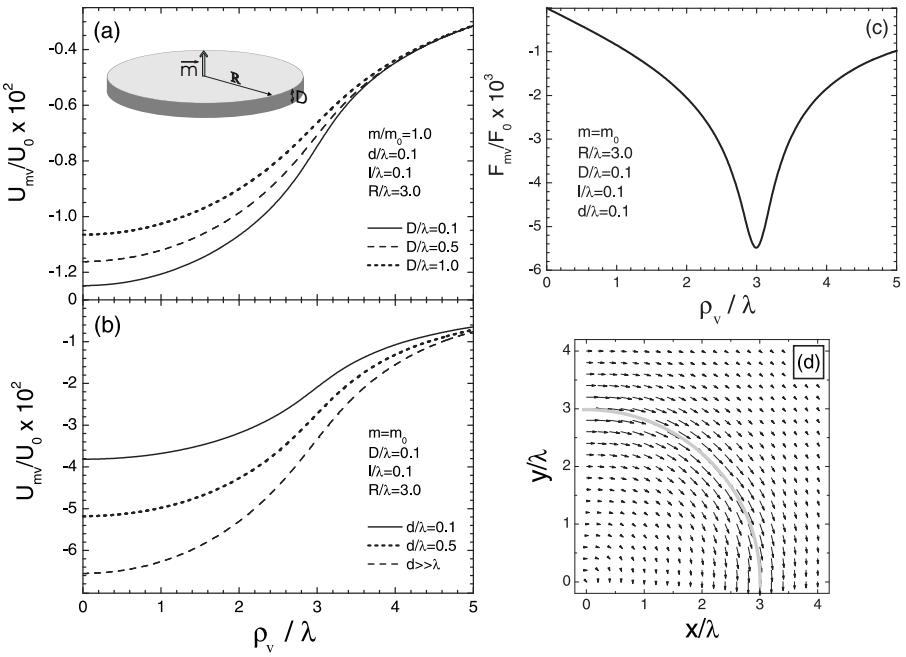


Fig. 2.13: The magnetic disk-vortex interaction energy as function of the distance between the vortex and the center of the FM disk: for several values of (a) the thickness of the FM disk, and (b) the thickness of the SC. (c) Plot of the FM-vortex force, and (d) a vectorplot of the current induced in the SC due to the presence of the FM (same parameters as in (c)). The grey semicircle in (d) indicates the position of the edge of the FM.

FM and SC, and arbitrary position of the FM above the SC) without a real increase of the complexity of the numerical calculation.

To better understand the attractive magnet-vortex behavior in this system, we calculated the supercurrent induced in the SC due to the presence of the magnet. As explained before, this current can be obtained after integration of Eq. (2.6). In the case of a flat magnetic disk, it has only an azimuthal component and reads

$$j_\varphi(\rho,z) = \frac{cMR\Phi_0}{\lambda^3}\int_0^\infty dq J_1(qR)J_1(q\rho)E\left(q,l,D\right)C\left(q,z\right), \tag{2.33}$$

where $\rho=\sqrt{x^2+y^2}$, and $C(q,z)$ is given by Eq. (2.8). For a FM placed under the SC, one should replace $z$ by $-z$. The vectorplot of the current is shown in Fig. 2.13(d). One should notice that the direction of the current is the one normally associated with an antivortex (the clockwise direction) and that the

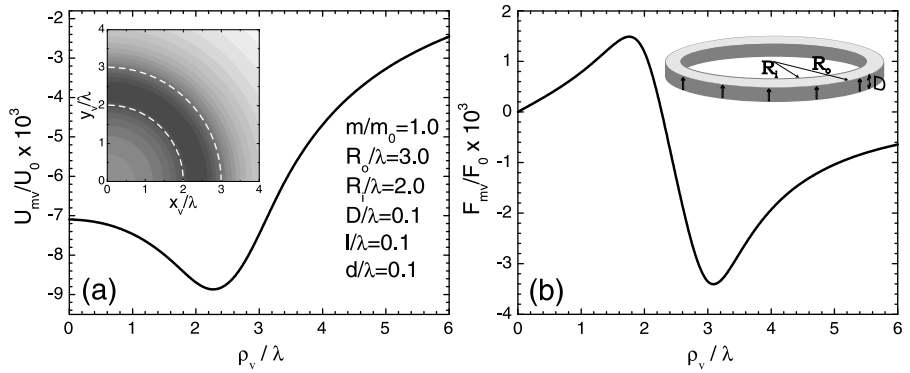


FIG. 2.14: The out-of-plane magnetized annulus-vortex interaction: (a) the interaction energy, and (b) plot of the FM-vortex force. The contourplot of the interaction energy is shown as inset in (a) (dark color illustrates low energy, as will be the case throughout the paper, the dashed white semicircles illustrate the edges of the magnet). A schematic outline of the magnetic annulus is shown in the inset of (b).

current is maximal at the magnetic disk edge. This agrees with our previous results: the direction of the current explains the attraction between the FM disk and the vortex, and the position of the maximum of the current corresponds to the maximal attractive force. The problem is cylindrically symmetric, and a vortex approaching the magnet from any direction will be attracted for parallel alignment and repelled in the anti-parallel case. This important point was not fully explained in Ref. [98].

Using the same procedure, for a magnetic annulus ($R_i < \rho < R_o$) with thickness $D$ and out-of-plane magnetization (inset in Fig. 2.14(b)) we have

$$\overrightarrow{M} = \frac{1}{V_{ann}}\Theta(\rho - R_i)\Theta(R_o - \rho)\Theta(z_1 - z)\Theta(z - z_0)m\overrightarrow{e_z}, \tag{2.34}$$

resulting in the vortex-magnet interaction energy

$$U_{mv} = \frac{M\Phi_0^2}{\lambda}\int_0^\infty dq \frac{1}{qQ} J_0\left(q\rho_v\right)\left(R_o J_1(qR_o) - R_i J_1(qR_i)\right) E(q, l, D). \tag{2.35}$$

The interaction energy and force curves for the magnetic annulus-vortex interaction are given in Fig. 2.14(a,b) and are in qualitative (but not quantitative) agreement with earlier results of Ref. [85], which were obtained in the limit of an extremely thin SC and FM, namely $d, D << \lambda$. Please notice again that in our calculation finite thicknesses of both SC and FM are fully taken into account. The most important result is that, in this case, the annulus-vortex interaction energy has a ring-like minimum, under the magnet. The exact radial position of this minimum depends on the SC parameters, the thickness of

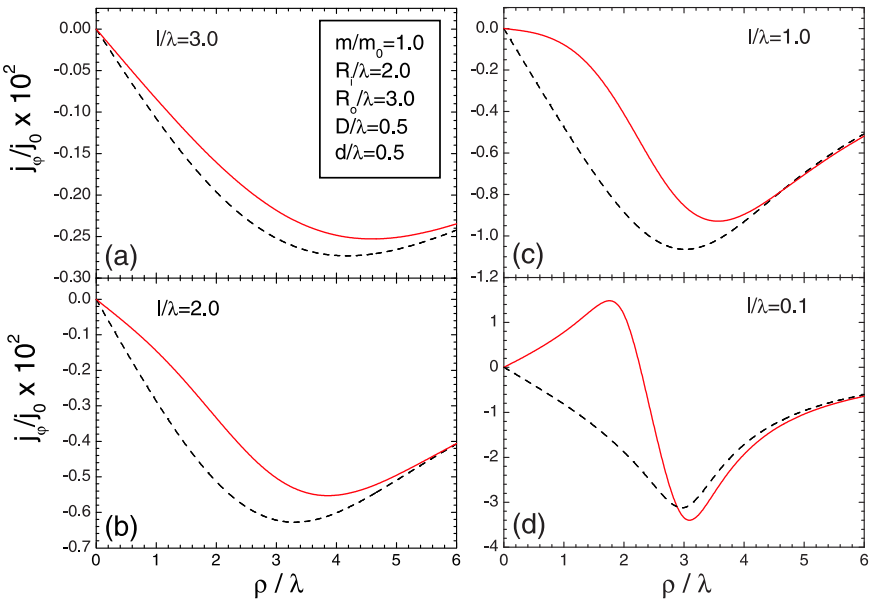


FIG. 2.15: Comparison between the current induced in a SC (in units of $j_0 = c\Phi_0/\pi\lambda^3$) by a magnetic disk (dashed curves) and a magnetic annulus (solid curves) with the same outer radius, as the FM-SC vertical distance $l$ decreases (a)-(d).

the magnet and its distance from the SC. The force acting on the vortex shows dual behavior - attractive outside the equilibrium ring and repulsive inside.

Due to the dual behavior of the FM-vortex force one naively expects different current flow in the superconductor inside and outside the annulus. We use again Eq. (2.6) and for the current induced in the superconductor we obtain

$$j_\varphi(\rho,z) = \frac{cM\Phi_0}{\lambda^3}\int_0^\infty dq\,(R_oJ_1(qR_o) - R_iJ_1(qR_i))\,J_1(q\rho)E(q,l,D)C\,(q,z) \quad (2.36)$$

In Fig. 2.15 we show a comparison between the currents induced in the SC in the case of a magnetic disk (dashed curves) and a magnetic annulus (solid curves), for different SC-FM vertical distances. When the magnet is positioned far above the superconductor, the vortex qualitatively does not feel the difference between the disk and the ring case, and the current induced in the SC shows a similar behavior (Fig. 2.15(a)). When approaching the superconductor, the influence of the central hole in the ring becomes more pronounced (Fig. 2.15(b,c)), and eventually the current changes sign (Fig. 2.15(d)).

Obviously, the qualitative behaviors of all quantities outside the annulus approach those for the case of a magnetic disk. However, inside the ring, the situation is different. The nature of the magnet-vortex force changes and

while the current flows in the clockwise direction outside the ring, inside the superconductor the direction of the current is anti-clockwise in the case of a small FM-SC distance (i.e. $l/\lambda = 0.1$, Fig. 2.15(d)). Please notice that due to the fact that the finite thickness of the SC is included in our calculations, the SC current contains also a z-dependence (i.e. through the $C(q, z)$ function).

From a look at Eqs. (2.35) and (2.36), one can see that the problem of a magnetic annulus actually can be modelled by two concentric magnetic disks with different radius and opposite magnetization. The problem is linear, and this will facilitate the calculation in the cases of non-cylindrically symmetric FMs.

### 2.4.2 Manipulation of the equilibrium vortex position with a magnetic disk containing a cavity

In previous section, we discussed the pinning of vortices by a magnetic disk or annulus (ring). We showed that the most energetically favorable position for the vortex is under the center of the magnetic disk (for parallel alignment) or under the annulus (equilibrium ring). Here we generalize the latter system and displace the hole in the disk from its central location.

Referring to the previous section, we may consider this problem as a superposition of effects of two magnetic disks with opposite magnetization. The smaller radius magnetic disk with the opposite magnetization models the hole in the larger disk. The parameters of the magnet are: the outer radius $R_o$, the radius of the hole $R_i$, the center of the hole is at $(x_h, y_h)$ and the thickness of the FM is denoted by D. Therefore, using Eqs. (2.28-2.33) for two magnetic disks, one with radius $R_o$, and the other with radius $R_i$, with opposite magnetization and centered at $(x, y) = (0, 0)$ and $(x_h, y_h)$, respectively, we investigate the pinning properties of such FM.

The results of this calculation are shown in Fig. 2.16 for a magnetic disk with $R_o = 3.0$, $R_i = 1.0$, $(x_h, y_h) = (0.5, 0)$, $l = 0.1$ and $D = d = 0.5$. In Fig. 2.16(a) we show the contourplot of the FM-vortex attractive force. It is clear that there are two local energy minima along the $y = 0$ direction, where the force equals zero: in front of and behind the hole. In Fig. 2.16(b) the plot of the interaction energy is given along this direction for three positions of the hole $x_h = 0.5, 0.8$, and 1.0. The important result is that the two minima are not equal: the one closer to the outer edge of the magnet has higher energy (metastable state) and the one near the magnet center is the actual ground state. However, due to the presence of the hole, the equilibrium position of a vortex is not exactly in the center, and depends on the position of the hole. The magnet is not cylindrically symmetric and we have two separate energy minima instead of a ring of minima as in the case of the magnetic annulus. Also, one could argue that a slowly moving vortex in a system with no temperature fluctuations could be trapped at the metastable position. Anyhow, the hole in

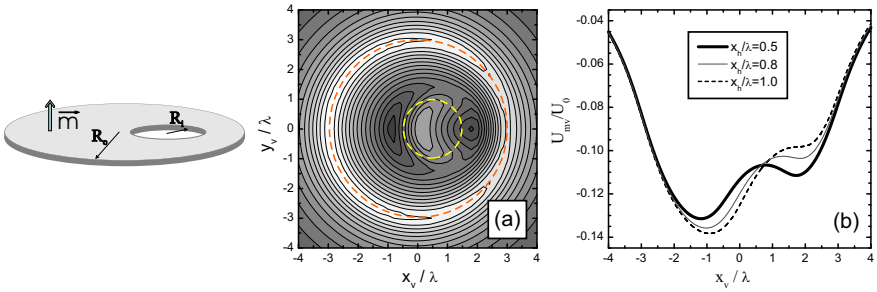


Fig. 2.16: The interaction of the vortex with a magnetic disk with an off-center hole (see left figure for schematics of the magnet configuration): (a) contourplot of the interaction energy for $R_o = 3.0$, $R_i = 1.0$, $(x_h, y_h) = (0.5, 0)$, $l = 0.1$ and $D = d = 0.5$, with $M = M_0$ (dashed circles indicate the edges of the magnet), and (b) the energy along the $x$-axis, for three different locations of the off-center hole in the magnetic disk.

a magnetic disk appears to be a powerful tool for a possible manipulation of the vortex position. However, one question arises: since there are two minima present in the interaction energy, is it possible to have two equilibrium states with the same energy?

In order to construct such a situation, we introduced a second hole in the magnet, at a symmetrical position to the first one with respect to the center of the magnet. As an example, we took the parameters of the magnet as $R_o = 3.0$, $R_i(for\ both\ holes) = 0.5$, $(x_h, y_h) = (\pm 1.0, 0)$. The interaction energy along the $x$-axis is given in Fig. 2.17. Two equal minima near the outer edge of the disk are found next to the magnet holes. However, the global minimum is still under the center of the magnet (see inset of Fig. 2.17). To eliminate this minimum we allow the holes to touch each other and to form an "eight-hole"

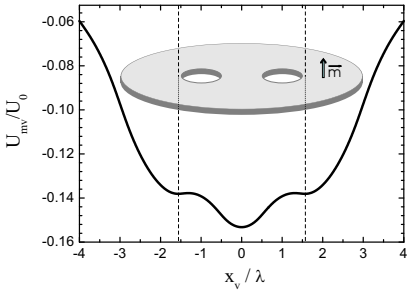


Fig. 2.17: The magnetic disk with two symmetrical holes: plot of the FM-vortex interaction energy illustrating the position of the metastable and ground vortex states with respect to the position of the holes (dashed vertical lines). The parameters of the system are $R_o = 3.0$, $R_i$(for both holes)$= 0.5$, $(x_h, y_h) = (\pm 1.0, 0)$, $l = 0.1$, $D = d = 0.5$ and $M = M_0$.

in the center of the magnet. The resulting interaction energy (Fig. 2.18(a)) has now only two equal minima along the $y = 0$ direction, outside the hole, near the magnet edge, and a plateau-like behavior in the central region. Still, these minima are not the lowest energy states. The central global minimum of the interaction energy from the previous case is now split by the joined holes into two minima along the $x = 0$ direction (see Fig. 2.18(b)). The latter minima represent the ground state for a vortex in the presence of a magnetic disk with an "eight-hole". The vortex has two absolutely equal ground states and the same probability of eventually sitting in one of those. Thanks to this feature, a possible use of this system for quantum computing can be analyzed, similarly to the quantum systems proposed before (see, for example, Ref. [99]).

In Fig. 2.18(c) the contourplot of the magnet-vortex interaction energy is given, together with a vectorplot of the current induced in the SC. The position of the eight-hole is denoted by the thick solid circles. Around the magnetic disk, the SC current flows in a clockwise direction, illustrating the general attraction between the FM and the vortex. However, under the magnet, current shows a dual behavior, and a vortex-antivortex-like current flow can be seen. Namely, at the equilibrium vortex-states we find "antivortex" current profiles while under the holes of the magnet a vortex-like current motion is present. This suggests the possibility that such a magnetic field configuration, for sufficiently

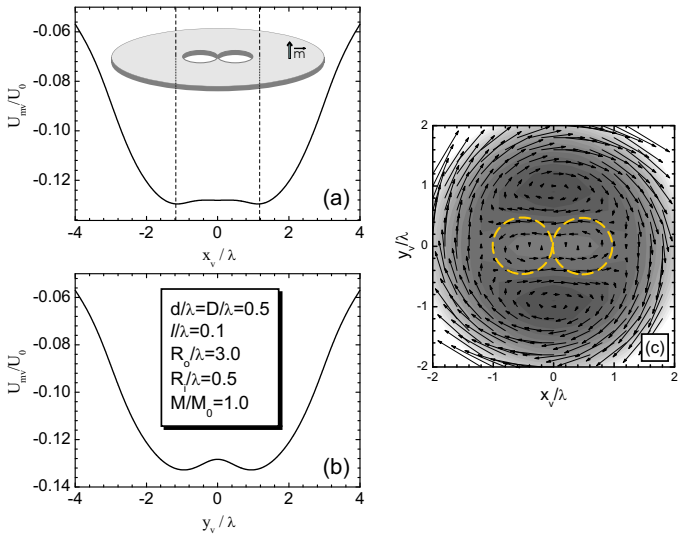


FIG. 2.18: The interaction energy of a vortex with a magnetic disk containing an "eight-hole": (a) interaction energy for the vortex positioned along the $x$-axis at the $y = 0$ line, (b) along the $y$-axis for $x = 0$, and (c) contourplot of the FM-vortex interaction energy (dark color-low energy). In (c) the vectorplot of the current induced in the SC in the presence of the FM is superimposed. Dashed circles denote the position of the holes in the FM above the SC.

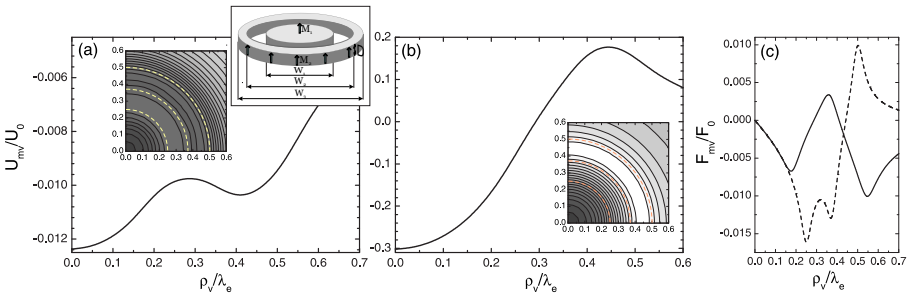


Fig. 2.19: Disk-ring magnetic structure (see inset of (a) for a schematic view of the configuration) above the SC: (a) FM-vortex interaction energy for $M_1 = M_2$, (b) for $M_2 = -M_1$. The contourplots of the energy are given as insets (dashed lines indicate the edges of the magnet). The force acting on the vortex is shown in (c), as the solid curve for case (a) and dashed one for case (b). The parameters are $W_1 = 0.5$, $W_2 = 0.75$, $W_3 = 1.0$, $D = 1.0$, and $l = 0.1$, all in units of the effective penetration depth $\lambda_e = \lambda^2/d$.

strong magnetization, could induce interesting vortex-antivortex configurations if placed near a superconducting film.

Using this approach, interaction of a vortex with magnets of more complicated shapes can be investigated. We have shown that the magnetic disk with a cavity is a nice example of how to control the vortex by the magnet-geometry. From the point of view of practical vortex manipulation, it would be interesting to move the vortex by changing the parameters of the system. Helseth [98] proposed a system in which a magnetic disk (with magnetization $M_1$) is placed in the center of a magnetic ring (with magnetization $M_2$), where the disk and the ring can have opposite magnetization. In Fig. 2.19 we show the outline of the system (upper inset), and the calculated interaction energy and force acting on the vortex, for the parameters $W_1 = 0.5\lambda_e$, $W_2 = 0.75\lambda_e$ and $W_3 = 1.0\lambda_e$ and $D = 0.1\lambda$ on top of a SC with thickness $d = 0.1\lambda$. Here $\lambda_e = \lambda^2/d$ denotes the effective penetration depth. We suppose a thin oxide layer between the SC and the FM with thickness $0.01\lambda$. First we consider the $M_1 = M_2$ case. Helseth claimed that in this case, a slowly moving vortex will be attracted and sit under the annulus. The plot of the interaction energy in Fig. 2.19(a) shows two energy minima, namely, under the disk, and under the annulus (ring-energy minimum, see inset of Fig. 2.19(a)).

From our calculations it is clear that the ground state for the vortex would be in the center of the magnetic vortex, while a metastable state exists under the annulus as claimed in Ref. [98]. However, one could argue that a vortex, slowly moving towards the magnet, could rest in a metastable state under the ring, if there are no fluctuations in the system. In Fig. 2.19(c), the solid line shows the force acting on the vortex. Please note that in our calculation, the positions of the extrema correspond to the magnet edges, while in Ref. [98] this

was not the case. Also, the peaks in the forces in our calculation are much smaller, due to the finite thickness of the magnet. It should be noted that the relation between the two energy minima and the acting forces strongly depends on the parameters and it can change in favor of the annulus if it is made wider.

In Ref. [98] it is also stated that in the opposite case, when the annulus magnetization changes sign, i.e. $M_2 = -M_1$, the vortex is attracted to the center of the disk. The interaction energy we calculated in this case is plotted in Fig. 2.19(b) (the force is given in Fig. 2.19(c) by the dashed line). It is clear that the annulus forms an energetic barrier which prevents a "slowly moving" vortex from reaching the central position. However, the global minimum of the energy is under the center of this magnetic structure (the energy shown in Fig. 2.19(b) decreases monotonously and reaches zero at infinity), implying that the vortex would definitely sit under the magnet for the considered parameters. Different values for $R_1,\ R_2,\ R_3$ could make the central minimum higher, and the energy barrier would then be able to repel the vortex. To conclude, in order to use this magnetic structure for vortex manipulation, one should not only overcome the experimental difficulties to realize such a structure, but also be careful about the influence of the parameters on the behavior of this system.

### 2.4.3 Square and triangular magnetic disks: influence of the corners on the vortex pinning

Up to this point, we have only considered the interaction of a vortex with magnets having circular symmetry, namely magnetic disks, rings, and combinations of those. Here we consider FMs with broken circular symmetry, namely square or triangular magnetic disks. We put the center of our Cartesian coordinates in the center of the magnet and the $x$ axis along one of its sides. In this case, Eq. (2.4) can not be solved analytically, and triple numerical integrations must be performed. In the case of a rectangular FM we have

$$U_{mv}(x_v, y_v) = \frac{M\Phi_0^2}{2\pi\lambda} \int_0^\infty \frac{dq}{Q}\ E(q,l,D) \int_{-A/2}^{A/2} dx \int_{-B/2}^{B/2} dy\ J_0\left(qR_v\right), \qquad (2.37)$$

where $R_v = \sqrt{(x-x_v)^2 + (y-y_v)^2}$. $A$ and $B$ are the dimensions of the magnet (with thickness $D$) in the $x$ and $y$ direction, respectively. As before, the distance between the FM and the SC surface is $l$.

The components of the current induced in the SC are obtained in an analogous way, by numerical integration of Eq. (2.6), using the expressions:

$$j_x^{md}(\vec{r}) = \frac{cm\Phi_0}{2\pi\lambda^3} \frac{y_m - y}{R_m} \int_0^\infty dq \exp\left[-q\left(|z_m| - \frac{d}{2}\right)\right] q^2 J_1(qR_m) C\left(q,z\right) \quad (2.38a)$$

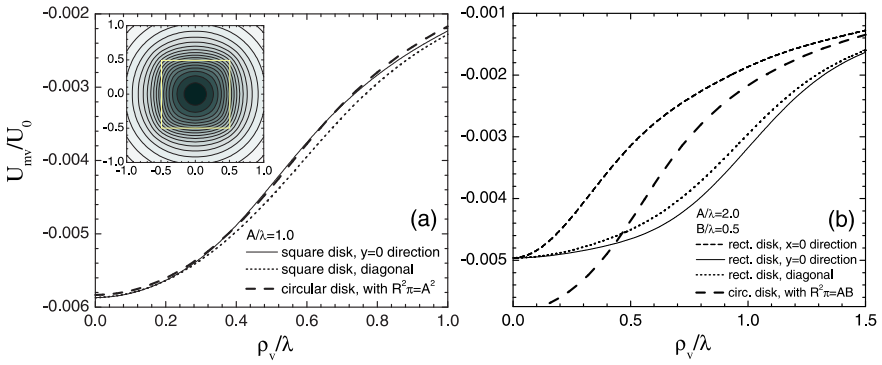


Fig. 2.20: Rectangular magnetic disk above a SC film: (a) FM-vortex interaction energy for a square magnet case, namely with sides $A = B = 1.0\lambda$, thickness $D = 0.1\lambda$ and magnetization $M = M_0$, at $l = 0.1$ above the SC with thickness $d = 0.1\lambda$ (the inset shows the contourplot of the energy, white line indicates the edge of the magnet), and (b) for $A = 4B = 2.0$. For comparison, the FM-vortex interaction energy in the case of the magnetic disk with the same volume is given by the thick dashed curves.

$$j_y^{md}(\vec{r}) = \frac{cm\Phi_0}{2\pi\lambda^3}\frac{x-x_m}{R_m}\int_0^\infty dq \exp\left[-q\left(|z_m| - \frac{d}{2}\right)\right] q^2 J_1(qR_m) C(q,z) \quad (2.38b)$$

where $C(q,z)$ is given by Eq. (2.8), and $R_m = \sqrt{(x-x_m)^2 + (y-y_m)^2}$ is the distance between the dipole and the point of interest. $\vec{r}_m = (x_m, y_m, z_m)$ denotes the position of the dipole.

In Fig. 2.20(a) the interaction energy with a vortex is shown, along two directions (lines of symmetry): (i) diagonal (dotted line); (ii) horizontal (solid line). In the inset, the contourplot of the energy is given. For comparison, we also give the results for a magnetic disk (thick dashed curve) with $R^2\pi = AB$ and the same thickness $D$. As far as the pinning potential of a square magnetic disk is concerned, the asymmetry is rather small and the result is not much different from the one of an equivalent circular disk. Only in the region near the edge of the magnet, some discrepancy between the pinning potential of the square magnet in the diagonal direction and the disk approximation is observed. Moving further from the magnet, this discrepancy disappears. The energetically favorable position of the vortex is under the center of the magnet. The situation is somewhat different for rectangular-shaped FM disks. In Fig. 2.20(b) we show the results for $A = 4B = 2.0$ and, in this case, the corresponding circular disk becomes a very poor approximation. Far away from the magnet, this approximation becomes better, as expected.

From the behavior of the interaction energy we have seen that the vortex is attracted to the center of the square or triangular magnet for parallel orientation of the magnetization and the vortex magnetic field. This corresponds

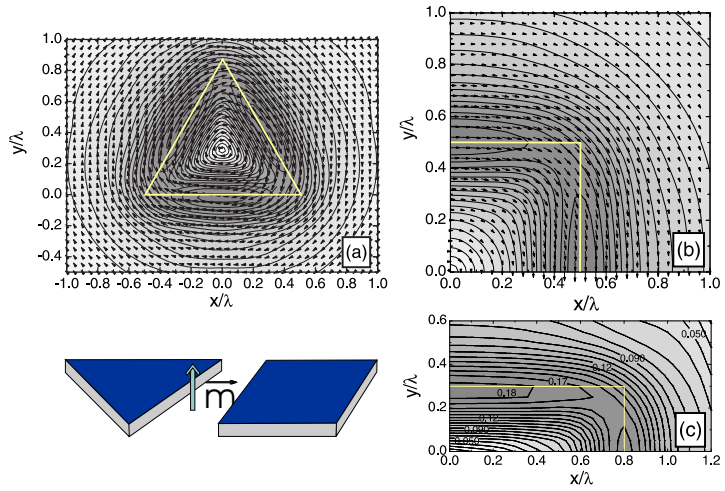


FIG. 2.21: The contourplots of the FM-vortex attractive force for parallel orientation of the magnetization and the vortex magnetic field, for: (a) an equilateral triangular magnetic disk, with sides $a = 1.0\lambda$, (b) square magnet, with sides $A = B = 1.0\lambda$. The other parameters correspond to the ones in Fig. 2.20. The vectorplots of the current are superimposed. In (c), the contourplot of the force for the rectangular magnet case is given, $A = 1.6\lambda$, $B = 0.6\lambda$. Dark color represents high force intensity. Positions of the edges of the magnets are given by white solid lines.

qualitatively to the case of a magnetic disk. However, the broken circular symmetry of the magnet introduces some changes in the magnet-vortex interaction. In Fig. 2.21 we show the contourplot of the force acting on the vortex and the vectorplot of the current induced in the SC, both for the case of a square and triangular magnetic disks. It is obvious that the attractive force is stronger at the sides than at the corners of the magnet. Therefore, the vortex approaching the magnet at the side of the magnet will be attracted stronger than on the diagonal direction. As far as the current is concerned, it has the direction associated with an antivortex. Near the magnet, the current follows the shape of the magnet and is maximal along the sides of the magnet. Further from the square or triangular magnet, the behavior of the current is more similar to the case of the circular magnetic disk. In Fig. 2.21(c) the rectangular magnet case is shown. One important feature should be noticed: the FM-vortex attraction force is stronger at the longer side of the rectangle.

As one can see in Fig. 2.21, the maxima of the FM-vortex interaction force are located on the sides of the magnet. Therefore, one may expect that the energetically preferable direction of vortex motion when attracted by the FM is perpendicular to its sides. To investigate this, we put the vortex in different positions (open dots in Fig. 2.22(a)) and follow its trajectory using molecular dynamics simulations. In our quasi-statical case, if the vortex moves, the

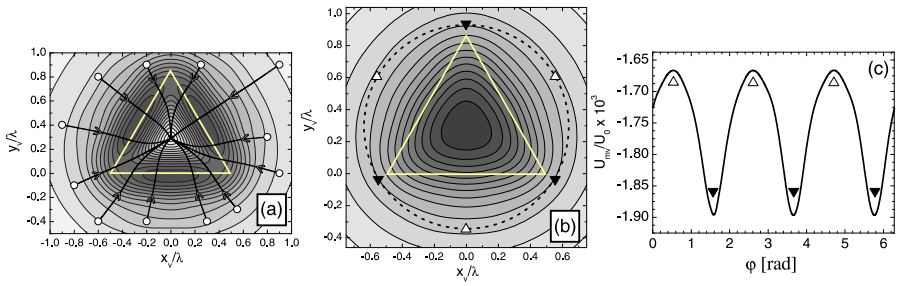


Fig. 2.22: The trajectory of the vortex when attracted by the triangular magnetic disk (same parameters as in Fig. 2.21(a)): (a) vortex paths with respect to the attractive force landscape (the edge of the magnet is illustrated by white line), (b) the contourplot of the triangular magnet-vortex interaction energy (dark color - low energy), and (c) the interaction energy along the ring indicated by dashed line in (b).

FM-vortex interaction force is opposed by viscous forces of the form $-\eta \cdot v_v$, where $\eta$ is the viscosity coefficient and $v_v$ the velocity of the vortex. Therefore, one can analyze the vortex motion on its path towards the equilibrium where previously mentioned forces are equal. Since we were not interested in real-time simulations, we assumed $\eta = 1$. The results are shown in Fig. 2.22(a). If the initial position of the vortex is along the lines of symmetry of the magnet, the vortex moves straight towards the center of the magnet. Otherwise, the trajectory of the vortex is distorted towards the corner of the magnet. It actually appears that the vortex **avoids** the maxima of the attractive force. This is counterintuitive but can be explained by the profile of the FM-vortex interaction energy, given in Fig. 2.22(b,c). One should notice the "wave" shape of the energy (if going along the ring around the magnet, see Fig. 2.22(b)). Following a circle around the magnet, the energy has its minima at the corners of the magnet (denoted by black triangles in Fig. 2.22(b,c)) and the saddle points are on the sides (white triangles). The periodicity in Fig. 2.22(c) corresponds to the number of corners of the ferromagnetic disk. From Fig. 2.22 it is obvious that the interaction energy for any position of the vortex lowers steep towards the center of the magnet, but also towards the corners. This induces the distortion of the vortex trajectory and gives the impression that the vortex approaching the magnet from the corners is more energetically favorable.

## 2.5 PINNING PROPERTIES OF IN-PLANE MAGNETIZED FERROMAGNETS OF DIFFERENT SHAPES

### 2.5.1 Magnetic stripe - vortex interaction

In this section, we investigate the interaction between a vortex in an infinite type II superconducting film with thickness $d$ ($-\frac{d}{2} < z < \frac{d}{2}$) and a thin magnetic stripe with height $D$ with *in-plane magnetization*, i.e. $\overrightarrow{M} = \delta(x)\Theta(z_1 - z)\Theta(z - z_0)M\overrightarrow{e_x}$ located at distance $l$ above the SC ($z_0 = l + d/2$, $z_1 = z_0 + D$). $M$ denotes the magnetic moment per unit of surface. The magnetic stripe actually represents a finite single plane of in-plane dipoles arranged perpendicular to the SC (see Fig. 2.23).

Inserting the well known expression for the magnetic field of a vortex outside the SC [52] (see paragraph 1.1.4.2 and Appendix) into Eq. (2.4) we find the expression for the magnetic stripe-vortex interaction

$$F_{mv} = \frac{ML_v\Phi_0^2}{\pi\lambda}\, U_{mv}(x_v), \tag{2.39a}$$

where $x = x_v$ denotes the position of the vortex with vorticity $L_v$ with respect to the infinitely thin magnetic stripe, and

$$U_{mv}(x_v) = \int_0^\infty \frac{dq}{qQ} \sin(qx_v)\exp(-ql)(1 - \exp(-qD)), \tag{2.39b}$$

with $Q = k(k + q\coth(kd/2))$. In the case of a thin superconductor ($d < \lambda$), Eq. (2.39b) can be rewritten as

$$U_{mv}(x_v) = f_-(l) - f_+(l) - f_-(l + D) + f_+(l + D), \tag{2.40a}$$

where

$$f_\pm(x) = \frac{i}{2}\left(\ln(x \pm ix_v) + \Gamma(0, (x \pm ix_v)d/2)\exp((x \pm ix_v)d/2)\right). \tag{2.40b}$$

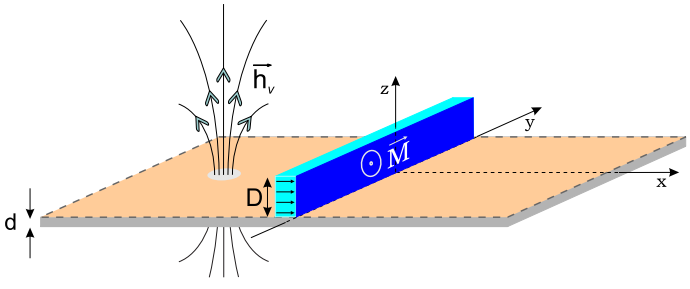


FIG. 2.23: Schematic view of the system: The superconducting film underneath an in-plane magnetized stripe interacting with an external flux line.

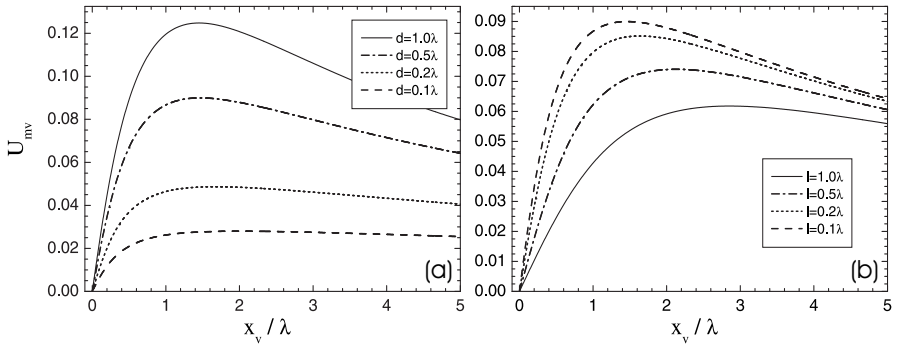


Fig. 2.24: The magnetic stripe-vortex interaction: (a) for different values of the thickness of the superconductor ($l = 0.1\lambda$, $D = 0.5\lambda$); (b) for different values of the distance $l$ between the stripe and the superconductor ($d = 0.5\lambda$, $D = 0.5\lambda$).

$i$ is the imaginary unit, and $\Gamma(a, x)$ denotes the incomplete Gamma function. Although complex, the latter expression is easier to handle in numerical calculations (one can easily show that Eq. (2.40a) is a real quantity).

For an extremely thin SC ($d << \lambda$), we obtained

$$f_-(x) - f_+(x) = -\frac{d}{2}\left(x \arctan\frac{x_v}{x} + \frac{x_v}{2}\ln(x^2 + x_v^2)\right). \tag{2.41}$$

As we have shown in Sec. 1.3.2, an in-plane magnetized dipole pins the vortex at its negative pole, where the magnetic field of the vortex is parallel to the one of the dipole. Due to the dual behavior of the interaction, an antivortex present in the system would be pinned on the opposite pole. In our case of an in-plane magnetized stripe, a similar qualitative behavior is found. However, in this case, due to the fact that the stripe stretches entirely over the SC, the interaction energy depends only on the distance from the stripe, and eventually the equilibrium position of the vortex becomes an "equilibrium channel" parallel to the stripe at distance $x_v^*$. The amplitude of the interaction energy as well as the position of its extrema strongly depends on the parameters. In Fig. 2.24(a) we show the influence of the thickness of the SC film on the vortex-FM interaction (the results for $x_v > 0$ are given, for $x_v < 0$ the function is antisymmetric). The vortex is repelled by the positive pole of the magnet ($x_v > 0$) and attracted on the opposite side. One should notice that for thicker films (and fixed $l$), the stripe-vortex interaction is stronger, and the "equilibrium channel" moves closer to the stripe due to the enhanced pinning.

A different interaction behavior is observed if the magnetic stripe is displaced further above the superconductor (i.e. increasing $l$). As one can see in Fig. 2.24(b), as the magnet is positioned higher above the SC, the interaction weakens, and the equilibrium moves further away from the stripe. The physical

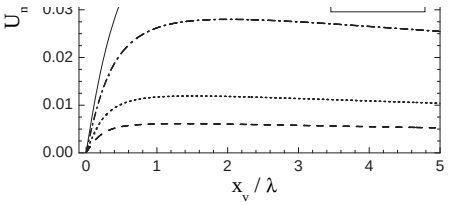


FIG. 2.25: The magnetic stripe ("wall")-vortex interaction: dependence of the interaction energy on the height of the magnetic stripe $D$ ($d = 0.1\lambda$, $l = 0.1\lambda$).

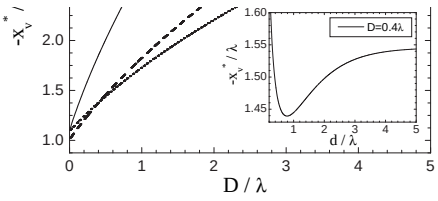


FIG. 2.26: The equilibrium position of the vortex when interacting with a magnetic "wall" as function of the height of the "wall", for different values of the thickness of the superconductor ($l = 0.1\lambda$). The inset shows the equilibrium vortex position as function of the thickness of the SC.

mechanism in this case is different, and the energetically favorable position of the vortex is now determined by the maximum of the FM magnetic field in the SC plane. If the magnet is placed higher above the SC, the position of that maximum moves further from the stripe, and therefore, the equilibrium position for the vortex shifts as well. One more parameter that influences the interaction is the height of the stripe ("wall"). Since in our calculation the magnetization is fixed ($M = M_0$, the energy rescales with $M$) as is usually the case in the experiment, changing $D$ in our calculation increases the total magnetic moment of our magnetic structure. From this point of view it is clear that the magnet-vortex interaction energy increases if the stripe is made higher (see Fig. 2.25). Similarly to the case in Fig. 2.24(b), the preferable position of the vortex is located further away from the "wall" due to the shift of the maximum applied field along the $x$-direction. However, from different curves in Fig. 2.25 one should notice that the position of the "equilibrium channel" $x_v^*$ depends almost linearly on the height of the "wall" $D$.

The results of the numerical calculation of the equilibrium position of the vortex with respect to the magnetic "wall" are given in Fig. 2.26. Independently of the thickness of the SC film, $x_v^*(D)$ becomes linear in the limit of large $D$ (i.e. for higher magnetic "walls"). Another interesting fact following from Fig. 2.26 is that for smaller heights of the "wall", a crossing of the curves, obtained for different SC thickness, can be seen. This actually means that for smaller $D$ the pinning site goes further away from the magnet as the thickness of the superconductor is increased, which is opposite to our analysis of Fig. 2.24(a). The reason is that with decreased $D$ the total magnetic moment (and field) decreases as well and the superconductor is able to "push" the magnetic field

further from the source. As one notices in Fig. 2.24(a), and which is made more clear in the inset of Fig. 2.26, if the thickness of the SC increases, the vortex is attracted closer to the "wall" as long as the SC thickness is smaller than $\lambda$. When the thickness of the SC film exceeds the penetration depth, it becomes harder for the magnetic field to penetrate the superconductor which shifts the pinning site further away from the magnetic wall. However, after a certain SC film thickness $d$, for fixed $D$, a saturation is reached and the equilibrium vortex position remains the same, independently of the thickness of the superconducting film.

To conclude, a magnetic stripe placed on top of a superconducting film clearly separates the superconductor into two regions: (i) $x_v > 0$ (for the orientation of the magnetization from Fig. 2.23) where external antivortices are attracted and (ii) $x_v < 0$, where additional vortex flux lines are pinned. Therefore, for the case of a superconductor in an external magnetic field, the use of a magnetic stripe ("wall") is a powerful tool to preserve a vortex-free superconducting area ((i) or (ii), depending on the polarity of the applied field) in the neighborhood of the FM. Although our calculations were done for the case of an infinite SC, the same conclusions can apply to finite size superconductors. Moreover, depending on the parameters (as we have shown in Figs. 2.24-2.26), the position of the pinning site can actually be quite far from the stripe, and the (anti)vortices can actually be expelled completely from the superconductor. Knowing that moving free vortex lines are responsible for the energy dissipation and lowering of the critical parameters in superconducting systems, our results could play a significant role in applied superconductivity.

So far, our calculations were done independently of the temperature, since all quantities in our analysis were scaled by units in which all the temperature dependent parameters were incorporated. Therefore, we include here the

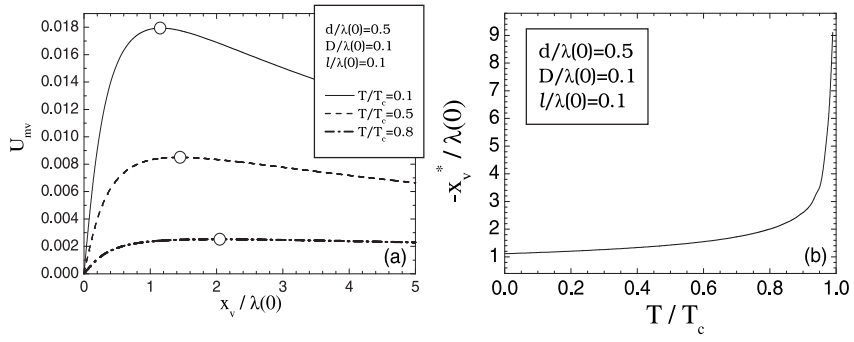


Fig. 2.27: (a) The magnetic stripe-vortex interaction energy (open dots denote the extrema in the energy) and (b) the equilibrium position of the vortex, as function of the temperature of the system.

temperature indirectly, through $\lambda$, whose temperature dependence is given by

$$\lambda(T) = \frac{\lambda(0)}{\sqrt{|1 - T/T_{c0}|}} \ , \tag{2.42}$$

where $\lambda(0)$ denotes the penetration depth at zero temperature and $T_{c0}$ is the critical temperature at zero magnetic field.

We repeat the calculations of the magnetic stripe-vortex interaction energy (Eq. (2.39b)), with a difference that now all the distances are measured in units of $\lambda(0)$ instead of $\lambda$ and magnetization is expressed in units of $M_0 = \Phi_0/\lambda(0)^2$. Eq. (2.39b) now becomes

$$F_{mv} = \frac{ML_v\Phi_0^2}{\pi\lambda(0)}\, U_{mv}(x_v), \tag{2.43a}$$

$$U_{mv}(x_v) = \int_0^\infty \frac{dqT_f}{qk(k + q\coth(kdT_f/2))} \sin(qx_vT_f) \times \exp(-qlT_f)(1 - \exp(-qDT_f)), \tag{2.43b}$$

where $T_f = \sqrt{|1 - T/T_{c0}|}$. The results of this calculation are given in Fig. 2.27, for three different temperatures, $T/T_c = 0.1,\ 0.5$, and 0.8. Obviously, as we approach the critical temperature, the interaction between the vortex and the magnetic stripe becomes weaker (see Fig. 2.27(a)). Analogously, the pinning weakens, and the equilibrium position of the vortex in this case moves further from the magnet (open dots in Fig. 2.27(a)). In Fig. 2.27(b) we show the dependence of the energetically favorable position of the vortex as function of the temperature. One should notice the abrupt increase of the magnet-vortex equilibrium distance when we approach the critical temperature. Therefore, at temperatures close to the superconducting/normal state transition the magnetic stripe can effectively protect the neighboring superconductor from vortices since they are pinned far from the stripe.

### 2.5.2 Field polarity dependent vortex pinning by an in-plane magnetized bar

In this section, we analyze the pinning properties of a magnetic bar, magnetized along its longer side (see Fig. 2.28 for definition of the variables). Using Eq. (2.4) and the well known expressions for the magnetic field of the vortex,

we obtain the pinning potential as

$$F_{mv} = \frac{ML_v\Phi_0^2}{2\pi\lambda}\, U_{mv}, \tag{2.44a}$$

$$U_{mv} = \int_0^\infty \frac{dq}{qQ} \int_{-w_y/2}^{w_y/2} dy (J_0(qR^+) - J_0(qR^-) \times \exp(-ql)(\exp(-qD) - 1), \tag{2.44b}$$

where $M$ denotes the magnetization of the bar, $D$ its thickness, and $R^\pm = \sqrt{(y-y_v)^2 + (w_x/2 \pm x_v)^2}$. $(x_v, y_v)$ gives the position of the vortex with vorticity $L_v$ where the coordinate center is located under the center of the magnet.

As one can see in Fig. 2.29, where the contourplot of the interaction energy is shown, the vortex is attracted to the *negative* pole of the magnetic bar where the magnetic field is parallel to the field of the vortex (and repelled in the opposite case), which is similar to the case of the out-of-plane magnetized dipole (magnetic moment parallel to the external flux lines attracts the vortex, and vice versa). This conclusion also follows from the observation of the interaction between the induced currents and the vortex. The vector plot of the Meissner current, calculated using Eq. (2.6) shows (see Fig. 2.29(b)) that the current has an antivortex-like direction at the position where the magnetic field of a magnetic bar is parallel to the vortex magnetic field (negative pole) and a vortex-like direction on the positive pole. Note that these are the Meissner currents which *oppose* to the field of the magnetic bar and do not correspond to the vortex/antivortex pair.

Obviously, in the case of in-plane magnetization, the vortex will be repelled at the pole of the magnetic bar to which the magnetic moment points to and

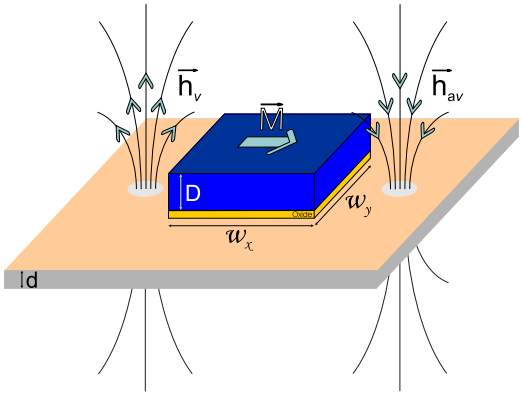


Fig. 2.28: The superconducting film with in-plane magnetized bar on top of it (separated by an oxide layer) interacting with a(n) (anti)vortex: an oblique view of the system.

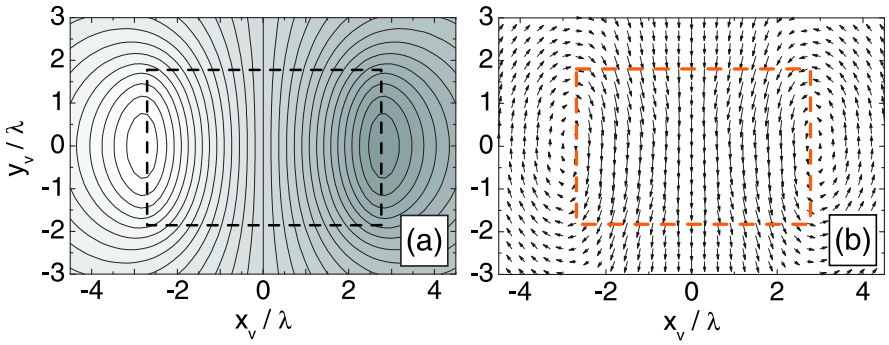


FIG. 2.29: (a) The contourplot of the magnetic bar-vortex interaction energy (white (dark) color - low (high) energy), and (b) the vectorplot of the Meissner current induced in the SC due to the presence of the magnetic bar. The dashed line indicates the edges of the magnet. The parameters used are $w_x = 5.4\lambda$, $w_y = 3.6\lambda$, $d = 0.5\lambda$, $D = 0.35\lambda$ and thickness of the oxide $l = 0.2\lambda$.

pinned on the opposite side (and vice versa for the antivortex). Thus, there is a field polarity dependent vortex pinning. However, the pinning position of the (anti)vortex depends not only on the direction of the external flux lines, but on the value of the magnetization of the bar as well. Namely, if the magnetization of the bar is strong enough to create a vortex-antivortex pair itself, the pinning properties of the system change. Such a case was recently experimentally investigated by Van Bael *et al.* [93], where it was found that the stray field of the in-plane magnetic dipole induces a vortex-antivortex pair (VA) at the poles, at positions predicted by our analysis (vortex towards negative pole, antivortex towards positive pole). Therefore, this asymmetric pinning potential provides stability for *vortex-antivortex* configurations. In order to compare our results with the experimental ones, we performed our analysis with the value of the parameters given in Ref. [93] (renormalized to our units): $w_x = 5.4\lambda$, $w_y = 3.6\lambda$, $d = 0.5\lambda$, $D = 0.35\lambda$, $l = 0.2\lambda$ and $\kappa \approx 1$.

Firstly, we determine the criterion for the nucleation of a vortex-antivortex pair. In order to obtain a threshold value of magnetization for which a state with a vortex-antivortex pair is more energetically favorable than the Meissner state, we compared the total energy of the system in these two cases. The contribution to the energy of the system due to the appearance of such a pair equals

$$\Delta F = F_{mv} + F_{mav} + F_{vav} + F_{sv} + F_{sav} \tag{2.45}$$

where $F_{vav}$ and $F_{sv}$ denote the vortex-antivortex interaction energy and the self energy of the vortex, respectively.

These energies are obtained from [52]

$$F_{vav} = -\frac{L_v L_{av} \Phi_0^2}{8\pi^2 \lambda} U_{vav}, \tag{2.46a}$$

$$U_{vav} = dK_0(R) + 2\int_0^\infty dq \frac{J_0(qR)}{k^2 Q}, \tag{2.46b}$$

where $R = \sqrt{(x_v - x_{av})^2 + (y_v - y_{av})^2}$ is the distance between the vortex and the antivortex, $K_0(x)$ is the MacDonald function, and $L_v$, $L_{av}$ are the vorticity of the vortex and anti-vortex, respectively, and

$$F_{sv} = \frac{L_v^2 \Phi_0^2}{16\pi^2 \lambda} U_{sv}, \tag{2.47a}$$

$$U_{sv} = d \ln \kappa + 2 \tanh\left(\frac{d}{2}\right) \ln\left(1 + \coth\frac{d}{2}\right). \tag{2.47b}$$

From the condition $\Delta F = 0$ the value of the FM magnetization necessary for the appearance of the vortex-antivortex pair can be estimated as

$$M^* = \frac{1}{8\pi} \frac{U_{sv} - U_{vav}}{U_{mv}}. \tag{2.48}$$

In the more general case, the transition from $L_v = L_{av} = L$ to the $L_v = L_{av} = L + 1$ state is determined by the FM magnetization

$$M^*_{L \to L+1} = \frac{(2L+1)}{8\pi} \frac{U_{sv} - U_{vav}}{U_{mv}}. \tag{2.49}$$

In order to use Eqs. (2.48-2.49), one should first determine the position of the vortex and the antivortex. This can easily be done if the total interaction energy in the system is calculated (Eq. (2.45), without the self energy terms) with the position of the vortex $x_v$ as a free parameter ($x_{av} = -x_v$, $y_v = y_{av} = 0$). The minimal interaction energy then determines the exact equilibrium position of the vortex-antivortex pair.

Using Eq. (2.48) for the parameters taken from the experiment of Van Bael *et al.* [93] we obtain $M^* \approx 0.08 M_0$. Unit $M_0$ in the SI system equals $M_0 = 4\pi\Phi_0\lambda/\mu_0 \approx 2.07 \cdot 10^6 A/m$ ($\lambda \approx 100$nm). Knowing that the typical magnetization of Co/Pt dots used in the experiments equals approximately $2.5 \cdot 10^5 A/m$, one can see that the $M/M_0$ ratio equals 0.12 and our analysis shows that such a magnetic bar can create exactly one vortex-antivortex pair, which corresponds to the experimental findings of Ref. [93]. It is important to emphasize that the critical magnetization of the bar to induce a vortex-antivortex pair depends strongly on the geometrical parameters of the bar. To investigate this, we repeated our analysis as function of the ratio between the sides of the bar, but keeping the volume of the magnet ($V_{fm} = S_{xy} D$) and other

parameters the same (magnetization is directed along the $x$-axis). The results shown in Fig. 2.30 suggest that the magnetic bar is more magnetically effective for pinning at its poles if it is magnetized along its longer side. However, the threshold magnetization for the nucleation of vortices decreases monotonously as the "magnetization side" of the magnetic bar is made shorter (see Fig. 2.30). However, the flux penetrating the superconductor approximately remains the same along the solid lines in Fig. 2.30. Using the magnetostatic calculation, we obtained the critical condition for the nucleation of the vortex-antivortex pairs as $\Phi^+/\Phi_0 = \nu(L_v + 1/2)$, where $\Phi^+$ denotes the flux through the region of the positive stray field of the magnet at the SC surface, and $\nu = 1.073,\ 1.064,\ 1.054$, for $w_y/w_x = 1,\ 2,\ 3$. Using the values of the parameters from Ref. [93] ($w_y/w_x = 0.667$), we obtain $\nu = 1.094$. Therefore, for the first stable vortex-antivortex pair a lower value of flux is needed, namely $\Phi^+/\Phi_0 = 0.547$, while the appearance of additional pairs is quantized in $\Delta\Phi^+/\Phi_0 = 1.094$. The smaller value of the threshold flux in the first case can be explained by the contribution of the local currents which effectively add an amount of flux to create a fluxoid of exactly $L_v\Phi_0$ at the pole if the stray field of both poles of the magnetic bar creates a (positive or negative) flux between $(L_v - 1/2)\Phi_0$ and $L_v\Phi_0$. Note that this is similar to the superconducting ring case [97] where the $L \to L+1$ ground vortex state transitions take place for $\Phi \approx (L+1/2)\Phi_0$ where the approximate sign becomes equality for large radius thin rings.

As we have shown before (see Fig. 2.29), if **no** vortex-antivortex pair is induced in the SC by the magnetic bar, an additional positive flux line (vortex) will be pinned on the negative pole of the bar (i.e. $x_v < 0$). Now, we assume

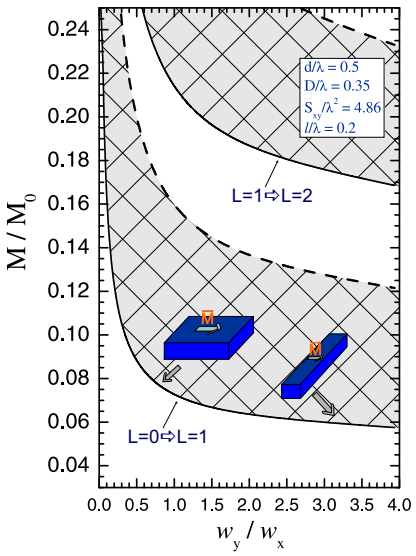


FIG. 2.30: The threshold magnetization of the magnetic bar necessary for the nucleation of the first and second vortex-antivortex pair (solid lines), as function of the geometrical ratio (between the sides) of the bar (for fixed volume of the magnet, where $S_{xy} = w_x w_y$, with parameters taken from Ref. [93]). The dashed lines denote the changing of the vortex pinning properties of the bar: in the shaded (white) regions, an external flux line is pinned at the positive (negative) pole of the FM.

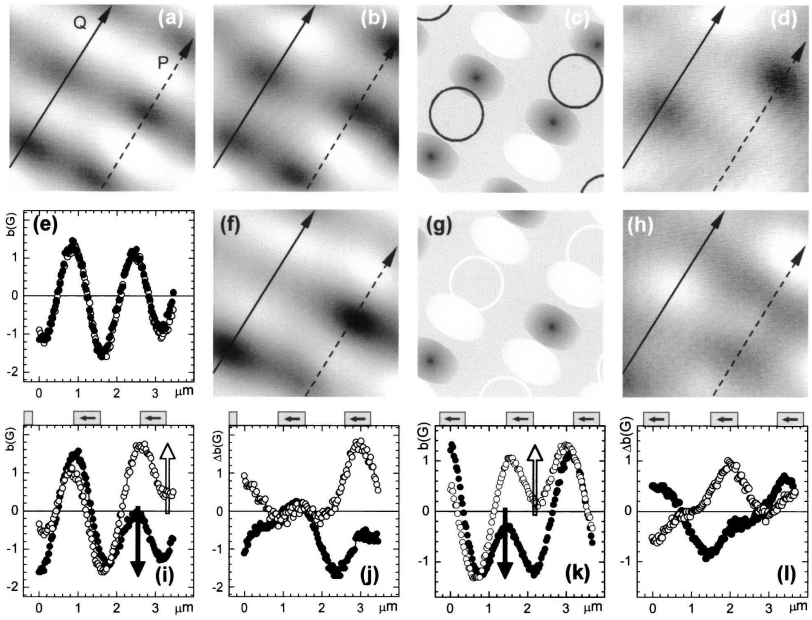


Fig. 2.31: SHPM images (a) at $T = 7.5\text{K} > T_c$ and $B/B_1 = -1/2$; (b) at $T = 6\text{K} < T_c$ and $B/B_1 = -1/2$; (d) image after subtracting (a) from (b); (f) image at $T = 6\text{K}$ and $B/B_1 = 1/2$; (h) image after subtracting the image at $T = 7.5\text{K}$ and $B/B_1 = 1/2$ [not shown, similar to (a)] from (f). All images are taken at the same position on the sample. (c) and (g) are schematic presentations of (b) and (f), respectively. The observed dipole fields are indicated and the FLs induced by the positive (negative) applied field are represented as white (black) circles. (e) Local field distribution at $T = 7.5\text{K}$ along arrow P in (a) for $B/B_1 = -1/2$ (filled symbols) and $B/B_1 = 1/2$ (open symbols). (i) and (k) local field distribution at $T = 6$ K along arrows P and Q, respectively, at $B/B_1 = 1/2$ (open symbols) and $-1/2$ (filled symbols). The white (black) arrow indicates the suggested position of the positive (negative) FL. (j) and (l) field distribution along arrows P and Q, respectively, after subtracting the dipole contribution, for $B/B_1 = 1/2$ (open symbols) and $-1/2$ (filled symbols). The dot positions are indicated on the top axis of $(i) - (l)$ [from Ref. [93]].

that the value of the magnetization of the bar is such that one vortex-antivortex pair appears on the poles of the bar (vortex at the negative pole and antivortex at the positive pole, for $0.08 < M/M_0 < 0.24$, for $w_y/w_x = 0.667$) and we add an extra vortex in the system. The total force acting on this vortex consists of the vortex-magnetic bar, vortex-vortex and vortex-antivortex interaction.

To investigate the interaction of a magnetic bar and its vortex-antivortex pair with an additional external flux line, we put the vortex in different positions (open dot in Fig. 2.32) and follow its trajectory using molecular dynamics (MD)

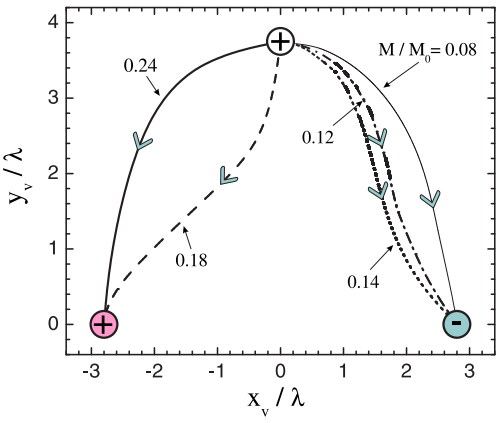


FIG. 2.32: The trajectory of the external flux line when interacting with a magnetic bar and its induced vortex-antivortex pair (colored dots), for different values of the magnetization of the bar (the remaining parameters are taken from Ref. [93]).

simulations, as described in section 2.4.3 (see Fig. 2.22). The components of the force were obtained by simple derivation of the expressions for the contributions to the total interaction energy, which were given before in this section. The results of this MD simulation are shown in Fig. 2.32 for different values of the magnetization $M$. We choose the initial position of the vortex at the same distance from the poles of the magnet, in order not to favor any of the possible pinning sites. Obviously, for smaller magnetization of the bar (just enough to create a vortex-antivortex pair at the poles), the external flux line is attracted by the antivortex and pinned on the *positive* pole of the bar, which is opposite to the situation for $M/M_0 < 0.08$ shown in Fig. 2.29. This is also illustrated in Fig. 2.33(a) where we show a contourplot of the spatial variation of the total energy on the position of the external vortex. However, the magnet-vortex interaction on the positive pole of the bar is still repulsive, and for larger magnetization ($M/M_0 = 0.12$) the vortex is attracted to the antivortex (where annihilation occurs), but its trajectory towards the equilibrium position is distorted, since the magnetic bar is trying to pin the vortex at its negative pole.

Eventually, for further increased magnetization (and still smaller than $M^*_{1\to 2}$) the magnet-vortex interaction overwhelms the vortex-antivortex attraction, and the vortex is pinned at the negative pole of the magnet, although a magnet-induced vortex is already present there. The shape of the most energetically favorable vortex state at the negative pole of the magnet (multi- or giant-vortex) depends on the parameters, mainly on the GL parameter $\kappa$, which determines the vortex-vortex interaction and the self-energy of vortices. As one can see in Fig. 2.33(b), the external vortex in this case is pinned next to the vortex induced by the FM dipole. In this calculation the position of the FM-induced vortex/antivortex pair is kept fixed when the external vortex is moved over the SC surface. The critical magnetization at which the pinning switches from the positive to the negative pole of the FM is shown by the thick dashed curve in Fig. 2.30. The physical reason for the switching of the pinning

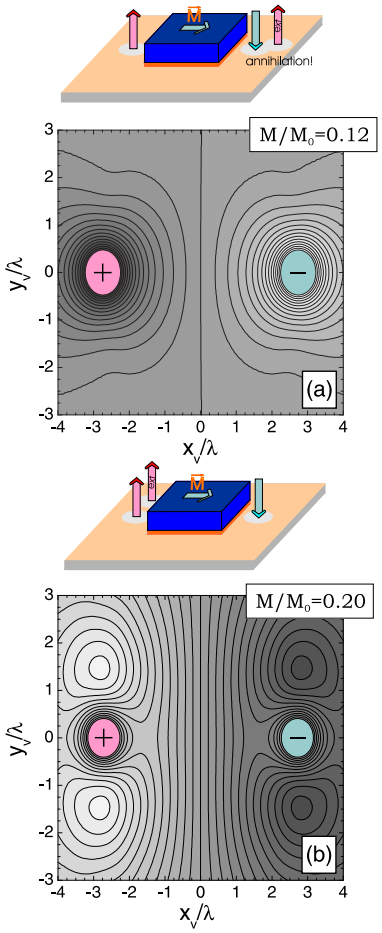


Fig. 2.33: Contourplot of the interaction energy of an external flux line with the screening currents induced by the FM in case that the FM bar induces a vortex/antivortex pair (white (dark) color - low (high) energy), for the magnetization of the magnetic bar (a) $M/M_0 = 0.12$, and (b) $M/M_0 = 0.20$. The position of the FM-induced vortex/antivortex pair is taken fixed.

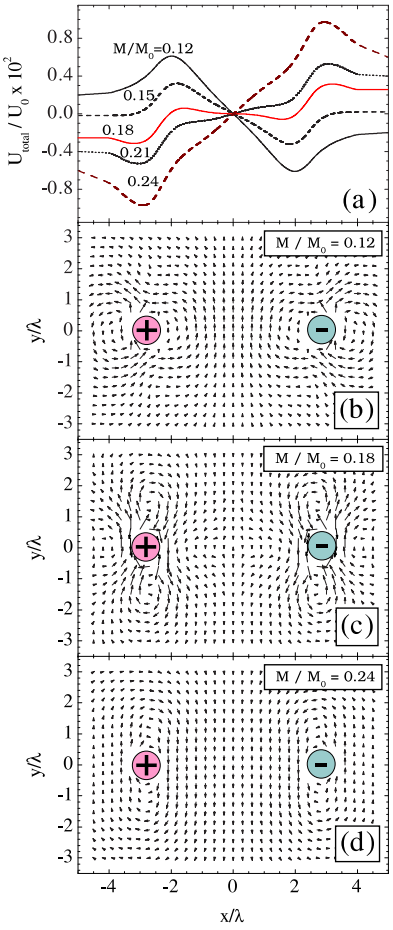


Fig. 2.34: (a) The interaction energy (in units of $U_0 = \Phi_0^2/\pi\lambda$) of an external flux line with the FM and induced vortex/antivortex pair along the $y_v = -x_v/2$ direction (see Fig. 2.33(b)), for different values of the magnetization of the magnetic bar. (b)-(d) Vectorplots of the screening currents in the SC due to the presence of the FM and the induced vortex/antivortex pair.

position is the reversal of the direction of the screening currents near the vortex and the antivortex. This is illustrated in Figs. 2.34(b-d). In Fig. 2.34(a) we show the interaction energy of the external vortex with the FM and the induced vortex/antivortex pair, along the $y_v = -x_v/2$ direction (which is approximately along the line where energy minimum and maximum are found in

Fig. 2.33(b)) for different values of the magnetization of the FM. The change of the pinning behavior of the FM bar is clearly visible. In Figs. 2.34(b-d) the corresponding vectorplots of the screening currents are shown. Obviously, with increasing magnetization of the magnetic bar, the current flow in the SC changes. At the negative pole of the FM, for lower magnetization (Fig. 2.34(b)), the current is vortex-like, due to the presence of an induced vortex there. However, as we increase the magnetization (Fig. 2.34(c)), an antivortex type of current flow appears close to the vortex site, resulting ultimately in a pure antivortex-like current at the negative pole of the magnet as the magnetization approaches the critical value for the nucleation of the next vortex-antivortex pair (Fig. 2.34(d)). In all cases, the stable position of an external vortex is determined by the position of this quasi-antivortex, which explains the switching of the pinning behavior with increasing magnetization of the magnetic bar.

To summarize, in Ref. [93] it was found experimentally that in the case of vortex pinning by magnetic bars with in-plane magnetization such that one vortex-antivortex pair is induced in the superconductor, an extra external vortex is attracted by the antivortex (and vice versa, for external antivortex) and they annihilate each other. The authors refer to this phenomenon as a field-polarity-dependent pinning. Our simulation shows that for the given experimental parameters this is indeed the case. But, our analysis shows that this phenomenon not only depends on the polarity of the external magnetic field, but also on the strength of the magnetization of the magnetic bar as well. For larger magnetization of the magnet, we found that the external vortex can be pinned on the opposite side, i.e. at the negative pole of the bar, next to the magnet-induced vortex (as shown in Figs. 2.32-2.34). This remarkable phenomenon should be easily observable using the same experimental procedure as in Ref. [93], if samples with micro-magnets with a larger magnetization are used. In that case, one should avoid the annihilation between the external flux line and the antivortex created by the neighboring dipole, and make the magnetic pinning lattice sparser.

### 2.5.3 Influence of corners/defects in the magnet geometry on the interaction energy

In this section, we investigate the influence of the magnet geometry on the pinning of vortices in the case when no vortex/antivortex pair is nucleated. For magnets with out-of-plane magnetization (see previous section) we found that the *qualitative* behavior of the magnet-vortex interaction does not depend on the geometry, as was found by comparing the results for disk, square and triangular FMs. However, a difference in the dynamics of pinning was noted, since the vortex approaches its equilibrium position under the magnet following the trajectory over the corners of the magnet, rather than perpendicular to the sides, in the case of square and triangular FMs. Also, by introducing hole(s)

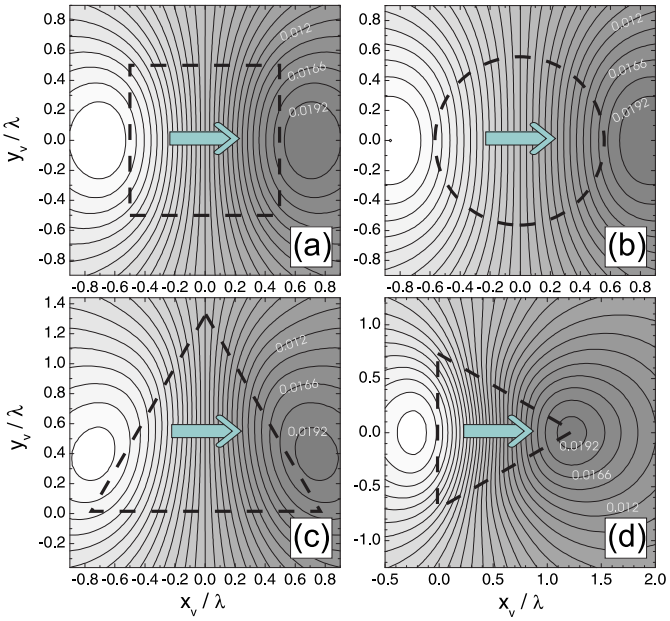


Fig. 2.35: The contourplots of the in-plane magnet-vortex interaction energy for different shapes of the magnet. Dashed lines indicate the edges of the magnetic structures ($d = 0.25\lambda$, $D = 0.25\lambda$, $l = 0.1\lambda$, $M = M_0$, surface of the magnet base is the same for all structures $S = \lambda^2$). All plots are given with the same energy scale (some of the values of the contourlines are indicated).

in the magnetic structure, it was shown how one can create different local minima in the interaction energy and manipulate the equilibrium position of the vortices.

We repeated this analysis for in-plane magnetization of the magnet, for the magnetic disk, square and triangle with fixed thickness and volume. We use Eq. (2.44b) to calculate numerically the magnet-vortex interaction energy profile, where in the integration over the magnet boundaries ($\pm w_x/2$) we substitute the functions describing the magnet's shape. The results are shown in Fig. 2.35. The qualitative behavior of the vortex-magnet interaction is the same in all cases. Moreover, the amplitudes of the interaction potential appear to be very similar (all the contourplots in Fig. 2.35 are given with the same energy scale). One can see that in the case of symmetric magnets with respect to the magnetization direction the contourlines follow the shape of the magnet and the extreme interaction energy regions are set parallel to the opposite sides of the magnet. However, if the symmetry is broken (see Fig. 2.35(d) for the case of a triangular magnet with magnetization perpendicular to one of its sides) the

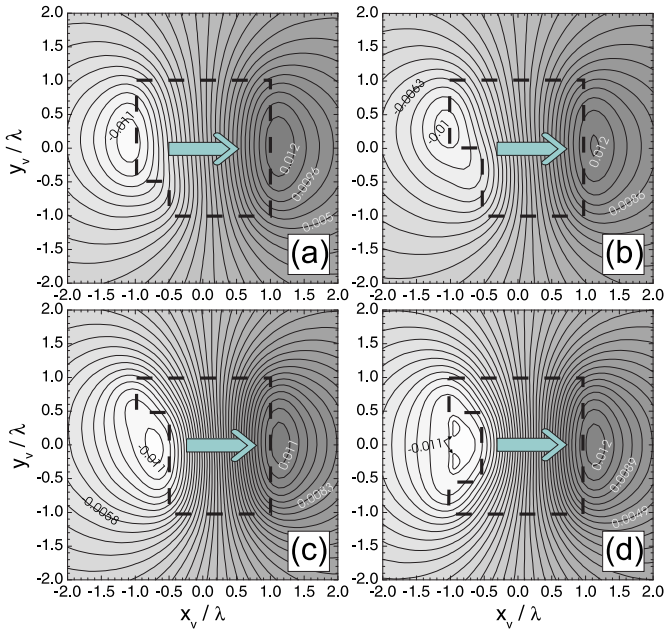


FIG. 2.36: The contourplots of the in-plane magnet-vortex interaction energy for different shapes of the magnet. Dashed lines illustrate the edges of the magnetic structures ($d = 0.25\lambda$, $D = 0.25\lambda$, $l = 0.1\lambda$, $M = M_0$). The plots are given with slightly different energy scales (some of the prominent contourlines are labelled).

interaction symmetry is broken and the amplitude of the energy is somewhat higher at the negative pole of the magnet.

Next we introduced an asymmetry in the geometry of the magnet not only by rotating the magnetization in the $xy$-plane but by introducing edge defects. According to the superposition principle, we may model the removed area as a superposition of two ferromagnets with opposite magnetization. The smaller size magnet with the opposite magnetization can model the hole (defect) in the larger magnetic structure. As one can see in Fig. 2.36, the equilibrium position of the vortex can be nicely manipulated by an edge defect on the side of the magnet. When a defect is located in the corner of the magnetic square (see Fig. 2.36(a)), the equilibrium position for the vortex shifts slightly away from the defect, and the symmetry of the positions of extrema in the interaction energy is broken. As we spread the defect further along the negative pole of the magnet, the energetically favorable position of the vortex moves further up, i.e. it "runs" away from the upper edge of the defect (Fig. 2.36(b)). However, when the inner edge of the defect becomes longer than the outer magnet edge, the ground state for the vortex moves back towards the central position (Fig. 2.36(c)). In this case, the part of the magnet that is sticking

out acts as a defect, and breaks the symmetry of the interaction. Therefore, to further investigate the competition of these two, + and - defects, we set an edge defect in the center of the magnetic structure (Fig. 2.36(d)). In this case (for given parameters), the central equilibrium vortex position breaks up into two, and the contourplot of the energy shows two equal minima close to the upper and lower edge of the defect. Thanks to this feature, a possible use of this system for quantum computing can be analyzed, similarly to the quantum systems proposed before (see, for example, Ref. [99]).

## 2.6 CONCLUSIONS

To summarize, we applied the London theory to investigate flux pinning in SC films due to the presence of a magnetic dipole (MD) or a finite-size ferromagnet (FM) above (or under) the SC. Depending on the direction of the dipole magnetic moment, we obtained exact analytic expressions for the MD-vortex interaction energy and screening currents. We obtained the asymptotic behavior of the interaction potential and the induced currents for specific values of the involved parameters. We calculated the pinning potential for both an in- and out-of-plane magnetized dipole. Our results show that an out-of-plane magnetized dipole attracts a vortex if aligned parallel to it, and opposite, for anti-parallel alignment the vortex is repelled. This is a consequence of the mono-directional superconducting current induced in the SC for out-of-plane magnetization of the MD. However, for in-plane magnetization, the dipole-vortex interaction shows a dual behavior, namely, the vortex is attracted to the negative pole of the MD and repelled on the other side. Moreover, the position of the pinning site depends on the position of the MD and thickness of the SC. We calculated these dependencies and showed that it is linear for thin superconductors, or large MD-vortex distances. Due to the dual behavior of the pinning potential, we explored the possible co-existence of vortices and antivortices in such systems. The total interaction energy calculation leads to the conclusion that the vortex and antivortex are separated by an energy barrier due to the short range interaction with the dipole, and therefore, these pairs could be stable. Both in- and out-of-plane magnetized dipoles are able to keep these vortices apart. We calculated analytically the interaction potential in the presence of vortex-antivortex pairs (or giant vortex-single antivortices) and gave estimates of the parameters necessary for stability of such fascinating configurations in a thin SC film.

To continue, we investigated flux pinning in SC films due to the out-of-plane magnetized ferromagnet situated above (or under) the SC, where the finite dimensions of the FM were fully taken into account. In the case of a magnetic disk or annulus (ring), we obtained analytic expressions for the FM-vortex interaction energy, force and the screening currents. We also derived the

asymptotic behavior of the interaction potential and the force for specific values of the involved parameters. In the case of a magnetic disk with an off-center hole we showed the existence of two local minima in the FM-vortex interaction energy - the ground state and the metastable one. By changing the position of the hole, the position of the equilibrium moves with respect to the magnetic disk center. We also showed that in the case of a FM disk with two touching holes ("eight-hole") two minima with equal energy but different vortex position appeared. The probability of a vortex sitting in one of these two states is the same, which makes this system interesting as a possible qubit. To further investigate the influence of the magnet geometry on its pinning properties, we calculated the pinning potential for square and triangular shaped ferromagnets. A substantial breaking of the circular symmetry occurs and the attractive force acting on the vortex is stronger at the sides of the magnet than at the corners. Also, making one side of the rectangular magnet longer enlarges the attractive force along it with respect to the other side. Although counterintuitive, we showed that the vortex approaches the non-circular magnet rather along the corners than perpendicular to the sides, following the gradient of the potential.

At the end, we considered flux pinning properties of an in-plane magnetized ferromagnet situated above the SC. In the case of a magnetic stripe on top of a superconductor, we obtained a semi-analytic expression for the FM-vortex interaction energy and analyzed the dependence of the interaction potential on the system parameters. We found that the equilibrium position for an external flux line pinned by the stripe lies in the channel, parallel to the magnetic structure. The exact position of this "equilibrium channel" depends on both thickness of the SC and the magnet. Also, all the flux lines of the same polarity are found to be pinned on the same side of the stripe. Therefore, using such a magnetic structure on top of a superconductor in the presence of a homogeneous magnetic field may lead to a superconducting region without vortices. In the case of finite size superconductors, if the pinning channel is relatively far from the stripe, the whole superconducting sample could be made vortex-free, which is highly important for applications.

In the case of pinning of vortices by an in-plane magnetic bar, we discussed the field-polarity dependent pinning. We found that a vortex or antivortex in these systems are pinned on the opposite poles of the bar. However, on which pole the vortex will be pinned depends on the strength of the magnetization of the magnet and the possible presence of a vortex-antivortex pair induced in the SC by the magnet itself (see Figs. 10-12). Our results agree with the experiment of Ref. [93] and give directives for future experimental considerations of similar heterostructures, since our analysis predicts that the position of the pinned vortex can be tuned by changing the strength of the magnetization of the FM.

We extended this approach further, to investigate the influence of edge defects of the magnetic structure on the pinning potential and we found that such defects break the symmetry of the vortex-magnet interaction. Moreover, different local minima in the energy were found. For symmetric position of the

defect with respect to the edges of the magnet, we found that two degenerate vortex states are possible which differ in the position of the vortex, making this SC-FM structure interesting as a possible qubit.

**Publications.** The results presented in this chapter were published as:

- M. V. Milošević, S. V. Yampolskii, and F. M. Peeters, *Magnetic Pinning of Vortices in a Superconducting Film: The (anti)vortex-magnetic dipole interaction energy in the London approximation*, Phys. Rev. B **66**, 174519 (2002).
- M. V. Milošević, S. V. Yampolskii, and F. M. Peeters, *The vortex-ferromagnet interaction in the London approximation*, Journal of Low Temp. Phys. **130**, 3-4, 321-331 (2003).
- M. V. Milošević and F. M. Peeters, *The interaction between a superconducting vortex and an out-of-plane magnetized ferromagnetic disk: influence of the magnet geometry*, Phys. Rev. B **68**, 094510 (2003).
- M.V. Milošević and F.M. Peeters, *Vortex pinning in a superconducting film due to in-plane magnetized ferromagnets of different shapes: the London approximation*, Phys. Rev. B **69**, 104519 (2004).

# *Appendix A*

## A.1 THE MAGNETIC FIELD OF A MAGNETIC DIPOLE IN THE PRESENCE OF A SUPERCONDUCTING FILM

The magnetic field of a vortex $\vec{h}_v = rot\vec{A}_v$, which is perpendicular to the plane of the film, is determined as the solution of the system of equations

$$\vec{A}_v\left(\vec{\rho},z\right)+\lambda^2\,\mathrm{rot}\,\mathrm{rot}\,\vec{A}_v\left(\vec{\rho},z\right)=\vec{\Phi}\left(\vec{\rho}-\vec{\rho}_v\right),\qquad |z|<d/2, \tag{A.1}$$

$$-\nabla^2\vec{A}_v\left(\vec{\rho},z\right)=0,\qquad |z|>d/2, \tag{A.2}$$

with the following boundary conditions: i) the continuity of the vector potential components at $z=\pm d/2$, and ii) their vanishing far from the superconductor (at $|z|\to\infty$). Here $\vec{\Phi}\left(\vec{\rho}-\vec{\rho}_v\right)$ takes into account the vortex, where $\vec{\rho}_v$ is the vortex position in the film plane. In cylindrical coordinates $\Phi_\rho=\Phi_z=0$, $\Phi_\varphi=L\Phi_0/2\pi\left|\vec{\rho}-\vec{\rho}_v\right|$ (so that $\mathrm{rot}\,\vec{\Phi}=L\Phi_0\delta\left(\vec{\rho}-\vec{\rho}_v\right)$). The solutions of Eqs. (A.1)-(A.2) are [52, 100]

$$A^{(i)}_{v\varphi}\left(\vec{\rho},z\right)=\frac{L\Phi_0}{2\pi\lambda}\int\limits_0^\infty dq\;\frac{J_1\left(qR/\lambda\right)}{k^2}\left[1-\frac{kq\cosh\left(kz/\lambda\right)}{Q\sinh\left(kd/2\lambda\right)}\right], \tag{A.3}$$

$$A^{(o)}_{v\varphi}\left(\vec{\rho},z\right)=\frac{L\Phi_0}{2\pi\lambda}\int\limits_0^\infty dq\frac{J_1\left(qR/\lambda\right)}{Q}\exp\left(-q\frac{2\left|z\right|-d}{2\lambda}\right). \tag{A.4}$$

Here $k = \left(1+q^2\right)^{1/2}$, $Q = k\left[k + q\coth\left(kd/2\lambda\right)\right]$, $R = |\vec{\rho} - \vec{\rho}_v| = \left[\rho^2 + \rho_v^2 - 2\rho\rho_v\cos\left(\varphi - \varphi_v\right)\right]^{1/2}$, $J_\nu\left(x\right)$ is the Bessel function, index "$i(o)$" denotes the field inside (outside) the superconductor. The components of the vortex magnetic field are given by [52]

$$h_{vz}^{(i)}\left(\rho, z\right) = \frac{L\Phi_0}{2\pi\lambda^2}\left[K_0\left(\frac{R}{\lambda}\right) - \int\limits_0^\infty \frac{dq\, q^2}{kQ} J_0\left(\frac{qR}{\lambda}\right)\frac{\cosh\left(kz/\lambda\right)}{\sinh\left(kd/2\lambda\right)}\right], \tag{A.5}$$

$$h_{v\rho}^{(i)}\left(\rho, z\right) = \frac{L\Phi_0}{2\pi\lambda^2}\int\limits_0^\infty \frac{dq\, q}{Q} J_1\left(\frac{qR}{\lambda}\right)\frac{\sinh\left(kz/\lambda\right)}{\sinh\left(kd/2\lambda\right)}, \tag{A.6}$$

$$h_{vz}^{(o)}\left(\rho, z\right) = \frac{L\Phi_0}{2\pi\lambda^2}\int\limits_0^\infty \frac{dq\, q}{Q} J_0\left(\frac{qR}{\lambda}\right)\exp\left(-q\frac{2\left|z\right| - d}{2\lambda}\right), \tag{A.7}$$

$$h_{v\rho}^{(o)}\left(\rho, z\right) = \frac{L\Phi_0}{2\pi\lambda^2}\,\mathrm{sgn}(z)\int\limits_0^\infty \frac{dq\, q}{Q} J_1\left(\frac{qR}{\lambda}\right)\exp\left(-q\frac{2\left|z\right| - d}{2\lambda}\right), \tag{A.8}$$

$$h_{v\varphi}^{(i)} = h_{v\varphi}^{(o)} = 0, \tag{A.9}$$

where $K_0\left(x\right)$ is the MacDonald function.

The magnetic field of a dipole, situated at the distance $l$ above the film, can be written in the following way (here and below $l = |a| - d/2$) (see, for example, Ref. [101])

$$\vec{h}_m\left(\vec{\rho}, z\right) = \begin{cases} \vec{h}_d\left(\vec{\rho}, z\right) + \vec{h}_{m,+}^{(o)}\left(\vec{\rho}, z\right), & z > d/2, \\ \vec{h}_m^{(i)}\left(\vec{\rho}, z\right), & -d/2 \le z \le d/2, \\ \vec{h}_{m,-}^{(o)}\left(\vec{\rho}, z\right), & z < -d/2, \end{cases} \tag{A.10}$$

where $\vec{h}_d\left(\vec{\rho}, z\right)$ is the direct contribution from the dipole, $\vec{h}_{m,+}^{(o)}\left(\vec{\rho}, z\right)$ is the induced field above the superconductor, $\vec{h}_m^{(i)}\left(\vec{\rho}\right)$ is the dipole field penetrating inside the superconductor and $\vec{h}_{m,-}^{(o)}\left(\vec{\rho}\right)$ denotes the field of the dipole below the film. The vector potential $\vec{A}_d\left(\vec{\rho}, z\right)$ is defined by the equation

$$\mathrm{rot}\,\vec{A}_d\left(\vec{\rho}, z\right) = 4\pi\vec{m}\delta\left(\vec{\rho}\right)\delta\left(z - a\right), \tag{A.11}$$

where $\vec{m}$ is the magnetic moment of the dipole. The potential $\vec{A}_m^{(i)}\left(\vec{\rho}\right)$ is found as the solution of Eq. (A.1) with zero right side and $\vec{A}_{m,\pm}^{(o)}\left(\vec{\rho}\right)$ as solution of Eq. (A.2). The integration constants have to be found through similar boundary conditions as for the vortex field distribution: i) the continuity of the vector potential components at $z = \pm d/2$ and ii) their vanishing at $|z| \to \infty$.

We consider two orientations of the MD magnetization.

I) The dipole is directed *perpendicular* to the film plane, i.e. $m_\rho = m_\varphi = 0$, $m_z = m$. In this case the vector potential has only an azimuthal component and is described by the following expressions:

$$A_{d\varphi}(\rho,z) = \frac{m}{\lambda^2}\int_0^\infty dq\ qJ_1\left(\frac{q\rho}{\lambda}\right)\exp\left(-\frac{q}{\lambda}\left|z-a\right|\right) = \frac{m\rho}{\left[\rho^2+(z-a)^2\right]^{3/2}}, \tag{A.12}$$

$$A^{(i)}_{m\varphi}(\rho,z) = \frac{1}{\lambda^2}\int_0^\infty dq\ qJ_1\left(\frac{q\rho}{\lambda}\right)\left[B_1(q)\exp\left(-\frac{kz}{\lambda}\right) + D_1(q)\exp\left(\frac{kz}{\lambda}\right)\right], \tag{A.13}$$

$$A^{(o)}_{m\varphi,\pm}(\rho,z) = \frac{1}{\lambda^2}\int_0^\infty dq\ qJ_1\left(\frac{q\rho}{\lambda}\right)B_{2,\pm}(q)\exp\left(-\frac{qz}{\lambda}\right), \tag{A.14}$$

where $B_1(q) = B(q)q(k-q)\exp(-kd/2\lambda)$, $D_1(q) = B(q)q(k+q)\exp(kd/2\lambda)$, $B_{2,+}(q) = -B(q)\sinh(kd/\lambda)\exp(qd/2\lambda)$, and $B_{2,-}(q) = 2B(q)kq\exp(qd/2\lambda)$, with $B(q) = 2m\exp(-ql/\lambda)/[(k+q)^2\exp(kd/\lambda) - (k-q)^2\exp(-kd/\lambda)]$.

Consequently, we obtain the following components of the dipole magnetic field

$$h^{(i)}_{mz}(\rho,z) = \frac{1}{\lambda^3}\int_0^\infty dq\ q^2J_0\left(\frac{q\rho}{\lambda}\right)\left[B_1(q)\exp\left(-\frac{kz}{\lambda}\right) + D_1(q)\exp\left(\frac{kz}{\lambda}\right)\right], \tag{A.15}$$

$$h^{(i)}_{m\rho}(\rho,z) = \frac{1}{\lambda^3}\int_0^\infty dq\ kqJ_1\left(\frac{q\rho}{\lambda}\right)\left[B_1(q)\exp\left(-\frac{kz}{\lambda}\right) - D_1(q)\exp\left(\frac{kz}{\lambda}\right)\right], \tag{A.16}$$

$$h_{dz}(\rho,z) = \frac{m}{\lambda^3}\int_0^\infty dq\ q^2J_0\left(\frac{q\rho}{\lambda}\right)\exp\left(-\frac{q}{\lambda}\left|z-a\right|\right) = \frac{m\left[2(z-a)^2-\rho^2\right]}{\left[\rho^2+(z-a)^2\right]^{5/2}}, \tag{A.17}$$

$$h_{d\rho}(\rho,z) = \frac{m\,\mathrm{sgn}(z-a)}{\lambda^3}\int_0^\infty dq\ q^2J_1\left(\frac{q\rho}{\lambda}\right)\exp\left(-\frac{q}{\lambda}\left|z-a\right|\right) = \frac{3m\rho(z-a)}{\left[\rho^2+(z-a)^2\right]^{5/2}}, \tag{A.18}$$

$$h^{(o)}_{mz,\pm}(\rho,z)=\frac{1}{\lambda^3}\int_0^\infty dq\; q^2 J_0\left(\frac{q\rho}{\lambda}\right)B_{2,\pm}(q)\exp\left(-\frac{qz}{\lambda}\right), \tag{A.19}$$

$$h^{(o)}_{m\rho,\pm}(\rho,z)=\frac{1}{\lambda^3}\int_0^\infty dq\; q^2 J_1\left(\frac{q\rho}{\lambda}\right)B_{2,\pm}(q)\exp\left(-\frac{qz}{\lambda}\right), \tag{A.20}$$

$$h^{(1)}_{m\varphi}=h^{(2)}_{m\varphi,\pm}=0. \tag{A.21}$$

II) The dipole is magnetized in the direction *parallel* to the SC film plane (in-plane magnetization). Following the same procedure as above, we obtain

$$\begin{aligned}h_{d\rho}(\rho,\varphi,z)&=\frac{m\cos\varphi}{2\lambda^3}\int_0^\infty dq\; q^2\exp\left(-\frac{q}{\lambda}|z-a|\right)\left[J_2\left(\frac{q\rho}{\lambda}\right)-J_0\left(\frac{q\rho}{\lambda}\right)\right]\\&=\frac{m\left[2\rho^2-(z-a)^2\right]\cos\varphi}{\left[\rho^2+(z-a)^2\right]^{5/2}},\end{aligned} \tag{A.22}$$

$$\begin{aligned}h_{d\varphi}(\rho,\varphi,z)&=\frac{m\sin\varphi}{\lambda^2\rho}\int_0^\infty dq\; q\exp\left(-\frac{q}{\lambda}|z-a|\right)J_1\left(\frac{q\rho}{\lambda}\right)\\&=\frac{m\sin\varphi}{\left[\rho^2+(z-a)^2\right]^{3/2}},\end{aligned} \tag{A.23}$$

$$\begin{aligned}h_{dz}(\rho,\varphi,z)&=-\frac{m\cos\varphi}{\lambda^3}\int_0^\infty dq\; q^2\exp\left(-\frac{q}{\lambda}|z-a|\right)J_1\left(\frac{q\rho}{\lambda}\right)\\&=-\frac{3m\rho|z-a|\cos\varphi}{\left[\rho^2+(z-a)^2\right]^{5/2}},\end{aligned} \tag{A.24}$$

$$\begin{aligned}h^{(i)}_{m\rho}(\rho,\varphi,z)&=\frac{\cos\varphi}{2\lambda^3}\int_0^\infty dq\; kq\left[J_2\left(\frac{q\rho}{\lambda}\right)-J_0\left(\frac{q\rho}{\lambda}\right)\right]\\&\quad\times\left[D_1(q)\exp\left(\frac{kz}{\lambda}\right)-B_1(q)\exp\left(-\frac{kz}{\lambda}\right)\right],\end{aligned} \tag{A.25}$$

$$\begin{aligned}h^{(i)}_{m\varphi}(\rho,\varphi,z)=\frac{\sin\varphi}{\lambda^2\rho}\int_0^\infty dq\; kJ_1\left(\frac{q\rho}{\lambda}\right)&\left[D_1(q)\exp\left(\frac{kz}{\lambda}\right)\right.\\&\left.-B_1(q)\exp\left(-\frac{kz}{\lambda}\right)\right],\end{aligned} \tag{A.26}$$

$$\begin{aligned}h^{(i)}_{mz}(\rho,\varphi,z)=-\frac{\cos\varphi}{\lambda^3}\int_0^\infty dq\; q^2J_1\left(\frac{q\rho}{\lambda}\right)&\left[D_1(q)\exp\left(\frac{kz}{\lambda}\right)\right.\\&\left.+B_1(q)\exp\left(-\frac{kz}{\lambda}\right)\right],\end{aligned} \tag{A.27}$$

$$h^{(o)}_{m\rho,\pm}(\rho,\varphi,z) = -\frac{\cos\varphi}{2\lambda^3}\int_0^\infty dq\; q^2 \exp\left(-\frac{qz}{\lambda}\right)\left[J_2\left(\frac{q\rho}{\lambda}\right) - J_0\left(\frac{q\rho}{\lambda}\right)\right] B_{2,\pm}(q)\,, \tag{A.28}$$

$$h^{(o)}_{m\varphi,\pm}(\rho,\varphi,z) = -\frac{\sin\varphi}{\lambda^2\rho}\int_0^\infty dq\; q \exp\left(-\frac{qz}{\lambda}\right) J_1\left(\frac{q\rho}{\lambda}\right) B_{2,\pm}(q)\,, \tag{A.29}$$

$$h^{(o)}_{mz,\pm}(\rho,\varphi,z) = -\frac{\cos\varphi}{\lambda^3}\int_0^\infty dq\; q^2 \exp\left(-\frac{qz}{\lambda}\right) J_1\left(\frac{q\rho}{\lambda}\right) B_{2,\pm}(q)\,, \tag{A.30}$$

## A.2 CALCULATION OF THE TWO CONTRIBUTIONS TO THE MAGNETIC DIPOLE-VORTEX INTERACTION ENERGY

The magnetic dipole-vortex interaction energy is given by

$$F_{mv} = \frac{1}{2c}\int dV^{(i)}\vec{j}_m\cdot\vec{\Phi}_v - \frac{1}{2}\int dV^{(md)}\vec{h}_v\cdot\vec{M} = I_1 + I_2 \tag{A.31}$$

where $\vec{\Phi}_v = (\Phi_\rho, \Phi_\varphi, \Phi_z) = (0, \Phi_0/(2\pi\rho), 0)$ denotes the vortex magnetic flux vector ($\Phi_0$ is the flux quantum), and $\vec{M}$ is the magnetization of the dipole. As one can see, the interaction energy in this system consists of two parts, namely, (i) the interaction between the Meissner currents generated in the SC ($\vec{j}_m$) by the MD and the vortex, and (ii) the interaction between the vortex magnetic field and the MD. We will now separately calculate these contributions. The superconducting current induced in an infinite superconducting film with thickness $d$ ($-\frac{d}{2} < z < \frac{d}{2}$) by a magnetic dipole with *out-of-plane magnetization*, i.e. $\vec{m} = m\vec{e}_z$ located at $z = a$ ($l = a - d/2$) above the SC, is given by Eqs. (2.7, 2.8). The components of the vortex magnetic field outside the superconductor are given by Eqs. (A.7, A.8) [52].

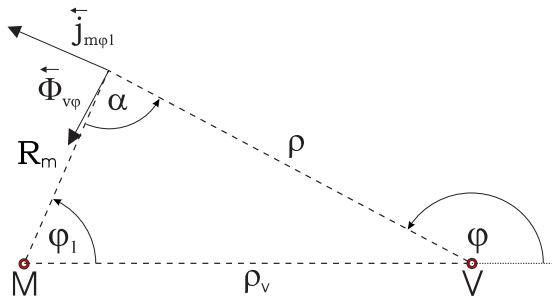


Fig. A.1: Sketch of the system in the plane of the superconductor ($xy$-plane). $V$ and $M$ denote the position of the vortex and the magnetic dipole, respectively.

The first integral in Eq. (A.31) now becomes (see Fig. A.1 for definitions of the distance variables)

$$I_1 = \frac{1}{2c}\int dV^{(i)}\vec{j}_m\cdot\vec{\Phi}_v = -\frac{m\Phi_0^2}{4\pi\lambda}\int_0^\infty dq\exp\left(-ql\right)q^2$$
$$\times\int_{-d/2}^{d/2} dz\ C\left(q,z\right)\int_0^{2\pi} d\varphi\int_0^\infty d\rho\ \rho J_1(qR)\frac{1}{2\pi\rho}\frac{\partial R_m}{\partial\rho}$$

where we make use of $\vec{j}_m\cdot\vec{\Phi}_v = j_{m\phi 1}\Phi_{v\phi}\cos\alpha = j_{m\phi 1}\Phi_{v\phi}\frac{\delta R_m}{\delta\rho}$.

$$\begin{aligned} I_1 &= \frac{m\Phi_0^2}{4\pi\lambda}\int_0^\infty dq\ C_1\left(q\right)\exp\left(-ql\right)q\frac{1}{2\pi}\int_0^{2\pi} d\varphi\int_0^\infty d\rho\frac{\partial\left(J_0(qR_m)\right)}{\partial\rho} \\ &= \frac{m\Phi_0^2}{4\pi\lambda}\int_0^\infty dq\ C_1\left(q\right)\exp\left(-ql\right)q\frac{1}{2\pi}\int_0^\infty d\rho\frac{\partial}{\partial\rho}\int_0^{2\pi} d\varphi\ J_0(qR_m). \end{aligned}$$

Using Ref. [102] we obtain

$$\begin{aligned} I_1 &= \frac{m\Phi_0^2}{4\pi\lambda}\int_0^\infty dq\ C_1\left(q\right)\exp\left(-ql\right)q\frac{1}{2\pi}2\pi J_0(q\rho_v)\int_0^\infty d\rho\frac{\partial\left(J_0(q\rho)\right)}{\partial\rho} \\ &= -\frac{m\Phi_0^2}{4\pi\lambda}\int_0^\infty dq\ qC_1\left(q\right)\exp\left(-ql\right)J_0(q\rho_v), \end{aligned} \tag{A.32}$$

where

$$C_1\left(q\right) = \frac{1}{k}\frac{k\ sinh(kd)+q\ cosh(kd)-q}{\left(k^2+q^2\right)\ sinh(kd)+2kq\ cosh(kd)}. \tag{A.33}$$

The integration of the second integral in Eq. (A.31) gives

$$\begin{aligned} I_2 &= -\frac{1}{2}\int dV^{(md)}\vec{h}_v\cdot\vec{M} = -\frac{1}{2}\int dV^{(md)}\vec{h}_{vz}\cdot\vec{M} \\ &= -\frac{m\Phi_0^2}{4\pi\lambda}\int_0^\infty\frac{dq\ q}{Q}\int_{-\infty}^\infty dz\ \delta(z-a)\exp\left(-q\left(|z|-d/2\right)\right) \\ &\quad\times\int_{-\infty}^\infty dy\ \delta(y-y_v)\int_{-\infty}^\infty dx\ \delta(x-x_v)J_0\left(q\sqrt{x^2+y^2}\right) \\ &= -\frac{m\Phi_0^2}{4\pi\lambda}\int_0^\infty\frac{dq\ q}{Q}\exp\left(-ql\right)J_0(q\rho_v). \end{aligned} \tag{A.34}$$

After simple trigonometric transformations it can be shown that $C_1(q) = 1/Q$, and therefore from Eqs. (A.32) and (A.34) follows $I_1 = I_2$. We are allowed to generalize this equality for the case of finite size ferromagnets with out-of-plane magnetization, due to the superposition principle.

# 3

# *The mesoscopic superconducting disk with a magnetic structure on top*

## 3.1 INTRODUCTION

Recent progress in microfabrication and measurement techniques makes it possible to study the properties of small superconducting structures, so called mesoscopic samples, with sizes comparable to the penetration depth $\lambda$ and the coherence length $\xi$. Mesoscopic disks have been one of the most popular and exciting study objects [45, 69, 103–113] in this respect. The behavior of such mesoscopic samples in an external magnetic field is strongly influenced by the boundary conditions, sample size and geometry and may lead to various superconducting states and phase transitions between them.

Motivated by recent experiments [6, 7], we study the properties of a superconducting disk in the presence of a step-like external magnetic field. The step-like field profile is a model magnetic field profile for a ferromagnetic dot or current loop placed on top of the superconductor. These profiles have the important property that the average magnetic field is zero. We investigate the influence of step height, step profile, and ratio between step width and radius of the disk, on the superconducting phase diagram. We also consider the real magnetic field profiles of the magnetic dot or a current loop, and compare the results with the experimental ones.

Previous investigations of structures with magnetic dots were limited to experiments with superconducting films deposited on regular arrays of magnetic

dots [2, 81, 82, 114] and theoretical studies of single magnetic dots embedded in a thin superconducting film [88, 89]. The common problem was that, for magnetic dots, the strong field present inside the ferromagnet suppresses the superconducting order parameter, and in such situations it is appropriate to adopt a boundary condition in which the order parameter itself vanishes. This seems to spoil the effect that leads to surface superconductivity, and it is not at first obvious why magnetic dots should support the relatively large supercurrents associated with multiple vortices. Although enhancement of superconducting order is preserved in the vicinity of the dot due to the fringing field of the dot itself [89] a possible oxide layer between the magnetic dot and the superconductor may restore the boundary condition to the one of a superconductor/insulator interface and make this effect more distinctive. We put a single magnetic dot on top of the superconductor and study the behavior of our sample in such a non-uniform magnetic field of the dot which enhances the possibility of obtaining various combinations of superconducting states. To better understand the problem we start from a simple theoretical model for the inhomogeneous magnetic field profile that, we believe, captures all aspects of the physics involved. Models used before vary from a representation of the magnetic dot by a perfect dipole [87] to a magnetic field profile calculated numerically for an infinitely thin magnetic disk [88]. To obtain a better insight we start first with a simple step-like field model and subsequently investigate the more complicated real magnetic field profiles, which we obtained numerically.

Theoretical studies have predicted that in mesoscopic disks surrounded by an insulating media three kinds of superconducting states can exist - giant vortex (a circular symmetric state with a fixed value of angular momentum), multi-vortex state (a collection of single vortices which can be obtained as a linear combination of giant vortices with different angular momentum), and ring-shaped vortex states [115, 116] with larger energy than giant and multi-vortex states. The ring-shaped two-dimensional vortex states have a cylindrically symmetric magnetic field profile and they are different from the ring-vortices which are e.g. found in three-dimensional superfluid liquid helium. In what we present here, we observe giant vortex states and first-order transitions between them [69, 106], and for sufficiently large disks, multi-vortex structures, which are the analogue of the Abrikosov flux-line lattice in a bulk superconductor. The latter results not only from a mixture of giant vortex states but also from giant-ring vortex combinations as well. The latter one may even lead to an off-center location of a single vortex or multi-vortices. Moreover, with changing the strength of the field there is a transition between giant-giant and giant-ring multi-vortex states. Increasing the step height of the magnetic field profile we found re-entrant behavior, i.e., transition from giant to multi-vortex state and back to the giant vortex state before superconductivity is destroyed [45]. We found that for sufficiently large magnetic disks vortex/anti-vortex structures can be formed (giant–multi anti-vortex state). In order to investigate these different vortex structures we use the method proposed by Schweigert *et*

*al.* [45] and Palacios [108, 109], with its semi-analytical extensions of Ref. [115] to determine the stability of the different multi-vortex configurations. In particular, the analysis of Ref. [115] showed that in a superconducting disk the ring-shaped vortices are unstable in the presence of a homogeneous magnetic field.

Our analysis is within the framework of the phenomenological Ginzburg-Landau (GL) theory. Although this theory has only a firm mathematical derivation in a narrow range of magnetic field close to the superconducting-normal state boundary, it has been found that it gives also very good results deep inside the superconducting phase diagram [69, 106].

This chapter is organized as follows. In the first section we present our theoretical model. Then we discuss the giant vortex states and study the influence of a step magnetic field profile, with zero average which is centered at the disk or has a ring symmetry, on the superconducting state. These step profiles are limiting cases of the actual experimentally realizable profiles. In the following section, the stability of multi-vortex states and transitions between them are investigated. In the Appendix we give the analytical approach/solution to this subject. The excitement in this study is shown through different $H_{in} - R$ phase diagrams in Sec. V, where $H_{in}$ is the magnitude of the magnetic field profile and $R$ represents the radius (of superconducting disk, magnetic dot, current loop, etc.). In last sections, we present the results of our approach applied to a superconducting disk in the presence of an experimentally realizable real magnetic dot and current loop field profile. We then extend our study to investigate the influence of an additional homogeneous background magnetic field $H_{ext}$. At the end, we will comment on the recent experimental results, in the light of our calculations and the constructed $H_{ext} - T$ diagrams.

## 3.2 THEORETICAL MODEL

We consider a mesoscopic superconducting disk with radius $R$ and thickness $d$ surrounded by vacuum. The external magnetic field $\vec{H} = (0, 0, H)$ is directed normal to the disk plane. In the following chapter we investigate two different magnetic field profiles: 1) step-like magnetic field in the center of the disk, and 2) a ring step-like magnetic field profile with inner radius of the ring $R_d$. The magnetic field strengths of the profile (Fig. 3.1) are chosen such that the total magnetic flux equals zero. These models should correspond to the magnetic field of a perpendicular magnetized magnetic dot placed in the center of the disk on top of the superconductor, and the magnetic field due to a current loop placed on the superconductor, respectively. We assume that the superconductor will not alter the magnetic state of the ferromagnetic disk. We have to solve the system of two coupled non-linear GL equations which determine the distribution of both the superconducting order parameter, $\Psi(\vec{r})$, and the

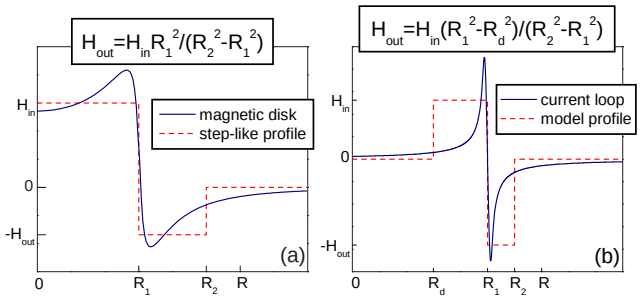


FIG. 3.1: The magnetic field profile of (a) a magnetic disk (solid curve) and the corresponding model step profile (dashed curve), and (b) a current loop (solid curve) and its corresponding model profile (dashed curve).

magnetic field (or vector potential $\vec{A}(\vec{r})$) inside and outside the superconductor

$$\frac{1}{2m}\left(-i\hbar\vec{\nabla}-\frac{2e}{c}\vec{A}\right)^2\Psi=-\alpha\Psi-\beta\Psi\left|\Psi\right|^2, \tag{3.1}$$

$$\vec{\nabla}\times\vec{\nabla}\times\vec{A}=\frac{4\pi}{c}\vec{j}, \tag{3.2}$$

where the density of the superconducting current $\vec{j}$ is given by

$$\vec{j}=\frac{e\hbar}{im}\left(\Psi^*\vec{\nabla}\Psi-\Psi\vec{\nabla}\Psi^*\right)-\frac{4e^2}{mc}\left|\Psi\right|^2\vec{A}. \tag{3.3}$$

Here $\vec{r}=(\vec{\rho},z)$ is the three-dimensional position in space. Due to the circular symmetry of the disk we use cylindrical coordinates: $\rho$ is the radial distance from the disk center, $\varphi$ is the azimuthal angle and the $z$-axis is taken perpendicular to the disk plane, where the disk lies between $z=-d/2$ and $z=d/2$.

Eqs. (3.1-3.3) has to be supplemented by boundary conditions (BC) for $\Psi(\vec{r})$ and $\vec{A}(\vec{r})$:

$$\left(-i\hbar\vec{\nabla}-\frac{2e}{c}\vec{A}\right)\Psi\Big|_n=0, \tag{3.4}$$

where the subscript $n$ denotes the component normal to the disk surface. The boundary condition for the vector potential has to be taken far away from the disk where the magnetic field becomes equal to the external field $H$

$$\vec{A}\Big|_{r\longrightarrow\infty}=0. \tag{3.5}$$

Using dimensionless variables and the London gauge $div\ \vec{A}=0$ we can rewrite the system of equations (3.1-3.3) and BC (3.4) in the following form

$$\left(-i\vec{\nabla}-\vec{A}\right)^2\psi=\psi-\psi\left|\psi\right|^2, \tag{3.6}$$

$$-\kappa^2\nabla^2\vec{A} = \frac{1}{2i}\left(\psi^*\vec{\nabla}\psi - \psi\vec{\nabla}\psi^*\right) - |\psi|^2\vec{A}, \tag{3.7}$$

$$\left(-i\vec{\nabla} - \vec{A}\right)\psi\Big|_n = 0. \tag{3.8}$$

Here all distances are measured in units of the coherence length $\xi = \hbar/\sqrt{2m\,|\alpha|}$, the order parameter in $\Psi_0 = \sqrt{|\alpha|/\beta}$, the vector potential in $c\hbar/2e\xi$, $\kappa = \lambda/\xi$ is the GL parameter, and $\lambda = c\sqrt{m/\pi}/4e\Psi_0$ is the London penetration depth. We measure the magnetic field in $H_{c2} = c\hbar/2e\xi^2 = \kappa\sqrt{2}H_c$, where $H_c = \sqrt{4\pi\alpha^2/\beta}$ is the thermodynamical critical field.

The free energy of the superconducting state, measured in $F_0 = H_c^2V/8\pi$ units, is determined by the expression

$$F = \frac{2}{V}\left\{\int dV\left[-|\psi|^2 + \frac{1}{2}|\psi|^4 + \left|-i\vec{\nabla}\psi - \vec{A}\psi\right|^2 + \kappa^2\left(\vec{h}\,(\vec{r}) - \vec{H}_0\right)^2\right]\right\}, \tag{3.9}$$

with the local magnetic field

$$\vec{h}\,(\vec{r}) = \vec{\nabla}\times\vec{A}(\vec{r}).$$

We restrict ourselves to sufficiently thin disks such that $d \ll \xi, \lambda$. In this case, to a first approximation, the magnetic field due to the circulating superconducting currents may be neglected and the total magnetic field equals the external one $\vec{H}_0$. Within this approximation we have to solve only the first GL equation (3.6) with $\vec{A} = \vec{A}_0$, where $\vec{H}_0 = \vec{\nabla}\times\vec{A}_0$. One should notice that in this approach, for different cases, we change only the vector potential profile $\vec{A}_0$. For our step profile

$$H_0\,(\rho) = \begin{cases} 0, & 0 \le \rho \le R_d, \\ H_{in}, & R_d \le \rho \le R_1, \\ -H_{out}, & R_1 \le \rho \le R_2, \\ 0, & R_2 \le \rho \le R. \end{cases}, \tag{3.10}$$

the vector potential is given by

$$A_0\,(\rho) = \begin{cases} 0, & 0 \le \rho \le R_d, \\ \frac{H_{in}}{2}\left(\rho - \frac{R_d^2}{\rho}\right), & R_d \le \rho \le R_1, \\ \frac{H_{in}}{2\rho}\left(R_1^2 - R_d^2\right) - \frac{H_{out}}{2}\left(\rho - \frac{R_1^2}{\rho}\right), & R_1 \le \rho \le R_2, \\ 0, & R_2 \le \rho \le R. \end{cases}, \tag{3.11}$$

where $H_{in}$ describes the positive step and $H_{out} = H_{in}(R_1^2 - R_d^2)/(R_2^2 - R_1^2)$ determines the value of the negative step (see Fig. 3.1, and the Appendix).

First, we determine the $z$-dependence of $\psi\,(\vec{r})$. Representing the order parameter as a series over cosines $\psi\,(\vec{r}) = \sum_{k=0}^{\infty}\psi_k(\vec{\rho})\cos\,(k\pi z/d)$ and using the same BC ( 3.8) at the disk sides ($z = \pm d/2$) and using the first GL equation

(3.1), one can verify that the uniform part of the order parameter, i.e. the $k = 0$ term, gives the main contribution for $(\pi\xi/d)^2 >> 1$. Therefore, we may assume that the order parameter is uniform along the $z$ direction of the disk and average the first GL equation over the disk thickness. After this averaging and for fixed value of the angular momentum it leads to $\psi(\vec{\rho}) = f(\rho)\exp(iL\varphi)$, and the problem for $f(\rho)$ is reduced to a one dimensional problem, like in Ref. [69]:

$$-\frac{1}{\rho}\frac{\partial}{\partial\rho}\rho\frac{\partial f}{\partial\rho} + \left\langle\left(\frac{L}{\rho} - A\right)^2\right\rangle f = f\left(1 - f^2\right), \tag{3.12}$$

and for the vector potential

$$-\kappa^2\left(\frac{\partial}{\partial\rho}\frac{1}{\rho}\frac{\partial\rho A}{\partial\rho} + \frac{\partial^2 A}{\partial z^2}\right) = \left(\frac{L}{\rho} - A\right) f^2\theta(\rho/R)\theta(2\,|z|\,/d), \tag{3.13}$$

where the function $\theta(x) = 1$ $(x < 1)$, 0 $(x > 1)$, and $R$, $d$ are the dimensionless disk radius and thickness, respectively. The brackets $\langle ...\rangle$ refer to averaging over the disk thickness.

## 3.3 GIANT-VORTEX STATES

The giant vortex state has cylindrical symmetry and consequently the order parameter can be written as $\psi(\vec{\rho}) = f(\rho)\exp(iL\varphi)$. The stable states are obtained in the following way. From the *linearized* GL equation we find $f(\rho)$ up to a multiplying constant. This function is then inserted into the free energy expression (3.9) which after minimization determines: (i) the constant in $f(\rho)$, and (ii) the energy value corresponding to the stable state. It can be shown that, for the case of giant vortex states, the present approach and the one of Ref. [69], which was based on a solution of the non-linear GL equation, result in same functional $F(H_{in})$ dependence.

The linearized GL equation for $f(\rho)$ takes the form

$$\hat{L}f = 0, \quad \hat{L} = -\frac{1}{\rho}\frac{\partial}{\partial\rho}\rho\frac{\partial}{\partial\rho} + \left(\frac{L}{\rho} - A_0\right)^2 - 1. \tag{3.14}$$

The superconducting state starts to develop when the minimal eigenvalue of the operator $\hat{L}$ becomes negative. For the zero angular momentum state, the normal state transforms to the superconducting one with decreasing magnetic field below the nucleation field $H_{nuc}$. For nonzero angular momentum, the superconducting state appears when we cross either the lower $H_{nuc,l}$ or the upper $H_{nuc,u}$ critical magnetic field which depends on the disk radius. The eigenvalues and eigenfunctions of the $\hat{L}$ operator are found from

$$\hat{L}f_{n,L}(\rho) = \Lambda_{n,L}f_{n,L}(\rho), \tag{3.15}$$

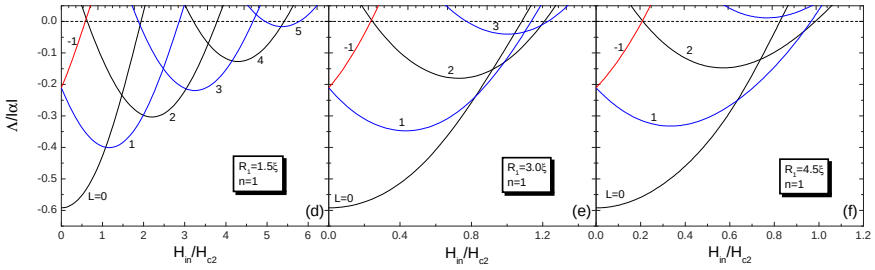


FIG. 3.2: The magnetic field dependence of the lowest eigenvalues of the linearized first GL equation for different angular momenta $L$ and for (a)$R_1/\xi = 1.5$, (b) $R_1/\xi = 3.0$, and (c) $R_1/\xi = 4.5$. The corresponding curves for the first radial excited state, i.e. $n = 1$, are presented in figures (d-f). The top axis gives the flux through the positive magnetic field region in units of the flux quantum.

where $f_{L,n}(\rho)$ satisfies $\rho(\partial f/\partial\rho)|_{\rho=0} = 0$ at the disk center. The index $n = 1, 2, ...$ enumerates the different states for the same $L$-value.

In general, the eigenfunctions of Eq. (3.15) can be obtained analytically in the case of our step magnetic field profile. We present the complete calculation in the Appendix for both considered cases. Alternatively, we solve Eq. (3.15) numerically through the finite difference technique. We put the order parameter on a space grid and find numerically the eigenfunctions and eigenvalues of the operator $\hat{L}$ using the Householder technique.

We start our analysis with the magnetic field profile shown in Fig. 3.1. First, we consider a magnetic dot on top of the center of the disk, i.e. with $R_d = 0$, and $R_2 = R = 6.0\xi$ and study the influence of $R_1$, i.e. the width of the positive field region, on the superconducting state.

The magnetic field dependence of $\Lambda$ for different angular momenta $L$ is shown in Figs. 3.2(a-c) for the lowest radial state, i.e. $n = 0$, and in Figs. 3.2(d-f) for the first radial state, i.e. $n = 1$ for three different values of $R_1$. The top axis shows the flux corresponding to the positive magnetic field region $\phi_{in} = H_{in}\pi R_1^2$, which in dimensionless units becomes $\phi_{in}/\phi_0 = (H_{in}/2H_{c2})(R_1/\xi)^2$ where $\phi_0 = ch/2e$ is the quantum of flux. All numerical calculations were done

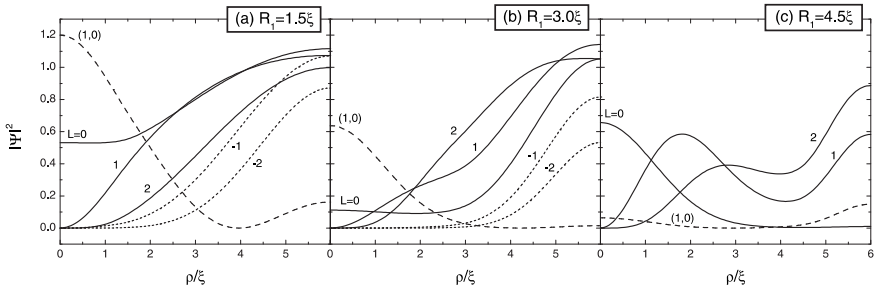


FIG. 3.3: The Cooper pair density for the giant vortex states with angular momenta $L = 0, 1, 2$ (solid curves), the antivortex states $L = -1, -2$ (dotted curves) and the ring vortex state $n = 1$, $L = 0$ (dashed curve) at the magnetic field $H_{in} = 0.75H_{C2}$ for (a) $R_1/\xi = 1.5$, (b) $R_1/\xi = 3.0$, and (c) $R_1/\xi = 4.5$.

for a disk thickness $d/\xi = 0.1$ which is within the thin disk approximation. The negative $L$ values (red curves in Fig. 3.2) correspond to "anti-vortices" in conventional superconductors. The thin horizontal line gives the $\Lambda = 0$ level. From Fig. 3.2 one notices that with increasing $R_1$: 1) the eigenvalues $\Lambda$ of the states with the same $L$ become more negative; 2) the magnetic field range over which solutions of Eq. (3.14) can be found decreases; 3) the number of possible solutions decreases; and 4) the $\Lambda(H_{in})$ dependences become more parabolic. The latter can be explained by the fact that increasing $R_1$ corresponds to a more homogeneous magnetic field profile inside the disk, i.e. we reach the case considered in Refs. [69, 115].

For small $R_1$ the curves $L$ and $L+1$ anti-cross for sufficiently large $L$ values and consequently the low vorticity states have lower energy even with increasing strength of the magnetic field profile. E.g. for $R_1/\xi = 1.5$ this occurs when $L > 4 = L^*$ and for $R_1/\xi = 3.0$ when $L > 5 = L^*$. Notice that the slope of $\Lambda$ for the $L > L^*$ curves is substantially smaller than for the $L \leq L^*$ curves in the high field region. Notice also that the $n = 1$ states have a higher $\Lambda$ value than the $n = 0$ states and their energy is also larger than those of the anti-vortex states for the same vorticity.

In Figs. 3.3(a-c) the radial dependence of the superconducting density $|\psi|^2$ is shown for $|L| < 3$ at $H_{in} = 0.75H_{c2}$ for the corresponding profiles of Fig. 3.2. Notice that, with increasing $R_1$, the Cooper-pair density near the edge of the sample becomes more non-homogeneous. The $|L| \neq 0$ states have a vortex sitting in the center of the disk, i.e. $\psi(\rho = 0) = 0$, which becomes larger with increasing $|L|$. For the situation of Fig. 3.3(c) there is a narrow, very negative magnetic field region of $H_{out}/H_{c2} = 0.9643$ in the region $4.5 < \rho/\xi < 6.0$ which leads to a considerable suppression of the Cooper pair density. For example, the $L = 0$ vortex state, i.e. the Meissner state, has a strongly reduced Cooper pair density for $\rho/\xi > 1$. For the excited state $(n, L) = (1, 0)$ (dashed curves in

Fig. 3.3) the order parameter vanishes inside the disk and a ring-shaped node in the wave function $\psi$ is formed [115, 116] which leads to a ring-like vortex.

The eigenvalues $\Lambda$ determine the free energy $F$ of the giant vortex state. For the giant vortex state we consider only states which lie below the $F = 0$ level. In this approximation the order parameter is

$$\psi\left(\vec{\rho}\right) = \left(-\Lambda \frac{I_2}{I_1}\right)^{1/2} f_{n,L}\left(\rho\right) \exp\left(iL\varphi\right), \tag{3.16}$$

and the minimal energy value is

$$F = -\Lambda^2 \frac{2\pi d}{V} \frac{I_2^2}{I_1}, \tag{3.17}$$

where

$$I_1 = \int_0^R \rho d\rho \; f_{n,L}^4\left(\rho\right), \quad I_2 = \int_0^R \rho d\rho \; f_{n,L}^2\left(\rho\right).$$

The dependence of the free energy on the magnetic field strength of the inner core of the magnetic field profile, $H_{in}$, is shown in Figs. 3.4(a-c) for the angular momenta $|L| < 11$ for different values of $R_1$. The free energy is expressed in units of $F_0 = H_C^2 V/8\pi$. The highest value of vorticity in this disk is $L = 15$ (see Figs. 3.2(a-c)). From a comparison of the magnetic field dependence of $F\left(H_{in}\right)$ for $R_1/\xi = 1.5$ (Fig. 3.4(a)) with the one for $R_1/\xi = 4.5$ (Fig. 3.4(c)) we clearly observe the reduction of superconductivity and the reduction of the maximal possible vorticity with increasing $R_1$. The envelope of the lowest parts of the curves in Fig. 3.4 represents the field dependence of the ground state energy. Notice that the increase of the width of the positive magnetic field region leads to an increase of the energy of the ground state. With increasing applied field the $L \longrightarrow L + 1$ vortex transitions take place at the field where the corresponding curves cross (for example, the $0 \longrightarrow 1$ transition occurs at $H_{in} = 0.8705 H_{c2}$ for $R_1/\xi = 1.5$). The crossing points are shifted towards lower field values when increasing $R_1$. The $L \longrightarrow L + 1$ transitions are of first order and lead to jumps in the magnetization of the sample. Notice that the positive flux captured in the superconducting disk for different $L$-states is not quantized. This is made very clear in the $\phi_{in} - R_1$ diagram presented in Fig. 3.4(d) which shows the ground state vortex configurations. Notice that the flux in the positive magnetic field region has to increase for more than one flux quantum $\phi_0$ before the vorticity of the superconducting state can increase for one unit. A similar phenomena was observed earlier for mesoscopic disks and rings in a homogeneous magnetic field [97]. Notice also that for higher $L$ values quantization is slowly restored, and $\Delta\phi$ decreases with enlarging $R_1$, i.e. the radius of the positive field region.

Following our assumption that field inside the superconductor equals the external one, we obtain the expression for the superconducting current density

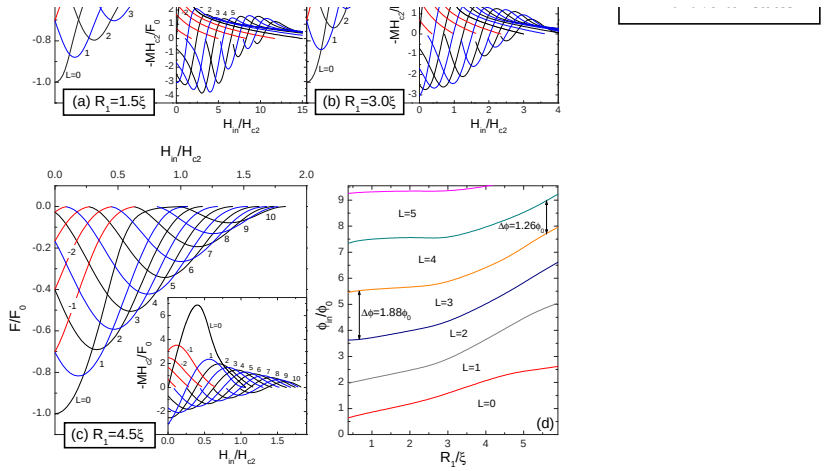


FIG. 3.4: The free energy of the giant vortex states with different angular momenta $L$ as a function of the applied magnetic field in the positive region for (a) $R_1/\xi = 1.5$, (b) $R_1/\xi = 3.0$, and (c) $R_1/\xi = 4.5$. Only the states with $|L| \leq 10$ are shown. The insets depict the magnetic field dependence of the disk magnetization for the ground giant vortex state for different values of the $R_1/\xi$ parameter. Figure (d) gives the positive flux captured in the superconducting disk for the different $L$-ground states as the ground state as function of $R_1/\xi$.

(see Ref. [115]):

$$j_{n,L} = \frac{\Lambda_{n,L} B_{n,L}}{A_{n,L}} \left(\frac{L}{\rho} - A_0\right) f_{n,L}^2(\rho) \tag{3.18}$$

where $\Lambda_{n,L}$ is determined by Eq. (3.15), $A_0$ represents the vector potential of the applied field and

$$A_{n,L} = \frac{2\pi d}{V} \int_0^R \rho d\rho \; f_{n,L}^4(\rho)\,, \; B_{n,L} = \frac{2\pi d}{V} \int_0^R \rho d\rho \; f_{n,L}^2(\rho)\,.$$

The magnetic field due to the supercurrents, neglected in our first order approximation, is calculated from

$$\vec{\nabla} \times \vec{H_{sc}} = \frac{1}{\kappa^2} \vec{j}. \tag{3.19}$$

Since the supercurrent has only an azimuthal component, and, is situated only in the superconductor plane, the $\rho$ component of $\vec{H_{sc}}$ can be neglected. Consequently, we obtain

$$H_{sc}(\rho) = -\frac{1}{\kappa^2}\int j_\varphi(\rho)d\rho, \tag{3.20}$$

and the magnetization of the superconductor is then defined as the magnetic field expelled from the superconductor.

$$M = \int \frac{H_{total} - H_0}{8\pi} dV = \frac{d}{4}\int_0^R H_{sc}(\rho)\rho d\rho, \tag{3.21}$$

where $H_0$ denotes the applied magnetic field, and $d$ is the disk thickness.

The corresponding $M\,(H_{in})$ curves are given as insets in Figs. 3.4(a-c). The phase transition from the superconducting to the normal state is of second order (all curves $F\,(H_{in})$ reach the $F = 0$ line with zero derivative). The curves $F\,(H_{in})$ in Fig. 3.4 which are situated above the ground state energy correspond to metastable giant vortex states. With increasing applied field the transition from the Meissner state ($L = 0$) to the normal state goes through a set of consecutive first order transitions between the $L$ and $L+1$ giant vortices which is finished by a second order transition to the normal state.

Our next step was to fix the magnetic field profile (we took $R_d/\xi = 0.0$, $R_1/\xi = 4.5$, $R_2/\xi = 6.0$) and enlarge the disk radius $R$. In Figs. 3.5(a-b) the radial dependence of the superconducting density $|\psi|^2$ is shown for $|L| < 3$ at $H_{in} = 0.75H_{c2}$ and for a superconducting disk of radius $R/\xi = 9.0$, and 12.0, respectively. One can see that, even for $L = 0$, superconductivity in the center of the disk is destroyed, which is opposite to the homogeneous magnetic field case where $|\Psi|^2$ is maximal at $\rho = 0$ [69]. The shape of the $L = 0$ curve changes drastically and this occurs already for small enlargement of the disk. This transition is shown in Fig. 3.6(a). By increasing $R/\xi$ from 6.1 to 6.5 the

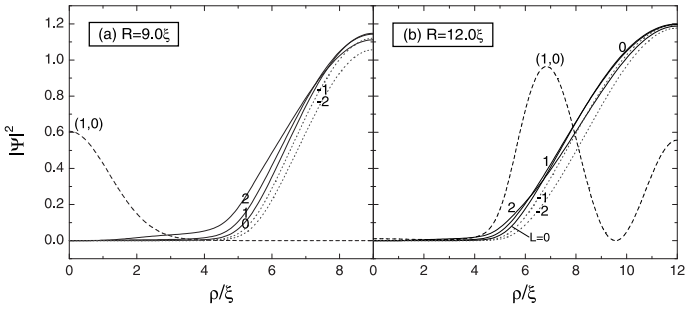


Fig. 3.5: The Cooper pair density for the giant vortex states with angular momenta $L = 0, 1, 2$ (solid curves), the anti-vortex states $L = -1, -2$ (dotted curves) and the ring-shaped vortex state $n = 1$, $L = 0$ (dashed curve) at the magnetic field $H_{in} = 0.75H_{C2}$ for (a) $R/\xi = 9.0$, and (b) $R/\xi = 12.0$.

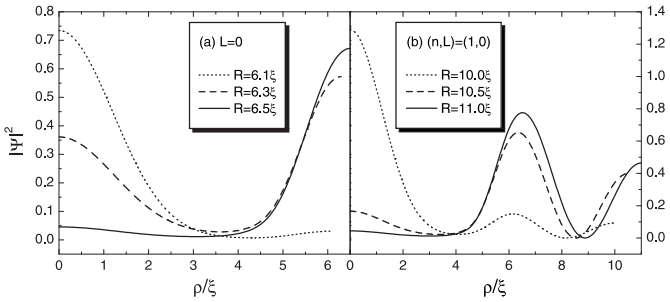


FIG. 3.6: The Cooper pair density for (a) the Meissner state ($L = 0$), and (b) the ring-shaped vortex state $n = 1$, $L = 0$ at the magnetic field $H_{in} = 0.75H_{c2}$ for different sizes of the superconducting disk.

Cooper pair density in the center of the superconducting disk decreases from 0.73 to 0.03. Furthermore, in Fig. 3.5(b) we see also qualitative changes in the Cooper pair density of the excited state $(n, L) = (1, 0)$ (dashed curve). Now the order parameter vanishes twice inside the disk and a double ring-like vortex is formed. This transition is shown in Fig. 3.6(b) with increasing disk size from $R/\xi = 10.0$ to 11.0.

The dependencies of the free energy on the magnetic field $H_{in}$ for different sizes of the superconducting disk are shown in Figs. 3.7(a-d). Notice that there are large differences in comparison with the previous cases. We still have the $L \longrightarrow L + 1$ transitions, which are of first order and which lead to jumps in the magnetization of the sample (see Figs. 3.8(a-c)). With increase of the applied field the transition from the Meissner state ($L = 0$) to the vortex state goes through consecutive first order transitions and is finished by a first order transition *back to the* $L = 0$ *state*, sometimes with an intermediate $L = 1$ state. For $R/\xi = 9.0$ we have $0 \to 1 \to 2 \to 3 \to 1 \to 0$ transitions, for $R/\xi = 12.0$ we have $0 \to 1 \to 2 \to 1 \to 0$, and for $R/\xi = 18.0$ only $0 \to 1 \to 0$. Moreover, for a sufficiently large disk (see Fig. 3.7(d) which corresponds practically to the $R/\xi \to \infty$ situation) we have no first order transitions but only the Meissner state as the ground state. The reason is that for $R/\xi \to \infty$ the non-zero magnetic field region is limited (relatively) to a small area and we can always define a circle with radius $\rho$ sufficiently large where the superconducting current is zero and, consequently one must have $L = 0$. But, this Meissner state is qualitatively different from the "usual" one. The radial distribution of the Cooper pair density is extremely inhomogeneous and superconductivity is strongly suppressed in the interior of the disk (see Figs. 3.5(b) and 3.6(a)). Notice that this kind of *re-entrant* behavior differs from those previously found in rings with large radius in homogeneous magnetic field (multi-vortex($L$)→ giant($L$)→multi-vortex($L + 1$)→...)[97] or in disks with enhanced surface superconductivity (giant($L$)→ multi-vortex($L$)→giant($L$))[115]. In our case, we

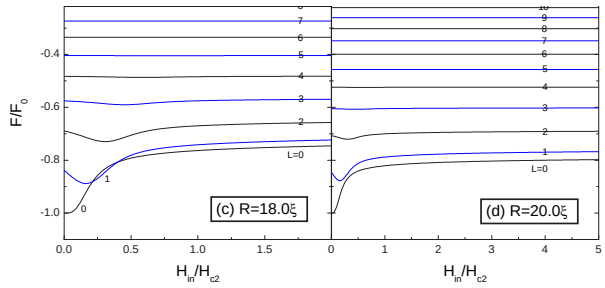


FIG. 3.7: The free energy of the giant vortex states with different angular momenta $L$ as a function of the applied magnetic field for (a) $R/\xi = 9.0$, (b) $R/\xi = 12.0$, (c) $R/\xi = 18.0$, and (d) $R/\xi = 20.0$, with $R_1/\xi = 4.5$, and $R_2/\xi = 6.0$. Vortex states with odd vorticity are denoted by blue lines, for clarity. Red curves represent the energy of the anti-vortex states.

have a re-entrance of the *total vorticity* and it happens due to the spatial inhomogeneity of the magnetic field.

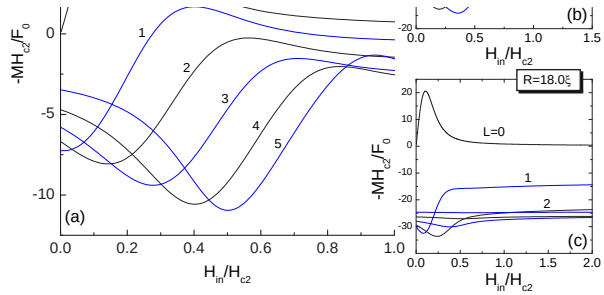


FIG. 3.8: The magnetic field dependence of the disk magnetization for the ground giant vortex state corresponding to the states in Fig. 3.7, for (a) $R/\xi = 9.0$, (b) $R/\xi = 12.0$, and (c) $R/\xi = 18.0$.

## 3.4 MULTI-VORTEX STATES

It is well known that for sufficiently large disks the giant vortex state can break up into multi-vortices [45, 108, 109]. In our analysis, we considered different field profiles and disk geometries to investigate the properties of this transition. For smaller disks, the confinement effect dominates and we found that only the giant vortex states are stable and possible multi-vortex states, if they exist, have always larger energies. In order to investigate such structures in our case we use the method proposed by Schweigert *et al.* [45] and Palacios [108, 109] and extend it to determine the stability of the different multi-vortex configurations as proposed in Ref. [115]. Following Refs. [45, 108, 117] the order parameter of the multi-vortex state is written as a linear combination of eigenfunctions of the linearized GL equation (3.14)

$$\psi\left(\vec{\rho}\right)=\sum_{L_j=0}^{L}\sum_{n=0}^{\infty}C_{n,L_j}f_{n,L_j}\left(\rho\right)\exp\left(iL_j\varphi\right), \tag{3.22}$$

where $L$ is, in the homogeneous magnetic field case, the value of the effective total angular momentum which is equal to the number of vortices in the disk, and $n$ enumerates the different radial states for the same $L_j$. Later on, we will see that for our inhomogeneous magnetic field case the assignment of the total vorticity can be tricky.

Substituting (3.22) in the free energy expression (3.9) we obtain $F$ as a function of the complex parameters $\{C_{n,L_j}\}$. Minimization of $F$ with respect to these parameters allows us to find the equilibrium vortex configurations, and to determine their stability. We use the procedure described in Refs. [115, 117] with full consideration of combinations of vortex configurations with different radial states.

We begin our analysis with states built up by only two components in Eq. (3.22). This brings quantitative bounds to our calculation but, nevertheless, facilitates the physical insight into the problem and will give the correct qualitative behavior of the system under consideration. As we will see later, the accounting of more components in Eq. (3.22) brings only minor quantitative corrections to the results of the two-component analysis.

The free energy of a two component state built out of states $(n_1, L_1)$ and $(n_2, L_2)$ is

$$\begin{aligned}F &= C_{n_1,L_1}^4A_{n_1,L_1}+C_{n_2,L_2}^4A_{n_2,L_2}+4C_{n_1,L_1}^2C_{n_2,L_2}^2A_{n_1,n_2,L_1,L_2}\\ &\quad +2\Lambda_{n_1,L_1}C_{n_1,L_1}^2B_{n_1,L_1}+2\Lambda_{n_2,L_2}C_{n_2,L_2}^2B_{n_2,L_2},\end{aligned} \tag{3.23}$$

where

$$A_{n_i,L_i}=\frac{2\pi d}{V}\int_0^R\rho d\rho\ f_{n_i,L_i}^4\left(\rho\right),$$

$$A_{n_1,n_2,L_1,L_2} = \frac{2\pi d}{V}\int\limits_0^R \rho d\rho\ f^2_{n_1,L_1}(\rho)\, f^2_{n_2,L_2}(\rho)\,,$$

$$B_{n_i,L_i} = \frac{2\pi d}{V}\int\limits_0^R \rho d\rho\ f^2_{n_i,L_i}(\rho)\,.$$

One should notice that we leave the possibility of combination of states with different radial states, i.e. $n_1$ and $n_2$. Although, in general, $C_{n_i,L_i}$ is a complex number, for our two component state $C_{n_i,L_i}$ is a real number. Minimization of Eq. (3.23) with respect to $C_{n_1,L_1}$ and $C_{n_2,L_2}$ gives for the multi-vortex states:

$$C^{(0)}_{n_1,L_1} = \pm\left(\frac{-\Lambda_{n_1,L_1}A_{n_2,L_2}B_{n_1,L_1} + 2\Lambda_{n_2,L_2}A_{n_1,n_2,L_1,L_2}B_{n_2,L_2}}{A_{n_1,L_1}A_{n_2,L_2} - 4A^2_{n_1,n_2,L_1,L_2}}\right)^{1/2}, \quad (3.24)$$

$$C^{(0)}_{n_2,L_2} = \pm\left(\frac{-\Lambda_{n_2,L_2}A_{L_1,n_1}B_{n_2,L_2} + 2\Lambda_{L_1,n_1}A_{n_1,n_2,L_1,L_2}B_{L_1,n_1}}{A_{n_1,L_1}A_{n_2,L_2} - 4A^2_{n_1,n_2,L_1,L_2}}\right)^{1/2},$$

and inserting these expressions into Eq. (3.23) leads to *the energy of the multi-vortex state*

$$\begin{aligned} F_{n_1,n_2,L_1,L_2} = {} & \frac{-\Lambda^2_{n_1,L_1}A_{n_2,L_2}B^2_{n_1,L_1} - \Lambda^2_{n_2,L_2}A_{n_1,L_1}B^2_{n_2,L_2}}{A_{n_1,L_1}A_{n_2,L_2} - 4A^2_{n_1,n_2,L_1,L_2}} \\ & + \frac{4\Lambda_{n_1,L_1}\Lambda_{n_2,L_2}A_{n_1,n_2,L_1,L_2}B_{n_1,L_1}B_{n_2,L_2}}{A_{n_1,L_1}A_{n_2,L_2} - 4A^2_{n_1,n_2,L_1,L_2}} \end{aligned} \quad (3.25)$$

The corresponding conditions for the stability of the vortex state are

$$\frac{\partial^2 F}{\partial C^2_{n_1,L_1}} = \frac{8A_{n_1,L_1}\left(-\Lambda_{n_1,L_1}A_{n_2,L_2}B_{n_1,L_1} + 2\Lambda_{n_2,L_2}A_{n_1,n_2,L_1,L_2}B_{n_2,L_2}\right)}{A_{n_1,L_1}A_{n_2,L_2} - 4A^2_{n_1,n_2,L_1,L_2}} > 0,$$

$$\frac{\partial^2 F}{\partial C^2_{n_2,L_2}} = \frac{8A_{n_2,L_2}\left(-\Lambda_{n_2,L_2}A_{n_1,L_1}B_{n_2,L_2} + 2\Lambda_{n_1,L_1}A_{n_1,n_2,L_1,L_2}B_{n_1,L_1}\right)}{A_{n_1,L_1}A_{n_2,L_2} - 4A^2_{n_1,n_2,L_1,L_2}} > 0,$$

$$\begin{aligned} & \frac{\partial^2 F}{\partial C^2_{n_1,L_1}}\cdot\frac{\partial^2 F}{\partial C^2_{n_2,L_2}} - \left(\frac{\partial^2 F}{\partial C_{n_1,L_1}\partial C_{n_2,L_2}}\right)^2 \\ & = \frac{64\left(-\Lambda_{n_1,L_1}A_{n_2,L_2}B_{n_1,L_1} + 2\Lambda_{n_2,L_2}A_{n_1,n_2,L_1,L_2}B_{n_2,L_2}\right)}{A_{n_1,L_1}A_{n_2,L_2} - 4A^2_{n_1,n_2,L_1,L_2}} \\ & \times\left(-\Lambda_{n_2,L_2}A_{n_1,L_1}B_{n_2,L_2} + 2\Lambda_{n_1,L_1}A_{n_1,n_2,L_1,L_2}B_{n_1,L_1}\right) > 0. \end{aligned} \quad (3.26)$$

In our analysis we investigated the influence of the width of the positive field region and radius of the disk on the phase diagram, and especially on the

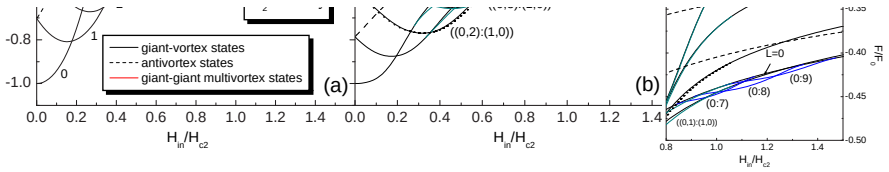


FIG. 3.9: The free energy of the giant vortex states with different angular momenta $L$ as a function of the external magnetic field for (a) $R_1/\xi = 5.25$, $R_2/\xi = R/\xi = 6.0$, and (b) $R_1/\xi = 4.5$, $R_2/\xi = 6.0$, $R/\xi = 9.0$. The inset shows an enlargement of the part of this figure. Dashed curves illustrate the energy of the anti-vortex states. In (a) red curves represent the giant-giant multivortex states while in (b) cyan curves depict the free energy of the giant-ring multi-vortex states, and the blue curves correspond to the giant-giant (giant–multi anti-vortex) states. Brown solid curve illustrates the energy of the ring vortex state, i.e. $(n, L) = (1, 0)$

stability of the multi-vortex states. For small values of $R_1/\xi$ these multi-vortex states are always metastable. However, with enlarging $R_1/\xi$ these states can obtain lower energy. The energies of the equilibrium vortex states are plotted in Fig. 3.9(a) for $R_1/\xi = 5.25$ and $R_2/\xi = R/\xi = 6.0$ and in Fig. 3.9(b) for $R_1/\xi = 4.5$ and $R_2/\xi = 6.0$ with a larger disk radius $R/\xi = 9.0$. The giant vortex states are given by solid curves, anti-vortex states by dashed and the multi-vortex states (colored curves) by $(L_1 : L_2)$, i.e. the angular momentum values they are composed of. As expected, when enlarging the disk, multi-vortex states become more stable and, moreover in Fig. 3.9(b), we observe the existence of multi-vortices as a combination of a giant and a ring-like vortex. These states have surprisingly low energy and become the ground state for specific range of magnetic field. Furthermore, when increasing the field, we observe a phase transition between this giant-ring and giant-giant multi-vortex states, when another type of multi-vortices becomes the ground state. The giant-ring multi-vortex states with lowest energy are given in Fig. 3.9(b) by the quantum numbers $((n_1, L_1) : (n_2, L_2))$. It should be noted that there are many other metastable combinations possible, which are not shown in the figures.

As shown in Fig. 3.9, with increasing $R_1/\xi$ and the size of the superconducting disk the multi-vortices become more stable and they can even become the minimum of the $F\,(C_{n_1,L_1}, C_{n_2,L_2})$ function. We focus our attention to Fig. 3.9(a). The solid and dashed curves represent the giant vortex and anti-vortex states, respectively. The red curves are the energies of the multi-vortices. For example, lets follow the $L = 0$ curve which splits into the $(0 : 4)$ multi-vortex

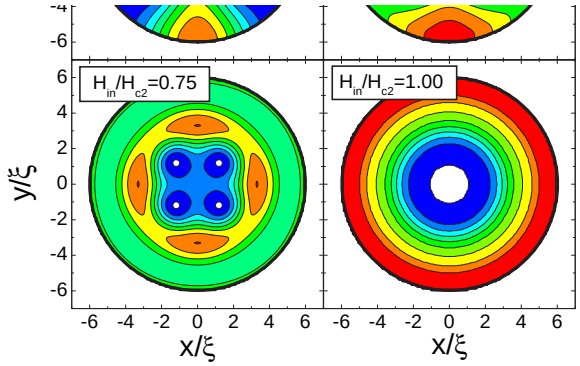


Fig. 3.10: Transition between two giant vortex states shown through the contour plots of the superconducting wave function density for the $(0:4)$ giant-giant multi-vortex state for different values of the magnetic field in the positive field region (corresponding to the magnetization of the dot).

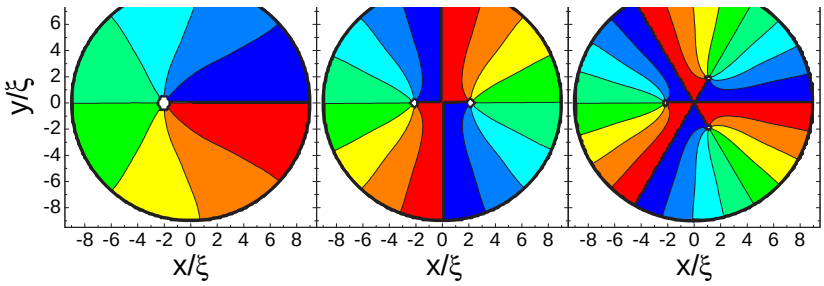


Fig. 3.11: Contour plots of the superconducting density for the ground state and the corresponding phase contour plots (see Fig. 3.9(b)) for different values of the magnetic field in the positive region.

state, at $H_{in}/H_{c2} = 0.28$ and with further increase of the field becomes another giant vortex state, but now with $L = 4$, at $H_{in}/H_{c2} = 1.0$. The concomitant change of the Cooper pair density is illustrated in Fig. 3.10. Vortices enter the disk from the boundary and move to the middle with increasing field, and join into a giant vortex again.

For a fixed magnetic field profile and with increasing size of the superconducting disk, we obtain a variety of different superconducting states. Let us discuss the giant-ring configurations first. We observe transitions between the giant and multi-vortex states with the *same* vorticity. The contour plots of the $|\psi|^2$ distribution for different multi-vortex states as ground states $(((0,1):(1,0))$, $((0,2):(1,0))$, $((0,3):(1,0)))$ are shown in Figs. 3.11(a-c) for a magnetic field profile with $R_1/\xi = 4.5$, $R_2/\xi = 6.0$ and $R/\xi = 9.0$, for different values of $H_{in}$ (red regions correspond to high density and blue regions to low density). The most interesting result we obtain for the $((0,1):(1,0))$ combination. This configuration becomes the ground state configuration for $H_{in}/H_{c2} = 0.75$. Surprisingly, the contour plot of the $|\psi|^2$ distribution is not circular symmetric - there is one vortex positioned off-center. In the lower part of the same figures we give the corresponding contour plots of the phase of the superconducting

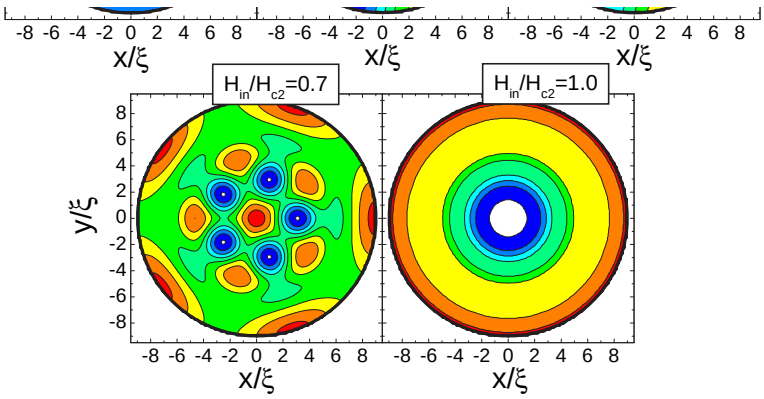


FIG. 3.12: Contourplot of the superconducting density for the $((5,0):(0,1))$ giant-ring multi-vortex state (see Fig. 3.9(b)) for different values of the applied magnetic field.

wave functions. The contour plot of the phase also nicely illustrates the off-center location of the vortex. For the two other cases more vortices are present which are located on a ring centered around the center of the superconducting disk. The giant-ring multi-vortex state can be seen as a transition between $(1,0)$ and $(0,5)$ state (see Fig. 3.9(b)). As function of the magnetic field we start from a ring vortex, for $H_{in}/H_{c2} = 0.03$, this state splits into a giant-ring vortex state, and finally, for $H_{in}/H_{c2} = 0.98$ we obtain a giant vortex state. This remarkable phenomenon is illustrated in Fig. 3.12.

However, giant-giant vortex combinations show completely different behavior. As shown in Fig. 3.9(b) with increasing magnetic field $H_{in}$, combinations $(0:7)$, $(0:8)$, $(0:9)$ etc. become the ground state. In the contour plot of the $|\psi|^2$ distribution we observe single vortices which are arranged on a ring with a low density area situated in the center of the disk (see Figs. 3.13(a-c)). This central area is associated with a giant vortex, and encircling it leads to a phase change showing the vorticity 7. Fig. 3.13(d) shows the contour plot of the corresponding phase with seven *anti-vortices* arranged in a circle around the giant vortex and the *total* vorticity is $L = 0$. Fig. 3.13(e) and Fig. 3.13(f) correspond, respectively, to the giant vortex states with vorticity 8 and 9 where, respectively, 8 and 9 anti-vortices are located between the giant vortex and the

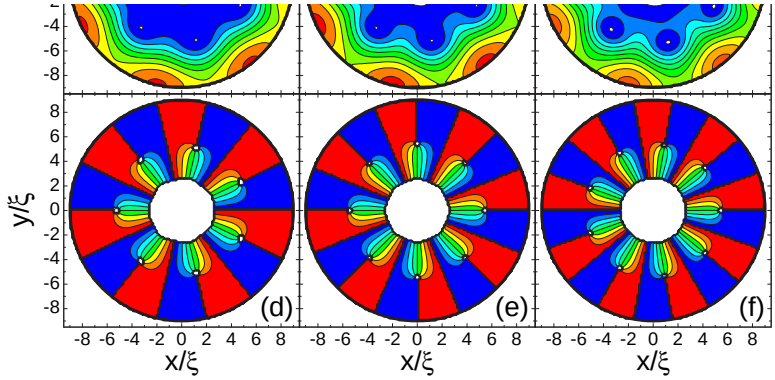


Fig. 3.13: (a-c) Contour plots of the superconducting density for the (0:7), (0:8), and, (0:9) giant-multi anti-vortex states, respectively, for different values of the magnetic field $H_{in}$; (d-f) the corresponding contour plots of the phase of the superconducting wave function density. Notice that the phase near the boundary is near 0 or $2\pi$ but due to the finite numerical accuracy it oscillates between $2\pi - \varepsilon$ and $2\pi + \varepsilon$ where $\varepsilon \sim 10^{-5}$.

boundary. Notice that the Cooper pair density for the $L = 0$ state for this disk geometry ($R_1/\xi = 4.5$, $R_2/\xi = 6.0$, $R/\xi = 9.0$) shows a similar behavior with a low density area in the center of the disk (see Fig. 3.5(b)). It is obvious that enlarging the superconducting disk enhances the influence of the negative part of the step-like magnetic field.

One could notice that a similar arrangement of the vortices was found in ring structures in the presence of a homogeneous magnetic field, where the giant vortex with $L > 1$ is surrounded by single vortices[97]. However, in our system with an inhomogeneous magnetic field *anti-vortices* surround the central giant vortex. Furthermore, in our case, when multi anti-vortices are involved, the *total* vorticity of the giant-giant multi-vortex state is equal to the lowest vorticity of the giant vortex states which compose the multi-vortex, contrary to the situation encountered in Ref. [97].

One more result should be noted. Following the ground state free energy diagram (Fig. 3.9(b)) we notice that the total vorticity doesn't change uniformly ($0 \to 1 \to 2 \to 3 \to 1 \to 0$) and that the jumps in vorticity $|\Delta L|$ are not always equal to 1. This differs from Ref. [118] where it was claimed that the lowest barriers are those between the $L$ and $L \pm 1$ states. We found that the $L \longrightarrow L \pm 1$ transitions take place in disks for a small maximum value of vorticity or at magnetic fields close to the "superconducting-normal state" transition point. Between these two limiting regimes $L \longrightarrow L \pm N$ transitions are possible with $|\Delta L| = N > 1$. Our results are also in agreement with Ref. [119] where it was found numerically that several vortices can enter (or exit) at once for disks with sufficiently large radius. In Sec. III, where we investigated the influence of $R_1/\xi$ (with $R_2/\xi = R/\xi = 6.0$) we only found $L \longrightarrow L + 1$ transitions.

In order to show the complexity of the system under study, we investigated one more field profile, the one shifted from the center of the disk i.e. a ring magnetic field. We keep all parameters from the previous case, and shift the field by $R_d = 2.0\xi$ ($R_1 - R_d = 4.5\xi$, $R_2 - R_d = 6.0\xi$, $R/\xi = 9.0$) towards the disk edge (a top view of this profile is given schematically in the inset of Fig. 3.14). As shown in Fig. 3.14, with $R_d \neq 0$ the multi-vortices become more stable and for $H_{in}/H_{c2} > 0.31$ they are the ground state. The solid curves represent the giant vortex states, dashed curves denote the energy of the anti-vortex states while the dotted curves correspond to the energy of the multi-vortices. Since giant vortex states show similar, *re-entrant* behavior as for the $R_d = 0$ case, the multi-vortex configurations behave analogously. Giant-giant multi-vortex states dominate the free energy diagram while the giant-ring combinations are present only as metastable states and are not shown in Fig. 3.14. However, one should notice the presence of giant–multi anti-vortex states, again strongly correlated with *re-entrant* behavior. The complete equilibrium phase diagram for $R_d \in [0.3, 3]$ is given in the next section.

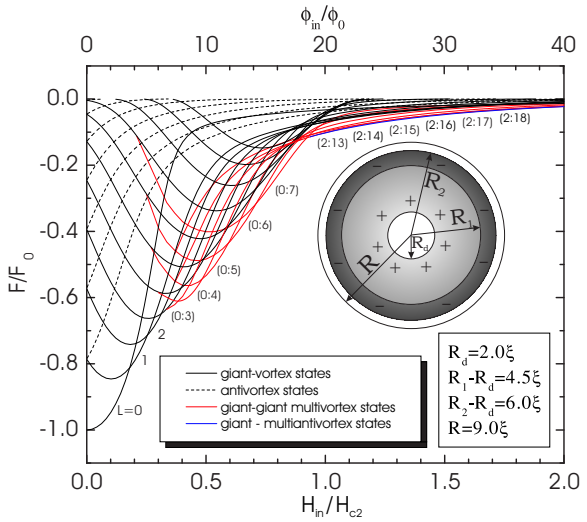


FIG. 3.14: The free energy of the giant vortex states with different angular momenta $L$ as a function of the external magnetic field for $R_d = 2.1\xi$, $R_1 = 6.6\xi$, $R_2 = 8.1\xi$, $R/\xi = 9.0$. Dashed curves depict the anti-vortex states and dotted curves represent the free energy of the giant-giant multi-vortex states. A bird view of the magnetic field profile is given in the inset.

We checked that for the disk parameters which we used, an increase of the number of components in Eq. (3.22) does not lead to different vortex configurations in the ground state. In order to investigate the region of stability of multi-vortex states in the above analysis we took the order parameter as a linear combination of three components in Eq. (3.22) and minimized the free energy with respect to the three variational parameters $C_{L_i}$. The giant and multi-vortex states considered before correspond to the extremum points of the $F(C_{L_1}, C_{L_2}, C_{L_3})$ function. This analysis has shown that accounting of third component in Eq. (3.22) gives all states obtained in two component consideration. Additionally, it results in 1) possible reducing of the region of existence of metastable multi-vortex states at the low magnetic field limit, 2) appearance of additional unstable states corresponding to the saddle points of the $F(C_{L_1}, C_{L_2}, C_{L_3})$ function, and, 3) no new vortex configurations in the ground state. We did a similar investigation using a numerical approach of Schweigert and Peeters [117]. This was done for five component vortex configurations, and same results were obtained. Using two different approaches, for three and five components, no new ground state configurations are found. Moreover, energies of same states found in both analysis for different number of components differ less than 0.2%. Because all multi-vortex configurations considered in this thesis are in the ground state, or near it, we conclude that two components in Eq. (3.22) are enough to describe the vortex structure in our system.

## 3.5 $H - R$ PHASE DIAGRAMS

First, we investigate the influence of the width of the positive magnetic field region on the different vortex configurations. Having the free energies of the different giant vortex configurations for several values of $R_1/\xi$, we construct an equilibrium vortex phase diagram. Fig. 3.15 shows this phase diagram for a superconducting disk with radius $R = 6.0\xi$ and thickness $d = 0.1\xi$ where we took $R_2 = R$. The dashed curves indicate where the ground state of the free energy changes from one $L$ state to another and the solid curve gives the normal/superconducting transition. Notice that the superconducting/normal transition moves towards lower fields with increasing radius of the positive field region. Also notice that we don't have any negative $L$ (anti-vortex) state as ground state, not even when the negative field area is much larger than the positive one.

As shown in previous section, an increase of $R_1/\xi$ is able to bring the energy of the multi-vortex states below those of the giant vortex states and they can become the ground state (see Fig. 3.9(a)). In our phase diagram, the area bounded by the thick curves denotes the region of existence of the giant-giant multi-vortex states as ground state. One can see that, with enlargement of the positive field region, ground state multi-vortices appear for $R_1/\xi = 4.42$ and $H_{in}/H_{c2} = 0.91$. Further increase of $R_1/\xi$ broadens this *multi-vortex area* to almost the whole superconducting region. These multi-vortex states consist of

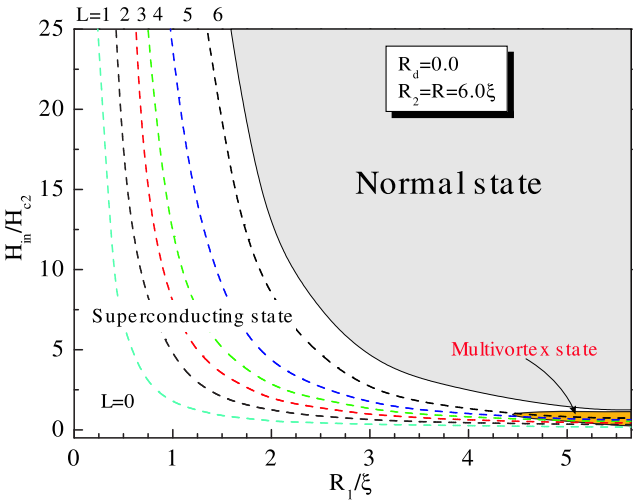


FIG. 3.15: The $H_{in} - R_1$ equilibrium vortex phase diagram for a thin superconducting disk with $R_d/\xi = 0.0$, $R_2/\xi = 6.0$, and $R/\xi = 6.0$. Dashed curves indicate transitions between different giant vortex states and the yellow shaded area denotes the multi-vortex region. The normal/superconducting state transition is given by the black solid curve.

vortices in a ring structure, and the total vorticity equals the highest vorticity of the giant vortex states involved (at least in the case when there are no anti-vortices present).

In order to show that the stabilization of the multi-vortex states due to an inhomogeneous magnetic field is not peculiar to the $R = 6.0\xi$ disks, we repeated the previous calculations for a larger superconducting disk. Furthermore, we investigated in detail the phenomena shown in previous section (Figs. 3.11, 3.12, 3.13).

The effect of the size of the superconducting disk on the phase diagram is illustrated in Fig. 3.16. The parameters considered are $R_d/\xi = 0.0$, $R_1/\xi = 4.5$, and $R_2/\xi = 6.0$. The solid lines indicate where the ground state of the free energy changes from one state to another (either giant or multi-vortex state) and dashed lines correspond to transitions between different giant vortex states as metastable states. One can clearly see the *re-entrant* behavior. For example, for $R/\xi = 9.0$ we observe the change of the total vorticity as $L = 0 \to 1 \to 2 \to 3 \to 1 \to 0$. The $L = 0$ and $L = 1$ states as ground state cover the largest part of the phase diagram. With increasing disk size, all other giant vortex states are strongly suppressed in favor of the various multi-vortex states. Different giant vortex states are present as the ground state for small disk sizes but with increase of disk size, islands with different multi-vortex configurations (*giant-ring* and *giant-giant* multi-vortex states) dominate the ground state diagram. Precisely, for $R = 6.38\xi$, giant-ring multi-vortex state appear as the ground state, and for $R = 6.77\xi$ we obtain the giant-giant multi-vortex states as the ground state. In the previous diagram in Fig. 3.15 we have shown the existence of the giant-giant multi-vortex states as the ground

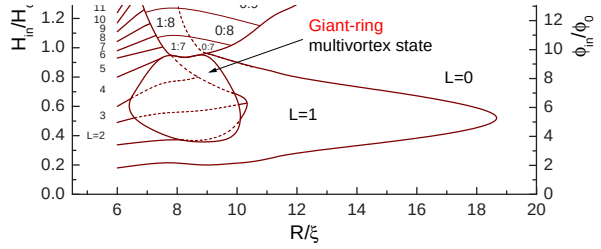


FIG. 3.16: The $H_{in} - R$ phase diagram for the ground state of a thin superconducting disk with $R_d/\xi = 0.0$, $R_1/\xi = 4.5$, and $R_2/\xi = 6.0$. Solid curves indicate transitions between different vortex states including multi-vortex (giant-multi anti-vortex and ring-giant) regions. Dashed curves denote the transitions between different metastable giant vortex states.

state for $R = 6.0\xi$. With slight increase of the disk size, these states become metastable, and with further enlargement of the superconducting disk, they become the ground state again. However, these states are different from the previous ones and in the contour plots of the Cooper pair density of these "new" giant-giant multi-vortex states (see Fig. 3.13) we found a giant vortex state in the middle of the superconducting disk surrounded by anti-vortices, and where the *total* vorticity is now equal to the lowest vorticity of the giant vortex states that the multi-vortex consists of. For $R > 12.33\xi$, the multi-vortex states become metastable again and the $L = 0$ and $L = 1$ states become the only ground states. Moreover, for $R > 19.34\xi$ we have the Meissner state for all values of the applied magnetic field.

To present the complexity and excitement in this study, we give one more diagram. As shown before, moving the step-like field profile along the radius of the superconducting disk, i.e. a ring magnetic field profile as in the case of a current loop, stabilizes the giant-giant multi-vortex states as the ground state. In Fig. 3.17, we present the phase diagram as function of $R_d$. The parameters of the magnetic field profile are $R_1 - R_d = 4.5\xi$, $R_2 - R_d = 6.0\xi$, and $R/\xi = 9.0$. Thick solid curves indicate the transitions between different vortex states and dashed lines denote the transitions between metastable giant vortex states. The *re-entrant* behavior, as in previous case, is clearly visible. The most important result is that the multi-vortex states dominate this diagram. Moreover, we have both types of multi-vortices, i.e. *giant-giant* and *giant-ring*, as stable and ground state, and with shifting the field profile towards the disk periphery, giant-giant multi-vortex configurations cover most of the

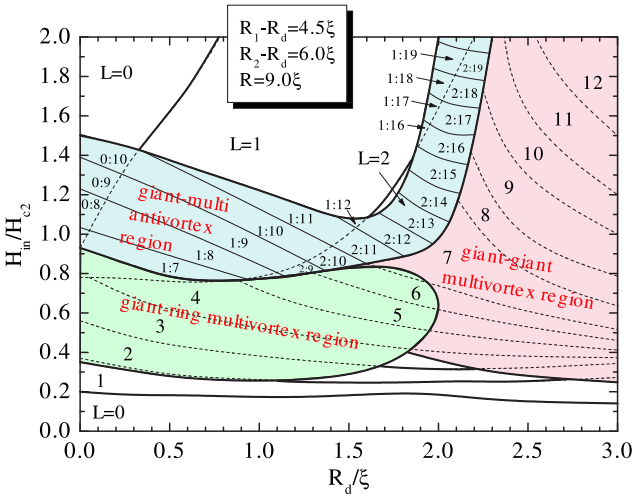


FIG. 3.17: The $H_{in} - R_d$ phase diagram for the ground state of a thin superconducting disk with $R_1 - R_d = 4.5\xi$ and $R_2 - R_d = 6.0\xi$, i.e. a ring inhomogeneous magnetic field distribution. The same curve convention is used as in Fig. 3.16.

superconducting region. The giant-giant multi-vortex states in this case appear both as states with no anti-vortices present, and as giant–multi anti-vortex states. Following the transition lines, a correspondence between different giant–multi anti-vortex states ($L_1$:$L_2$) can be seen: $L_2$ remains the same, while $L_1$ increases from 0 to 2. As one can see, the latter is strongly correlated with re-entrant behavior. In the rest of the diagram, the multi-vortex states with the "classical" geometry (both *giant-giant* and *giant-ring*) dominate. However, a difference between those two states exists. As shown in Fig. 3.12, in the case of a giant-ring state, vortices are preferentially distributed within a ring-shaped lower density area. Further, considering the high density areas at the disk periphery, a shift in phase of $\Delta\theta = \pi/L$ is observed, in comparison with corresponding giant-giant state (see, for example, Fig. 3.10), where $L$ is the total vorticity. Although these states have a different origin, sometimes they can exhibit a similar distribution of vortices, but the phase is always able to distinguish between them.

## 3.6 COMPARISON WITH REAL MAGNETIC FIELD PROFILE

As emphasized before, our step-like field model can be considered as a simplification of the magnetic field profile of a ferromagnetic dot (see solid curve in Fig. 3.1) as shown schematically in Fig. 3.18. In this case, the radius of the dot corresponds to $R_1$, and $R_2$ is always equal to $R$. The magnetic field and vector potential were calculated through numerical integration of

$$H_z(\rho,z) = m_z \int_0^{R_1} dr' \frac{4r'(z'-z)}{\sqrt{(r'-\rho)^2+(z'-z)^2}((r'+\rho)^2+(z'-z)^2)} \times E\left[-\frac{4r'\rho}{(r'+\rho)^2+(z'-z)^2}\right]\Bigg|_{z_0'}^{z_1'}, \quad (3.27)$$

and

$$A_\varphi(\rho,z) = \frac{1}{\rho}\int_0^{\rho} rH_z(r,z)dr,$$

where $m_z$ denotes the magnetic moment of a dot directed along the $z$ -axis, $R_1$ is the radius of the dot, $z_0'$ gives the distance from the plane of interest, and $d_d = z_1' - z_0'$ is the thickness of the dot. $E(x)$ is the complete elliptic integral of the second kind. The calculations were done for $z \to 0$, which allowed us to neglect the radial component of the magnetic field.

In order to examine the quality of our previous model we repeated the analysis from previous sections. First, we enlarge $R_1$, i.e. the radius of the magnetic dot, investigating the influence of the magnetic field on the vortex structure

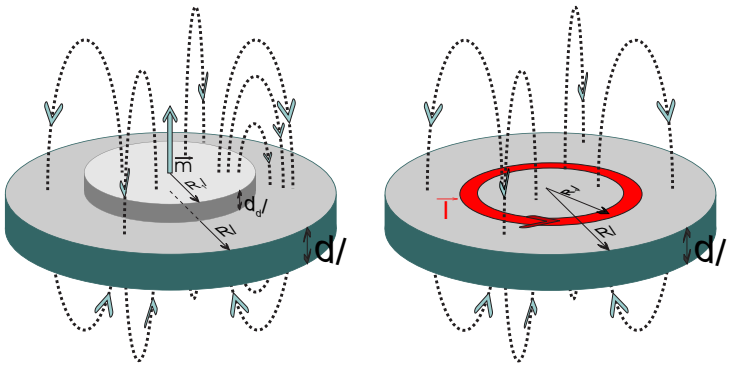


FIG. 3.18: The configuration: a superconducting disk with radius $R$ and thickness $d$ with a ferromagnetic dot with thickness $d_d$, or a current loop, with radius $R_1$ placed on top of it.

and especially on the stability of the multi-vortex states, and secondly we studied the vortex configurations resulting from an increase of the superconducting disk size.

For small values of $R_1/\xi$ the multi-vortex states are always metastable. However, with enlarging this parameter these states lower in energy. The energies of the equilibrium vortex states as function of magnetization of the dot measured in units of $M_0 = H_{c2}$, are plotted in Fig. 3.19(a) for radius of the dot $R_1/\xi = 4.0$ and $R/\xi = 6.0$ and in Fig. 3.19(b) for $R_1/\xi = 4.0$ with a larger disk radius $R/\xi = 9.0$. Dashed curves correspond to anti-vortex states and dotted curves represent the energy of the multi-vortex states. The giant-giant multi-vortex states are given by $(L_1 : L_2)$, i.e. the angular momentum values they are composed of, and the giant-ring multi-vortex states with lowest energy are given in Fig. 3.19(b) by $((n_1, L_1) : (n_2, L_2))$. It should be noted that there are many other metastable combinations possible, which are not shown in the figures. Notice from Fig. 3.19(a) that the results are qualitatively similar to the results obtained with our step magnetic field model (see Fig. 3.9). The difference is caused by the fact that part of the negative magnetic flux does not penetrate the superconducting disk. Because the positive field region in the center dictates the behavior of the phase diagram even when the total flux is zero (see, for example, Fig. 3.9(a)), we obtain very similar results with the real magnetic field profile, but with an increased number of possible superconducting states. However, increasing the size of the superconductor brings some qualitative changes. First, it is clear from Fig. 3.19(b) that there is no *re-entrant* behavior, and, second, no giant-giant multi-vortex configurations are ground state. But, this was expected since in our model field profile the whole magnetic flux is trapped in the center of the disk, with total flux equal zero. For the real profile, the total flux would be zero if our disk is infinitely

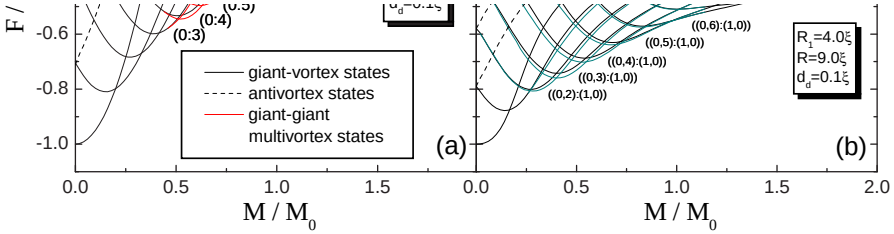


Fig. 3.19: The free energy of different vortex states as a function of the magnetic moment of the ferromagnetic dot with (a) $R_1/\xi = 4.5$, $R_2/\xi = R/\xi = 6.0$, and (b) $R_1/\xi = 4.5$, $R_2/\xi = R/\xi = 9.0$. In (a), red curves depict the free energy of the giant-giant multi-vortex states while in (b) cyan curves denote giant-ring states. The brown curve gives the energy of the ring vortex state, i.e. $(n, L) = (1, 0)$. The energy of the anti-vortex states is given by the dashed curves.

extended, and, more importantly, the flux is now spread over the whole disk area. Naturally, smaller magnetic dots in combination with large superconductors would make the correspondence better, since most of the flux would be captured inside the disk.

A similar discussion holds for the results for the real magnetic field profile of a current loop placed on top of a superconductor. This field profile (solid curve) is compared with our model in Fig. 3.1(b) (red dashed curve). The magnetic field and vector potential were calculated numerically from

$$H_z(\rho, z) = \frac{Ik}{4\sqrt{R_1\rho}} \left[ \frac{R_1^2 - \rho^2 - z^2}{(R_1 - \rho)^2 + z^2} E(k^2) + K(k^2) \right], \tag{3.28}$$

and

$$A_\varphi(\rho, z) = \frac{I}{k} \sqrt{\frac{R_1}{\rho}} \left[ \left( 1 - \frac{k^2}{2} \right) K(k^2) - E(k^2) \right], \tag{3.29}$$

with

$$k = 2\sqrt{\frac{R_1\rho}{(R_1 + \rho)^2 + z^2}}, \tag{3.30}$$

where $K(x)$ is the complete elliptic integral of the first kind and $R_1$ denotes the radius of the loop with current $I$.

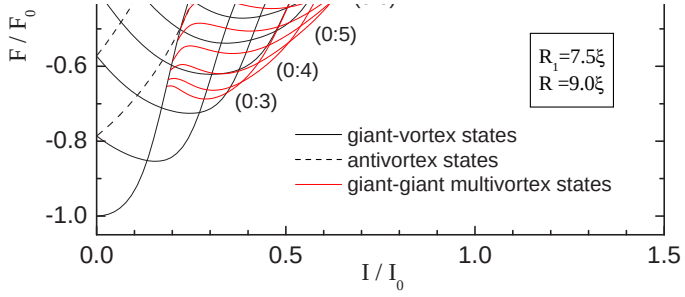


FIG. 3.20: The free energy of different vortex states as a function of the current in a loop with (a) $R_1/\xi = 7.5$, $R_2/\xi = R/\xi = 9.0$. Dashed curves depict the free energy of the anti-vortex states and red curves denote the giant-giant multi-vortex states.

The free energy is shown in Fig. 3.20 for a loop with radius $R_1 = 7.5\xi$, with superconductor disk size $R = 9.0\xi$, as a function of current $I$ measured in units of $I_0 = \pi\xi H_{c2}/\mu_0$. Typical values of $I_0$ are $3.29mA$, for aluminum, to $0.823A$ for high-temperature superconductors. One should compare these results with those presented in the $H_{in} - R_d$ phase diagram (Fig. 3.17) and find that our previous model contains most of the essential physics of the system. The free energy diagrams of both Fig. 3.14 and Fig. 3.20 show the *re-entrant* behavior in total vorticity and the existence of the giant-giant multi-vortex configurations over a large region of the phase diagram.

## 3.7 INFLUENCE OF THE BACKGROUND HOMOGENEOUS MAGNETIC FIELD

In addition, we investigated the vortex structure of a superconducting disk in the presence of an inhomogeneous magnetic field profile resulting from a ferromagnetic dot and a homogeneous external background magnetic field. In Figs. 3.21(a-c) we present the free energy as function of the external homogeneous field, for different magnetic dot thicknesses. The parameters were - radius of the dot $R_1/\xi = 4.0$, radius of the superconducting disk $R/\xi = 6.0$ with thickness $d = 0.1\xi$ and fixed magnetic field profile of the ferromagnet ($M = H_{c2}$) which is shown as inset of Figs. 3.21(a-c). As expected, when a negative external field overwhelms the average of the positive magnetic field of the dot

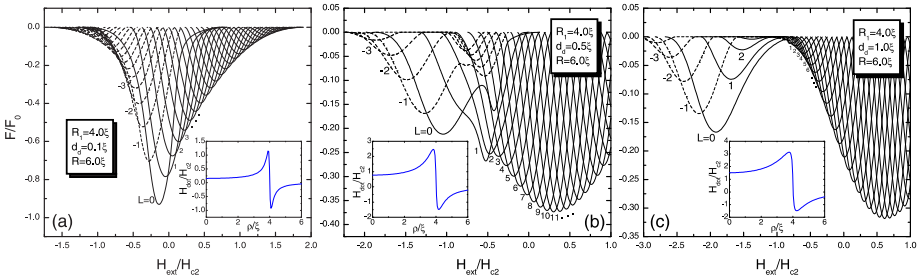


Fig. 3.21: The free energy of giant vortex states as a function of the external magnetic field in a superconducting disk with magnetic dot on top of it with parameters $M = M_0$, $R_1/\xi = 4.0$, $R/\xi = 6.0$ and (a) $d_d = 0.1\xi$, (b) $d_d = 0.5\xi$, and (c) $d_d = 1.0\xi$. Dashed curves depict the free energy of the anti-vortex states. Insets show the magnetic field profile inside the superconducting disk created by the magnetic dot.

in the disk center, the anti-vortex states become energetically more favorable, and, opposite, when the positive external field becomes larger than the average negative value of the ferromagnetic dot field, we see that the ground state goes through successive giant vortex states towards the normal state. For example, for a thickness of the magnetic dot $d_d = 0.1\xi$ we obtain an almost symmetrical figure with respect to $H_{ext} = -0.14H_{c2}$. However, with increasing magnetic dot thickness, the magnetic field of the ferromagnetic dot (given as inset in Figs. 3.21(a-c)) becomes more pronounced and we obtain two sets of curves corresponding with the vortex and anti-vortex states, each of which having a minimum. These local minima occur at an external field values which are approximately equal to the average field of the positive and negative region of the magnetic dot profile, respectively. The region between these two minima is characterized by a strong interplay of states.

For a current loop on top of the superconducting disk in a homogeneous external field we obtained qualitatively similar results. Also two sets of curves, with two local minima are visible in the free energy for sufficiently large currents in the loop (see Figs. 3.22(b-c)). We show numerical results for a system consisting of a superconducting disk with $R/\xi = 9.0$ and thickness $d = 0.1\xi$, and current loop with radius $R_1 = 7.5\xi$ (see Fig. 3.1(b)). Just like in the previous case, minima in the free energy are related to average fields in positive and negative region of the current loop magnetic field profile. However, several differences exist. First, with increase of the thickness of the magnetic dot in previous situation, the magnetic field profile becomes more similar to our step-like field model. For the current loop case this is not so, and with increasing current in the loop the magnetic field becomes strongly inhomogeneous, rapidly increasing in the vicinity of the loop. As a consequence the minimum in the free energy for negative external field is lower in energy, and, moreover, the other minimum slowly diminishes with further increase of the current in the

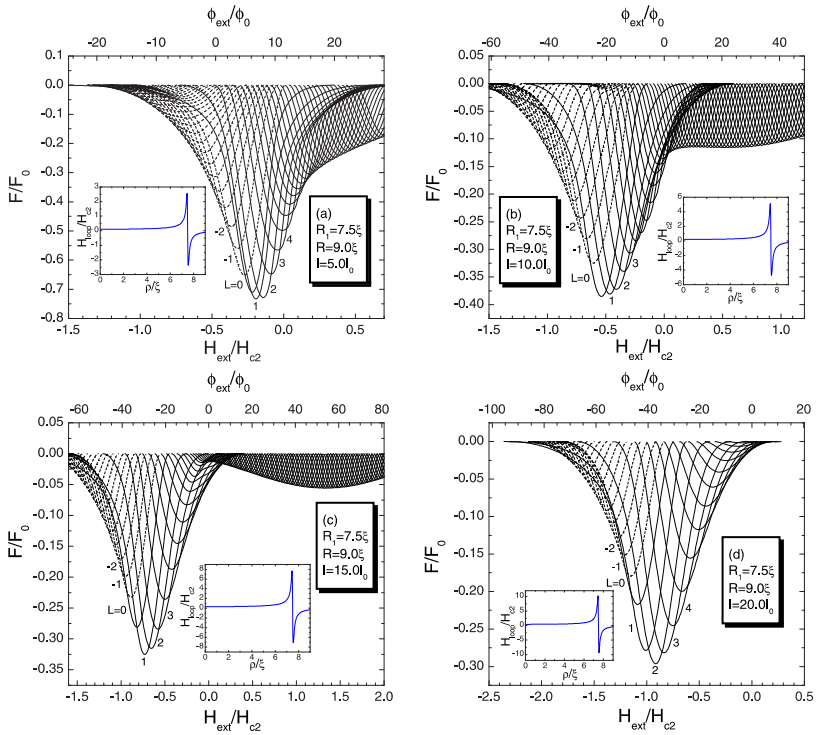


FIG. 3.22: The free energy of giant vortex states as a function of the external magnetic field in a superconducting disk with current loop on top of it with parameters $R_1/\xi = 7.5$, $R/\xi = 9.0$ and (a) $I/I_0 = 5.0$, (b) $I/I_0 = 10.0$, (c) $I/I_0 = 15.0$, and (d) $I/I_0 = 20.0$. Dashed curves depict the free energy of the anti-vortex states. Insets show the magnetic field profile inside the superconducting disk created by the current loop.

loop. In this case even for negative applied external field, the positive peak in the magnetic field profile of the current loop is responsible for the stabilization of the positive $L$ -states, up to large $H_{ext} < 0$ (see Fig. 3.22(d)). It is obvious that the interplay between the external and the current loop magnetic field exhibits more interesting physics due to the strong field inhomogeneity.

### 3.7.1 $H_{ext} - T$ diagrams and comparison with experiment

Very recently, Golubović *et al.* investigated the nucleation of superconductivity in an *Al* mesoscopic disk, with a out-of-plane magnetized dot on the top (see Fig. 3.23). The *Al* disk and magnetic dot are separated by an insulating layer, which ensures that there is only magnetic interaction between them, just as we assumed in our theoretical approach. The main accent in this paper was on the appearance of the maximum critical temperature for a finite value of the

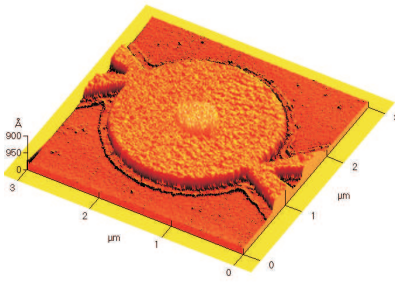


Fig. 3.23: An AFM topography image of the superconducting disk with magnetic dot on top. [From Ref. [7].]

perpendicular applied magnetic field, which is parallel to the magnetization of magnetic dot. Therefore, in order to compare our theoretical results with the experimental ones, we introduced temperature in our formalism through the temperature dependence of the characteristic length scale $\xi$:

$$\xi(T) \quad = \quad \frac{\xi(0)}{\sqrt{|1 - T/T_{c0}|}} \ , \tag{3.31}$$

where $\xi(0)$ denotes the coherence length at zero temperature and $T_{c0}$ is the critical temperature of the SC disk at zero magnetic field.

Since all units in our formalism depend on $\xi$, the temperature is in this way indirectly introduced in the calculation. For clarity, and to facilitate the comparison with experiments, we will use SI units in this section. The dimensions of the system are as given in Ref. [7]: the superconducting disk is a 60nm thick $Al$, whereas the magnetic dot consists of 2.5nm $Pd$ buffer layer and 10 bilayers of 0.4nm $Co$ and 1nm $Pd$. A 10nm thick $Si$ spacer layer was evaporated before the magnetic dot. The radius of the $Al$ disk is $R = 1.08\mu$m, whereas the dot has the radius of $R_1 = 270$nm. Therefore, we took the thickness of the dot $d_d = 16.5$nm ($d_d = z_1' - z_0'$, see Eq. 3.27), and we calculate the magnetic field in the center of the superconducting disk, namely in Eq. 3.27, $z_0' = 40$nm.

In the same manner as in the previous section, we now add the external homogeneous magnetic field, and for fixed angular momentum we investigate the stability of the vortex state while increasing the applied field, for given temperature. After quite demanding calculation, we are left with the complete $H_{ext} - T$ diagram, where the transitions between different vortex states and the superconducting/normal boundary are visible. However, we still have two free parameters: the coherence length $\xi(0)$ and the magnetization of the dot $M$, which considerably influence both the transition fields and the transition temperatures. In Fig. 3.24, we show the comparison with the experiment of Golubović *et al.* ($B_a$ corresponds to our $H_{ext}$). One should notice the *perfect*

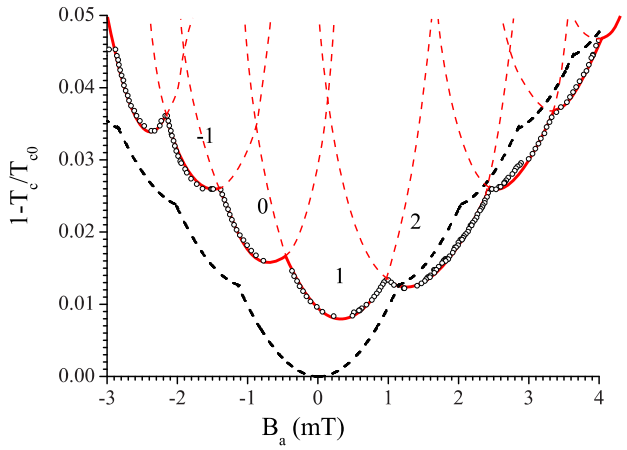


FIG. 3.24: The experimental data for the phase boundary of the superconducting disk with magnetic dot (open dots) and the theoretical phase boundary of an identical superconducting disk without magnetic dot (black dashed line) [taken from Ref. [7]]. The red curves denote our theoretical phase boundary. The temperatures are normalized to the zero-field critical temperature of the disk without magnetic dot. The numbers indicate the vorticity of the hybrid structure.

agreement between the theoretical curve and the experimental data. The best fit was obtained for $\xi = 102$nm and $M = 3.08 \cdot 10^5$A/m. The value of coherence length is consistent with the values obtained before for mesoscopic $Al$ superconductors and the value of magnetization is $\sim 20\%$ larger than the magnetization of pure $Co$ dots, and is therefore adequately chosen. Each cusp in the phase boundary corresponds to the transition between the states with different vorticities. According to these results, there is one vortex in the disk in the absence of the external magnetic field. The superconducting phase boundary strongly depends upon the polarity of an external magnetic field. The direction of the shift of $T_c(H)$ phase boundary near $T_{c0}$, for a fixed orientation of the magnetization $M$, depends upon the intensity of the stray field of magnetic dot (see Fig. 3.25). As was speculated by Golubović, the shift can come about as a result of the cancellation of the total flux generated by the magnetic dot, or due to a change in the kinetic energy of the superconducting condensate in the disk, accompanied by a switch in the vorticity by one. The former shifts the phase boundary in the direction opposite to the magnetization of the dot and the maximum critical temperature is observed for a finite negative applied field, whereas the latter provides that the maximum critical temperature is achieved for a finite applied field parallel to the magnetization of the dot, that is for a finite positive field. Which of these competing effects prevails strongly depends upon the intensity of magnetization of magnetic dot, as well as upon the parameters of the superconducting structure. As one can see in Fig. 3.25,

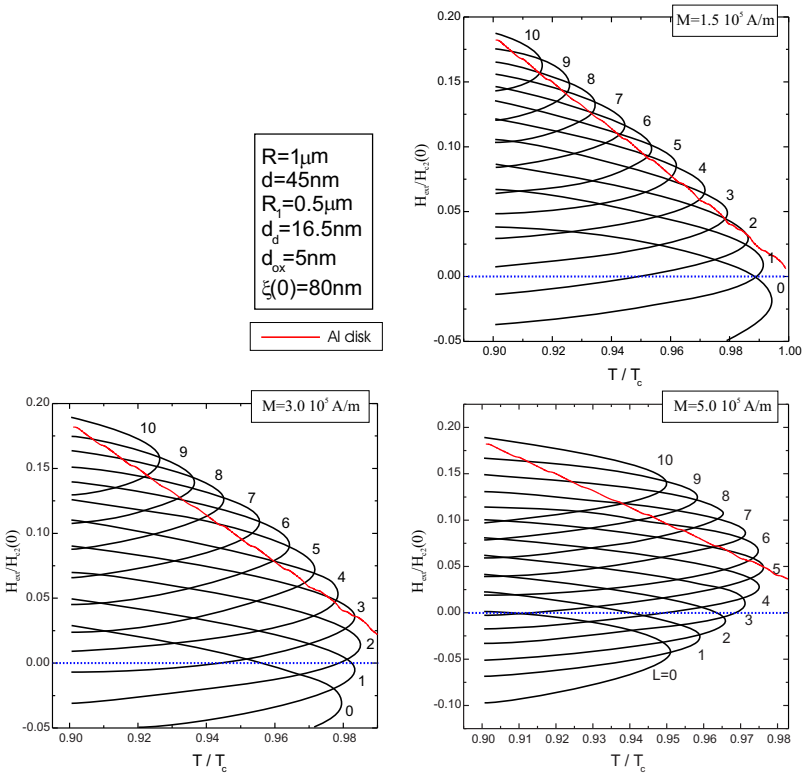


Fig. 3.25: The theoretical $H_{ext} - T$ phase diagram for a superconducting disk with magnetic dot on top, for different magnetization of the dot.

for given parameters, the shift changes sign with increasing magnetization of the dot. Further, as expected, increased magnetization induces higher sample vorticity in zero applied field. One more interesting phenomenon in this hybrid structure is the additional shift of the phase boundary along the $T$-axis, caused by a difference in the maximum critical temperature of the disk with and without the dot. As the stray field of the dot is spatially inhomogeneous, it cannot be cancelled out by an externally applied homogeneous magnetic field. For this reason, there is always a finite flux through a disk with a magnetic dot and its maximum critical temperature is reduced compared to the disk without a magnetic dot. We can, therefore, conclude that the effect of the inhomogeneous magnetic field on the nucleation of superconductivity is twofold: it shifts the phase boundary along the $H$-axis, as well as distorts the phase boundary along the $T$-axis, altering the values at which the structure switches between different vorticities.

## 3.8 CONCLUSIONS

We studied the superconducting state of a thin superconducting disk in the presence of an inhomogeneous magnetic field. A "model" step-like magnetic field profile was considered which is an approximation for the magnetic field profile resulting from a magnetic disk or from a current loop. The superconducting disk is assumed sufficiently thin that the magnetic field produced by the superconducting currents can be neglected. The effects of the width of the positive field region, the position of the field and the size of the superconducting disk on the vortex configuration were investigated. Numerous phase transitions were found, between states with different angular momentum number and between giant and multi-vortex states, plus transitions of the ground state between different multi-vortex configurations (*giant-ring* and *giant-giant* multi-vortex states). The model step-like magnetic field (total flux through the system equals zero) is found to stabilize the multi-vortex states both as the ground state (i.e., with minimal energy) and as metastable states. Increase of the width of the positive field region enhances the stability of the giant-giant multi-vortices, while enlarging the superconducting disk decreases the energy of the giant-ring multi-vortex state. In this case, the giant-giant multi-vortex states can also be the ground state but it represents a new configuration - a giant vortex surrounded by anti-vortices, and the *total* vorticity equals the lowest vorticity of the giant vortex states which are involved. We found that with an increase of the disk size, *re-entrant* behavior of the total vorticity is possible. This behavior can also be seen by shifting the field profile towards the disk boundary, i.e. for the current loop magnetic field, when giant-giant multi-vortex configurations cover most of the superconducting phase diagram region. Comparison with results obtained for a real magnetic field profile shows very good correspondence with our step-like models for the cases when most of the magnetic flux is captured inside the superconducting disk. For a magnetic dot with a larger radius, the positive magnetic field region of the inhomogeneous magnetic field profile dominates and with increasing magnetic dot radius, the total flux in the superconductor also increases, which is different from our model where the total flux always equals zero. Thus, the positive part of the magnetic field profile determines mainly the superconducting states, which leads to slightly different physics - no *re-entrant* behavior is present, more different superconducting states are possible, but without the giant-giant multi-vortex states with anti-vortices, since they are strongly correlated with a re-entrance of the total vorticity.

Adding a homogeneous background magnetic field, besides the inhomogeneous field resulting from the magnetic dot, brings a qualitative difference in the free energy diagram. When the external magnetic field is between the average field of the dot in the positive and the negative region, we observe a strong interplay of the different superconducting giant states. Moreover, with

increase of the thickness of the dot, we obtain two strong minima in the free energy, when the total field is approximately equal to zero in the $\rho < R_1$, and the $\rho > R_1$ region, respectively, where $R_1$ is the radius of the dot. After introducing the temperature in our calculation, we constructed a $H_{ext} - T$ phase boundary. We found that the effect of the inhomogeneous magnetic field on the nucleation of superconductivity is twofold: it shifts the phase boundary along the $H$-axis, as well as distorts the phase boundary along the $T$-axis, altering the values at which the structure switches between different vorticities. The calculated phase boundary is in perfect agreement with experimental data.

Here, we must emphasize that our results are only valid in the limit of very thin disks. It allowed us to separate the two GL equations and thus we neglected the magnetic field created by the superconducting currents.

**Publications.** The results presented in this chapter were published as:

- M. V. Milošević, S. V. Yampolskii, and F. M. Peeters, *Multi-vortex states of a thin superconducting disk in a step-like external magnetic field*, Physica C **369**, 343-346 (2002).
- M. V. Milošević, S. V. Yampolskii, and F. M. Peeters, *Vortex structure of thin mesoscopic disks in the presence of the inhomogeneous magnetic field*, Phys. Rev. B **66**, 024515 (2002) (20 pages).

# *Appendix B*

## *Eigenfunctions of the linearized first GL equation in the presence of an inhomogeneous magnetic field*

### B.1 DISK MAGNETIC FIELD PROFILE

The vector potential distribution is determined by the piecewise function (see Eq. 3.11 with $R_d = 0$)

$$A_0(\rho) = \begin{cases} H_{in}\rho/2, & 0 \le \rho \le R_1, \\ -H_{out}\rho/2 + H_{out}R_2^2/2\rho, & R_1 \le \rho \le R_2, \\ 0, & R_2 \le \rho \le R. \end{cases} \tag{B.1}$$

The eigenfunctions of Eq. (3.15) are expressed in the following way:

$$f_{L,n}(\rho) = \begin{cases} f_{11}(\rho), & 0 \le \rho \le R_1, \\ b_1 f_{21}(\rho) + b_2 f_{22}(\rho), & R_1 \le \rho \le R_2, \\ d_1 f_{31}(\rho) + d_2 f_{32}(\rho), & R_2 \le \rho \le R, \end{cases} \tag{B.2}$$

where

$$\begin{aligned}
f_{11}(\rho) &= \left(H_{in}\rho^2/2\right)^{|L|/2}\exp\left(-H_{in}\rho^2/4\right)M\left(-\nu_{n,1}(\Lambda),|L|+1,H_{in}\rho^2/2\right),\\
f_{21}(\rho) &= \left(H_{out}\rho^2/2\right)^{|L_2^*|/2}\exp\left(-H_{out}\rho^2/4\right)M\left(-\nu_{n,2}(\Lambda),|L_2^*|+1,H_{out}\rho^2/2\right),\\
f_{22}(\rho) &= \left(H_{out}\rho^2/2\right)^{|L_2^*|/2}\exp\left(-H_{out}\rho^2/4\right)U\left(-\nu_{n,2}(\Lambda),|L_2^*|+1,H_{out}\rho^2/2\right),\\
f_{31}(\rho) &= J_{|L|}\left(\sqrt{1+\Lambda}\rho\right),\\
f_{32}(\rho) &= Y_{|L|}\left(\sqrt{1+\Lambda}\rho\right),
\end{aligned}$$

with $L_2^* = L - H_{out}R_2^2/2$, $\nu_{n,1}(\Lambda) = -(1+|L|-L)/2 + (1+\Lambda)/2H_{in}$, and $\nu_{n,2}(\Lambda) = -(1+|L_2^*|+L_2^*)/2 + (1+\Lambda)/2H_{out}$. Here $J_m(x)$ and $Y_m(x)$ are the Bessel functions of the first and second kind, $M(a,c,y)$ and $U(a,c,y)$ are the Kummer functions. To find the unknown constants $b_{1(2)}$, $d_{1(2)}$ and the eigenvalue $\Lambda$ we have to join the different parts of $f_{L,n}(\rho)$ and their first derivatives at $R_1$ and $R_2$ as well as to use the boundary condition $(\partial f/\partial\rho)|_{\rho=R} = 0$. After a straightforward calculation we obtained

$$b_1 = \frac{f_{111}f'_{221} - f_{221}f'_{111}}{f_{211}f'_{221} - f_{221}f'_{211}}, \qquad b_2 = \frac{f_{211}f'_{111} - f_{111}f'_{211}}{f_{211}f'_{221} - f_{221}f'_{211}}, \tag{B.3}$$

$$d_1 = \frac{b_1\left(f_{212}f'_{322} - f_{322}f'_{212}\right) + b_2\left(f_{222}f'_{322} - f_{322}f'_{222}\right)}{f_{312}f'_{322} - f_{322}f'_{312}},$$

$$d_2 = \frac{b_1\left(f_{312}f'_{212} - f_{212}f'_{312}\right) + b_2\left(f_{312}f'_{222} - f_{222}f'_{312}\right)}{f_{312}f'_{322} - f_{322}f'_{312}},$$

and the non-linear equation for $\Lambda$:

$$\begin{aligned}
&\left(f_{111}f'_{221} - f_{221}f'_{111}\right)\left[f'_{31}(R)\left(f_{212}f'_{322} - f_{322}f'_{212}\right)\right.\\
&\left.+f'_{32}(R)\left(f_{312}f'_{212} - f_{212}f'_{312}\right)\right] + \left(f_{211}f'_{111} - f_{111}f'_{211}\right)\\
&\times\left[f'_{31}(R)\left(f_{222}f'_{322} - f_{322}f'_{222}\right) + f'_{32}(R)\left(f_{312}f'_{222} - f_{222}f'_{312}\right)\right] = 0.
\end{aligned} \tag{B.4}$$

where we introduced notations $f_{ijk} = f_{ij}(R_k)$, $f'_{ijk} = (\partial f_{ij}/\partial\rho)|_{\rho=R_k}$. To obtain the correct $\Lambda$ values we have to exclude from the spectrum of solutions of Eq. (B.4) those which result in zeros of $f_{211}f'_{221} - f_{221}f'_{211}$ and $f_{312}f'_{322} - f_{322}f'_{312}$.

In the large radius limit $R \to \infty$, the result in the third region of the piecewise function can be replaced by asymptotics of the Bessel functions. Substituting them in Eq. (B.4) we obtain

$$\Lambda = -1 + \frac{1}{R^2}\left[\frac{\pi}{4}(3+2|L|) - \arctan\frac{d_1}{d_2}\right]^2. \tag{B.5}$$

The value of $f_{L,n}(\rho)$ near the sample edge is equal to $\sqrt{d_1^2 + d_2^2}$.

## B.2 RING MAGNETIC FIELD PROFILE

The vector potential distribution is given by Eq. (11) and, therefore, the eigenfunctions of Eq. (3.15) can be expressed as follows:

$$f_{L,n}(\rho) = \begin{cases} f_{11}(\rho), & 0 \le \rho \le R_d, \\ b_1 f_{21}(\rho) + b_2 f_{22}(\rho), & R_d \le \rho \le R_1, \\ d_1 f_{31}(\rho) + d_2 f_{32}(\rho), & R_1 \le \rho \le R_2, \\ e_1 f_{41}(\rho) + e_2 f_{42}(\rho), & R_2 \le \rho \le R, \end{cases} \tag{B.6}$$

where

$$\begin{aligned} f_{11}(\rho) &= f_{41}(\rho) = J_{|L|}\left(\sqrt{1+\Lambda}\rho\right), \\ f_{21}(\rho) &= \left(H_{in}\rho^2/2\right)^{|L_2^*|/2} \exp\left(-H_{in}\rho^2/4\right) M\left(-\nu_{n,2}(\Lambda), |L_2^*|+1, H_{in}\rho^2/2\right), \\ f_{22}(\rho) &= \left(H_{in}\rho^2/2\right)^{|L_2^*|/2} \exp\left(-H_{in}\rho^2/4\right) U\left(-\nu_{n,2}(\Lambda), |L_2^*|+1, H_{in}\rho^2/2\right), \\ f_{31}(\rho) &= \left(H_{out}\rho^2/2\right)^{|L_3^*|/2} \exp\left(-H_{out}\rho^2/4\right) M\left(-\nu_{n,3}(\Lambda), |L_3^*|+1, H_{out}\rho^2/2\right), \\ f_{32}(\rho) &= \left(H_{out}\rho^2/2\right)^{|L_3^*|/2} \exp\left(-H_{out}\rho^2/4\right) U\left(-\nu_{n,3}(\Lambda), |L_3^*|+1, H_{out}\rho^2/2\right), \\ f_{42}(\rho) &= Y_{|L|}\left(\sqrt{1+\Lambda}\rho\right), \end{aligned}$$

with $L_2^* = L + H_{in}R_d^2/2$, $L_3^* = L - H_{out}R_2^2/2$, $\nu_{n,2}(\Lambda) = -(1+|L_2^*|-L_2^*)/2 + (1+\Lambda)/2H_{in}$, and $\nu_{n,3}(\Lambda) = -(1+|L_3^*|+L_3^*)/2 + (1+\Lambda)/2H_{out}$. The constants $b_{1(2)}$, $d_{1(2)}$ and $e_{1(2)}$ are given by the following expressions

$$b_1 = \frac{f_{11d}f'_{22d} - f_{22d}f'_{11d}}{f_{21d}f'_{22d} - f_{22d}f'_{21d}}, \quad b_2 = \frac{f_{21d}f'_{11d} - f_{11d}f'_{21d}}{f_{21d}f'_{22d} - f_{22d}f'_{21d}}, \tag{B.7}$$

$$d_1 = \frac{b_1\left(f_{211}f'_{321} - f_{321}f'_{211}\right) + b_2\left(f_{221}f'_{321} - f_{321}f'_{221}\right)}{f_{311}f'_{321} - f_{321}f'_{311}},$$

$$d_2 = \frac{b_1\left(f_{311}f'_{211} - f_{211}f'_{311}\right) + b_2\left(f_{311}f'_{221} - f_{221}f'_{311}\right)}{f_{311}f'_{321} - f_{321}f'_{311}},$$

$$e_1 = \frac{d_1\left(f_{312}f'_{422} - f_{422}f'_{312}\right) + d_2\left(f_{322}f'_{422} - f_{422}f'_{322}\right)}{f_{412}f'_{422} - f_{422}f'_{412}},$$

$$e_2 = \frac{d_1\left(f_{412}f'_{312} - f_{312}f'_{412}\right) + d_2\left(f_{412}f'_{322} - f_{322}f'_{412}\right)}{f_{412}f'_{422} - f_{422}f'_{412}},$$

and the spectrum of $\Lambda$ values is determined by the non-linear equation

$$\begin{aligned} &\left[\left(f_{11d}f'_{22d} - f_{22d}f'_{11d}\right)\left(f_{211}f'_{321} - f_{321}f'_{211}\right) + \left(f_{21d}f'_{11d} - f_{11d}f'_{21d}\right)\right. \\ &\left.\times\left(f_{221}f'_{321} - f_{321}f'_{221}\right)\right]\left[f'_{41}(R)\left(f_{312}f'_{422} - f_{422}f'_{312}\right) + f'_{42}(R)\left(f_{412}f'_{312} - f_{312}f'_{412}\right)\right] \\ &+\left[\left(f_{11d}f'_{22d} - f_{22d}f'_{11d}\right)\left(f_{311}f'_{211} - f_{211}f'_{311}\right) + \left(f_{21d}f'_{11d} - f_{11d}f'_{21d}\right)\right. \\ &\left.\times\left(f_{311}f'_{221} - f_{221}f'_{311}\right)\right]\left[f'_{41}(R)\left(f_{322}f'_{422} - f_{422}f'_{322}\right) + f'_{42}(R)\left(f_{412}f'_{322} - f_{322}f'_{412}\right)\right] = 0 \end{aligned} \tag{B.8}$$

(like in the previous case, we have to exclude those solutions which result in zeros of $f_{21d}f'_{22d} - f_{22d}f'_{21d}$, $f_{311}f'_{321} - f_{321}f'_{311}$ and $f_{412}f'_{422} - f_{422}f'_{412}$).

In the large radius limit $R \to \infty$, $f_{L,n}(\rho)$ value near the sample edge is approximately equal to $\sqrt{e_1^2 + e_2^2}$, and $\Lambda$ is given by Eq. (B.5) with $d_{1(2)}$ replaced by $e_{1(2)}$.

# 4

# *Superconducting Wigner vortex molecule near a magnetic disk*

## 4.1 INTRODUCTION

Almost half a century ago, Abrikosov used the Ginzburg-Landau (GL) equations to predict that the magnetic field penetrates a type II superconductor in bundles arranged in a regular lattice, i.e. the vortex lattice [13]. Nowadays, it is well known that the motion of Abrikosov vortices gives rise to dissipation which is the limiting factor for the size of the critical current of a superconductor. The last decade has seen an increased interest in vortex matter in inhomogeneous superconductors, where defects (random and ordered) are used to pin the Abrikosov lattice in order to increase the critical current which is crucial for practical applications. Irradiation by heavy ions allowed to create dense random arrays of columnar defects which increased the critical current density [56]. Thanks to substantial progress in the preparation of magnetic microstructures in combination with superconductors [2], superconductor/ferromagnet hybrid systems became very interesting both theoretically and experimentally. In Ref. [88] Marmorkos *et al.* investigated the problem of a magnetic cylinder with out-of-plane magnetization embedded in a superconducting film. They solved the non-linear Ginzburg-Landau equation numerically, with appropriate boundary conditions, and found a correspondence between the value of the magnetization and the vorticity of the giant-vortex states.

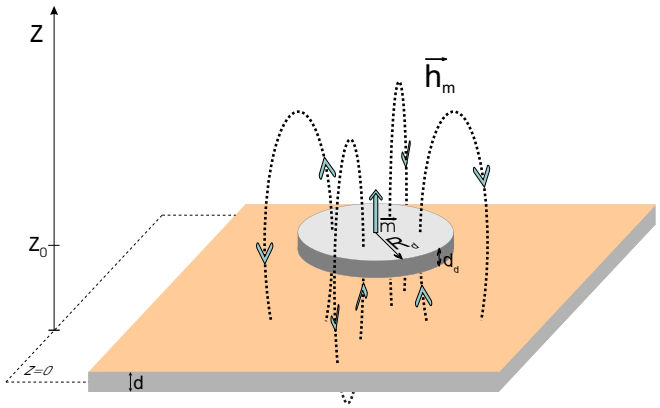


FIG. 4.1: Magnetic disk above a superconducting film: oblique view of the system.

More recently, the interest shifted to the pinning behavior of regular arrays of submicron ferromagnetic disks where additional pinning contributions arise due to the magnetic nature of the pinning centers [123, 124]. The most prominent feature of the vortex lattice pinned by a lattice of artificial defects is the existence of matching fields $H_n = n\Phi_0/S$, where $\Phi_0$ is the flux quantum, and $S$ is the area of the primitive cell of the artificial lattice. For matching fields, the number of vortices per unit cell of the artificial lattice becomes an integer number. As expected, such a vortex lattice is pinned much stronger by such artificial defects and the film resistivity exhibits deep minima [123] at those matching fields. These artificial pinning arrays were successfully used to gain insight into the macroscopic commensurability effects, but the origin and microscopic nature of this phenomena have not yet been fully explained. Moreover, the role of the self-magnetic field of a ferromagnet in the vicinity of the superconductor is not fully understood.

Therefore, in this chapter we consider the interaction between a single ferromagnetic disk (FD) and a superconducting thin film (SC) (see Fig. 4.1), within the non-linear GL theory. The FD lies on top of the superconductor ($xy$ plane) and it is magnetized in the positive $z$-direction. To avoid the proximity effect and exchange of electrons between FD and SC we separate them by a thin layer of insulating oxide, as is usually the case in experimental conditions. Moreover, we consider the magnetic disk to be made of a hard magnet whose uniform magnetic moment and internal currents are not affected by nearby circulating supercurrents. The ferromagnetic disk is the only source of magnetic field and we study in detail how the system is perturbed in the neighborhood of the disk. The creation of vortices due to this field, as well as their behavior strongly influence the pinning of additional external flux lines. Furthermore, we find new ordered vortex/antivortex structures.

## 4.2 THEORETICAL FORMALISM

For thin superconductors ($d < \xi, \lambda$) it is allowed to average the GL equations over the film thickness and write them as

$$\left(-i\vec{\nabla}_{2D} - \vec{A}\right)^2 \Psi = \Psi\left(1 - |\Psi|^2\right), \tag{4.1}$$

$$-\Delta_{3D}\vec{A} = \frac{d}{\kappa^2}\delta(z)\,\vec{j}_{2D}, \tag{4.2}$$

where

$$\vec{j}_{2D} = \frac{1}{2i}\left(\Psi^*\vec{\nabla}_{2D}\Psi - \Psi\vec{\nabla}_{2D}\Psi^*\right) - |\Psi|^2\,\vec{A}, \tag{4.3}$$

is the density of superconducting current and $\vec{A}$ is the total vector potential from the FD and supercurrents, with boundary condition $\vec{A} = 0$ far away from the FD. Here the distance is measured in units of the coherence length $\xi$, the vector potential in $c\hbar/2e\xi$, and the magnetic field in $H_{c2} = c\hbar/2e\xi^2 = \kappa\sqrt{2}H_c$. The indices $2D$, $3D$ refer to two- and three-dimensional operators, respectively. In order to ensure time relaxation and convergence of our calculation, we add the time derivatives of the order parameter and the vector potential to the left-hand sides of Eqs. (4.1-4.2), respectively. To solve the system of Eqs. (4.1-4.2), we apply a finite-difference representation of the order parameter and the vector potential on a uniform Cartesian space grid (x,y), with typically 512 grid points along the width of the rectangular simulation region $L_{x(y)}$, and use the link variable approach [44], and an iteration procedure based on the Gauss-Seidel technique to find $\Psi$. The vector potential is then obtained with the fast Fourier transform technique. The first GL equation is solved with an iteration procedure [45]. The dimensionless Gibbs free energy is calculated as $F = V^{-1}\int(2(\vec{A} - \vec{A}_0)\vec{j}_{2D} - |\Psi|^4)d\vec{r}$, where integration is performed over the primitive cell volume $V$, and $\vec{A}_0$ is the applied vector potential, i.e. the vector potential of the magnetic disk. The periodic boundary conditions for $\vec{A}$ and $\Psi$ have the form [43]

$$\vec{A}(\vec{\rho} + \vec{b}_i) = \vec{A}(\vec{\rho}) + \vec{\nabla}\eta_i(\vec{\rho}), \tag{4.4}$$

$$\Psi(\vec{\rho} + \vec{b}_i) = \Psi exp(2\pi i\eta_i(\vec{\rho})/\Phi_0), \tag{4.5}$$

where $\vec{b}_i$, $i = x, y$ are the lattice vectors, and $\eta_i$ is the gauge potential which cannot be chosen freely but must preserve the single valuedness of $\vec{A}$ and $\Psi$. These boundary conditions mean that $\vec{A}$, $\Psi$ are invariant under lattice translations combined with specific gauge transformations [43]. Other quantities, such as the magnetic field, the current and the order parameter density are periodic. Since far from the magnetic disk its vector potential vanishes, we choose $\eta_x = 0$, $\eta_y = 0$. The simulation region is typically hundred times larger than the magnetic disk, i.e. $L_x >> R_d$, which implies the quantization of the flux,

namely total flux through the superconductor equals zero. These boundary conditions result in a periodic repetition of not only the superconductor but the magnetic disk lattice as well. However, due to the large simulation region, these disks are far from each other and we are allowed to treat this problem as a single disk on top of an infinite superconductor.

## 4.3 CIRCULAR MAGNETIC DISK CASE

### 4.3.1 Shell vortex structure

To find the different vortex configurations, which include the metastable states, we search for the steady-state solutions of Eqs. (4.1) and (4.2) starting from different randomly generated initial configurations. Then we increase/decrease slowly the magnetic moment of the magnetic disk $m$ and recalculate each time the exact vortex structure. We do this for each vortex configuration in a magnetic moment ($m$) range where the number of vortices remains constant. By comparing the Gibbs free energies of the different vortex configurations we obtain the ground state. The results are shown in Fig. 4.2 for the magnetic disk with radius $R_d/\xi = 1$ and thickness $d_d/\xi = 0.5$, on top of the superconductor with thickness $d/\xi = 0.5$. The magnetic moment is expressed in units of $m_0 = c\hbar\xi/2e = H_{c2}\xi^3$. Demagnetization effects are taken into account in this calculation and the Ginzburg-Landau parameter $\kappa$ was chosen to be 1, which

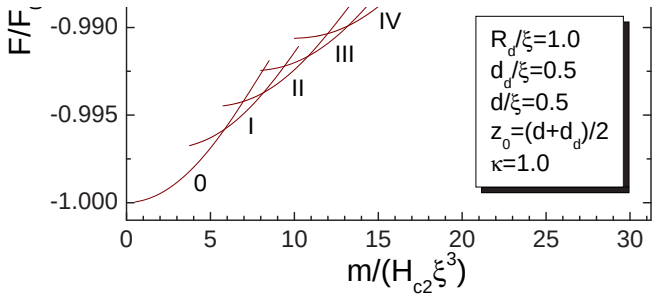


FIG. 4.2: The Gibbs free energy as a function of the magnetization of the dot placed on top of the superconductor. Top axis shows the flux from the positive stray field area of the magnetic dot as captured by the superconductor.

approximately corresponds to the experimental values found for Pb, Nb, or Al films.

As one can see, with increasing magnetization of the dot, the ground state goes through states denoted by successive Roman numbers. As we have shown in the previous chapter of this thesis, in the case of a finite extend of the superconducting film, i.e. mesoscopic disks, with a magnetic dot on top, the Roman numbers correspond to the vorticity of the ground state. However, in that case, the total flux penetrating the superconductor is positive, and therefore, the states with positive vorticity dominate the free energy diagram. In the present case, the magnetic dot is on top of an infinite SC film, and consequently all flux is captured by the superconductor. Since the magnetic field changes polarity in the vicinity of the edge of the magnetic disk, the total penetrating flux equals zero. Due to phase conservation, vortices cannot appear individually, but only as vortex-antivortex pairs. The vortex is located under the dot, and the antivortex just outside the positive field region. In Fig. 4.2, each new vortex state corresponds to the appearance of a new vortex-antivortex pair. Because the magnetic dot is rather small, vortices are strongly confined by the positive magnetic field under the dot, and the symmetry of the applied field imposes the creation of a giant-vortex as an energetically favorable state, while antivortices are symmetrically arranged on a ring around the central vortex (see Fig. 4.3). The Cooper pair density contourplots in Fig. 4.3 show the states in question for the particular value of the magnetization when they become the ground state, namely at the crossing points of the free energy curves shown in the Fig. 4.2. Please note that the total vorticity always equals zero and that

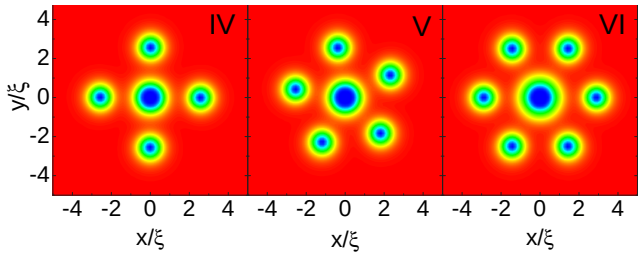


Fig. 4.3: Contourplot of the Cooper pair density (red/blue - high/low density) for the ground state vortex configurations corresponding to those in Fig. 4.2. A giant-vortex is surrounded by antivortices, and the total vorticity is equal to zero. Only 1/16 of the total simulation area is shown.

these multivortex configurations are similar to those found previously in the case of mesoscopic superconducting disks with a magnetic disk on top of it, when the superconducting disk is much larger than the magnetic dot radius (see Chapter 3).

The configurations shown in Fig. 4.3 are the result not only of the applied magnetic field, but also of the interaction between vortices. While the giant-vortex strongly attracts the antivortices, the antivortices repel each other. One therefore expects that the vortex configurations strongly depend on the size of the magnetic dot, since it determines the distance between the giant vortex and the antivortices.

### 4.3.2 Size-magnetization dependent "magic" numbers and other size effects

First, let us increase the magnetization of the magnetic dot. As we have stated before, the vortex configuration is determined by the balance between the giant vortex-antivortex attraction and the repulsion between antivortices. Because of that, it is clear that the number of antivortices in a ring around the giant-vortex cannot increase monotonously. Actually, the formation of a second, or even more rings is possible with increasing $m$. The results of our simulation are given in Fig. 4.4, for the states with $N = 7-12$, where $N$ denotes the number of antivortices. A second ring is formed when the number of antivortices reaches a saturation value $n_s$, in this case $n_s = 6$. This however does not mean that the

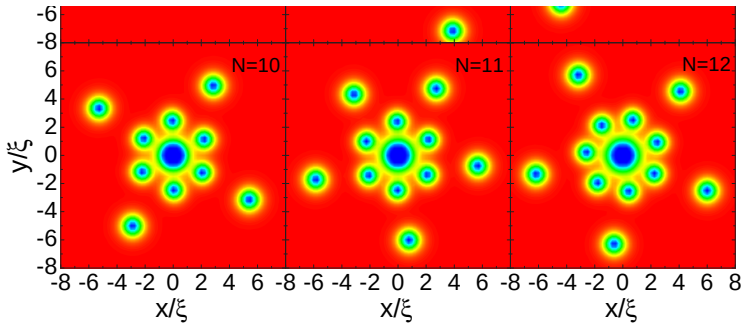


FIG. 4.4: The ground state vortex-antivortex configurations with increasing the magnetization of the disk: formation of the second ring of antivortices.

number of vortices in the first ring stays constant with increasing magnetization - one should remember that the vorticity of the giant vortex constantly increases and that the vortex-antivortex attraction becomes stronger. An example is the $N = 12$ state (see Fig. 4.4) where one more antivortex fits in the first ring to form the ground-state configuration.

Since the antivortices are arranged around the positive magnetic field region, the saturation number $n_s$ should depend on the size of the magnetic disk. Furthermore, for larger disks the wider area of the positive field region under the magnetic disk could allow the giant-vortex under the disk to split into individual vortices. Therefore, we investigated the influence of the disk size on the vortex structure of the superconducting film. We enlarged the magnetic disk from $R_d/\xi = 0.5$ to 5 keeping the thickness $d_d$ and the parameters of the SC fixed. In doing so, we obtain the equilibrium vortex phase diagram, shown in Fig. 4.5. Colored solid lines correspond to transitions between the successive $N$ states, and the thick dashed lines give the number of antivortices needed for the formation of an additional ring of antivortices. In the white (shaded) region the giant- (multi-) vortex state is found under the magnetic disk.

Notice that with enlarging the magnetic disk the number of antivortices needed before a new ring is formed increases, as expected. But, on the other hand a larger magnetic moment is needed for the appearance of a new vortex-antivortex pair in the ground state. However, the volume of the disk also

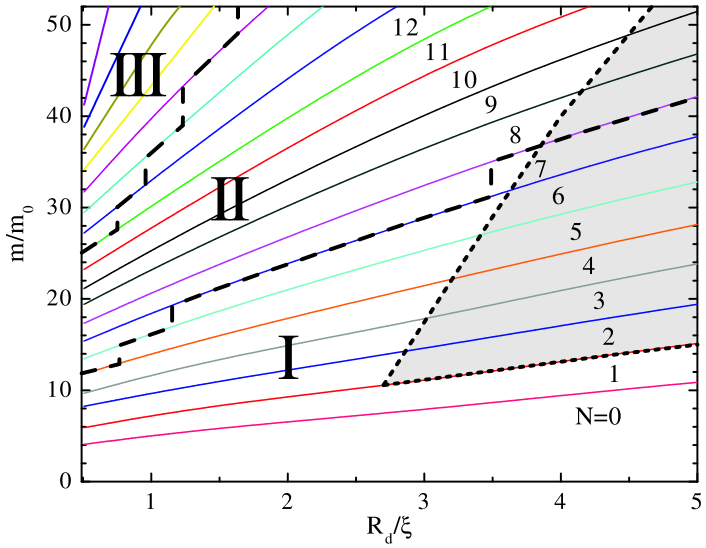


Fig. 4.5: Phase diagram: the relation between the radius of the disk, its magnetic moment, the number of antivortices (N), the number of antivortex rings (Roman numbers) and the vortex state under the magnetic disk (shaded area: multivortex state).

increases, which diminishes the effects of the magnetic moment increase. Therefore, we calculated the flux $\Phi^+$ through the SC, due to the positive part of the stray field in the $z = 0$ plane, namely in the center of the superconductor and up to the radius $R_0 \simeq R_d$ where the magnetic field changes its polarity. The top axis in Fig. 4.2 shows the value of this flux. Such a calculation tells us that if we keep the magnetic moment constant and increase the radius (volume) of the disk, the flux $\Phi^+$ decreases, making the positive (and negative) flux through the SC approximately constant along the transition line between the successive states in Fig. 4.5. Obviously, a larger flux is needed to create the first vortex-antivortex pair, i.e. $\Delta\Phi^+/\Phi_0 = 2.112$, due to the high stability of the Meissner state and the asymmetry of the $N = 1$ state (see Fig. 4.3). Further increase of the flux $\Phi^+$ decreases $\Delta\Phi^+$ and for larger $N$ it approaches the value $\Delta\Phi^+/\Phi_0 = 1.073$. Notice that the flux $\Phi^+$ is not exactly quantized in units of $\Phi_0$ which is a mesoscopic effect. The quantization condition $\Phi = \oint_C \vec{A} \cdot d\vec{l} = L\Phi_0$ cannot be used because it is not possible to construct a contour $C$ around the positive stray field region where the current is zero.

With increasing radius of the disk, the giant-vortex splits into individual vortices, as shown in Fig. 4.6(a). Figure 4.6(b) shows the phase of the superconducting order parameter, from which the location of the vortices and antivortices can be easily deduced. With increasing magnetic moment, these

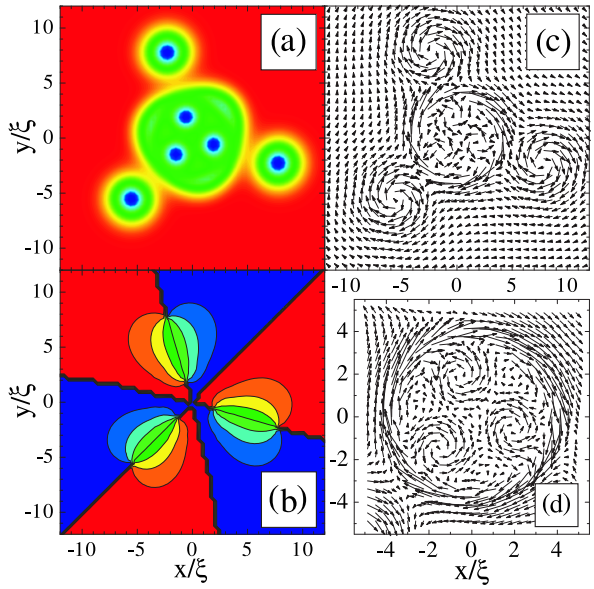


FIG. 4.6: Splitting of the giant-vortex under the disk into a multivortex: a) Cooper pair density, b) superconducting phase contourplot (zero - blue, $2\pi$ - red), for $N = 3$, $R_d/\xi = 4.0$, and $m/m_0 = 18.5$. (c) is a vectorplot of the corresponding supercurrents and (d) is an enlargement of the central area.

vortices move closer together, resulting ultimately in the formation of a giant-vortex. Figs. 4.6(c,d) show the current distribution in the SC: the supercurrents around each vortex and antivortex flow in opposite directions, which are determined by the direction of the change of the phase of the order parameter. However, the current around the central vortices (i.e. at the edge of the magnetic disk) has the same direction as the one around the antivortices, although the phase change implies otherwise. The reason is that the direction of this supercurrent is governed by the vector potential of the magnetic field of the ferromagnetic disk which is maximal near the edge of the disk. The value of the total current will be maximal in the same region.

To illustrate the complexity of the vortex configurations in this system, we repeat our calculations for larger magnetic disk, i.e. for the magnetic disk with radius $R/\xi = 4.5315$, and thickness $D/\xi = 1$, on top of a superconducting film with thickness $d/\xi = 0.1$ and Ginzburg-Landau parameter $\kappa = 1.2$. In our previous investigation we showed vortex structures for a small radius magnetic disk, in which case the multivortices under the disk collapse into a single giant vortex. In the present case (see insets of Fig. 4.7) of a large radius magnetic disk, the multivortex state is more energetically favorable than the giant vortex state. Individual vortices follow the circular symmetry of the magnetic potential and are arranged on a ring, close to the edge of the magnetic disk. The antivortices are situated on a larger ring outside the magnetic disk region (see insets of Fig. 4.7)). With increasing magnetization of the dot and fixed vortex state, the vortices come closer together while the antivortices move further away from the magnetic dot (see our calculations in the London approximation, Fig. 2.9). As was shown previously, the exact number of antivortices in the

Fig. 4.7: The free energy of the superconducting film with a **circular** magnetic disk on top of it. Insets show the Cooper-pair density of the different vortex-antivortex states (vortices under the disk, antivortices around, with total vorticity zero). $\Phi^+$ is the magnetic flux penetrating the area with positive magnetic field.

ring around the magnetic disk depends on the size of the disk and its magnetic moment. Due to the competition of the vortex-antivortex attraction and the repulsion between the antivortices, more than one ring of antivortices can be formed (see, for example, state VIII in Fig. 4.7). Note also the suppression of the superconductivity under the edge of the magnetic disk. In this region the induced currents in the SC are maximal, and the new vortex-antivortex pairs nucleate when the critical value of the parameters is reached.

### 4.3.3 Nucleation of vortex-antivortex pairs

In the previous sections we have shown the (anti)vortex configurations in this system, and their behavior depending on the parameters of this hybrid FM/SC structure. As we have emphasized before, the total vorticity in this system equals zero (equal number of vortices under the disk and antivortices in shells), due to the specific magnetic field profile of the magnetic disk and zero total flux penetrating the superconductor. Therefore, one question arises: how do new vortices enter the sample? In the case of finite superconductors, as we have shown in previous chapter, the vortices enter the sample from its boundary (see Fig. 3.10). In the present case, all the flux is captured by the superconductor and vortices and antivortices should appear simultaneously. To analyze the generation of new vortices, we start from one specific initial condition, for example, the ground state configuration for $N = 3$. Then we increase slowly the magnetic moment of the magnetic disk $m$ and recalculate the vortex structure

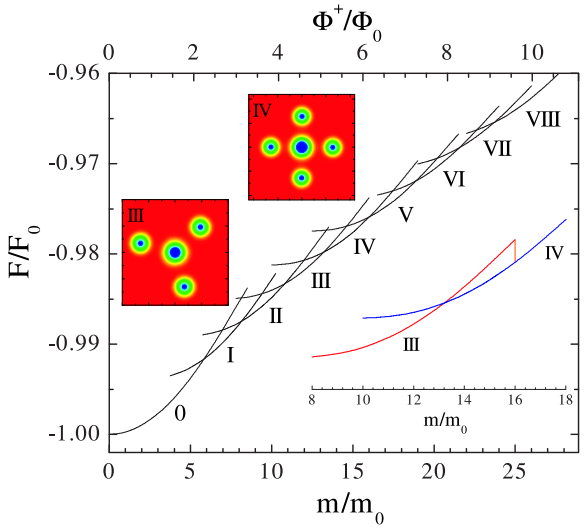


FIG. 4.8: The Gibbs free energy depending on the magnetic moment of the dot with $R_d/\xi = 2.0$ and $d_d/\xi = 0.125$ (same volume of the magnetic disk as in Fig. 4.2). Of particular interest is the transition from III to IV state (see contourplot insets) illustrated by orange line in the free energy zoom.

within $10^5$ iteration steps for each value of $m$, moving along the $N = 3$ energy line in Fig. 4.2, even in the metastable regime. In this way we can reach the magnetic moment for which the initial state changes from $N = 3$ to the $N = 4$ configuration (see Fig. 4.8) and we observe the nucleation of a new vortex-antivortex pair by plotting the intermediate results during the different iteration steps.

The result for the III→IV transition is shown in Fig. 4.9. The Cooper pair density plot in Fig. 4.9(a) shows only a distorted central vortex, but the superconducting phase plot (b) reveals the real vortex structure. Namely, in addition to the configuration similar to the state III, one can notice a vortex-antivortex pair nucleating under the edge of the dot. As presented in Fig. 4.9(i)-(v), further iterations in our calculation show that the vortex from this pair will move towards the central giant-vortex and eventually merge, and the antivortex moves to the periphery, causing the rearrangement of the shell of antivortices into the configuration IV. The nucleation of vortex-antivortex pairs under the edge of the magnetic disk is not a surprise, since the current induced in the superconductor due to the presence of the magnet is largest there (see Fig. 4.6(c,d)), and consequently, the order parameter is suppressed in a ring-like

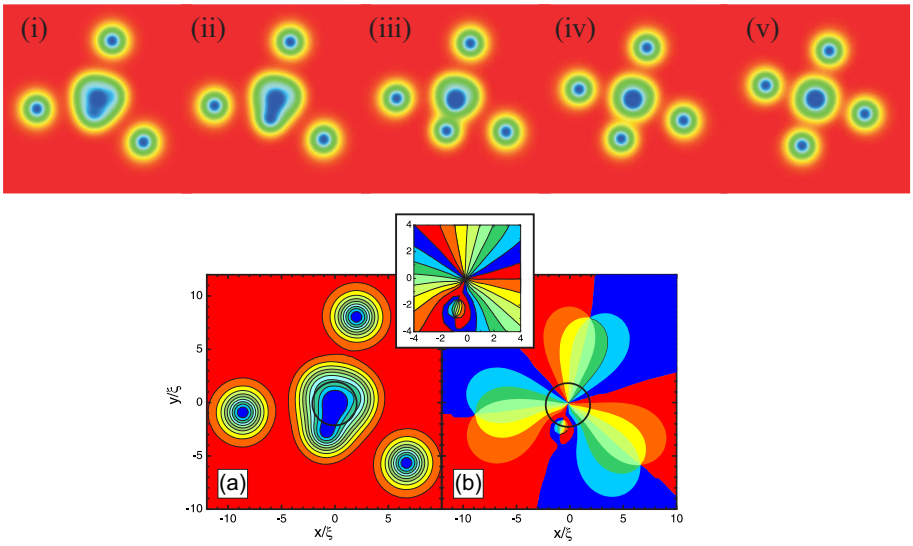


Fig. 4.9: (i)-(v) The Cooper pair density plots (red/blue - high/low density) illustrating generation of a new vortex-antivortex pair during evolution of the vortex configuration from $N = 3$ to $N = 4$ state (orange line in Fig. 4.8). (a) The Cooper pair density, and (b) superconducting phase contourplot (blue/red - zero/$2\pi$), as a snapshot from the transition. Black ring shows the edge of the magnetic disk. The inset shows an enlargement of the phase of the central area which more clearly shows the newly generated vortex-antivortex pair.

region under the disk edge in the Meissner state. However, the appearance of the vortex-antivortex pair is not directly associated to the induced current and the value of magnetization for which the maximal current under the disk reaches the depairing current. The critical conditions for vortex entry in this system will be thoroughly discussed in the next chapter of this thesis.

## 4.4 SQUARE MAGNETIC DISK CASE - THE VORTEX STATES IMPOSED BY THE MAGNET GEOMETRY

To investigate the effect of corners in the magnet geometry on the vortex/antivortex distribution, we considered a square magnetic disk, with the same thickness and volume as the circular magnetic disk of Sec. 4.3.2, namely $D/\xi = 1.0$, and $a/\xi = 8.0$ (see Fig. 4.10). The free energy and the contourplots of the Cooper-pair density are given in Fig. 4.11.

Note that the free energy does not change significantly, as compared to the case of the circular magnetic disk. The values of the magnetic moment of the magnet for which the transitions between the successive states occur are similar as well. However, the vortex configurations are considerably influenced by the geometry of the magnet. Since the vortices are confined by the magnetic potential under the disk, they are the ones mostly influenced by the shape of this magnetic "trap". In the circular magnet case (Fig. 4.7), all the vortex states were degenerate with respect to rotation, due to the circular shape of the magnet. This is not the case for the square magnetic disk, since the vortex-antivortex pairs occupy specific positions with respect to the corners of the magnet. For example, in the configurations I and II, vortices and antivortices are aligned along the diagonal of the magnetic square. In the state III, the symmetry of the vortex state is similar to the one of the circular magnetic disk

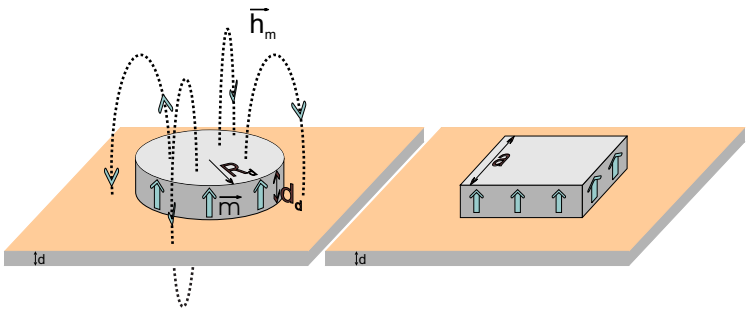


FIG. 4.10: Schematic view of a superconducting film (with thickness $d$) with a circular or square magnetic disk (with radius $R_d$ or size $a$, respectively, thickness $d_d$, and magnetic moment $m$) on top of it.

Fig. 4.11: The same as Fig. 4.7 but now for a **square** magnetic disk on top of the superconducting film.

in spite of the change of the magnet geometry. An interesting phenomenon happens for the state IV, where the vortices are placed along the diagonals of the square but the antivortices form a square which is rotated by 45°. The state IV shown in Fig. 4.11 is taken from the region close to the IV→V transition, and is slightly distorted due to the expected appearance of the new vortex-antivortex pair close to the top right corner.

Obviously, all the configurations have in common that the vortices prefer to sit near the corners of the magnetic square. The fact that the magnetic square-vortex interaction energy is lower along the diagonals of the magnet was shown previously within the London approach. Therefore, it is not surprising that in the state V, four vortices sit near the corners, while the fifth one is pressed into the center, as imposed by the magnet geometry, while the antivortices form a pentagon. In the case of the circular magnetic disk, both vortices and antivortices were arranged on rings, and they were situated across each other. In the present case, the specific vortex configurations are the result of the competition between the geometry of the magnetic confinement and the interaction between the (anti)vortices. In the state VI, the vortices are forming a structure compatible with the magnetic square, i.e. two overlapping equilateral triangles which are rotated by 180° with respect to each other. The antivortices in this case are also situated on equilateral triangles but with very different sizes. In fact three of the antivortices are almost situated in the middle of the sides of the big triangle. Alternatively, we may say that the antivortices form a two-ring structure. The state VIII consists of a square arrangement of vortices with additional vortices placed in the middle of the sides of the square while the antivortices form a deformed hexagon with additional two antivortices placed further away along the one of the diagonals.

## 4.5 CONCLUSIONS

To summarize, we applied the coupled, non-linear Ginzburg-Landau equations to investigate the vortex structure of a thin SC film with a magnetic disk on top of it. We found that due to the inhomogeneity of the magnetic field of the magnetic disk, having a net total zero flux through the superconductor, the most energetically favorable superconducting state always consists of vortex-antivortex pairs, with total vorticity equal to zero. In such a situation, we investigated the generation and evolution of the equilibrium vortex configurations. For smaller magnetic dots, a giant vortex is formed under the dot which is surrounded by single antivortices. With increasing the magnetization of the dot, the superconductor goes through successive vortex states, where the vorticity of the giant-vortex and the number of antivortices increase. However, for given size of the dot and sufficiently large magnetic field, the number of antivortices reaches a critical value, when the repulsion between them imposes their rearrangement: instead of a single ring, they are distributed over two (or more) concentric circles around the giant-vortex. This critical number of antivortices depends both on the magnetization and the size of the magnetic dot. Further, with increase of the dot size, not only do antivortices rearrange, but it is even possible that the giant-vortex splits into multivortices. With increasing magnetic field vortices move to the center of the dot, tending to merge, while antivortices are repelled further from the dot. The multivortex under the magnetic disk as well as the antivortex shells are significantly influenced by the magnet geometry. Vortex configurations tend to conform with the imposed geometry. Regardless of the magnet shape, new vortex-antivortex pairs nucleate in the sample under the edge of the magnetic disk, where the induced current in the superconductor is maximal. We described the dynamical process of nucleation of new vortex-antivortex pairs and gradual evolution of the vortex state between two stable states, where the vortex from the new pair merges the central giant-vortex (for small magnetic disks), and the antivortex moves to the periphery, causing the rearrangement of the shell of antivortices into the stable configuration.

The predicted new vortex configurations can be observed experimentally by using e.g. scanning probe techniques like Hall and Magnetic Force Microscopy. Furthermore, these vortex structures will influence the pinning properties and the superconducting phase diagram [8].

**Publications.** The results presented in this chapter were published as:

- M. V. Milošević and F. M. Peeters, *Superconducting Wigner vortex molecule near a magnetic disk*, Phys. Rev. B **68**, 024509 (2003).
- M. V. Milošević and F. M. Peeters, *Vortex Matter in the Presence of Magnetic Pinning Centra*, Journal of Low Temp. Phys. **130**, 3-4, 311-320 (2003).
- F. M. Peeters, B. J. Baelus, and M. V. Milošević, *Vortex states in mesoscopic superconductors*, Physica E **18**, 312-315 (2003).
- M. V. Milošević and F. M. Peeters, *Vortex-antivortex molecules near a magnetic disk on top of a superconducting film*, Physicalia Mag. **25**, 185-197 (2003).
- M. V. Milošević and F. M. Peeters, *Vortex molecules in superconducting films with magnetic disk on top - influence of the magnet geometry*, Physica C **404**, 281-284 (2004).

# 5

# *Superconducting films with regular arrays of magnetic pinning centers*

## 5.1 INTRODUCTION

The physics of vortex-antivortex pairs in superconductors and superfluids has been of general interest for a long time. For instance, such pairs are predicted to exist in thin superconducting films at finite temperatures due to thermal fluctuations [120]. Entropy considerations show that above the sharply defined Kosterlitz-Thouless transition temperature $T_{KT}$, these vortex pairs start to unbind, causing the appearance of a finite resistance. Recently it was shown that symmetry-induced antivortices can be formed in mesoscopic superconducting polygons [121] in a certain parameter-range, such that the vortex-antivortex configuration complies with the symmetry of the polygon. In the previous chapter of this thesis, we studied the vortex structure of a superconducting film with a single out-of-plane magnetized dot on top. The total flux penetrating the superconductor equals zero, and vortices cannot form in isolation; vortices and antivortices nucleate in pairs. A shell vortex structure was observed, with a vortex nucleus surrounded by an antivortex core (the so-called "vortex-molecule") with size-magnetization controlled magic numbers. These vortex configurations resemble the ones of electron dimples on the surface of liquid helium, electrons in quantum dots, colloidal suspensions and dusty particles in complex plasmas [122].

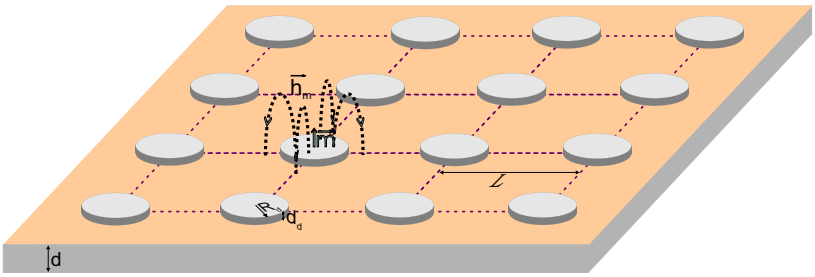


FIG. 5.1: The superconducting film (with thickness $d$) with a regular array of magnetic dots (radius $R_d$, thickness $d_d$, magnetic moment $m$ and period of the lattice $L$) on top of it: schematic diagram of the analyzed system.

Recent experiments [2, 81, 82, 124, 125] involving thin-film superconductors in a homogeneous external magnetic field have investigated the efficiency of ferromagnetic dots as nanosize artificial pinning centers. The most prominent feature of the vortex lattice pinned by the lattice of artificial defects is the existence of matching fields $H_n = n\Phi_0/S$, where $\Phi_0 = hc/2e = 2.07{\cdot}10^{-7}\ Gcm^2$ is the flux quantum, and $S$ is the area of the primitive cell of the artificial lattice. For matching fields, $H_n$, the number of vortices per unit cell of the lattice, $n$, becomes an integer number, the vortex lattice is pinned strongly, and the film resistivity exhibits deep minima [2, 123, 126]. Such effects are known to occur in regular arrays of empty holes in thin film superconductors [57]. The magnetization shows plateau-like behavior at $H_{n-1} < H < H_n$ with cusp- or peak-like magnetization anomalies at $H = H_n$ [57, 127, 128]. The vortex lattice in the presence of the square lattice of holes was observed using Lorentz microscopy in Ref. [62], where vortex configurations were found for integer $n = 1, 4$ as well as for fractional $n = 1/2, 3/2, 5/2$ matching fields.

Our analysis is within the framework of the phenomenological Ginzburg-Landau (GL) theory. Although this theory has only a firm mathematical derivation in a narrow range of magnetic field close to the superconducting-normal state boundary, it has been found that it gives also very good results deep inside the superconducting phase diagram [69, 106]. We investigated the superconducting state of a superconducting film (SC) thinner than penetration and coherence length with a regular magnetic dot (MD) lattice deposited on it, with or without an uniform perpendicular magnetic field. One of our aims is to investigate the matching phenomena (for integer and fractional matching fields) and their dependence on the size of the dots and distance between them. The magnetic dots are considered to be made of hard magnetic material whose uniform magnetic moment and internal currents are not affected by nearby circulating supercurrents. If the magnetic dots are the only source of magnetic

field, we study in detail not only how the system is perturbed in the neighborhood of the dots but also the ordering of the vortex/antivortex mixed state depending on the MD-lattice parameters. Attention will also be given to the fractional vortex states, distinguished from the integer ones by the fact that multiple possible degenerate states exist under MD-lattice symmetry transformations. The artificial pinning arrays were successfully used to gain insight into the macroscopic commensurability effects, but the origin and microscopic nature of this phenomena still lack complete explanation. To our knowledge, the role of the self-magnetic field of a FM in the vicinity of the superconductor is not fully understood and this is one of the important objectives of this thesis.

## 5.2 THEORETICAL FORMALISM

We consider a thin superconducting film immersed in an insulating media in a perpendicular uniform applied magnetic field $H_{ext}$. On top of the superconductor, a regular array of magnetic dots is placed, with periodicity $L$, where each of the dots exposes the SC to additional, inhomogeneous magnetic field $H_{md}$ (see Fig. 5.1). As we have shown in section 1.1.2.3, in thin films($d \ll \xi, \lambda$), it is allowed to average the GL equations over the film thickness and write them as

$$\left(-i\vec{\nabla}_{2D} - \vec{A}\right)^2 \Psi = \Psi(1 - |\Psi|^2), \tag{5.1}$$

$$-\triangle_{3D}\vec{A} = \frac{d\xi}{\lambda^2}\delta(z)\vec{j}_{2D}. \tag{5.2}$$

Here, the indices $2D$, $3D$ refer to two-dimensional and three-dimensional operators;

$$\vec{j}_{2D} = \frac{1}{2i}\left(\Psi^*\vec{\nabla}_{2D}\Psi - \Psi\vec{\nabla}_{2D}\Psi^*\right) - |\Psi|^2\vec{A}, \tag{5.3}$$

is the density of superconducting current in the plane ($\vec{\rho} = (x, y)$). We measure the distance in units of the coherence length $\xi$, the vector potential $\vec{A}$ in $c\hbar/2e\xi$, and the order parameter $\Psi$ in $\sqrt{-\alpha/\beta}$ with $\alpha$, $\beta$ being the GL coefficients [29].

In general, we took for the simulation region a rectangle, with area $S_s = L_xL_y$, where $L_x$, $L_y$ are the sides of the rectangle. In the present case, we considered $L_x = L_y = 16L$, where $L$ is the period of the square regular array of MDs deposited on top of the superconductor (i.e. we simulate a $16 \times 16$ supercell (in Fig. 5.1) $4 \times 4$ supercell is shown). The magnitude of the applied magnetic field $H = n\Phi_0/S_s$ is determined by the number $n$ of flux quanta $\Phi_0 = hc/2e = 2.07 \cdot 10^{-7}\ Gcm^2$ piercing through the simulation area ($S_s = L_xL_y$). The periodic boundary conditions for $\vec{A}$ and $\Psi$ result in [43]

$$\vec{A}(\vec{\rho} + \vec{b}_i) = \vec{A}(\vec{\rho}) + \vec{\nabla}\eta_i(\vec{\rho}), \tag{5.4}$$

$$\Psi(\vec{\rho} + \vec{b}_i) = \Psi exp(2\pi i\eta_i(\vec{\rho})/\Phi_0), \tag{5.5}$$

where $\vec{b}_i$, $i = x, y$ are the lattice vectors, and $\eta_i$ is the gauge potential. These boundary conditions imply that $\vec{A}$, $\Psi$ are invariant under lattice translations combined with specific gauge transformations. Therefore, the choice of gauge potential for given applied magnetic field is essential and will be discussed in the following paragraphs. Since the vector potential of a regular array of magnetic dots is periodic by itself, we choose $\eta_x = \eta_y = 0$. If the sample is exposed to an additional homogeneous perpendicular magnetic field $\vec{H}_{ext}$ ($\vec{H}_0 = \vec{H}_{md} + \vec{H}_{ext}$) we use the Landau gauge $\vec{A}_{ext} = H_{ext} x \vec{e}_y$ for the external vector potential and $\eta_x = H_{ext} L_x y$ while $\eta_y = 0$. Note that $H_{ext}$ may not be chosen freely and must fulfill the quantization requirement following from the virial theorem [43].

We solve the system of Eqs. (5.1-5.2) using the link variable approach [44] for a finite-difference representation of the order parameter and the vector potential on a uniform cartesian space grid $(x, y)$ with a typical grid spacing less than $0.1\xi$. The vector potential is obtained with the fast Fourier transform technique. The first GL equation is solved with an iteration procedure from Ref. [45]. The dimensionless Gibbs free energy is calculated as $F = V^{-1} \int (2(\vec{A} - \vec{A}_0)\vec{j}_{2d} - |\Psi|^4) d\vec{r}$, where integration is performed over the primitive cell volume $V$, and $\vec{A}_0$ is the applied vector potential (the magnetic field of the dots and/or external uniform magnetic field) which we use as the initial condition in our calculation (for details, see section 1.1.2.3).

## 5.3 COMMENSURATE VORTEX CONFIGURATIONS IN THIN SUPERCONDUCTING FILMS NANOSTRUCTURED BY SQUARE LATTICE OF MAGNETIC DOTS

In this section, within the phenomenological Ginzburg-Landau (GL) theory and the numerical approach described above, we investigate the vortex structure of a thin superconducting film (SC) with a regular matrix of low-magnetized (magnetic moment $m$), circular ferromagnetic dots (radius $R_d$) deposited on top of it, in a homogeneous external magnetic field. The low-magnetization condition leads to a low perturbation of the order parameter in the vicinity of the dots. In other words, possible appearance of vortices in this system is caused *only* by the external magnetic field. The main goal here will be to study the vortex pinning properties of such a magnetic dot lattice. One expects a large variety of different vortex configurations, depending on the size of the magnetic dots, their polarity, periodicity of the MD-rooster and the properties of the SC expressed through the effective Ginzburg-Landau parameter $\kappa_*$.

### 5.3.1 Asymmetric flux pinning at integer matching fields

Let us first concentrate on the matching effects when the number of external flux lines in our simulation region is an integer multiple of the number of pinning centers (magnetic dots). The exact vortex configuration depends not only on these numbers but also on the parameters of the dots, i.e. their size and magnetization. Bigger dots, or higher magnetization make it possible for each dot to pin more than one vortex (saturation number $n_s > 1$), and the magnetic field of the dot itself may be able to create extra vortex-antivortex pairs. In the present work we restrict ourselves to the case of weakly magnetized dots, with saturation number $n_s = 1$. All the dots have a circular shape, with radius $R_d = 2\xi$ and are arranged in a square lattice with $a = 10\xi$ period. The thickness of the magnetic dots and the superconductor in this calculation are $d_d = 0.1\xi$ and $d = 0.2\xi$, respectively. Demagnetization effects are taken into account, and the GL parameter $\kappa$ equals 1.2 (i.e. approx. value for Pb and Nb films). The results of our simulation are shown in Fig. 5.2 for the magnetic moment of each dot $m = 0.5m_0$ ($m_0 = H_{c2}\xi^3$) for two cases, when the applied magnetic field is parallel (left column of Fig. 5.2) or antiparallel (right column of Fig. 5.2) to the magnetic moment of the dots. First important feature that should be noted is that vortices are attracted by the magnetic dots in the parallel case (strong pinning) and repelled in the antiparallel case (weak pinning). Therefore, in the case of weak pinning, vortices are situated at the interstitial sites, which leads to a significant decrease in the critical current.

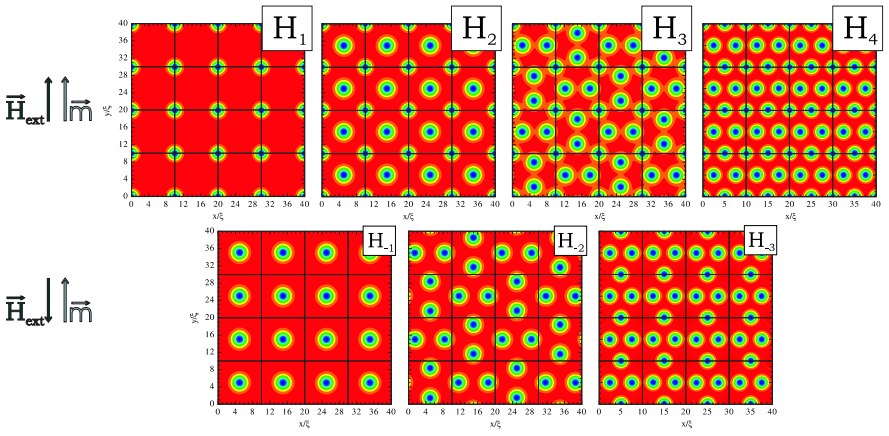


Fig. 5.2: Contourplots of the Cooper-pair density (blue/red color - low/high density) showing the arrangement of external flux lines when pinned by magnetic dots (with saturation number $n_s = 1$) for different matching values of the external magnetic field ($H_n$) in two cases: (i) for parallel alignment between the magnetic moment of the dots and the external field (upper figures, $n > 0$), and (ii) antiparallel case (lower figures, $n < 0$). Dotted lines illustrate the position of the magnetic dot lattice.

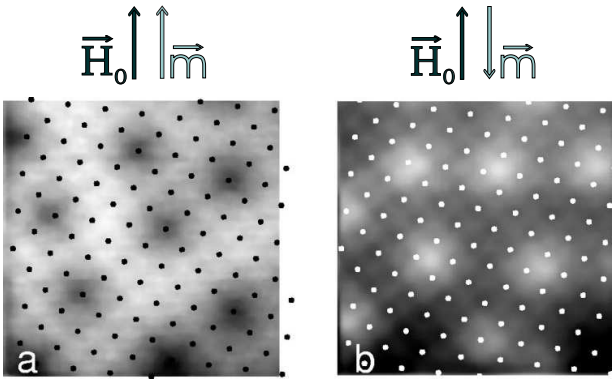


FIG. 5.3: SHPM images of a $(10.5\mu\text{m})^2$ area of the sample in $H_{ext} = -1.6$Oe (a) and $H_{ext} = 1.6$Oe (b), at $T = 6.8$K (field-cooled). The black/white dots indicate the positions of the magnetic dots, which are all aligned in the negative sense ($m < 0$). The flux lines emerge as diffuse dark ($H < 0$) or bright ($H > 0$) spots in the SHPM images [from Ref. [125]].

This phenomenon was recently observed experimentally by Van Bael *et al.* [125] using scanning Hall probe microscopy, and was referred to as an *asymmetric flux pinning* (see Fig. 5.3). In the parallel case, one notices that the vortex configurations for integer matching fields correspond to those found in the case of vortex pinning by regular arrays of antidots, as was reported in Ref. [62]. However, in the case of magnetic dots the distribution of the order parameter around the vortices at the magnetic dots and those at the interstitial sites is not the same. The vortex current and the screening currents induced by the dots partially compensate each other resulting in a smaller area of suppressed order parameter around the pinned vortices as compared to the one of the interstitial vortices.

One should notice that the vortex configurations for integer matching fields in the antiparallel case $H_{-n}$, correspond to those for $H_{n+1}$ in the parallel case, if the vortices pinned by the magnetic dots are ignored. This is understandable, since the magnetic dot in the antiparallel case repels the vortices and takes over the role of a pinned vortex in the parallel case. Presumably, this phenomenon will depend on the exact value of the parameters in the system, especially geometrical properties of the magnetic dots.

The field polarity-dependent pinning can be explained by considering a balance of several interactions. The most relevant energy contributions come from the magnetic dot-flux line interaction and the interaction between vortices themselves. The nature of the magnet-vortex interaction depends on the orientation of the magnetic moment as was thoroughly discussed in section 2.4 of this thesis, and this is the real cause of the polarity dependent pinning.

However, the exact vortex configurations depend not only on the magnet polarization, but also on its geometrical properties, magnetic strength, as well as the properties of the superconductor. Also, the question of vortices nucleated in the sample by magnetic dots should be addressed.

Field polarity-dependent pinning has also been observed in a superconductor with in-plane oriented magnetic dipoles, which we discussed in section 2.5.2. Those findings are also in agreement with the direct SHPM observations [93].

### 5.3.2 Vortex lattices at rational matching fields

As we have explained before, the virial theorem proposed by Doria *et al.* puts restrictions on our numerical approach and specific periodic boundary conditions, requiring integer number of flux lines piercing through the simulation region. So far, we have investigated pinning of external vortices for integer matching fields, where we had integer number of vortices per primitive cell of our simulation region. In principle, we can "throw" any integer number of vortices in the sample, where in some cases the number of vortices averaged over the number of primitive cells becomes a rational number. For example, in Fig. 5.4, we show few characteristic fractional states for the same parameters as in previous section, with slightly larger lattice constant ($L/\xi = 9.0$), for clarity. Note that for $H_{3/2}$ case, we have 1.5 vortices per cell, where besides the pinned vortices, the interstitial ones arrange in a $0-1-0-1$ manner. Similar phenomenon we found for $H_{5/2}$ rational field, where not only different number of vortices sit in the neighboring cells, but they feel each other's presence, preserving the diagonal symmetry of the vortex structure. In $H_{7/2}$ case, two-fold symmetry exists. The positions of vortices in these fractional states are stable, but due to the non-homogeneously distributed interaction-energy-profile, the pinning is much weaker than in the matching fields case. That is

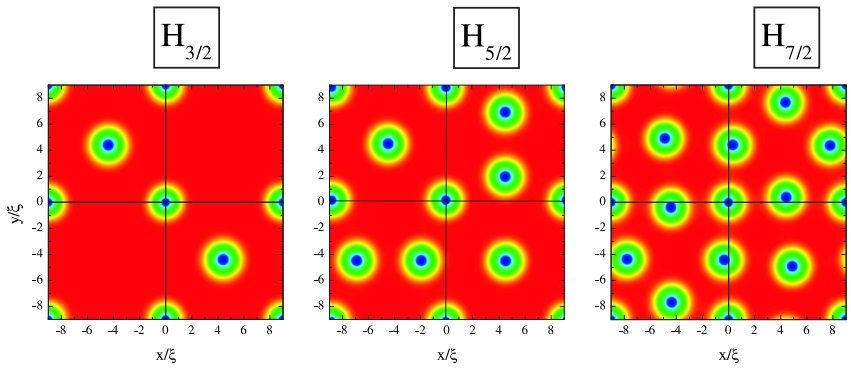


Fig. 5.4: Cooper-pair density plots, for the half-fractional matching fields, obtained in a simulation on a $2 \times 2$ supercell.

why the enhancement of the critical current at these rational fields is much less pronounced (see, for example Ref. [76]).

One should notice that the exact vortex structure for rational fields depends on the number of primitive cells in the simulation region $N_{cells}$. Not only that integer number of vortices is required, but the vortex structure must conform in some way with the magnetic dot lattice. For example, if we simulate 3 flux lines in a $2 \times 2$ unit-cell region, the stable solution cannot be reached, because the periodic boundary conditions cannot be fulfilled. Such (larger) simulation region must be used, in which found vortex structure will be periodic. Even in the case of $N_{5/2}$ shown in Fig. 5.4, if we periodically repeat the found solution and artificially create the $4 \times 4$ cell, the obtained vortex structure will reflect one of the possible metastable states (in order to get the ground state, the $2 \times 2$ cells should be rotated by $90^\circ$ with respect to each other). To conclude, we investigated several rational matching structures from phenomenological point of view. Finding all stable vortex patterns for rational fields is very complicated, and out of the scope of this thesis.

### 5.3.3 Dependence of the pinning phenomena on the magnetic lattice parameters

As we have emphasized before, the parameters of the magnetic dots have a crucial influence on the ground-state vortex configuration. Namely, bigger dots, or higher magnetization make it possible for each pinning center to pin more than one vortex. Here we investigated the arrangement of the external flux lines if the magnetic dots have radius $R_d = \xi$ and thickness $d_d = 0.5\xi$, and the thickness of the SC equals $\xi$. We fix the value of the external magnetic field to the fourth matching field $H_4$ and investigate the vortex structure of the SC film if the magnetic moment of the dots $m$ and the periodicity of the dot lattice $L$ are changed. The equilibrium phase diagram is given in Fig. 5.5.

For low magnetization of the dots, vortices are arranged in a commensurate structure as expectable for the fourth matching field (inset $IV$ in Fig. 5.5, see also Fig. 5.2). With increasing magnetization, we obtain more than *one vortex per site* pinning (pinned vortices form a giant vortex) and the remaining interstitial vortices reconfigure to lower matching structures ($III \rightarrow II \rightarrow I$). The vortex arrangement outside the magnetic dots is determined only by their number and does not depend on the number of vortices pinned by the dots. Finally, we end up in the first matching field configuration (I) with $L = 4$ giant vortices at each pinning site. One should also notice that with increasing period of the lattice it becomes more difficult for the pinning centers to capture the flux lines and higher dot magnetization is needed for the transitions between the successive matching configurations. With decreasing $\kappa^\star$ the critical magnetic moment of the dots decreases due to the reduction of the vortex-vortex repulsion.

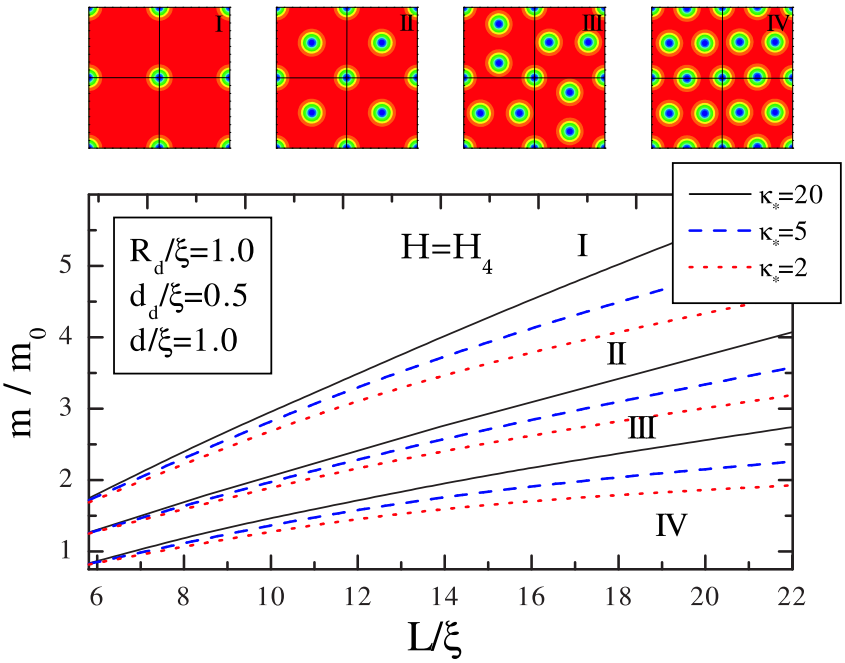


Fig. 5.5: The equilibrium vortex phase diagram: the dependence of the vortex configuration on the magnetic moment of the dots $m$, the period of the magnetic lattice $L$, and the effective GL parameter $\kappa^\star$. The top figures $(I - IV)$ illustrate the matching vortex structures in a 2x2 unit-cell region.

Larger magnetic dots, i.e. with larger radius $R_d$, not only favor pinning of multiple vortices per site, but the pinned giant vortex becomes less energetically favorable and may split into multiple flux lines, as illustrated in Fig. 5.6(a). In this particular case of the third matching field, two individual vortices are pinned by each pinning site, and are arranged in such a way that they form a low energy "zig-zag" vortex chain along the magnetic dot array and the interstitial vortices form a square lattice. Therefore, this can serve as a nice illustration that although pinned and interstitial vortices are separated by the magnetic potential of the dots, they indeed feel each other's presence.

For the corresponding antiparallel case ($H_{-3}$, see Fig. 5.6(b)) the vortex arrangement outside magnetic dots is determined not only by the number of vortices but also depends on the size of the magnetic dots which limits the available space. In the case shown in Fig. 5.6(b), the configuration of vortices does not correspond to the one for the interstitial vortices in the $H_4$ case, as found previously in section 5.3.1. We find a characteristic "zig-zag" vortex

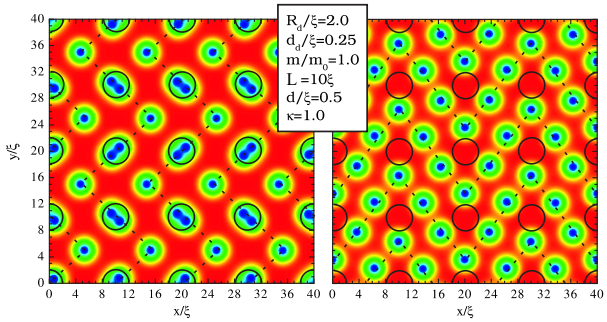


FIG. 5.6: Specific low-energy arrangement of vortices pinned by magnetic dot array, for the third matching field: (a) parallel, and (b) antiparallel case (circles illustrate the magnetic dots).

chain, which avoids the pinning sites. Therefore, as long as the vortex configurations are concerned, the magnetic dot in the antiparallel case takes over the role of the pinned vortex in the parallel case, only if they are comparable in size, i.e. for $R_d \sim \xi$.

It should be mentioned here that saturation number, i.e. the maximum number of vortices that each magnetic dot can pin, strongly depends on the radius of the dot. With increasing size, even for the same magnetic moment (and consequently smaller magnetization), larger magnetic dots pin more vortices, as was illustrated in Fig. 5.7. Due to the spread magnetic potential of such dots, the multivortex is formed under each dot, indicating that larger magnetic dots in the case of higher matching fields might exhibit some very interesting pinning phenomena, with vortex structure under the dot resembling the one of 2D confined mesoscopic superconductors.

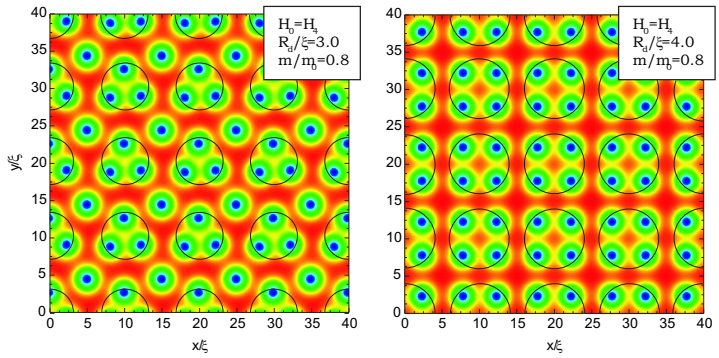


FIG. 5.7: Increasing saturation number of the magnetic dots with larger radius, illustrated in the case of a fourth matching field (circles denote the magnetic dots). The contourplots of the Cooper-pair density (blue/red - low/high density) show that even for fixed magnetic moment, larger magnetic disk pins more external flux lines.

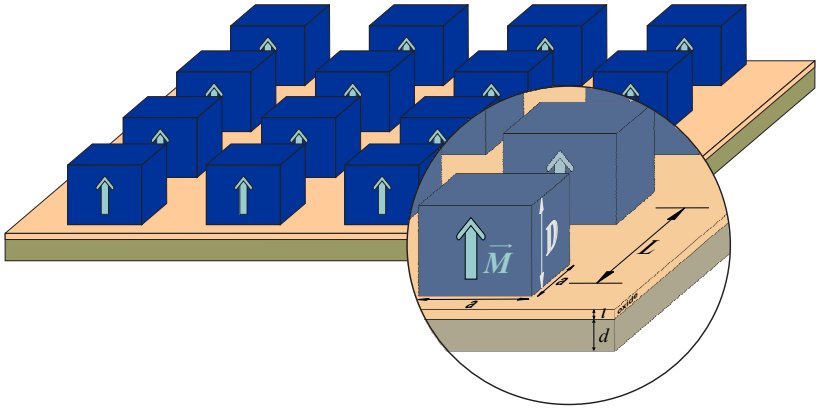


Fig. 5.8: Schematic view of the system: The superconducting film (and oxide layer, with thicknesses $d$ and $l$, respectively) underneath a regular array (with period $L$) of cubic magnetic dots (with size $a \times a \times D$).

## 5.4 VORTEX-ANTIVORTEX LATTICES IN SUPERCONDUCTING FILMS WITH MAGNETIC PINNING ARRAYS

So far, we considered only the magnetic dots with small magnetization, such that the order parameter is mainly perturbed by an external magnetic field. In this section, similarly to chapter 4, we discuss the vortex structure of a superconducting film with regular array of magnetic dots on top of it, in the absence of any external field. In particular, we will consider an array (with period $L$) of square magnetic disks with magnetization $M$ and size $a \times a \times D$ (see Fig. 5.8). We follow a numerical approach proposed by Schweigert *et al.* (see Ref. [45] and references therein) on a uniform Cartesian space grid (x,y) with typically 512 (1024 for larger samples) grid points in each direction. To find the different vortex configurations, which include the metastable states, we search for the steady-state solutions of two coupled GL equations starting from different randomly generated initial configurations. Then we increase/decrease slowly ("sweep up/down") the magnetization of the magnetic dots $M$ and recalculate each time the vortex structure. We do this for each vortex configuration in a magnetization range where the number of vortices remains constant. In addition, for given $M$, we recalculate the vortex structure of the film starting from the superconducting ($\Psi = 1$) or the normal state ($\Psi \approx 0$) as initial condition. By comparing the Gibbs free energies of all found vortex configurations we obtain the ground state.

### 5.4.1 States with integer number of vortex-antivortex pairs per unit cell

The $M-L$ equilibrium vortex phase diagram is shown in Fig. 5.9 for the case of a superconducting film with thickness $d = 0.2\xi$ (it is, for example, an adequate value for a 50nm Pb film at $T/T_c = 0.97$ [125]) and GL parameter $\kappa = 1.2$ (approximately corresponding to the experimental values found for Pb, Nb, or Al films) with a regular lattice of cubic magnetic dots ($a = 2\xi$, $D = 2\xi$) on top of it. As the period of the magnetic lattice $L$ is made smaller, the amplitudes of the magnetic field in the vicinity of the dots decrease, due to the compensation effects (for each dot, the magnetic field is positive under the dot and negative elsewhere). One should keep in mind that because of the perfect periodicity in our calculations, the $L = a$ situation (infinite magnetic film on top of a SC film) leads to the magnetic field equal zero everywhere. Therefore, in the leftmost part of Fig. 5.9, the threshold S/N transition magnetization decreases with increasing the distance between dots. In this region, we found that it

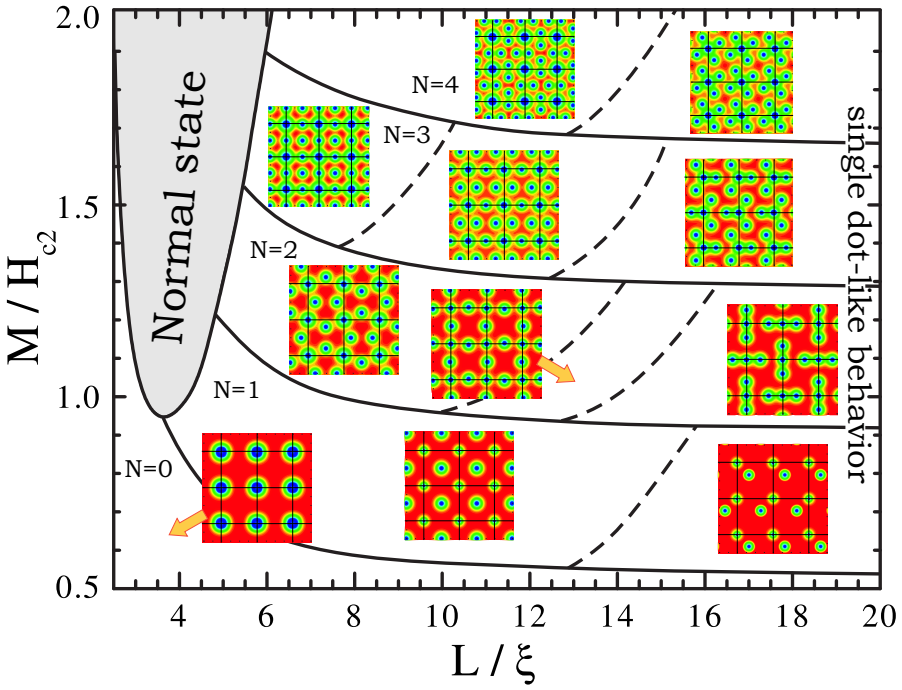


FIG. 5.9: Dependence of the vortex-antivortex configurations on the magnetization ($M$) and period of the magnetic dot (MD) lattice ($L$). Solid lines denote transitions between states with different number of vortex-antivortex pairs per unit cell ($N$), while dashed lines indicate second order configurational transformations for fixed $N$. The vortex structure is illustrated by the Cooper-pair density contourplots as insets, where the lines denote the unit cells of the MD lattice.

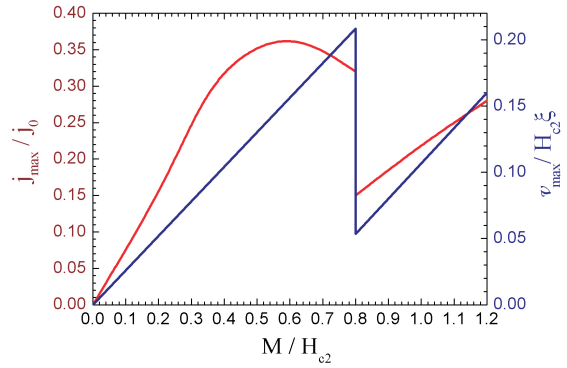


Fig. 5.10: The maximal value of the induced supercurrent in the sample (red curve) and the corresponding supervelocity (blue curve) as function of the dot magnetization.

is energetically favorable for the SC to go directly to the normal state with increasing magnetization $M$, without any vortices appearing in the sample.

Our analysis showed that the vortex nucleation is controlled by one single quantity: the supervelocity $\vec{v} = \vec{\nabla}\phi - \vec{A}$ (in dimensionless units) on the sample surface. It should be emphasized that with increasing $M$ the current density has its maximum under the magnetic dot edge and may reach the Ginzburg-Landau depairing current $j_{GL}$, however vortex-antivortex pairs do not enter the sample yet. With further increase of the magnetization, the current density slowly decreases (see Fig. 5.10). On the other hand, the supervelocity monotonously increases and as soon as its maximal value in the sample (also under the MD edge) reaches the critical value $v_{cr}$, a modulation instability of the superconducting order parameter occurs. However, for dense MD lattice (i.e. small $L$), the nucleated vortex and the antivortex under the dot edge (see section 4.3.3) are forced to sit close to each other, resulting in a huge superfluid velocity between them, leading again to exceeding the value of $v_{cr}$ (just opposite sign) and a new vortex-antivortex pair must be created (consequently annihilating with the previously existing one). The only escape for the superconductor from this dynamical process is a quick exit to the normal state. However, for larger period of the lattice $L$, for magnetization values when $v_{cr}$ is reached, the nucleated vortex-antivortex pairs at each magnetic dot are stabilized in a regular lattice, with vortices under the dots and antivortices placed at interstitial sites (see inset in Fig. 5.9). The critical magnetization necessary for the nucleation of the first vortex-antivortex pair is denoted in the lower part of the equilibrium vortex phase diagram in Fig. 5.9 by a solid line. Using magnetostatic calculations, we determined that along this line, the positive flux under each MD is approximately constant, and equals $\Phi^{+}_{0\mapsto 1}/\Phi_0 = 1.291 \pm 0.012$. Relating the vortex nucleation condition to the amount of applied flux is not a

surprise, since in thin SC films, due to the large effective GL parameter (in our case $\kappa_* = 2\kappa^2/d = 14.4$) the local magnetic field practically equals the applied one (consequently, under the MD edge $v \approx A_{md} \sim \Phi^+$). It appears that the positive magnetic flux necessary for the nucleation of the additional vortex-antivortex pairs is quantized in units of $\Delta\Phi^+/\Phi_0 = 1.07 \pm 0.01$. This value weakly depends on the parameters of the SC, but strongly on the properties of the magnetic field determined by geometrical data of the MDs (e.g. $\Phi^+_{0\mapsto 1}$ increases significantly with the size of the dots ($a$)). Although $\Phi^+_{0\mapsto 1}$ does not depend on the lattice parameter $L$, the nucleation mechanism is not immune to the distance between the dots. In the dense lattice case ($L < 10$, see Fig. 5.9) it is clear that vortex-antivortex pairs must nucleate somewhere under the dot edge, where the Cooper-pair density is strongly suppressed due to the maximal induced current there (see Fig. 5.9, $N = 0$ inset). We found that the local instability appears under the corners of the magnetic dots where this current (and consequently $v = j/|\psi|^2$) is maximal. From the results of our quasi-time-dependent simulation of such transition for $L/\xi = 5$, shown in Fig. 5.11, it is clear that this is the case under the corners of the magnetic dots. During the iteration procedure, pairs induce at opposite corners of neighboring dots, antivortices slowly move further from the dots (and under-confined vortices) forming a regular structure. However, in section 2.4.3 we have shown that in the case of a single square magnetic disk on top of a SC, the induced current has its maximum under the disk side, and the vortex-antivortex nucleation is assumed to occur there. This counterintuitive difference in vortex nucleation mechanism between the single dot and dot lattice cases follows from the current compensation due to the regularity of the lattice. Namely, the currents induced

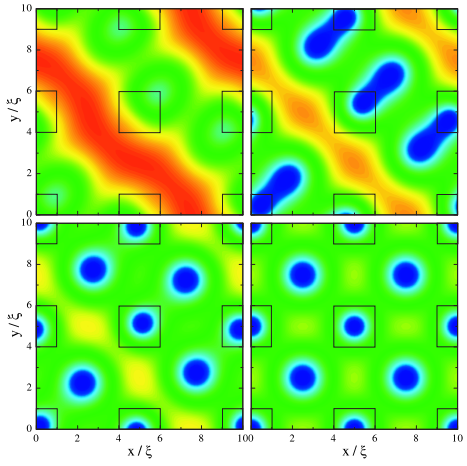


FIG. 5.11: The *nucleation* of the vortex-antivortex pairs under the magnetic dot edge and the formation of the regular lattice, for $L/\xi = 5$ case. All Cooper-pair density plots are given on the same scale: red color - $|\Psi|^2 = 1$, blue - $|\Psi|^2 = 0$.

in the SC by the neighboring dots compensate along the sides of the dots in the dense lattice case, leading to $v_{max}$ at the dot corners. With increasing $L$, the compensation diminishes, moving $v_{max}$ towards the central position under the dot edge.

Another salient feature of the regular magnetic lattice as a field source is the symmetry of the magnetic potential, causing formation of regular vortex lattices. As we stressed before, while the vortices are confined under the dots, the antivortices are situated at interstitial sites. The exact configuration depends on the number of nucleated vortex-antivortex pairs $N$ and the properties of the magnetic lattice ($a$, $L$, and $M$) as shown in Fig. 5.9. Solid lines indicate first order transitions between different $N$-states, while dashed lines denote the second order transitions within the same $N$-state. The physical mechanism causing the lattice arrangement of vortices in our sample is hidden behind the competition between three interactions: (i) MD-(anti)vortex (repulsion) attraction, (ii) the giant vortex-antivortex attraction, and (iii) the interaction between the interstitial antivortices themselves. One should notice that although both vortices and antivortices are present in our system, some of the lattices are similar to the ones observed experimentally for vortices pinned by regular array of holes (antidots) (see Ref. [62]). Moreover, the vortex-antivortex $N$-state configuration in some cases perfectly matches the $N + 1$ matching vortex configuration from Ref. [62] (see Fig. 5.9, for $N = 1$, 2 or 3 (hexagonal lattice case)). One difference is that in the case of Ref. [62] the hole-vortex attraction is balanced by the pinned vortex-interstitial vortex repulsion (contrary to interactions (i) and (ii) described above). Secondly, with increasing distance between the MDs, the vortex-antivortex lattice symmetry gradually breaks, leading to the Cooper-pair density profiles resembling the ones shown in chapter 4, in the case of a single magnetic dot on top of a SC. In the case of vortices and antidots, with increasing period of the pinning lattice its influence decreases and the Abrikosov vortex lattice takes over. Third difference is that in our case, for ground state configurations, only an integer number of vortex-antivortex pairs per unit cell is possible, as opposed to the rational matching effects found for vortices pinned by antidots.

### 5.4.2 Fractional states

In the previous section, the emphasis was on the vortex states with integer number of vortex-antivortex pairs per unit cell. However, the phase conservation condition, coming from the specific magnetic flux of the magnetic dots, is always satisfied for total vorticity zero, regardless of the number of the vortex-antivortex pairs. From the other point of view, in our simulations, all magnetic dots are treated equally, and all of them simultaneously reach the critical condition for (anti)vortex nucleation. Therefore, one expects equal number of vortex-antivortex pairs in each cell. The ground-state configurations shown in

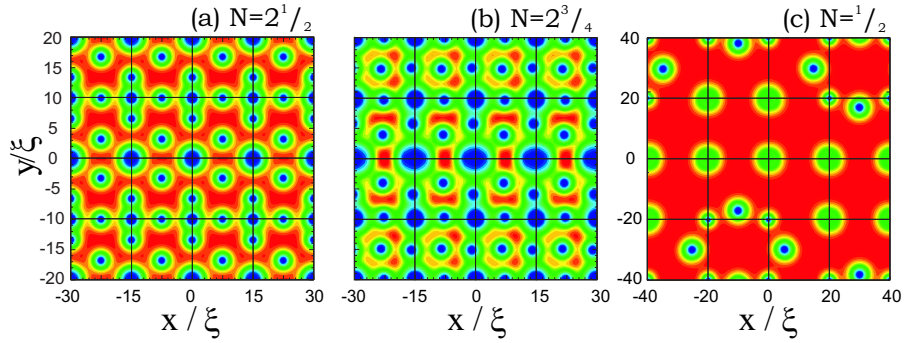


FIG. 5.12: The $|\Psi|^2$ contourplots of typical *fractional* vortex-antivortex states for the $4 \times 4$ unit cell simulation region.

Fig. 5.9 confirm such a claim. However, in the $N = 3$ case and for sparser magnetic lattice, one should notice that the distribution of antivortices does not obey the square symmetry imposed by the magnetic potential (cubic MDs). Because of that, some of the vortex-antivortex pairs may annihilate in order to preserve the square symmetry at expense of the energy. In such manner, *fractional* states are formed as metastable states, where some MDs "share" a vortex-antivortex pair, and consequently, the number of pairs per unit cell becomes a rational number. In Fig. 5.12(a,b) we show two typical fractional states for the square magnetic lattice $N = 2^1/_2$ and $N = 2^3/_4$. Note that the giant vortices under the dots now have different vorticities, while all the antivortices between them are the single flux lines. In Fig. 5.12(a), in odd rows, vortices have vorticity 2, and in even rows 3. Similarly, in Fig. 5.12(b), the central row contains vortices with vorticity 2, while all other giant vortices are triple. Note that in both figures vortices with lower vorticity have *larger* areas of suppressed order parameter around them. Apparently, lower vorticity facilitates the vortex core distortion by the surrounding antivortices.

The physical origin of these states we find to be mainly geometrical, since in case of a dense magnetic lattice (smaller $L$, see Fig. 5.9), the $N = 3$ lattice is very rigid, and no fractional states are found to be stable. To support this claim, we show in Fig. 5.12(c) the fractional $N = 1/_2$ state, found as metastable configuration for large magnetic dot lattice parameter $L$, when $N = 1$ state looses two-fold symmetry (see Fig. 5.9).

These states are expected to be favored energetically for large $\kappa_*$ values (in strong type II, or extremely thin superconductors) due to enhanced vortex-antivortex attraction.

## 5.5 EFFECTS OF THE MAGNETIC FIELD INTERPLAY ON THE CRITICAL PARAMETERS

In the case of the hybrid SC/FM structure discussed in this chapter, exposed to the external magnetic field, one expects strong interplay of two magnetic fields - the inhomogeneous one resulting from the magnetic dots and the homogeneous background field. In the previous sections, we assumed either small magnetization of the dots, effectively diminishing their magnetic field, or zero background field. In what follows, the interaction of these magnetic field and their influence on the critical parameters of the superconductor will be analyzed.

### 5.5.1 Magnetic-field-enhanced critical current

As we have shown in the previous section, sufficiently strong magnetic dots induce vortex-antivortex pairs in the superconductor, which follow the pattern imposed on them by the magnetic field profile. These vortex-antivortex structures strongly influence the pinning properties and the superconducting phase diagram. If one of the samples discussed in this chapter is exposed to a homogeneous external magnetic field, in cases when the number of additional flux quanta matches the number of antivortices at the interstitial sites, one expects that annihilation occurs, resulting in a well known matching vortex configuration with all remaining vortices pinned by magnetic dots. This leads to a peak in the critical current, as a function of the applied external field.

In order to verify this, we exposed our sample with $L/\xi = 6.25$ to the homogeneous magnetic field corresponding to the first matching field (one vortex per unit cell) and changed gradually the magnetization $M$, starting each time from the normal state. Then we apply current in the $x$-direction as $A_{cx} = const.$ (now $A_0 = A_{md} + A_{ext} + A_c$) which does not interfere with our boundary conditions, measuring the resulting current of the system. When the critical value of $A_{cx}$ is reached, the motion of (anti)vortices can no longer be prevented and superconductivity is destroyed. The results of our calculations for the critical current $j_c$ as a function of the magnetization of the magnetic dots are shown in Fig. 5.13 for the sample with and without applied first matching field. If no external field is present (dark dots in Fig. 5.13), $j_c$ monotonously decreases, starting from the value of the depairing current $j_{GL}/j_0 = 0.38$ ($M = 0$, pure SC film case). The appearance of vortex-antivortex pairs decreases the total current in the sample and leads to somewhat enhanced critical current which decreases further with magnetization and tends to zero. On the contrary, in the case of the applied first matching field (open dots in Fig. 5.13) the critical current equals zero if no pinning is present, since for $M = 0$ vortices are free to move, causing dissipation. With increasing magnetization, the antivortex-like currents induced in the sample by magnetic dots are increasing, compensating the current of external vortices pinned by the dots. Therefore, for $M/H_{c2} = 0.418$

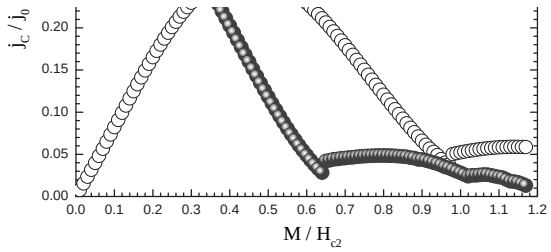


FIG. 5.13: Critical current (in units of $j_0 = cH_{c2}\xi/4\pi\lambda^2$) versus the magnetization of the magnetic dot lattice ($a/\xi = 2$, $D/\xi = 2$, $L/\xi = 6.25$) in the case of no applied external magnetic field $H_{ext}$ (dark dots) and for the first matching field (open dots).

the compensation of the currents is maximal, and the critical current reaches its extreme value. Notice that the value of GL current cannot be achieved, since the magnetic-dot-induced and the vortex currents cannot fully compensate due to their different profiles. With further increased magnetization, the qualitative behavior of $j_c$ is similar to the $H_{ext} = 0$ case. Nevertheless, if external magnetic field is present, the critical current of the sample for given $M$ is found to be actually *higher*. This demonstrates that, contrary to conventional superconductors, the superconductivity in SC-FM heterostructures is effectively *enhanced* by an applied magnetic field.

### 5.5.2 Magnetic-field-induced superconductivity

When the applied magnetic field exceeds a certain threshold value, superconductivity is suppressed. This general property of superconductors sets strong limits for their practical applications, since, in addition to applied magnetic fields, the current sent through a superconductor also generates magnetic fields, which can lead to a loss of zero resistance. Materials that are not only able to withstand magnetic fields, but in which superconductivity can even be induced by applying a magnetic field, are very rare and, to our knowledge, only $(EuSn)Mo_6S_8$, organic $\lambda$-$(BETS)_2FeCl_4$ materials and $HoMo_6S_8$ show this unusual behavior. This phenomenon was interpreted in terms of the Jaccarino-Peter effect [48], where the exchange fields from the paramagnetic ions compensate an applied magnetic field (for details, see Sec. 1.1.3).

Recently, Lange *et al.* [8] demonstrated experimentally what is now often referred to FIS (field-induced-superconductivity) effect. The basic idea is quite straightforward: a lattice of magnetic dots with magnetic moments aligned

along the positive $z$-direction is placed on top of a superconducting film. The magnetic stray field of each dot has a positive direction under the dots and a negative one in the area between the dots. Added to a homogeneous magnetic field $H_{ext}$, these dipole fields *enhance* the $z$-component of the effective magnetic field in the small area just under the dots and reduce total field everywhere else in the SC film, thus providing the condition necessary for the FIS observation (see Fig. 1.24). This new field compensation effect is not restricted to specific superconductors, so that FIS could be achieved in any superconducting film with a lattice of magnetic dots.

The sample consisted of a 85nm superconducting Pb film, covered by a 10nm Ge layer for protection from oxidation and the proximity effect between Pb and Co/Pd. The magnetic dots were made as Pd(3.5nm)/$[$Co(0.4nm)/Pd(1.4nm)$]_{10}$ multilayers, and arranged in a regular square array with period 1.5$\mu$m. All dots had a square shape (side length about 0.8$\mu$m) with slightly irregular edges. Knowing values of these parameters, we can apply our numerical approach to the investigated system.

In Fig. 5.14 the $H_{ext} - T$ diagrams are shown for demagnetized dots (a), as well as for the magnetic dots positively (b) and negatively (c) polarized. The $H_{ext}$-$T$ phase boundary is clearly altered by changing the magnetic state of the dot array. A conventional symmetric (with respect to $H_{ext}$) phase boundary is obtained for demagnetized dots (Fig. 5.14(a)) with kinks in the curve the first matching field (positive or negative, $H_{\pm 1}$), at which the applied flux per unit cell of the dot array is exactly one flux quantum. In contrast to that, the $H_{ext}$-$T$ boundary is strongly asymmetric with respect to $H_{ext}$ when the dots are magnetized in positive or negative directions (Figs. 5.14(b,c)). The maximum critical temperature was found for the second matching field $H_{ext} = 2H_1$ when $m > 0$ and to $-2H_1$ when $m < 0$. As one can see, the critical magnetic field of the superconductor at given temperature is *enhanced* by SC nanostructuring by magnetic dots. Obviously, the behavior of the system is analogous for opposite

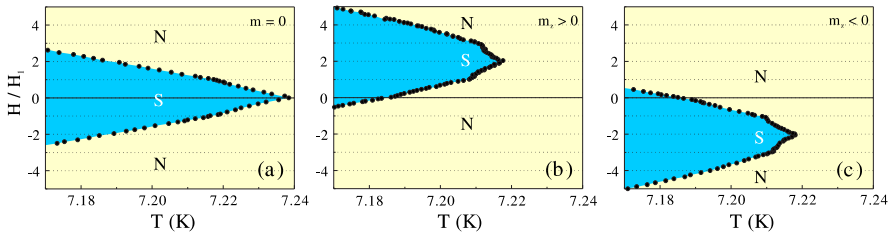


Fig. 5.14: Field - induced superconductivity (FIS) in a Pb film with an array of magnetic dots. Blue and yellow areas correspond to the superconducting (S) and the normal state (N), respectively. The $H_{ext}$-$T$-phase diagrams are obtained after (a) demagnetization ($m = 0$), (b) saturation of the dots in a large positive $H_{ext}$ ($m_z > 0$), (c) saturation in a large negative $H_{ext}$ ($m_z < 0$) [from Ref. [8]].

orientations of the magnetic moment of the dots. Therefore, in what follows, we focus only on the magnetic dots magnetized in positive $z$-direction.

The results of our theoretical approach described in preceding paragraphs are given in Fig. 5.15. The temperature is introduced in our calculation through the temperature dependence of the coherence length $\xi$, similarly to the approach used in section 3.7.1. One notices, that due to the dimensionless rescaling of GL equations, the value of coherence length in zero temperature is crucial for the outcome of the calculation. One more "free" parameter is the magnetization of the dots $M$. The best agreement between the experimental and theoretical $H_{ext} - T$ diagrams was obtained for $\xi(0) \approx 28$nm and magnetization value of $M = 3.32 \times 10^5$A/m. While the magnetization corresponds to expected values (between the Co and Pd values), the coherence length we found is rather small. However, it is well known that $\xi$ is hardly controllable quantity, and strongly depends on the preparation of the sample (small values of $\xi$ would correspond to "dirty" samples). Our results are shown in Fig. 5.15 as yellow dots. Notice that because of the so-called "virial theorem" [43], our approach works only for integer number of external flux lines per simulation cell. In this particular case, we used $4 \times 4$ supercell, so we were able to calculate the phase boundary only in points described by $H_{ext} = \frac{n}{16} H_1$, where $n$ is an integer number. The magnetic field of the magnetic dots does not alter our boundary conditions, since their total flux penetrating the superconductor equals zero.

The shape of the $H_{ext} - T$ phase boundary seems easily understandable. Lange *et al.* estimated the negative flux (of the MD stray field) between the magnetic dots to $\Phi^- \approx 2.1\Phi_0$ per unit cell. From the field compensation effect described above, one expects the maximal critical temperature when external

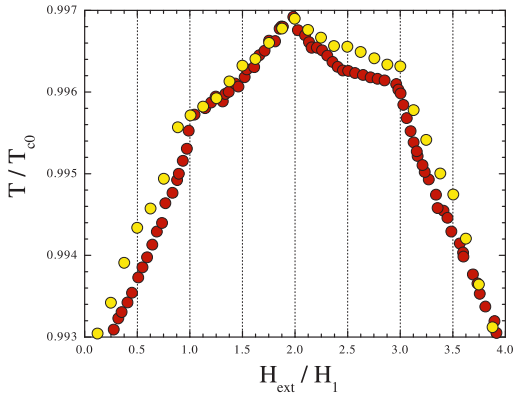


FIG. 5.15: The $H_{ext} - T$ diagram for the values of the parameters given in Ref. [8]. Red dots give the experimental data, and the yellow ones correspond to the theoretical results.

flux matches the flux of the negative stray field of the dots, which is indeed the case in Fig. 5.15. However, this effect is not related to the field-compensation, but the vortex-antivortex annihilation. In our calculation, the negative flux of the dots per unit cell was higher than $2.8\Phi_0$ and the behavior of the $H-T$ boundary was still same, with maximal $T_c$ found for the applied second matching field. Actually, we found same qualitative behavior for a range of magnetization of the dots, giving the values of the negative flux $\Phi^-/\Phi_0 = 2.21 - 3.22$. In this range of magnetization, each magnetic dot creates two vortex-antivortex pairs, vortices under the dots and antivortices at interstitial sites. Obviously, for the applied second matching field, the external flux lines annihilate with the interstitial antivortices, decreasing the total number of (anti)vortices in the sample and giving rise to the critical temperature. Similar phenomenon happens for the first and third matching field. For $H_{ext} = H_1$, one antivortex and one external vortex annihilate, leaving one antivortex per unit cell at the central interstitial position. This configuration is very stable and leads to the increase of $T_c$. On the other hand, for $H_{ext} = H_3$, antivortices disappear in interaction with two external vortices, and the third external flux line is pinned by the magnetic dot, together with two vortices remaining from the vortex-antivortex pairs. However, temperature fluctuations affect this vortex configuration much less than the one for $H_{ext} = H_1$, since antivortices at interstitial sites are easily pushed out of the equilibrium position. That is the reason for observed asymmetry in the $H-T$ boundary with respect to the second matching field for which the maximal critical temperature was found. Note that we also find small kinks in the phase boundary for rational fields, $H_{i/2}$, $i = 1,\ 3,\ 5,\ 7$, indicating interesting fractional vortex-antivortex configurations with positive net vorticity.

## 5.6 CONCLUSIONS

To summarize, we applied the complete, non-linear Ginzburg-Landau theory to investigate the vortex structure of a thin SC film with regular array of out-of-plane magnetic disks on top of it. In section 5.3, we assumed the small magnetization of the magnetic dots, and we exposed the sample to homogeneous external magnetic field. Therefore, the magnetic field of the dots is not sufficiently strong to create any vortices in the sample, but is able to pin the external flux lines, important for practical applications since due to decreased dissipation, such a pinning increases the critical current in the sample. We found that the vortex pinning properties of the magnetic dot firstly depend on its polarization. For parallel orientation of the magnetic moments with respect to the external magnetic field, vortices are attracted by the magnetic dots, and vice versa. Our findings are in agreement with experimental ones [125]. In the parallel case, first vortices are always pinned by the dots, until the saturation

number of the magnetic dots is reached. The following vortices arrange at interstitial sites, forming rigid lattices, similar to the ones found experimentally in the case of vortex pinning by arrays of antidots [62]. In the antiparallel case, vortices avoid the magnetic dots, and fill in the interstitial regions, again in a regular fashion. For small magnetic disks, not able to pin more than one vortex, we found that the vortex configurations for integer matching fields in the antiparallel case $H_{-n}$, correspond to those for $H_{n+1}$ in the parallel case, if the vortices pinned by the magnetic dots are ignored. Obviously, the magnetic dot in the antiparallel case repels the vortices and takes over the role of a pinned vortex in the parallel case. Naturally, this phenomenon depends on the exact value of the parameters in the system, especially geometrical properties of the magnetic dots. Namely, if the magnetization of the dots is increased, the saturation number of each dot increases as well, resulting in changed vortex configuration. Namely, starting from a higher matching field, with increasing magnetization, more vortices are pinned by the dots, while the remaining interstitial vortices arrange in a configuration typical for lower matching numbers (see Fig. 5.5). Increasing the size of the dots has similar effect, with difference that larger dot radius makes possible for multiple vortices to be pinned by each dot individually, not as a giant-vortex in the case of small magnetic disks. Although magnetically separated from other vortices, pinned vortices still feel their presence, arranging in low energy patterns. In the antiparallel case, larger size of the dots reduces the available space for vortices at interstitial sites, forcing them to form different "zig-zag" configurations. It should be emphasized that the saturation number of the dots depends on their radius, even for fixed magnetic moment. With increasing size of the dots, even though the magnetization decreases, the number of pinned vortices per dot increases.

In the following section, we considered the case of a thin superconducting film (SC), covered with a lattice of cubic out-of-plane magnetized magnetic dots (MDs). In this case, the accent was on vortex configurations induced in the sample by magnetic dots themselves, in the absence of any background magnetic field. Apparently, due to the phase conservation and the specific magnetic field profile of the dots with total flux penetrating the superconductor equal zero, isolated vortices can not appear and vortex-antivortex pairs nucleate in the sample. The vortices are confined to the MD regions, and antivortices form regular lattices at interstitial sites, which relax through several second order transitions towards single-dot vortex-antivortex configurations with increasing period of the magnetic array (see chapter 4). Creation of vortex-antivortex pairs with increasing MD-magnetization is controlled by a single quantity - the superfluid velocity. An effort to conform with the geometry of the imposed magnetic field at expense of the energy results in metastability of fractional states, where some of the magnetic dots share a vortex-antivortex pair. The predicted new vortex configurations can be observed experimentally by using e.g. scanning probe techniques like Hall and Magnetic Force Microscopy.

In the case of a superconducting sample nanostructured by magnetic dots in a homogeneous external magnetic field, we demonstrated that due to the vortex-antivortex pairs and the supercurrents induced by the MDs, the critical current in the sample actually increases when exposed to external magnetic field, contrary to conventional SC behavior. We also discussed the so-called magnetic field-induced-superconductivity, when the external magnetic field actually compensates part of the stray field of the dots, restoring superconductivity in those particular regions. We found that magnetic nanostructuring enhances the critical field of the sample, and explained it by vortex-antivortex annihilation which occurs when external flux lines interact with existing vortex-antivortex pairs induced in the sample by magnetic dots. The excellent agreement with experimental results [8] was demonstrated through $H_{ext} - T$ phase boundary, with several observed features that we explained from the point of view of characteristic vortex structure.

**Publications.** The results presented in this chapter were published as:

- M. V. Milošević and F. M. Peeters, *Commensurate vortex configurations in thin superconducting films nanostructured by square lattice of magnetic dots*, Physica C **404**, 246-250 (2004).
- M. V. Milošević and F. M. Peeters, *Vortex-Antivortex Lattices in Superconducting Films with Magnetic Pinning Arrays*, submitted to Phys. Rev. Lett.

# *Summary*

In this thesis we investigated theoretically the vortex structure, flux pinning and the critical parameters of magnetically textured superconductors. In particular, we considered mesoscopic superconducting samples (disks and thin films) with single or regular arrays of ferromagnets on top, with sizes comparable to one of the two characteristic length scales: the coherence length $\xi$ or the magnetic penetration length $\lambda$. Mesoscopic superconductors became very interesting study objects in the last decade, since the critical parameters and the vortex configurations of such samples are determined not only by the material and the properties of the external field, but also by the shape of the boundary and the characteristic sizes of the sample.

All material presented in this thesis is concentrated around one key question: *What is the effect of magnetic nanostructuring on the superconducting properties*?

First of all, it is well known that vortices in superconducting films (and bulk samples) arrange in a triangular lattice (so-called Abrikosov lattice) due to the mutual interactions between the vortices. However, even the smallest fluctuations in the system would cause vortices to move, increase dissipation and reduce all important superconducting effects. Therefore, for practical applications, it is crucial to prevent motion of vortices. In this respect, magnetic particles on (in) the sample can serve as excellent **artificial pinning centers**, because of the interaction of their magnetic field with the vortices present in the superconductor. At the same time, this inhomogeneous stray field of the

magnet(s) may strongly modulate the order parameter in the underlying superconductor. The fact that the total magnetic flux of each magnetic particle is zero, promises the appearance of a number of new phenomena, especially fascinating vortex-antivortex structures. Adding the possibility of different magnetic anisotropy of the magnets (for example, in- or out-of-plane magnetization) only enhances the **rich phenomenology** of these superconductor/ferromagnet hybrid systems. And last but not least, since the usefulness of a superconductor is determined by its critical parameters, the maximal temperature, current and magnetic field it can sustain, it is interesting to see how the magnetic nanostructuring influences its properties. One can expect that magnetic nanoengineering, through **local structuring of the magnetic field** in the sample could be a powerful tool for controlling the critical parameters of the superconductor.

In what follows, we summarize our theoretical findings in order they are presented in this thesis, *à-propos* above defined directions.

**Chapter 1** gives a short introduction to some theoretical and experimental aspects of superconductivity and magnetism. We present the derivation of the Ginzburg-Landau equations which are the central equations in the theoretical framework of this thesis. The characteristic length scales and the difference between type-I and type-II superconductors are discussed. For mesoscopic superconductors we define giant vortex and multivortex states, and the vorticity $L$ which characterizes the different vortex configurations. We also discuss briefly vortex pinning in type-II superconductors. The second part of this chapter is devoted to the basic concepts of magnetism and provides a description of magnetostatic calculations. Finally, the applications of hybrid ferromagnet/superconductor nanosystems and their experimental realizations are discussed.

**Chapter 2** concerns magnetic pinning of vortices in superconducting films (SC) by single magnets. We applied the London theory to investigate vortex interaction with a magnetic dipole (MD) or a finite-size ferromagnet (FM) above (or under) the SC. Depending on the direction of the dipole magnetic moment, we obtained exact analytic expressions for the MD-vortex interaction energy and screening currents. The asymptotic behavior of the interaction potential and the induced currents for specific values of the involved parameters are obtained, which is crucial for experiments. We calculated the pinning potential for both an in- and out-of-plane magnetized FMs. Our results show that an out-of-plane magnet attracts a vortex if aligned parallel to it, and opposite, for anti-parallel alignment the vortex is repelled. This is a consequence of the mono-directional superconducting current induced in the SC for out-of-plane magnetization of the FM. However, for in-plane magnetization, the FM-vortex interaction shows a dual behavior, namely, the vortex is attracted to the negative pole of the MD and repelled on the other side. Due to the dual behavior of the pinning potential, we explored the possible co-existence of vortices and antivortices in such systems. The total interaction energy calculation leads to

the conclusion that the vortex and antivortex are separated by an energy barrier due to the short range interaction with the magnet, and therefore, these pairs could be stable. Both in- and out-of-plane magnets are able to keep these vortices apart. We calculated analytically the interaction potential in the presence of vortex-antivortex pairs (or giant vortex-single antivortices) and gave estimates of the parameters necessary for stability of such fascinating configurations in a thin SC film.

In the following analysis, we considered the influence of the geometry of the magnet on flux pinning. In the case of a magnetic disk with an off-center hole we showed the existence of two local minima in the FM-vortex interaction energy - the ground state and the metastable one. We also showed that in the case of a FM disk with two touching holes ("eight-hole") two minima with equal energy but different vortex position appeared. The probability of a vortex sitting in one of these two states is the same, which makes this system interesting as a possible qubit. We also calculated the pinning potential for square and triangular shaped ferromagnets. A substantial breaking of the circular symmetry occurs and the attractive force acting on the vortex is stronger at the sides of the magnet than at the corners. Although counterintuitive, we showed that the vortex approaches the non-circular magnet rather along the corners than perpendicular to the sides, following the steepest energy-gradient.

Geometry also plays a significant role in the pinning properties of an in-plane magnetized FM situated above the SC. In the case of a magnetic stripe on top of a superconductor, we found that the equilibrium position for an external flux line pinned by the stripe lies in the channel, parallel to the magnetic structure. The exact position of this "equilibrium channel" depends on both thickness of the SC and the magnet. Also, all the flux lines of the same polarity are found to be pinned on the same side of the stripe. Therefore, using such a magnetic structure on top of a superconductor in the presence of a homogeneous magnetic field may lead to a superconducting region without vortices. In the case of finite size superconductors, if the pinning channel is relatively far from the stripe, the whole superconducting sample could be made vortex-free, which is highly important for applications.

For an in-plane magnetic bar as a pinning center, we discussed the field-polarity dependent pinning. We found that a vortex or antivortex in these systems are pinned on the opposite poles of the bar. However, on which pole the vortex will be pinned depends on the strength of the magnetization of the magnet and the possible presence of a vortex-antivortex pair induced in the SC by the magnet itself. Being more general, our results agree with the experiment of Ref. [93] and give directives for future experimental considerations of similar structures, since our analysis predicts that the position of the pinned vortex can be tuned by changing the strength of the magnetization of the FM.

In **Chapter 3** the superconducting state of a thin mesoscopic superconducting disk with a magnetic dot (or current loop) on top is described within the Ginzburg-Landau formalism. The superconducting disk is assumed sufficiently

thin so that the magnetic field produced by the superconducting currents can be neglected. The effects of the size and magnetization of the dot, and the size of the superconducting disk on the vortex configurations were investigated. Numerous phase transitions were found, between states with different angular momentum number and between giant and multivortex states, plus transitions in the ground state between different multivortex configurations (*giant-ring* and *giant-giant* multivortex states). Larger radius of the magnetic dot enhances the stability of the giant-giant multivortices, while enlarging the superconducting disk decreases the energy of the giant-ring multivortex state. In this case, the giant-giant multivortex states can also be the ground state but it represents a new configuration - a giant vortex surrounded by anti-vortices, and the *total* vorticity equals the lowest vorticity of the giant vortex states which are involved. We found that with an increase of the disk size, *re-entrant* behavior of the total vorticity is possible.

Adding a homogeneous background magnetic field, besides the stray field of the magnetic dot, brings a qualitative difference in the free energy diagram. When the external magnetic field has value between the average field of the dot in the positive and the negative region, we observe a strong interplay of the different superconducting states. Moreover, with increase of the thickness of the dot, we obtain two strong minima in the free energy as a function of the applied field, when the total field is approximately equal to zero in the $\rho < R_d$, and the $\rho > R_d$ region, respectively, where $R_d$ is the radius of the dot. After introducing the temperature in our calculation, a $H_{ext} - T$ phase boundary was constructed. We found that the effect of the inhomogeneous magnetic field on the nucleation of superconductivity is twofold: it shifts the phase boundary along the $H$-axis, as well as distorts the phase boundary along the $T$-axis, altering the values at which the structure switches between different vorticities. The calculated phase boundary is in perfect agreement with experimental data [7].

We further extend our approach in **Chapter 4** to investigate the vortex structure of an infinite superconducting film with a single magnetic dot on top. Due to the phase conservation and a net total zero flux through the superconductor, we found, within the Ginzburg-Landau theory, a shell-structured vortex-antivortex configuration with total vorticity zero. In such a situation, we investigated the generation and evolution of the equilibrium vortex configurations. For smaller magnetic dots, a giant vortex is formed under the dot which is surrounded by single antivortices. With increasing the magnetization of the dot, the superconductor goes through successive vortex states, where the vorticity of the giant-vortex and the number of antivortices increase. However, for given size of the dot and sufficiently large magnetic field, the number of antivortices reaches a critical value, when the repulsion between them imposes their rearrangement: instead of a single ring, they are distributed over two (or more) concentric circles around the giant-vortex. This critical number of antivortices depends both on the magnetization and the size of the magnetic

dot. Further, with increase of the dot size, not only do antivortices rearrange, but it is even possible that the giant-vortex splits into multivortices. With increasing the magnetization vortices move to the center of the dot, tending to merge, while antivortices are repelled further from the dot. The multivortex under the magnetic disk as well as the antivortex shells are significantly influenced by the magnet geometry. Vortex configurations tend to conform with the imposed geometry. Regardless of the magnet shape, new vortex-antivortex pairs nucleate in the sample under the edge of the magnetic disk, where the induced current in the superconductor is maximal. We described the dynamical process of nucleation of new vortex-antivortex pairs and gradual evolution of the vortex state between two stable states, where the vortex from the new pair merges the central giant-vortex (for small magnetic disks), and the antivortex moves to the periphery, causing the rearrangement of the shell of antivortices into the stable configuration.

We expect that the predicted new vortex configurations will be observed experimentally in the near future by using e.g. scanning probe techniques like Hall and Magnetic Force Microscopy. Furthermore, these vortex structures will influence the pinning properties and the superconducting phase diagram [8], as was demonstrated in **Chapter 5**. We applied the complete, non-linear Ginzburg-Landau theory to investigate the vortex structure of a thin SC film with regular array of out-of-plane magnetic disks on top of it. First, we assumed a small magnetization of the magnetic dots, and we exposed the sample to a homogeneous external magnetic field. In this case, the magnetic field of the dots is not strong enough to create vortices in the sample, it merely suppresses superconductivity under the magnetic dot. As a consequence, it is able to pin the external flux lines, important for practical applications since such a pinning increases the critical current in the sample. We found that the vortex pinning properties of the magnetic dot firstly depend on its polarization. For parallel orientation of the magnetic moments with respect to the external magnetic field, vortices are attracted by the magnetic dots, and vice versa. Our findings are in agreement with experimental ones [125]. In the parallel case, first vortices are always pinned by the dots, until the saturation number of the magnetic dots is reached. Subsequently vortices arrange at interstitial sites, forming rigid lattices, similar to the ones found experimentally in the case of vortex pinning by arrays of antidots [62]. In the antiparallel case, vortices avoid the magnetic dots, and fill in the interstitial regions, again in a regular fashion. For small magnetic disks, not able to pin more than one vortex, we found that the vortex configurations for integer matching fields in the antiparallel case $H_{-n}$, correspond to those for $H_{n+1}$ in the parallel case, if the vortices pinned by the magnetic dots are ignored. Obviously, the magnetic dot in the antiparallel case repels the vortices and takes over the role of a pinned vortex in the parallel case. Naturally, this phenomenon depends on the exact value of the parameters in the system, especially geometrical properties of the magnetic dots. Namely, if the magnetization of the dots is increased, the saturation number of each dot

increases as well, resulting in a changed vortex configuration. Namely, starting from a higher matching field, with increasing magnetization, more vortices are pinned by the dots, while the remaining interstitial vortices arrange in a configuration typical for lower matching numbers. Increasing the size of the dots has a similar effect, with the difference that a larger dot radius allows multiple vortices to be pinned by each dot individually, not as a giant-vortex in the case of small magnetic disks. Although magnetically separated from other vortices, pinned vortices still feel their presence, arranging in low energy patterns. In the antiparallel case, larger size of the dots reduces the available space for vortices at interstitial sites, forcing them to form different "zig-zag" configurations. It should be emphasized that the saturation number of the dots depends on their radius, even for fixed magnetic moment. With increasing size of the dots, even though the magnetization decreases, the number of pinned vortices per dot increases.

We considered also the case of a thin superconducting film (SC), covered with a lattice of cubic out-of-plane magnetized dots (MDs). In this case, the accent was on vortex configurations induced in the sample by magnetic dots themselves, in the absence of any background magnetic field. Apparently, due to the phase conservation and the specific magnetic field profile of the dots with total flux penetrating the superconductor equal zero, isolated vortices can not appear and vortex-antivortex pairs nucleate in the sample. The vortices are confined to the MD regions, and antivortices form regular lattices at interstitial sites, which relax through several second order transitions towards single-dot vortex-antivortex configurations with increasing period of the magnetic array (described in Chapter 4). Creation of vortex-antivortex pairs with increasing MD-magnetization is controlled by a single quantity - the superfluid velocity. An effort to conform with the geometry of the imposed magnetic field at expense of the energy results in metastability of fractional states, where some of the magnetic dots share a vortex-antivortex pair.

In the case of a superconducting sample nanostructured by magnetic dots in a homogeneous external magnetic field, we demonstrated that due to the vortex-antivortex pairs and the supercurrents induced by the MDs, the critical current in the sample actually increases when exposed to external magnetic field, contrary to conventional SC behavior. We also discussed the so-called magnetic field-induced-superconductivity, when the external magnetic field actually compensates part of the stray field of the dots, restoring superconductivity in those particular regions. We found that magnetic nanostructuring enhances the critical field of the sample, and explained it by vortex-antivortex annihilation which occurs when external flux lines interact with existing vortex-antivortex pairs induced in the sample by magnetic dots. The excellent agreement with experimental results [8] was demonstrated through $H_{ext} - T$ phase boundary, with several observed features that we explained from the point of view of the characteristic vortex structure.

# *Samenvatting*

In deze thesis onderzoeken we theoretisch de vortexstructuur, flux pinning en de kritische parameters van magnetische gestructureerde supergeleiders. In het bijzonder, beschouwen we mesoscopische supergeleidende systemen (schijfjes en dunne films) bedekt met ferromagneten, en dit met een afmeting vergelijkbaar met één van de twee karakteristieke lengte-schalen: de coherentielengte $\xi$ of de magnetische penetratielengte $\lambda$. Mesoscopische supergeleiders zijn de laatste jaren een interessant studieonderwerp geworden, aangezien de kritische parameters en de vortexconfiguraties van zulke stalen niet alleen bepaald worden door het materiaal en de eigenschappen van het extern magnetisch veld, maar ook door de vorm van de rand en de karakteristieke omvang van het monster.

De studie voorgesteld in deze thesis is geconcentreerd rond één vraag: *Wat is het effect van magnetische nanostructurering op de supergeleidende eigenschappen*?

Vooreerst, is het algemeen geweten dat vortices in supergeleidende films (en bulkmonsters) zich organiseren in een driehoekig rooster door de wederzijdse interactie. Maar zelfs de kleinste fluctuaties in het systeem zullen leiden tot het bewegen van de vortices, het toenemen van dissipatie en het verminderen van alle belangrijke supergeleidingseffecten. Daarom is het cruciaal voor praktische toepassingen om de beweging van vortices te voorkomen. In dit opzicht, kunnen magnetische deeltjes op (in) het preparaat dienen als uitstekende **artificiële pinning centra**, omwille van de interactie van hun magnetisch veld met de vortices in de supergeleider. Tegelijkertijd kan dit niet-homogeen storingsveld

van de magneet (magneten) de andere parameters van de onderliggende supergeleider sterk beïnvloeden. Het feit dat de totale magnetische flux van ieder magnetisch deeltje nul is, geeft aanleiding tot de verschijning van een aantal nieuwe fenomenen, in het bijzonder vortex-antivortex structuren. Het toevoegen van verschillende magnetische anisotropieën in de magneet (bijvoorbeeld, in-, uit- of uit het-vlak-magnetisering) verhoogt de **rijke fenomenologie** van deze supergeleider/ferromagnetische hybride systemen. En tot slot, aangezien de bruikbaarheid van supergeleiders bepaald wordt door zijn kritische parameters: de maximale temperatuur, stroom en magnetisch veld, is het interessant om te zien hoe de magnetische nano-structurering de eigenschappen beïnvloedt. Men kan verwachten dat nano-engineering, door het **lokaal definiëren van het magnetische veld** in het preparaat, een krachtig werktuig kan zijn om de kritische parameters van een supergeleider te controleren.

In wat volgt, vatten we de theoretische bevindingen samen zoals voorgesteld in deze thesis.

**Hoofdstuk 1** geeft een korte introductie van theoretische en experimentele aspecten van supergeleiding en magnetisme. We geven een afleiding van de Ginzburg-Landau vergelijkingen, welke de centrale vergelijkingen zijn in het kader van deze thesis. De karakteristieke lengte-schalen en de verschillen tussen type-I en type-II supergeleiders worden besproken. Voor mesoscopische supergeleiders definiëren we de giant vortex toestand en de multivortex toestanden alsook de vorticiteit $L$ die de verschillende vortexconfiguraties karakteriseert. We bespreken ook in het kort de vortex-pinning in type-II supergeleiders. Het tweede deel van dit hoofdstuk is geweid aan de basisconcepten van magnetisme en levert een beschrijving van de magnetostatische berekeningen. Ten slotte worden de toepassingen van hybride ferromagnetische/supergeleidende nano-systemen en hun experimentelen toepassingen besproken.

In **hoofdstuk 2** bespreken we het magnetisch pinnen van vortices in supergeleidende films (SG) ten gevolge van enkelvoudige magneten. Om de vortex interactie te onderzoeken met een magnetisch dipoolmoment (MD) of een ferromagneet (FM) van eindige afmetingen (FM) boven (of onder) de SG, pasten we de London-theorie toe. Afhankelijk van de richting van het magnetisch dipoolmoment, verkregen we exacte analytische uitdrukkingen voor de MD-vortex interactie-energie en de zogenaamde screening stroom. Het asymptotisch gedrag van de interactie-potentiaal en de geïnduceerde stromen voor specifieke waarden van de relevante parameters werd verkregen, hetgeen cruciaal is voor de experimenten. We berekenden de pinning-potentiaal voor zowel de in-het-vlak als uit-het-vlak gemagnetiseerde FMs. Onze resultaten tonen aan dat de magneet uit-het-vlak een vortex aantrekt als hij evenwijdig gealinieerd staat en omgekeerd, de magneet stoot de vortex af wanneer hij omgekeerd evenwijdig staat. Dit is een gevolg van de mono-directionele supergeleidende stroom die in de SG geïnduceerd wordt voor een uit-het-vlak magnetisatie van de FM. Voor de in-het-vlak magnetisatie echter, toont de FM-vortex interactie een duaal gedrag. De vortex wordt namelijk aangetrokken tot de negatieve pool van

de MD en afgestoten aan de andere kant. Omwille van dit duaal gedrag van de pinning-potentiaal, hebben we de mogelijke coëxistentie van vortices en antivortices onderzocht in zulke systemen. De berekening van de totale interactie energie hebben ons naar de conclusie geleid dat een vortex en een antivortex gescheiden worden door een energie barriére die te wijten is aan de korte-dracht interactie met de magneet. Hierdoor kunnen deze paren stabiel zijn. Zowel de in-het-vlak als uit-het-vlak magneten zijn in staat deze vortices uit elkaar te houden. In de aanwezigheid van vortex-antivortex paren (of zogenaamde giant vortex-single antivortices), berekenden we de interactie potentiaal analytisch. Eveneens gaven we schattingen van de parameters die nodig zijn om de stabiliteit te kunnen garanderen van zulke boeiende configuraties in een dunne SG film.

In de analyse die volgt, beschouwden we de invloed van de geometrie van de magneet op het pinnen van de flux. In het geval van een magnetische schijf met een gat dat zich niet gecentreerd bevindt, toonden we aan dat er twee lokale minima bestaan in de FM-vortex interactie energie: de grondtoestand en de metastabiele toestand. We toonden ook aan dat er in het geval van een FM schijf met twee rakende gaten (een "acht-gat") twee minima bestaan met dezelfde energie maar met verschillende posities voor de vortices. Er bestaat een gelijke kans dat een vortex zich in één van deze twee toestanden bevindt. Dit maakt het systeem interessant als mogelijke qubit. We berekenden eveneens de pinning-potentiaal voor vierkantige en driehoekige ferromagneten. Er vindt een substantiële symmetrie-breking plaats en de aantrekkende kracht die op de vortex inwerkt is sterker aan de zijden van de magneet dan aan de hoekpunten. Hoewel, contra-intuïtief, toonden we aan dat de vortex de niet-circulaire magneet eerder langs de hoekpunten benadert dan loodrecht op de zijden, alzo de steilste energie-gradiënt volgend.

De geometrie speelt ook een belangrijke rol voor de pinning eigenschappen van een in-het-vlak gemagnetiseerde FM die zich boven de SG bevindt. In het geval van een magnetische strip bovenop de supergeleider, vonden we dat de evenwichtspositie voor een uitwendige flux lijn die gepind wordt door de strip, in een "kanaal" ligt, evenwijdig aan de magnetische structuur. De exacte positie van dit evenwichtskanaal hangt af van zowel de dikte van de SG en de magneet.

We vonden eveneens dat alle flux lijnen met dezelfde polariteit gepind werden aan dezelfde zijde van de strip. Daarom is het mogelijk dat, wanneer een magnetische structuur zich bovenop een supergeleider bevindt in de aanwezigheid van een homogeen magnetisch veld, er een supergeleidende zone ontstaat zonder vortices. Als het pinningkanaal relatief ver ligt van de strip, is het mogelijk om, in het geval van een supergeleider van eindige grootte, de volledige supergeleider vortex-vrij te maken en dit is erg belangrijk voor toepassingen.

Voor een magnetische in-het-vlak staaf als pinning centrum, bespraken we de pinning die afhangt van de veldpolariteit. We vonden dat een vortex of een antivortex in deze systemen gepind wordt aan tegenovergestelde polen van

de staaf. Aan welke pool de vortex gepind zal worden, hangt echter af van de sterkte van de magnetisatie van de magneet en de mogelijke aanwezigheid van een vortex-antivortex paar, dat door de magneet zelf geïnduceerd is in de SG. Onze resultaten zijn meer algemeen geldig maar komen overeen met de experimenten van M.J. Van Bael *et al.* [Phys. Rev. Lett. **86**, 155 (2001)]. Onze analyse voorspelt dat de positie van de gepinde vortex afgesteld kan worden door de sterkte van de magnetisatie van de FM aan te passen.

In **hoofdstuk 3** wordt de supergeleidende toestand van een dunne mesoscopische supergeleidende schijf met een magnetische stip (of stroom-lus) erop beschreven in het Ginzburg-Landau formalisme. We veronderstellen dat de supergeleidende schijf voldoende dun is zodat het magnetisch veld dat ontstaat door de supergeleidende stromen, verwaarloosd kan worden. Het effect van de grootte en de magnetisatie van de stip, en de grootte van de supergeleidende schijf op de vortex configuraties werd onderzocht.

We vonden verscheidene fase-overgangen tussen toestanden met verschillende angulaire momenten en tussen giant en multi-vortex toestanden, alsook overgangen in de grondtoestand tussen verschillende multi-vortex configuraties (giant-ring en giant-giant multivortices toestanden). Een grotere straal van de magnetische stip verbetert de stabiliteit van de giant-giant multivortices en als de supergeleidende schijf vergroot wordt, daalt de energie van de giant-ring multivortex toestand. In dit geval kan de giant-giant multivortex toestand ook de grondtoestand zijn maar het vertegenwoordigt een nieuwe configuratie: een giant vortex die omringd wordt door antivortices en de totale vorticiteit is gelijk aan de laagste vorticiteit van de giant vortex toestanden die in het spel zijn. We vonden dat wanneer de grootte van de schijf vergroot wordt, er mogelijk re-entrant gedrag optreedt van de totale vorticiteit.

Wanneer behalve het stray veld van de magnetische stip, ook een homogeen magnetisch achtergrondveld wordt aangelegd, zien we een kwalitatief verschil in het diagram van de vrije energie. Wanneer het uitwendig veld een waarde heeft tussen de gemiddelde waarde van de stip in de positieve en negatieve zone, zien we een sterke interplay van de verschillende supergeleidende toestanden. Meer nog, met stijgende waarden van de dikte van de stip, verkrijgen we twee sterke minima in de vrije energie als functie van het aangelegde veld wanneer het totale veld ongeveer nul is in de zone voor $\rho < R_d$ en de zone voor $\rho > R_d$ met $R_d$ de straal van de stip. Nadat we temperatuur introduceerden in onze berekeningen, werd een $H_{ext} - T$ fase lijn geconstrueerd. We vonden dan een tweevoudig effect van een inhomogeen magnetisch veld op de nucleatie van de supergeleiding: de fase-lijn wordt verschoven langs de $H$-as en verstoort eveneens de fase-lijn langs de $T$-as. Dit heeft tot gevolg dat de waarden waarop de structuur verspringt tussen verschillende vorticiteiten, veranderd worden. De fase-lijn die berekend wordt, komt perfect overeen met de experimentele data van D.S. Golubović *et al.* [Europhys. Lett. **65**, 546 (2004)].

In **Hoofdstuk 4** breiden we onze aanpak verder uit om de vortexconfiguratie van een oneindige supergeleidende film met één enkele magnetische stip

erbovenop te onderzoeken. Ten gevolge van het behoud van de fase en het nul zijn van de totale netto flux door de supergeleider vonden we, in de Ginzburg-Landau theory, een schilgestructureerde vortex-antivortex configuratie met totale vorticiteit nul. In zulk een situatie onderzochten we de creatie en evolutie van de evenwichts-vortexconfiguraties. Voor kleinere magnetische stippen wordt een giant vortex gevormd onder de stip die omringd wordt door enkelvoudige antivortices. Wanneer de magnetisatie van de stip toeneemt gaat de supergeleider door opeenvolgende vortex toestanden, waarbij de vorticiteit van de giant vortex en het aantal antivortices toeneemt. Voor een gegeven afmeting van de stip en een voldoende groot magneetveld zal het aantal antivortices een kritische hoeveelheid bereiken, wanneer hun onderlinge afstoting de configuratie herschikt: in plaats van op één cirkel, zijn ze dan verdeeld op twee (of meer) concentrische cirkels rond de giant vortex. Deze kritische hoeveelheid van antivortices hangt zowel af van de magnetisatie als van de afmetingen van de stip. Bovendien is het mogelijk dat met toenemende grootte van de stip niet alleen de antivortices zich herschikken maar dat ook de giant vortex zich opsplitst in multivortices. Met toenemend magnetisch veld verschuiven de vortices naar het midden van de stip. Zowel de multivortices onder de stip als de schilstructuur van de antivortices worden duidelijk beïnvloed door de geometrie van de magneet. De vortex configuratie komt overeen met de opgelegde symmetrie. Onafhankelijk van de vorm van de magneet ontstaan nieuwe vortex-antivortex paren onder de rand van de magnetisch schijf, waar de geïnduceerde stroom in de supergeleider maximaal is. We beschreven het dynamische proces van het ontstaan van vortex-antivortex paren en de geleidelijke overgang van de vortex configuratie tussen twee stabiele toestanden, waarbij de vortex van het nieuwe paar samensmelt met de giant vortex (voor kleine magnetische schijven) terwijl de antivortex verschuift naar de buitenkant, met als gevolg een herschikking van de antivortices naar de stabiele toestand.

We verwachten dat de voorspelde vortex structuren binnenkort zullen waargenomen kunnen worden met behulp van scanning technieken zoals bijvoorbeeld Hall en Magnetische Kracht Microscopie. Deze structuren beïnvloeden ook de pinning eigenschappen en het supergeleidende fase-diagram [zie M. Lange *et al.*, Phys. Rev. Lett. **90**, 197006 (2003)] zoals werd aangetoond in **hoofdstuk 5**.

We hebben de volledige, niet-lineaire Ginzburg-Landau theorie toegepast om de vortex structuren van een dunne SG film te onderzoeken met daarop een regelmatige verdeling van uit-het-vlak magnetische schijven. We veronderstelden eerst een kleine magnetisatie voor de magnetische schijfjes, en stelden dan het systeem bloot aan een extern magneetveld. Dit magneetveld is niet voldoende sterk om vortices te maken, maar kan wel de externe flux-lijnen invriezen, wat belangrijk is voor praktische toepassingen aangezien een verminderde dissipatie de kritische stroom verhoogt. We vonden dat vortex-pinnende eigenschappen van een magnetisch schijfje afhangen van de polarisatie.

Als het magnetische moment evenwijdig is met het aangelegde veld worden de vortices aangetrokken door de schijfjes, en omgekeerd. Dit resultaat is in goede overeenkomst met de metingen van M.J. Van Bael *et al.* [Phys. Rev. B **68**, 014509 (2003)]. In dit geval worden de vortices eerst gepind door de schijfjes tot verzadiging van de magnetische schijfjes optreedt. Latere vortices groeperen zich op interstitiële plaatsen en vormen een stijf rooster, gelijkaardig aan roosters die experimenteel gevonden worden in het geval van vortex-pinning door antidots [zie K. Harada *et al.*, Science **274**, 1167 (1996)].

In het anti-parallelle geval vermijden de vortices de schijfjes en vullen de interstitiële ruimte in een regelmatig patroon. In het geval van kleine magnetische schijfjes, die niet in staat zijn om meer dan één vortex te pinnen, vonden we dat de vortexstructuur voor geheel matching velden in het antiparallel geval $H_{-n}$ overeenkomt met die van het $H_{n+1}$ in het evenwijdige geval (indien de vortices gepind bij de magnetische punten verwaarloosd worden). Het is duidelijk dat het magnetische schijfje in het antiparallel geval de vortices afstoot, en de rol overneemt van de gepinde vortex in het evenwijdige geval.

Natuurlijk hangt dit af van de parameters van het systeem, in het bijzonder van de geometrische eigenschappen van de schijfjes. Als de magnetisatie van de schijfjes toeneemt verhoogt hun verzadigingsgetal ook, en dat verandert de vortexstructuur. Vertrekkende van een hoger matching veld, worden meer vortices gepind door de schijfjes, terwijl de overblijvende interstitiële vortices zich opstellen in een structuur die overeenkomt met een lager matching-getal. Een toename van de grootte van de schijfjes heeft een vergelijkbaar effect, met als verschil dat de grotere schijfjes meer vortices kunnen pinnen.

Ondanks het feit dat ze magnetisch gescheiden zijn van andere vortices voelen gepinde vortices nog steeds hun buren, en structureren ze zich in een lage-energie structuur. In het antiparallel geval verminderen grotere schijfjes de beschikbare ruimte voor vortices op interstitiële posities, en dit resulteerd in een zig-zag patroon. Het moet benadrukt worden dat het verzadigingsgetal van de schijfjes afhangt van hun straal, zelfs voor een vast magnetisch moment. Het aantal gepinde vortices per schijfje toeneemt als hun grootte toeneemt, zelfs als de magnetisatie afneemt.

We beschouwden ook het geval van een dunne supergeleidende (SG) film, met daarop een rooster van kubische, uit-het-vlak gemagnetiseerde schijfjes (MSs). De nadruk ligt op de vortex struktuur geïnduceerd door de magnetische punten zelf, zonder een extern aangelegd magnetisch veld. Door het fase-behoud en het specifieke magnetisch veld profiel van de schijfjes (met totale flux nul dat doorheen de supergeleider dringt) kunnen geïsoleerde vortices niet voorkomen en enkel vortex-antivortex paren vormen zich. Deze kunnen enkel onder het MS gebied voorkomen, en antivortices vormen een regelmatig rooster op interstitiële rooster posities, die relaxeren door verscheidene tweede-orde fase-overgangen naar een toestand van één vortex-antivortex paar per schijfje als de periode van de magnetische matrix toeneemt (zie hoofdstuk 4). Het ontstaan van vortex-antivortex paren bij verhoging van de MS-magnetisatie wordt geregeld door

slechts één parameter: de supergeleidende snelheid. Een poging om de geometrie van het aangelegde magnetische veld te volgen, ten koste van de energie, leidt ertoe dat de fractionele toestanden metastabiel worden, en dat sommige van de magnetische punten een vortex-antivortex paar delen.

In het geval er een extern homogeen magnetische veld aangelegd wordt, toonden we aan dat de kritische stroom in het systeem toeneemt, in tegenstelling met gewone supergeleiding. De reden hiervoor is dat er vortex-antivortex paren en superstroom gevormd worden in het preparaat ten gevolge van de MSs. We bespraken ook het zogenaamde 'magnetisch veld geïnduceerde supergeleiding', waarbij het externe magnetische veld het veld van de schijfjes kompenseert en daarbij het systeem opnieuw supergeleidend maakt. We vonden dat de magnetische nanostrukturen het kritische veld van het systeem vergroten, en verklaarden dit door de vernietiging van vortices met antivortices. Dit treedt op wanneer externe magneetlijnen interageren met bestaande vortex-antivortex paren gevormd door een schijfje. Goede overeenkomsten met de experimentele resultaten van M. Lange *et al.* [Phys. Rev. Lett. **90**, 197006 (2003)] werden aangetoond doorheen de $H_{ext} - T$ fase-grens, waarbij we verschillende eigenschappen van de waarnemingen verklaarden met behulp van de karakteristieke vortexstructuur.

# *References*


1. Ž. Radović, M. Ledvij, Lj. Dobrosavljević-Grujić, A. I. Buzdin, and J. R. Clem, Phys. Rev. B **44**, 759 (1991).

2. J. I. Martin, M. Velez, J. Nogues, and I. K. Schuller, Phys. Rev. Lett. **79**, 1929 (1997).

3. V. V. Moshchalkov, ESF-conference *Vortex Matter in Superconductors II*, lecture-CD (2001).

4. V. V. Moshchalkov, L. Gielen, C. Strunk, R. Jonckheere, X. Qiu, C. Van Haesendonck and Y. Bruynseraede, Nature (London) **373**, 319 (1995).

5. A. K. Geim, I. V. Grigorieva, S. V. Dubonos, J. G. S. Lok, J. C. Maan, A. E. Filippov, and F. M. Peeters, Nature (London) **390**, 256 (1997).

6. D. S. Golubović, W. V. Pogosov, M. Morelle, and V. V. Moshchalkov, Appl. Phys. Lett. **83**, 1593 (2003).

7. D. S. Golubović, W. V. Pogosov, M. Morelle, and V. V. Moshchalkov, Europhys. Lett. **65**, 546 (2004).

8. M. Lange, M. J. Van Bael, Y. Bruynseraede, and V. V. Moshchalkov, Phys. Rev. Lett. **90**, 197006 (2003).

9. H. Kamerlingh Onnes, Commun. Phys. Lab. **12**, 120 (1911).

10. W. Meissner and R. Ochsenfeld, Naturwiss. **21**, 787 (1933).

11. F. London and H. London, Proc. Roy. Soc. **A149**, 71 (1935).

12. V. L. Ginzburg and L. D. Landau, Zh. Eksp. Teor. Fiz. **20**, 1064 (1950).

13. A. A. Abrikosov, Sov. Phys. JETP **5**, 1175 (1957).

14. J. Bardeen, L. N. Cooper, and J. R. Schrieffer, Phys. Rev. **108**, 1175 (1957).

15. A.J. Leggett, Revs. Mod. Phys. **47**, 331-414 (1975).

16. L. P. Gor'kov, Sov. Phys. JETP **9**, 1364 (1959).

17. J. G. Bednorz and K. A. Müller, Z. Phys. B **64**, 189 (1986).

18. A. Schilling, M. Cantoni, J. D. Guo, and H. R. Ott, Nature (London) **363**, 56 (1993).

19. S. N. Putilin, E. V. Antipov, A. M. Abakumov, M. G. Rozova, K. A. Lokshin, D. A. Pavlov, A. M. balagurov, D. V. Sheptyakov, M. Marezio, Physica C **338**, 52 (2000).

20. B. J. Baelus, *Vortex matter in mesoscopic superconductors*, PhD thesis, UIA, Antwerpen, 2002.

21. A. F. Hebard, M. J. Rosseinsky, R. C. Haddon, D. W. Murphy, S. H. Glarum, T. T. M. Palstra, A. P. Ramirex, and A. R. Kortan, Nature (London) **350**, 600 (1991).

22. E. Dagotto, Science **293**, 2410 (2001).

23. M. Côté, J. C. Grossman, M. L. Cohen, and S. G. Louie, Phys. Rev. Lett. 81, 697 (1998).

24. J. Nagamatsu, N. Nakagawa, T. Muranaka, Y. Zenitani, and J. Akimitsu, Nature (London) **410**, 63 (2001).

25. L. D. Landau and E. M. Lifshitz, *Statistical Physics*, 3rd edn., part 1 (Pergamon Press, Oxford, 1980).

26. A. Schmid, Phys. Kond. Materie **5**, 302 (1966).

27. K. Takanaka, Phys. Stat. Sol. B **68**, 623 (1975).

28. H. W. Weber, F. M. Sauerzopf, and E. Seidl, Physica B **107** 429 (1981).

29. P. G. de Gennes, *Superconducting of Metals and Alloys* (Benjamin, New York, 1966).

30. J. Romijn, T. M. Klapwijk, M. J. Renne, and J. E. Mooij, Phys. Rev. B **26**, 3648 (1982).

31. M. Tinkham, *Introduction to Superconductivity* (McGraw Hill, New York, 1975).

32. V. V. Schmidt, P. Müller, A. V. Ustinov, *The Physics of Superconductors: Introduction to Fundamentals and Applications* (Springer-Verlag, Berlin Heidelberg, 1997).

33. D. Saint-James, G. Sarma, and E. J. Thomas, *Type II Superconductivity* (Pergamon Press, Oxford, 1969).

34. H. B. Nielsen and P. Olesen, Nucl. Phys. B **160**, 380 (1979).

35. J. Ambjørn and P. Olesen, Phys. Lett. B **218**, 67 (1989).

36. L. N. Cooper, Phys. Rev. **104**, 1189 (1956).

37. L. Neumann and L. Tewordt, Z. Phys. **189**, 55 (1966).

38. S. V. Yampolskii and F. M. Peeters, Phys. Rev. B **62**, 9663 (2000).

39. B. J. Baelus, S. V. Yampolskii, F. M. Peeters, E. Montevecchi, and J. O. Indekeu, Phys. Rev. B **65**, 024510 (2002).

40. P. Singha Deo, V. A. Schweigert, F. M. Peeters, and A. K. Geim, Phys. Rev. Lett. **79**, 4653 (1997).

41. M. Tinkham, Rev. Mod. Phys. **36**, 268-276 (1964).

42. R. Prozorov, E. B. Sonin, E. Sheriff, A. Shaulov, and Y. Yeshurun, Phys. Rev. B **57**, 13845 (1998).

43. M. M. Doria, J. E. Gubernatis, and D. Rainer, Phys. Rev. B **39**, 9573 (1989).

44. R. Kato, Y. Enomoto, and S. Maekawa, Phys. Rev. B **47**, 8016 (1993).

45. V. A. Schweigert, F. M. Peeters, and P. Singha Deo, Phys. Rev. Lett. **81**, 2783 (1998).

46. A. C. Rose-Innes and E. H. Rhoderick, *Introduction to Superconductivity* (Pergamon Press, Oxford, 1969).

47. H. W. Meul, C. Rossel, M. Decroux, Ø. Fischer, G. Remenyi, and A. Briggs, Phys. Rev. Lett. **53**, 497 (1984).

48. V. Jaccarino and M. Peter, Phys. Rev. Lett. **9**, 290 (1962).

49. M. Giroud, O. Pena, R. Horyn, and M. Sergent, J. Low Temp. Phys. **69**, 419 (1987).

50. S. Uji, H. Shinagawa, T. Terashima, T. Yakabe, Y. Terai, M. Tokumoto, A. Kobayashi, H. Tanaka, and H. Kobayashi, Nature (London) **410**, 908 (2001).

51. E. H. Brandt, Braz. J. Phys. **32**, 675 (2002).

52. M. Fusco-Girard and F. Mancini, Physica B&C **123**, 75 (1983).

53. J. Pearl, Appl. Phys. Lett. **5**, 65 (1964).

54. Yu. E. Lozovik and E. A. Rakoch, Phys. Rev. B **57**, 1214 (1998).

55. R. B. Vandover, E. M. Gyorgy, L. F. Schneemeyer, J. W. Mitchell, K. V. Rao. R, Puzniak, and J. V. Waszczak, Nature (London) **342**, 55 (1989).

56. L. Civale, A.D. Marwick, T. K. Worthington, M. A. Kirk, J. R. Thompson, L. Krusin-Elbaum, Y. Sun, J. R. Clem, and F. Hotzberg, Phys. Rev. Lett. **67**, 648 (1991).

57. M. Baert, V.V. Metlushko, R. Jonckheere, V.V. Moshchalkov, and Y. Bruynseraede, Phys. Rev. Lett. **74**, 3269 (1995).

58. J. Evetts (ed.), *Concise Encyclopedia of Magnetic and Superconducting Materials* (Pergamon Press, Oxford, 1992).

59. Ž. Radović and Lj. Dobrosavljević, in "Recent Developments in Condensed Matter Physics", Vol. 4, Ed. J. T. Devreese (Plenum Publishing Corporation, 1981).

60. A. G. Meshkovskii and A. I. Shalnikov, Zh. Eksp. Teor. Fiz. **17**, 851 (1947).

61. H. F. Hess, R. B. Robinson, R. C. Dynes, J. M. Valles, Jr., and J. V. Waszczak, Phys. Rev. Lett. **62**, 214 (1989).

62. K. Harada, O. Kamimura, H. Kasai, T. Matsuda, A. Tonomura, and V.V. Moshchalkov, Science **274**, 1167 (1996).

63. A. Oral, S. J. Bending, R. G. Humphreys, and M. Henini, Supercond. Sci. Technol. **10**, 17 (1997).

64. S. J. Bending, *Local magnetic probes in superconductors*, Advances in Physics **48**, 449 (1999).

65. P. E. Goa, H. Hauglin, M. Baziljevich, E. Il'yashenko, P. L. Gammel, and T. H. Johansen, Supercond. Sci. Technol. **14**, 729 (2001).

66. G. F. Zharkov, V. G. Zharkov, and A. Yu. Zvetkov, Phys. Rev. B **61**, 12293 (2000).

67. B. J. Baelus and F. M. Peeters, Phys. Rev. B **65**, 104515 (2002).

68. L. R. E. Cabral, B. J. Baelus, and F. M. Peeters, submitted to Phys. Rev. B.

69. V. A. Schweigert and F. M. Peeters, Phys. Rev. B **57**, 13817 (1998).

70. D.J. Craik and R.S. Tebble, *Selected Topics in Solid State Physics: Ferromagnetism and Ferromagnetic Domains*, (North-Holland Publishing Company, Amsterdam, Netherlands and John Wiley and Sons, New York, NY, 1965).

71. David D. Awschalom and David P. DiVincenzo, *Complex Dynamics of Mesoscopic Magnets*, Phys. Today **48** (4), 43 (1995).

72. J. D. Jackson, *Classical Electrodynamics*, 2nd ed. (John Wiley and Sons, New York, 1975).

73. S. D. Bader, J. Magn. Magn. Mater. **100**, 440 (1991).

74. J.P. Wikswo, *SQUID Magnetometers for Biomagnetism and Nondestructive Testing: Important Questions and Initial Answers*, in: IEEE T. Appl. Supercon. **5**(2), 293 (1995).

75. L. N. Bulaevskii, E. M. Chudnovsky, and M. P. Maley, Appl. Phys. Lett. **76**, 2594 (2000).

76. D. J. Morgan and J. B. Ketterson, Phys. Rev. Lett. **80**, 3614 (1998).

77. M. A. Nielsen and I. L. Chuang, *Quantum Computation and Quantum Information* (Cambridge Univ. Press, Cambridge, 2000).

78. D. S. Golubović, W. V. Pogosov, M. Morelle, and V. V. Moshchalkov, Phys. Rev. Lett. **92**, 177904 (2004).

79. J. E. Villegas, S. Savelev, F. Nori, E. M. Gonzalez, J. V. Anguita, R. García, J. L. Vicent, Science **302**, 1188 (2003).

80. V. V. Shmidt, Sov. Phys.- JETP **30**, 1137 (1970).

81. M. J. Van Bael, L. Van Look, K. Temst, M. Lange, J. Bekaert, G. Guentherodt, V. V. Moshchalkov, and Y. Bruynseraede, Physica C **332**, 12 (2000).

82. M. Lange, M. J. Van Bael, L. Van Look, K. Temst, J. Swerts, G. Guentherodt, V. V. Moshchalkov, and Y. Bruynseraede, Europhys. Lett. **53**, 646 (2001).

83. I. F. Lyuksyutov and V. L. Pokrovsky, Phys. Rev. Lett. **81**, 2344 (1998).

84. I. F. Lyuksyutov and V. L. Pokrovsky, cond-mat/9903312.

85. S. Erdin, A. F. Kayali, I. F. Lyuksyutov, and V. L. Pokrovsky, Phys. Rev. B **66**, 014414 (2002).

86. A. F. Kayali, Phys. Lett. A, **298**, 432 (2002).

87. R. Sasik and T. Hwa, cond-mat/0003462.

88. I. K. Marmorkos, A. Matulis, and F. M. Peeters, Phys. Rev. B **53**, 2677 (1996).

89. Sa-Lin Cheng and H. A. Fertig, Phys. Rev. B **60**, 13107 (1999).

90. J. H. Xu, J. H. Miller, Jr., and C. S. Ting, Phys. Rev. B **51**, 424 (1995).

91. J. C. Wei, J. L. Chen, L. Horng, and T. J. Yang, Phys. Rev. B **54**, 15429 (1996).

92. Mark W. Coffey, Phys. Rev. B **52**, R9851 (1995).

93. M. J. Van Bael, J. Bekaert, K. Temst, L. Van Look, V. V. Moshchalkov, Y. Bruynseraede, G. D. Howells, A. N. Grigorenko, S. J. Bending, and G. Borghs, Phys. Rev. Lett. **86**, 155 (2001).

94. L. D. Landau and E. M. Lifshitz, *Theoretical Physics*, *Electrodynamics of continuous media* (Pergamon, Oxford, 1989).

95. A. S. Mel'nikov, Yu. N. Nozdrin, I. D. Tokman, and P. P. Vysheslavtsev, Phys. Rev. B **58**, 11672 (1998).

96. S. H. Autler, J. Low Temp. Phys. **9**, 241 (1972).

97. B. J. Baelus, F. M. Peeters, and V. A. Schweigert, Phys. Rev. B **61**, 9734 (2000).

98. L. E. Helseth, Phys. Rev. B **66**, 104508 (2002).

99. L. B. Ioffe and M. V. Feigelman, Phys. Rev. B **66**, 224503 (2002).

100. Yu. M. Ivanchenko, A. I. Kozinskaya, and Yu. V. Medvedev, Fiz. Tverd. Tela, **21**, 3445 (1979) [Sov. Phys.– Solid State **21**, 1989 (1979)].

101. A. Badia, Phys. Rev. B **63**, 094502 (2001).

102. I. S. Gradshteyn, I. M. Ryzhik, *Table of Integrals, Series, and Products* (Academic Press, London, 1994), Eq. 6.684 (p. 758).

103. O. Buisson, P. Gandit, R. Rammel, Y. Y. Wang, and B. Pannetier, Phys. Lett. A **150**, 36 (1990).

104. L. F. Chibotaru, A. Ceulemans, V. Bruyndoncx, and V. V. Moshchalkov, Nature (London) **408**, 833 (2000).

105. A. K. Geim, I. V. Grigorieva, S. V. Dubonos, J. G. S. Lok, J. C. Maan, A. E. Filippov, and F. M. Peeters, Nature (London) **390**, 259 (1997).

106. P. S. Deo, V. A. Schweigert, F. M. Peeters, and A. K. Geim, Phys. Rev. Lett. **79**, 4653 (1997).

107. R. Benoist and W. Zwerger, Z. Phys. B **103**, 377 (1997).

108. J. J. Palacios, Physica B **256-258**, 610 (1998).

109. J. J. Palacios, Phys. Rev. B **58**, R5948 (1998).

110. E. Akkermans and K. Mallick, J. Phys. A **32**, 7133 (1999).

111. P. S. Deo, F. M. Peeters, and V. A. Schweigert, Superlatt. and Microstruct. **25**, 1195 (1999).

112. G. M. Braverman, S. A. Gredeskul, and Y. Avishai, Phys. Rev. B **59**, 12039 (1999).

113. B. J. Baelus, F. M. Peeters, and V. A. Schweigert, Phys. Rev. B **63**, 144517 (2001).

114. J. I. Martin, M. Velez, A. Hoffmann, Ivan K. Schuller, and J. L. Vicent, Phys. Rev. B **62**, 9110 (2000).

115. S. V. Yampolskii and F. M. Peeters, Phys. Rev. B **62**, 9663 (2000).

116. J. Govaerts, G. Stenuit, D. Bertrand, and O. van der Aa, Phys. Lett. A **267**, 56 (2000).

117. V. A. Schweigert and F. M. Peeters, Phys. Rev. Lett. **83**, 2409 (1999).

118. J. J. Palacios, Phys. Rev. Lett. **84,** 1796 (2000).

119. V. A. Schweigert and F. M. Peeters, Physica C **332**, 266 (2000).

120. J.M. Kosterlitz and D.J. Thouless, J. Phys. C: Solid State Phys. **6**, 1181 (1973); M.R. Beasley, J.E. Mooij, and T.P. Orlando, Phys. Rev. Lett. **42**, 1165 (1979).

121. L. F. Chibotaru, A. Ceulemans, V. Bruyndoncx and V. V. Moshchalkov, Nature (London) **408**, 833 (2000); *ibid.* Phys. Rev. Lett. **86**, 1323 (2001);

V.R. Misko, V. M. Fomin, J. T. Devreese, and V. V. Moshchalkov, Phys. Rev. Lett. **90**, 147003 (2003).

122. V.M. Bedanov and F.M. Peeters, Phys. Rev. B **49**, 2667 (1994).

123. J.I. Martin, M. Velez, A. Hoffmann, I.K. Schuller, and J.L. Vicent, Phys. Rev. Lett. **83**, 1022 (1999).

124. M.J. Van Bael, K. Temst, V.V. Moshchalkov, and Y. Bruynseraede, Phys. Rev. B **59**, 14674 (1999).

125. M.J. Van Bael, M. Lange, S. Raedts, V.V. Moshchalkov, A.N. Grigorenko, and S.J. Bending, Phys. Rev. B **68**, 014509 (2003).

126. Y. Jaccard, J.I. Martin, M.-C. Cyrille, M. Velez, J.L. Vicent, and I.K. Schuller, Phys. Rev. B **58**, 8232 (1998).

127. V.V. Metlushko, L.E. DeLong, M. Baert, E. Rosseel, M.J. Van Bael, K. Temst, V.V. Moshchalkov, and Y. Bruynseraede, Europhys. Lett. **41**, 333 (1998).

128. V.V. Moshchalkov, M. Baert, V.V. Metlushko, E. Rosseel, M.J. Van Bael, K. Temst, Y. Bruynseraede, and R. Jonckheere, Phys. Rev. B **57**, 3615 (1998).

# *List of publications*

1. M. V. Milošević, S. V. Yampolskii, and F. M. Peeters, *Multi-vortex states of a thin superconducting disk in a step-like external magnetic field*, Physica C **369**, 343-346 (2002).
2. M. V. Milošević, S. V. Yampolskii, and F. M. Peeters, *Vortex structure of thin mesoscopic disks in the presence of the inhomogeneous magnetic field*, Phys. Rev. B **66**, 024515 (2002) (20 pages).
3. M. V. Milošević, S. V. Yampolskii, and F. M. Peeters, *Magnetic Pinning of Vortices in a Superconducting Film: The (anti)vortex-magnetic dipole interaction energy in the London approximation*, Phys. Rev. B **66**, 174519 (2002) (14 pages).
4. M. V. Milošević and F. M. Peeters, *Vortex Matter in the Presence of Magnetic Pinning Centra*, Journal of Low Temp. Phys. **130**, 311-320 (2003).
5. M. V. Milošević, S. V. Yampolskii, and F. M. Peeters, *The vortex-ferromagnet interaction in the London approximation*, Journal of Low Temp. Phys. **130**, 321-331 (2003).
6. F. M. Peeters, B. J. Baelus, and M. V. Milošević, *Vortex states in mesoscopic superconductors*, Physica E **18**, 312-315 (2003).
7. M. V. Milošević and F. M. Peeters, *Superconducting Wigner vortex molecule near a magnetic disk*, Phys. Rev. B **68**, 024509 (2003) (4 pages).

8. M. V. Milošević and F. M. Peeters, *Vortex-antivortex molecules near a magnetic disk on top of a superconducting film*, Physicalia Mag. **25**, 185-197 (2003).

9. M. V. Milošević and F. M. Peeters, *The interaction between a superconducting vortex and an out-of-plane magnetized ferromagnetic disk: influence of the magnet geometry*, Phys. Rev. B **68**, 094510 (2003) (12 pages).

10. G. R. Berdiyorov, B. J. Baelus, M. V. Milošević, and F. M. Peeters, *Stability and transition between vortex configurations in square mesoscopic samples with antidots*, Phys. Rev. B **68**, 174521 (2003) (19 pages).

11. M.V. Milošević and F.M. Peeters, *Vortex pinning in a superconducting film due to in-plane magnetized ferromagnets of different shapes: the London approximation*, Phys. Rev. B **69**, 104519 (2004) (10 pages).

12. G. R. Berdiyorov, B. J. Baelus, M. V. Milošević and F. M. Peeters, *The superconducting state in square mesoscopic samples with two and four antidots*, Physica C **404**, 56-60 (2004).

13. M. V. Milošević and F. M. Peeters, *Commensurate vortex configurations in thin superconducting films nanostructured by square lattice of magnetic dots*, Physica C **404**, 246-250 (2004).

14. M. V. Milošević and F. M. Peeters, *Vortex molecules in superconducting films with magnetic disk on top - influence of the magnet geometry*, Physica C **404**, 281-284 (2004).

15. G. R. Berdiyorov, M. V. Milošević, B. J. Baelus, and F. M. Peeters, *Superconducting vortex states in disks with a blind hole*, to appear in Phys. Rev. B **70** (2004) (17 pages).

16. M. V. Milošević and F. M. Peeters, *Vortex-Antivortex Lattices in Superconducting Films with Magnetic Pinning Arrays*, submitted to Phys. Rev. Lett.

# *Curriculum Vitae*

***Milošević Milorad***

Born on June 30, 1977
in Smederevo / Serbia

**Oct. 1995 - Sept. 2000**: Faculty of Electrical Engineering, Department of Physical Electronics, Microelectronics, Optoelectronics and Laser Techniques, University of Belgrade, Yugoslavia. Obtained degree of Graduate Engineer of Physical Electronics, with thesis "Quantum Wire Lasers".

**Sept. 1996 - July 2000**: Technical Assistant at Faculty of Physical Chemistry, University of Belgrade, Yugoslavia.

**Sept. 2000 - Sept. 2004**: Research Assistant in Condensed Matter Theory group, Physics Department, University of Antwerp (Campus Drie Eiken), Belgium.

Promotor: Prof. dr. F. M. Peeters

*Scientific awards*

**2002** Best oral presentation in NATO advanced research workshop on Vortex Dynamics in High Temperature Superconductors (VDHTS 2002), Tashkent, Uzbekistan.

**2003** Third prize in the best oral presentation contest at the International Scientific Meeting of the Belgian Physical Society in Ghent, Belgium.

**2004** Second prize in the best poster presentation contest at the International Scientific Meeting of the Belgian Physical Society in Mons, Belgium.